Construction of the electromagnetic calorimeter detector and study of charmonia production using hadronic final states in the LHCb experiment

S. Barsuk

LAL-14-216
Septembre 2014

Laboratoire de l'Accélérateur Linéaire

Habilitation à diriger des recherches
présentée à l'Université Paris-Sud

Construction of the electromagnetic calorimeter detector and study of charmonia production using hadronic final states in the LHCb experiment

Sergey Barsuk

Soutenue le 2 septembre 2014 devant le jury composé de

M. Yuanning Gao
M. Valery Khoze
M. Jacques Lefrançois
M. Andreas Schopper (Rapporteur)
M. Joachim Spengler (Rapporteur)
M. Achille Stocchi (Président)
Mme. Isabelle Wingerter-Seez (Rapporteur)

Contents

List of Figures

List of Tables

Chapter 1

Introduction

Everything in this book may be wrong.

Richard Bach

This document presents a written part of an "Habilitation à diriger des recherches" at Paris Sud university. Selected topics on the LHCb electromagnetic calorimeter construction and physics analysis are discussed.

Two main topics are discussed with the first one focusing on design and construction of the LHCb electromagnetic calorimeter detector modules; and the second one addressing measurements of charmonia production cross-section using charmonia decays to hadronic final states, and measurement of branching fractions of B_s^0 meson decays to ϕ mesons. The choice of the subjects follows two major principles observed in many previous Ph.D. thesis and HDR thesis topic selections, an archeological principle and a principle of combining the least correlated subjects.

Despite the fact, that the two parts center around the LHCb experiment at CERN, the principle of combining the least correlated subjects is obeyed since neither the reconstruction of charmonia production via their decays to hadronic final states, nor the reconstruction of B_s^0 meson decays to ϕ mesons, in LHCb, rely on performance or operation of the LHCb electromagnetic calorimeter [1].

[1] Minor effects, such as the use of information from the electromagnetic calorimeter in hadronic trigger operation, or triggering by electromagnetic particles, can be neglected.

The archeological principle assumed going back in time by uncovering more and more ancient layers of calorimeter construction. While within the previous LHCb-related HDR works at LAL Frédéric Machefert and Patrick Robbe discussed the front-end electronics and trigger development, as well as some operational aspects of the LHCb calorimeters, an early period, mostly before 2005, of design, construction and quality control of the electromagnetic calorimeter detector units, is addressed by the present writing.

Working for the LHCb electromagnetic calorimeter project, I was a part of ITEP Moscow and then CERN teams, closely working with LAL Orsay and LAPP Annecy groups on the electromagnetic calorimeter construction. In view of the construction of electromagnetic calorimeter detector part, discussed below, and in addition to the pleasure of sharing the work with many colleagues and friends, a contribution of several students from Moscow ITEP and MIPT, as well as CERN summer students should be acknowledged in particular to some early test beam studies of calorimeter prototypes, operation of the test setup that used cosmic rays, and mounting of the optical fibers of the calorimeter monitoring system. Charmonia production measurements and studies of B_s^0 meson decays to ϕ mesons were attacked together with other physicists at LAL and became subject of several internships for students from Paris Sud and Kiev T.Shevchenko universities.

The document is organised as follows. After the introduction, in chapter 2 the LHCb experiment is described, addressing the experiment operation at the LHC (section 2.1), physics program (section 2.2), and detector issues (section 2.3) describing reconstruction of tracks and vertices, particle identification, trigger and plans for detector upgrade. Then, in chapter 3 the LHCb calorimeters are adressed in section 3.1. Design, construction, quality control and installation of of the LHCb electromagnetic calorimeter detector is discussed in greater detail in section 3.2. Chapter 4 is devoted to charmonium production studies (section 4.1) using decays to hadronic final states in the LHCb experiment. Both prompt production (section 4.2) and inclusive charmonium yield from b-hadron decays (section 4.3) are addressed. Mass of the η_c state is measured using low-background sample of charmonia from b-hadron decays in section 4.4. In chapter 5 measurements of branching fractions for B_s^0-meson decays to ϕ mesons, $B_s^0 \to \phi\phi$ (section 5.1) and $B_s^0 \to \phi\phi\phi$ (section 5.2), are discussed. Finally, main results are reminded in chapter 6.

Chapter 2

The LHCb experiment

Vast perspective, discovering from the hill,
where Russian batteries defending the bridge were based,
suddenly became lost behind a muslin curtain of slanting rain,
then suddenly expanded, and by the rays of the sun, far
and clearly, objects became visible, as if varnished.

Lev Tolstoi

2.1 The LHCb experiment at the LHC

ALICE, ATLAS, CMS and LHCb are the four big experiments hosted by Large Hadron Collider (LHC) at CERN. Their positions are indicated on the schematic view of the CERN accelerator complex on Fig. 2.1. The LHC machine provides collisions of proton beams for these four major experiments.

Protons are successively accelerated by LINAC, PS Booster, PS and SPS. The proton bunches are injected in LHC from the SPS ring at the energy of 450 GeV.

LHC is a 27 km powerful circular accelerator, employing superconducting magnets. The LHC machine beams operated first at the injection energy of 450 GeV in 2009, at the beam energy of 3.5 TeV in 2010 and 2011, and with the beam energy of 4 TeV in 2012. The machine is being upgraded to provide a beam energy of 6.5 TeV, close to the

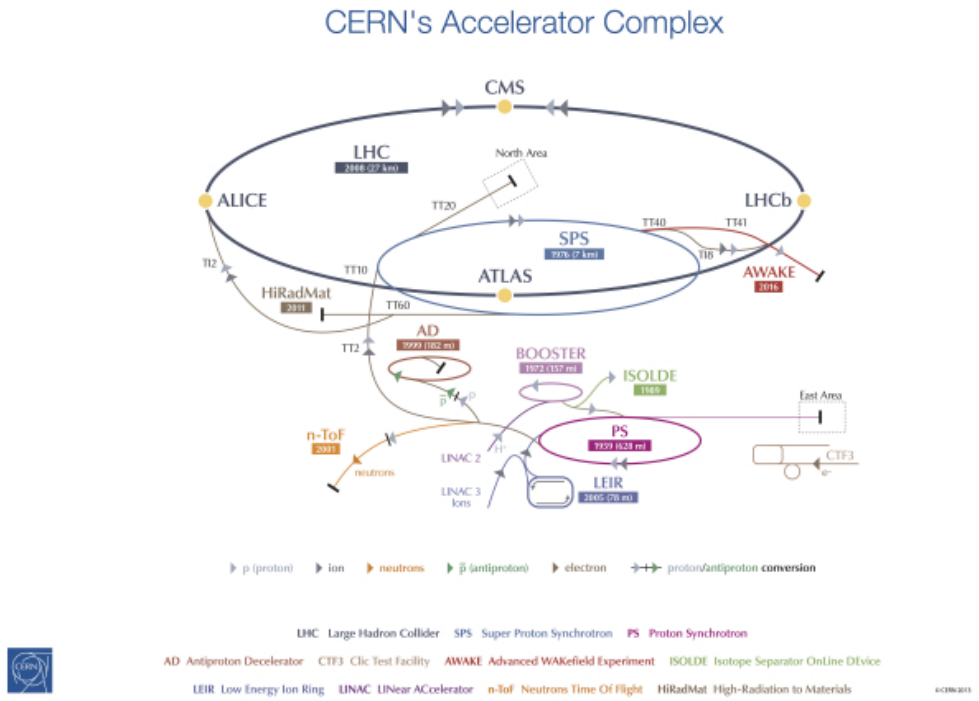

Figure 2.1: Accelerator complex at CERN

design value of 7 TeV.

Unlike ATLAS and CMS experiments, which are using clean pre-defined event signatures and high trigger thresholds for their core physics program, the LHCb experiment aims at collecting data at reduced luminosity having a limited number of pp interactions per bunch crossing. The LHCb experiment operates at a reduced LHC luminosity of $2 - 5 \times 10^{32}$ cm^{-2}s^{-1}, tuneable by defocusing or displacing beams. The initial intention was to maximize the number of beam crossings with a single pp interaction, however reliable and robust experiment operation and efficient exploitation of the collected data made it possible to increase the number of pp interactions per beam crossing. A natural limit on the luminosity increase comes when an average minimum distance between pp collision vertices in the same beam crossing becomes comparable to the average b-hadron travel distance of about 10 mm. A levelling procedure, based on the beam displacement, devoloped for the LHCb experiment, allowed to deliver to LHCb stable optimal luminosity over almost all the LHC fill duration (Fig. 2.2). Typical lifetime of the fill in a stable LHC operation mode reaches approximately 10 hours. When the luminosity delivered to ATLAS and CMS experiments becomes too low to continue

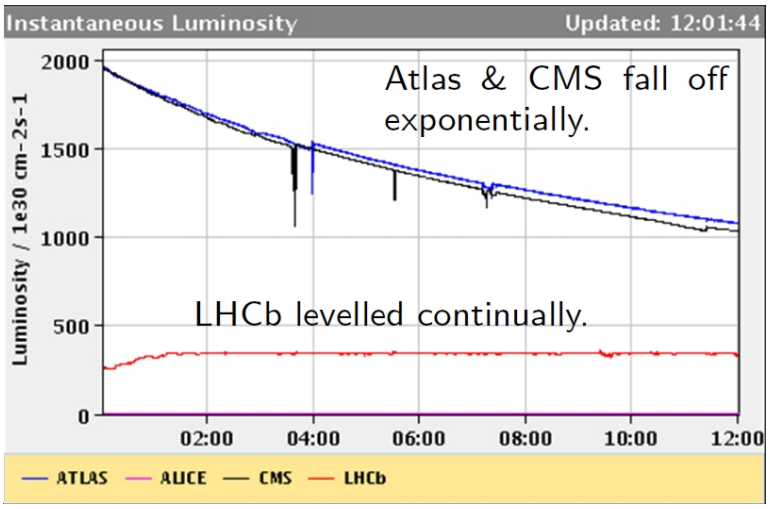

Figure 2.2: Luminosity levelling at the LHCb beam interaction point

data taking, the beam is dumped.

The LHCb experiment recorded the integrated luminosity of about 38 pb^{-1} in 2010, 1.1 fb^{-1} in 2011, 2.1 fb^{-1} in 2012 (Fig. 2.3). LHCb efficiently recorded the luminosity

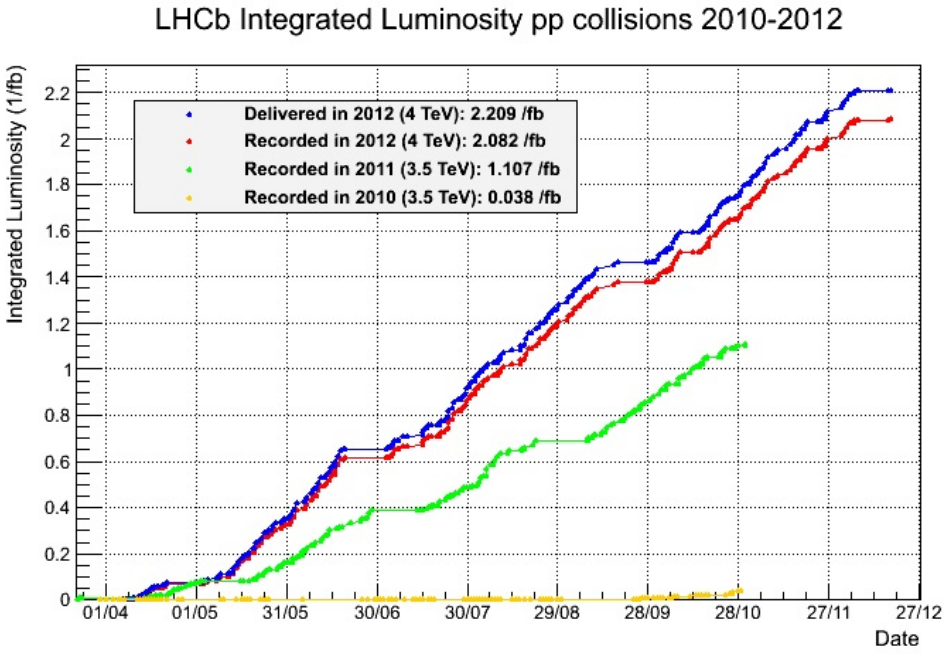

Figure 2.3: Integrated luminosity recorded by the LHCb experiment during the 2010, 2011 and 2012 data taking periods. For the 2012 data, the luminosity recorded by the LHCb experiment is compared to the luminosity delivered by the LHC machine

delivered by the LHC machine, less than 7% inefficiency are explained by the chart on Fig. 2.4.

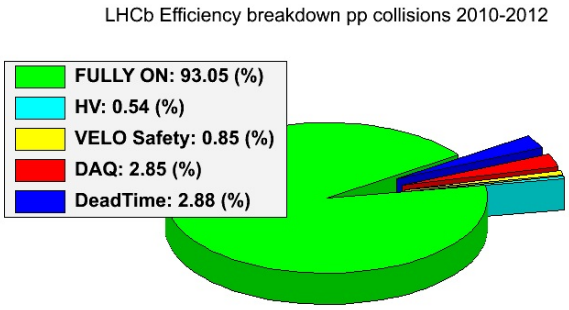

Figure 2.4: The LHCb data taking efficiency breakdown for the period from 2010 to 2012

While the LHC machine operates at 40 MHz and the design separation between the bunch crossings is 25 ns, until now a 50 ns minimum separation between the bunch crossings was used. The tests have been accomplished and experiments prepare to take data with 25 ns bunch crossings separation. This requires to minimize dead time of the individual detectors and reduce spill-over between the data samples corresponding to close bunch crossings.

2.2 Physics with LHCb

LHCb is an experiment dedicated to precision studies of rare phenomena in b and c decays in order to precisely constrain the Standard Model (SM) parameters and search for phenomena non-explainable within SM. Through quantum loop processes, potentially involving new particles or new couplings, bottom and charm quark systems are sensitive to energy scales far beyond the centre-of-mass energy of the LHC. The potential of the heavy flavour approach to discover signatures of physics beyond the SM and to distinguish between different new physics scenarios, is thus complementary to the direct searches performed by the ATLAS and CMS experiments.

The LHC is presently the richest source of c and b hadrons, reconstructed by all the LHC experiments, and LHCb is designed to fully exploit this potential. Assuming

$\sigma_{b\bar{b}} = 1.04$ mb and $\sigma_{c\bar{c}} = 8.31$ mb cross sections, about 5×10^{11} $b\bar{b}$ pairs and 3×10^{12} $c\bar{c}$ pairs will be produced per 1 fb^{-1} of integrated luminosity at a centre-of-mass energy $\sqrt{s} = 14\,\text{TeV}$. At lower LHC energies heavy flavour production rates are reduced, and about 3×10^{11} $b\bar{b}$ pairs and 2×10^{12} $c\bar{c}$ pairs per 1 fb^{-1} were produced at $\sqrt{s} = 7\,\text{TeV}$. The LHC provides a powerful tool for testing quantum chromodynamics (QCD) at high energies.

The LHCb experiment performs systematic studies of heavy flavour production and spectroscopy. Open heavy flavour production has been studied at a centre-of-mass energy $\sqrt{s} = 7\,\text{TeV}$ for B^0, B^+ and B_s^0 mesons [1] [1], promptly produced charm hadrons, D^0, D^+, D_s^+, D^{*+} mesons and Λ_c^+ baryons [2]. Production cross-section has also been measured for B_c^+ meson [3]. These measurements are in general successfully described by well-developed tools, such as fixed order with next-to-leading-log resummation (FONLL) and next-to-leading order with parton showering (POWHEG or MCatNLO) with an overview given in Ref. [4].

The theory is less predictive in describing quarkonia production, and none of the available approaches can reproduce in a consistent way the experimental results on both cross-section and polarisation [5]. The LHCb experiment studied production of $J^{PC} = 1^{--}$ charmonium states, J/ψ and $\psi(2S)$ in pp collisions at a centre-of-mass energy $\sqrt{s} = 2.76\,\text{TeV}$ [6], $\sqrt{s} = 7\,\text{TeV}$ [6], $\sqrt{s} = 8\,\text{TeV}$ [7], and in proton-lead collisions at $\sqrt{s}_{NN} = 5\,\text{TeV}$ [8]. The next-to-leading order (NLO) non-resonant QCD calculations are in general able to provide a satisfactory agreement with the observed values of the production cross-section. The production of χ_c states has been studied using their radiative decays to J/ψ [9–11], using converted and non-converted photons. Reconstruction of low-energy photons reduces the experimental precision. The NLO NRQCD calculations [12] describe the experimental results in the region of large p_{T} values. Charmonium states production, prompt production in partonic interactions and production in b-hadron decays, using charmonium decays to hadronic final states, are addressed in chapter 4. Similar studies of bottomonia production [7, 13–15] have been performed, and the measurements are successfully described by the direct next-to-next-to-leading-order NNLO* colour-singlet (CS) model [16].

Over two years of operation, LHCb has observed several new heavy flavour states, and decay modes, measured masses and lifetimes with best-to-date or competitive

[1] Throughout the document, charge-conjugate states are equally implied.

precision, provided a decisive analysis of the angular distribution in $B^+ \to X(3872)K^+$ decays to measure the quantum numbers of the X(3872) state to be $J^{PC} = 1^{++}$, supporting a $D\overline{D}^*$ molecular interpretation.

One of the main task of the LHCb experiment is to systematically study *CP*-violating effects in the b and c-hadrons. LHCb delivered the world most precise measurements in the related effect of flavour mixing, in both B^0 and B_s^0 systems. An important strategy to search for physics effects beyond SM is to compare tree-mediated processes to those involving quantum loops. Measurement of the angle γ of the Cabibbo-Kobayashi-Maskawa (CKM) unitarity triangle is a promising candidate to search for physics beyond SM. LHCb has recently provided the most precise single measurement of the angle γ of the unitarity triangle, using tree-level $B^- \to Dh^-$ decays, $\gamma = 67 \pm 12^o$ [17]. LHCb provided new important measurements of the *CP*-violating phase ϕ_s, which is very small in SM, $\phi_s = -0.0363 \pm 0.0017$ rad, via $B_s^0 \to \phi\phi$ [18] and $B_s^0 \to J/\psi\, h^+h^-$ [19] decays, and a constraint from the measurement of $B_s^0 \to K^+K^-$ effective lifetime [20]. Comparison between ϕ_s measurements using tree-level and penguin processes is important to disentangle potential new physics effects entering quantum loops. In addition LHCb is performing searches for *CP*-violation in charm sector, where interpretation of the observed *CP*-violating effects at the percent level is more direct. A tension observed between the experimental measurements and the SM value in the analysis using $D^0 \to K^+K^-$ and $D^0 \to \pi^+\pi^-$ decays, is no longer present [21]. Increased statistical samples, and considering other modes, in particular those that separate contributions from direct and indirect *CP*-violation, will provide a new insight on potential presence of effects beyond SM.

LHCb performs searches for very rare decays, where new physics models predict observables, that are significantly different from the SM expectations. The $B_{(s)} \to \mu^+\mu^-$ decay is a pure loop process, helicity and CKM suppressed, with well-predicted branching fraction of $\mathcal{B}(B_s^0 \to \mu^+\mu^-) = (3.56 \pm 0.30) \times 10^{-9}$ [22–24]. However large enhancements can occur in supersymmetry and alternative new physics models. LHCb has observed the $B_s^0 \to \mu^+\mu^-$ decay for the first time and measured a branching fraction $\mathcal{B}(B_s^0 \to \mu^+\mu^-) = (2.9^{+1.1}_{-1.0}) \times 10^{-9}$ [25] to be consistent to the SM prediction, ruling out the minimal sypersymmetric extention to the SM with a light pseudoscalar Higgs at large tanβ. An event with fully reconstructed $B_s^0 \to \mu^+\mu^-$ candidate is shown on Fig. 2.5. Clear separation between the pp interaction vertex and the vertex formed by

two muon candidates is visible on the zoom to the vertex region in the bottom left part of the plot. LHCb measured forward-backward asymmetry zero-crossing point

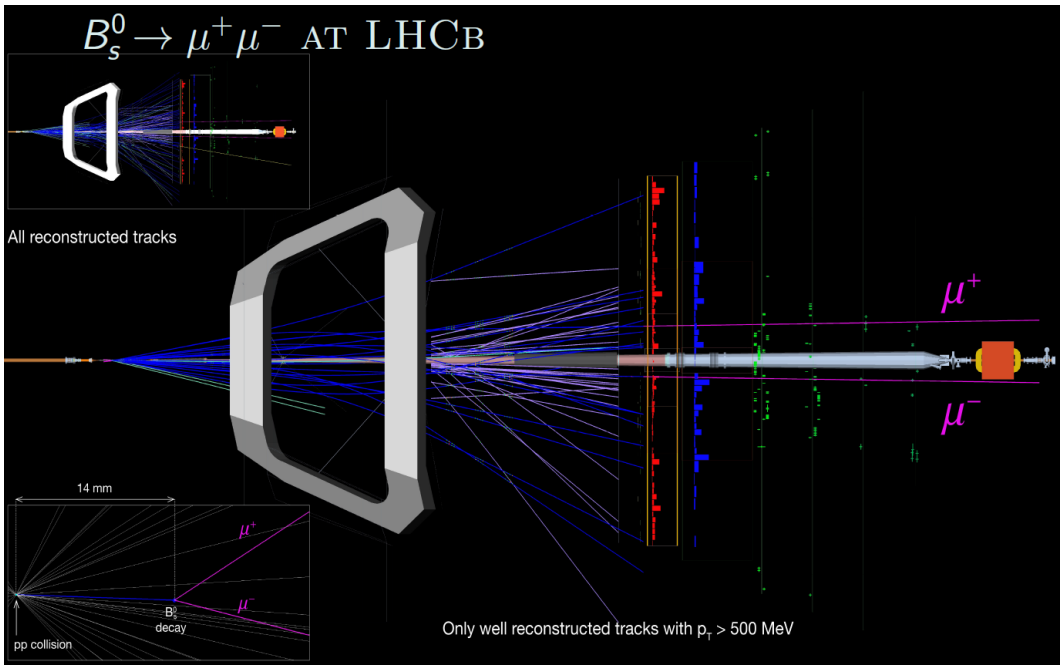

Figure 2.5: LHCb event with fully reconstructed $B_s^0 \to \mu^+\mu^-$ candidate

$q_0^2 = 4.9 \pm 0.9\,\mathrm{GeV}^2/c^4$ of the rare decay mode $B^0 \to K^{*0}\mu^+\mu^-$, consistent with the SM predictions, sensitive to new physics contributions and allowing to distinguish between them. Another example is the search for rare $D^0 \to \mu^+\mu^-$ decay, dominated by long-distance contributions from the $\gamma\gamma$ intermediate state, helicity and GIM suppressed, with an expected SM branching fraction below 6×10^{-11}. LHCb set an upper limit on $\mathcal{B}(D^0 \to \mu^+\mu^-) < 7.6 \times 10^{-9}$ at 95% confidence level [26], two orders of magnitude lower than previous searches.

LHCb is well suited to study heavy flavour physics. It benefits from good track and precise vertex recontruction, powerful particle identification, large rapidity coverage, high statistical yields, and a robust trigger. However, analysis has to cope with high event multiplicities at the LHC environment, forward detector geometry which prevents full event reconstruction, and a trigger compromise between b and c physics targets.

2.3 The LHCb detector

2.3.1 Detector outline

The LHCb detector (Fig. 2.6) is a single-arm forward spectrometer, installed in the former DELPHI cavern, with the collision point of the proton beams displaced by about a half-cavern length with respect to the e^+e^- collision point, in order to accomodate forward geometry adopted to the high energy proton beams collisions. The size of the existing DELPHI cavern limited the LHCb experiment to a single-arm solution, unlike the double-arm BTEV project [27] at FNAL, terminated by the US government in 2005.

The evolution of the LHCb detector concept can be seen by comparing the LOI detector design [28], the LHCb version of technical proposal [29], technical design reports [30–39], the reoptimized LHCb design [40] and actual detector performance [41]. Major LHCb detector evolution occured, minimizing amount of material in front of the electromagnetic calorimeter by reducing the number of tracking stations, and in particular removing the stations inside the magnet; introducing fully silicon tracking station upstream the magnet and leaking magnetic field upstream to provide momentum measurement early at the trigger level using upstream tracking and following re-design, a 90 degrees rotation, of the RICH1 detector; trigger reoptimization and introducing the deferred high level trigger.

At LHC energies, production of b and $\bar{b}$ quarks is highly correlated with respect to the boost (Fig. 2.7), so that if a b quark enters the detector acceptance, the corresponding $\bar{b}$ quark products are also captured with high probability. With only about 4% solid angle instrumented, LHCb captures about 40% of the heavy flavour production cross section. This proves the high efficiency of a single arm spectrometer concept, where only a factor 2 is lost compared to a 4π geometry. Moreover owing to better acceptance in forward direction, a factor 2 higher $b\bar{b}$ cross section is achieved at the LHCb compared to the ATLAS or CMS experiments.

The LHCb acceptance is unique amongst the LHC experiments, provides complementary production studies to the ATLAS and CMS experiments (Fig. 2.8), and gives access to valuable QCD studies in the forward region.

The LHCb detector (Fig. 2.6) covers 10-300 (15-250) mrad acceptance in x(y)

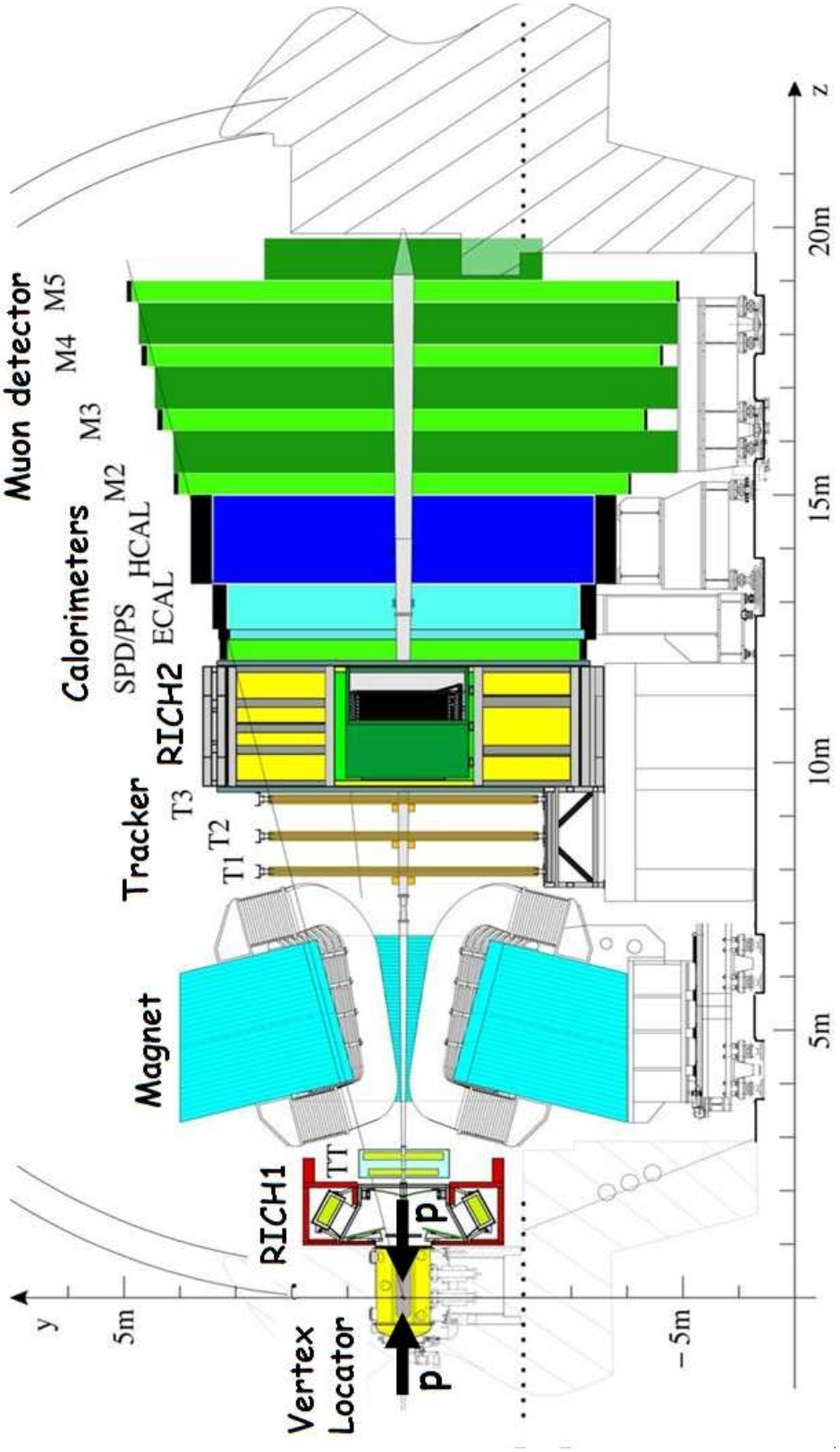

Figure 2.6: Side view of the LHCb detector (magnetic field lines are vertical) from inside of the LHC machine loop

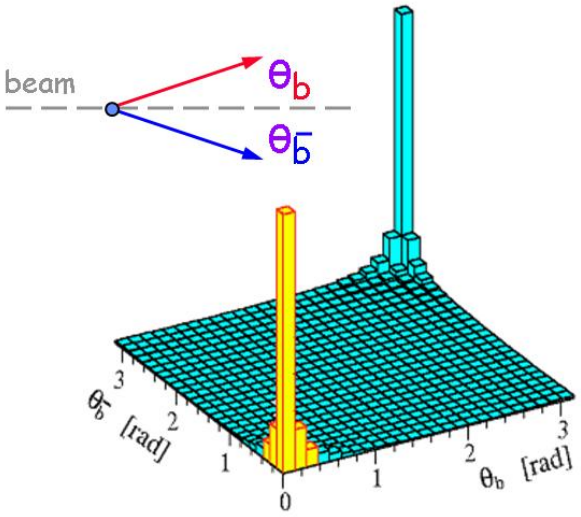

Figure 2.7: Polar angle distribution of the b and $\bar{b}$ hadrons produced at the LHC

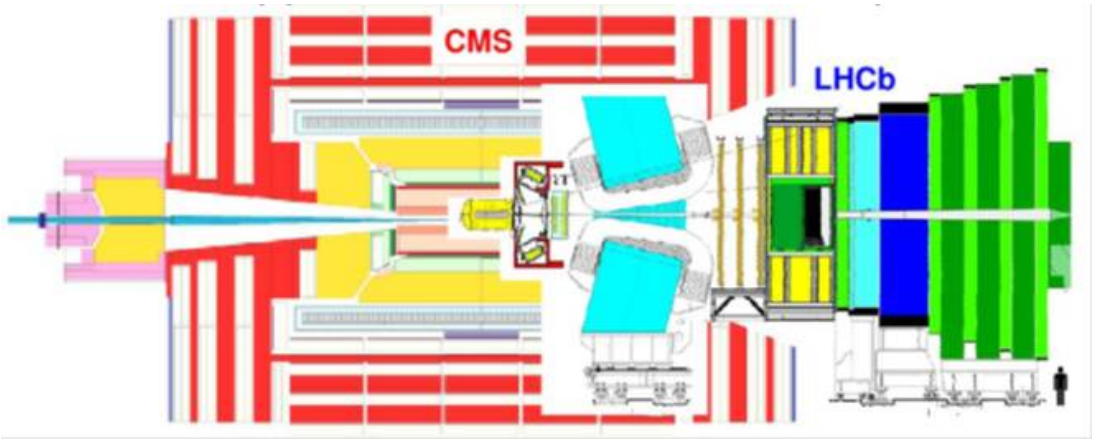

Figure 2.8: Acceptance comparison for the CMS and LHCb experiments at the LHC

projections. A high precision tracking system comprises a silicon-strip vertex detector surrounding the pp interaction region, a large-area silicon-strip detector located upstream of a dipole magnet with a bending power of about 4 Tm, and three stations of silicon-strip detectors and straw drift-tubes placed downstream. The combined tracking system has a momentum resolution $\Delta p/p$ that varies from 0.4% at 5 GeV/c to 0.6% at 100 GeV/c, and an impact parameter resolution of 20 µm for tracks with high transverse momentum. Charged hadrons are identified using two ring-imaging Cherenkov detectors. Photon, electron and hadron candidates are identified by a calorimeter system consisting of scintillating-pad and pre-shower detectors, an electromagnetic calorimeter and a hadronic

calorimeter. Muons are identified by a muon system composed of alternating layers of iron and multiwire proportional chambers. The LHCb trigger consists of a hardware stage, based on information from the calorimeter and muon systems, followed by a software stage which applies a full event reconstruction. In the following reconstruction of tracks and vertices, particle identification, trigger and foreseen detector upgrade for operation at higher luminosity, are discussed.

2.3.2 Reconstruction of tracks and vertices

The LHCb tracking system aims at efficient tracking providing high momentum and impact parameter resolution for charged particles, precise reconstruction of the proton-proton collission point (*primary vertex*), and vertices, corresponding to heavy flavour hadrons decays via weak interaction, providing excellent decay time resolution capable of resolving the fast oscillations of the B_s^0 meson [42]. The LHCb tracking system comprises silicon stations of VErtex LOcator (VELO), Trigger Tracker (TT) station upstream the magnet, and the three tracking stations T1-T3 downstream the magnet, and warm dipole magnet with a bending power of 4 Tm.

Silicon micro-strip technology is employed in VELO, TT and inner regions of T1-T3 tracking stations (IT), while straw tubes are used for large area outer regions of the T1-T3 stations. The total sensitive area of silicon amounts to approximately 12 m^2.

The VELO system comprises 21 stations of two semicircular silicon sensors (Fig. 2.9) each yielding a polar coordinate, radius r or azimuthal angle ϕ, measurement. VELO is arranged in two retractable detector halves in order to provide safe conditions during injection and until stable beams are achieved by the LHC machine. At closed position during operation, the sensitive area is as close as 8 mm to the beam axis, while the sensors are 30 mm away during injection. VELO is a silicon microstrip detector of a 180k readout channels, installed inside the vacuum vessel (Fig. 2.10) around the interaction region [30]. The modules are built from 300 μm thick silicon sensors with the pitch varying from 40 to 120 μm depending on radius (Fig. 2.11, left). The sensors are mounted on a carbon fibre support.

Both detector halves are operated in a secondary vacuum, separated from the primary vacuum of the LHC beam by a 300 μm thick Aluminium foil. The foil also

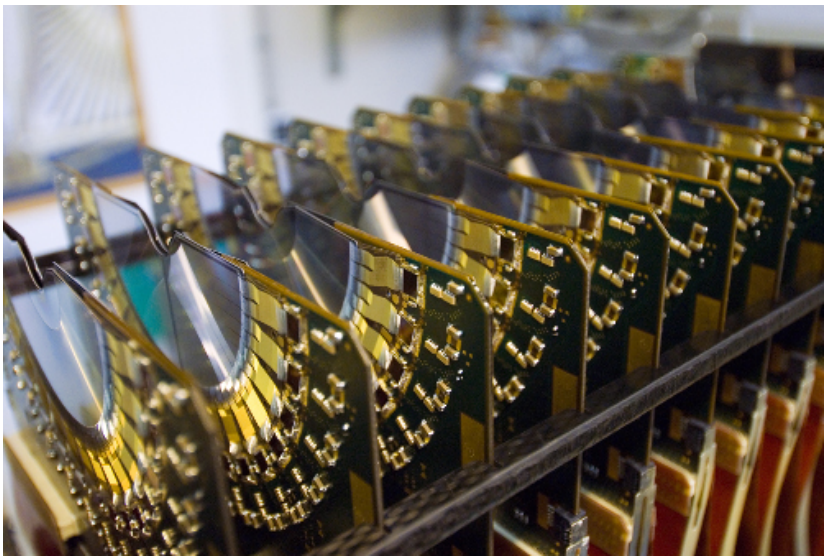

Figure 2.9: VELO semi-circle stations

Figure 2.10: Vacuum vessel for VELO

insulates the VELO sensors from the radio frequency pick-up of the proton beams. The system is cooled maintaining the sensors at a temperature of -7^{o}C.

The VELO detector allows to achieve spatial resolution down to about 4 μm, and excellent primary vertex reconstruction precision of $\sigma_x = \sigma_y = 13$ μm and $\sigma_z = 69$ μm for a vertex defined by 25 tracks. Impact parameter resolution was obtained to be $\sigma_{IP} = 11.6 + 23.4/p_T$ μm (Fig. 2.12), and is dominated by the effect of material before

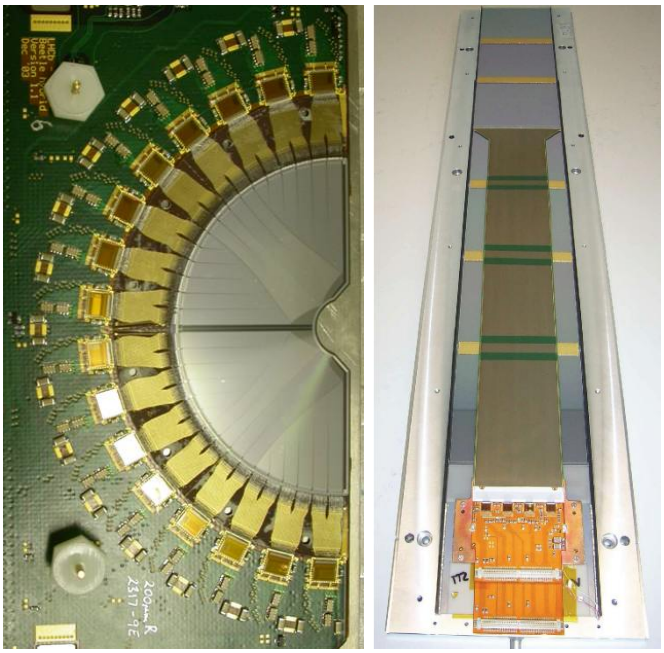

Figure 2.11: Left: the VELO hybrid with silicon sensor and readout chips; right: sensor ladder for TT and IT with electronics hybrid, low mass Kapton cable and silicon sensors

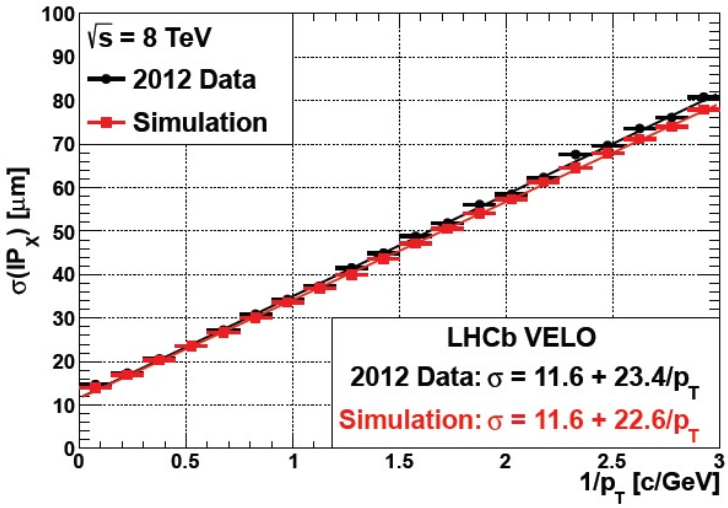

Figure 2.12: Impact parameter dependence on the track transverse momentum

the first measured point. The data and simulation are well understood and agree with each other. VELO provides excellent proper time resolution of about 40 fs, as determined from numerous b-hadron lifetime measurements [43–49].

Being positioned close to the interaction region and to the beam axis, VELO is

exposed to high particle fluence. Irradiation of the VELO sensors is non-uniform and varies with radius and z-position. The innermost sensitive area of the station upstream of the interaction region is exposed to the range of fluences of about 60×10^{12} 1 MeV $\mathrm{n}_{eq}/\,\mathrm{cm}^2$. Consequent effects of leakage current and change of effective depletion voltage are well understood and allow efficient operation to an integrated luminosity of 9 fb^{-1} [50].

The LHCb VELO is small, having 0.2×10^6 channels, compared to the ATLAS Pixel and SCT strips vertex detectors [51, 52] with 82×10^6 and 6×10^6 channels, respectively, and CMS Pixel and Strip vertex detectors [53, 54] with 66×10^6 and 10×10^6 channels, respectively. However, the LHCb VELO is more precise, approching closer the beam line, 0.8 cm against 5.1 cm and 4.4 cm for the ATLAS and CMS pixels, successfully operating in challenging radiation environment, and plays important role in the trigger.

In addition to VELO, the LHCb tracking system comprises four planar tracking stations, trigger tracker (TT) upstream of the dipole magnet and T1-T3 stations downstream of the magnet. While TT and the region close to the beam pipe of T1-T3 employ silicon microstrips, the straw tubes are used for the outer region of T1-T3.

TT is a silicon strip detector covering full acceptance upstream the magnet, with a total surface of 8 m^2 of 500 μm thick silicon, 144k readout channels [32]. T1-T3 stations also exploit silicon strips for inner part (IT), covering regions around the beam pipe with the highest particle fluence, and employ 129k readout channels [32]. These detectors are p^+-on-n micro-strip detectors with the sensors operating at a temperature of 8^oC. Within each detector station, four detector planes are arranged with a tilt of 0^o, $+5^o$, -5^o, 0^o with respect to the vertical axis. The sensor thickness of 500 μm for TT and 320 μm and 410 μm for IT, together with a pitch of 183 μm for TT and 198 μm for IT, is used. The sensors are mounted on a carbon fibre support, hosting also electronics hybrid and low mass Kapton cable (Fig. 2.11, right).

More than 99% and 98% of channels are operational in the TT and IT, respectively, with a hit efficiency of more than 99%. The hit resolution, including alignment effects, was found to be about 61 μm for TT and 54 μm for IT.

Outer part of the T1-T3 tracking stations (OT), 5×6 m^2 is covered by 12 double layers (four stereo layers per each station) of long straw tube chambers with 54k readout channels [31]. The straw tubes are filled with $Ar/CO_2/O_2$: 70/28.5/1.5 gas mixture,

where a small percentage of oxygen was added to reduce aging effect [55] caused by a wrong plastifier used during the chamber manufacturing. A high single hit efficiency averaged over the detector module was found to be 98.8%, together with high spatial resolution of better than 200 μm [56]. During the operation 0.4% channels were found to be dead or noisy. Time calibration was performed four times a year with all the channels stable to ± 0.5 ns. No OT damage caused by irradiation have been observed so far.

The warm dipole magnet [33] (Fig. 2.13) provides an integrated field of 4 Tm. The dipole was built in Saint-Petersburg and installed in 2005. Several measurements of

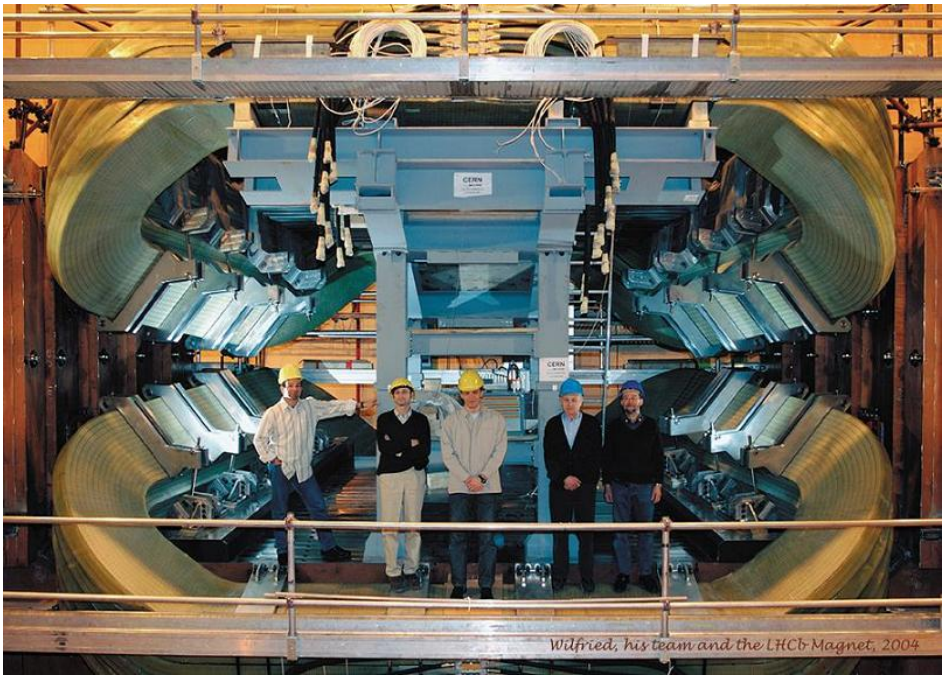

Figure 2.13: The LHCb magnet

the 3D mapping of magnetic field have been performed, and the results have been introduced in the simulation. Effect of the limited knowledge of the magnetic field together with a larger effect from remaining misalignment is evaluated by comparing reconstructed mass value and resolution for particles of different masses to their known values [57]. The measure of the above effects is a required correction to decay product momenta, $\alpha \sim 0.0003$. A difference between the α coefficients for the J/ψ meson mass reconstructed via its decay $J/\psi \to \mu^+\mu^-$ for the two different magnet polarities is below 0.0001. Additional momentum scale calibration [58] allows to achieve a residual α values

below $\alpha \sim 0.00003$ in the range between kaon masses and the mass of $\Upsilon(3S)$. The magnetic field is regularly reversed to reduce systematic error in many CP asymmetry studies.

The LHCb tracking system provides high tracking efficiency, above 95%, over wide range of momentum and pseudo-rapidity. Tracking efficiency results are consistent for both magnet polarities, for positively and negatively charged tracks.

Vertex reconstructed precision using the LHCb tracking system is illustrated by the reconstruction of rapid $B_s^0\overline{B}_s^0$-oscillations [59]. Fig. 2.14 shows decay time distribution

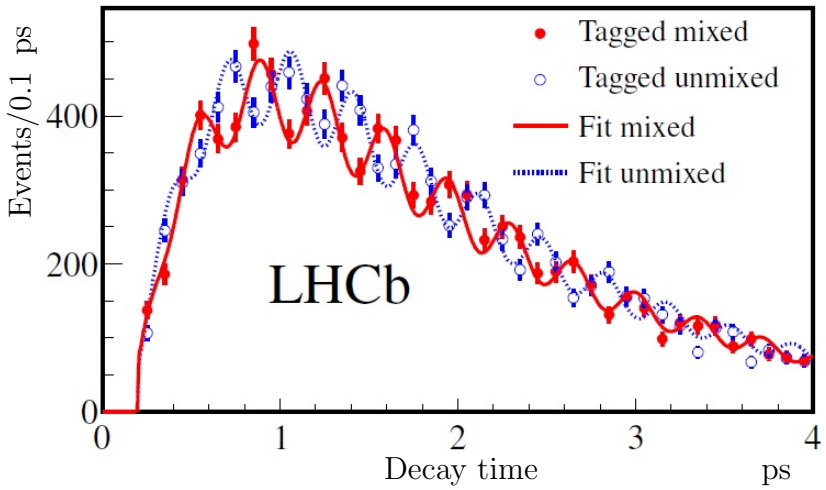

Figure 2.14: Decay time distribution for B_s^0 candidates tagged as mixed (different flavour at decay and production; red, continuous line) or unmixed (same flavour at decay and production; blue, dotted line). The data and the fit projections are plotted in a signal window around the reconstructed B_s^0 mass of $5.32 - 5.55\,\mathrm{GeV}/c^2$

for B_s^0 candidates, reconstructed via $B_s^0 \to D_s^-\pi^+$, with the D_s^- decaying via $D_s^- \to \phi\pi^-$, $D_s^- \to K^{*0}K^-$, $D_s^- \to K^+K^-\pi^-$ nonresonant, $D_s^- \to K^-\pi^+\pi^-$ and $D_s^- \to \pi^-\pi^+\pi^-$, tagged as mixed or unmixed.

The tracking system provides a 0.4% momentum resolution with an efficiency of 94% for fast $p > 10\,\mathrm{GeV}/c$ tracks and a ghost rate of a 3% for tracks with transverse momenta $p_\mathrm{T} > 0.5\,\mathrm{GeV}/c$.

The LHCb tracking system was aligned [60] independently from VELO, which was used as a constraint. The $D^0 \to K^-\pi^+$ candidates with mass constraint and other

tracks were used. However, after alignment a particle momentum calibration residual of up to 0.03% was still present, while in order to obtain precise mass measurement a residual below or about 0.01% was needed. This was achieved by applying a momentum scale calibration [58]. In the decay $B^+ \to J/\psi K^+$, a mass constraint was applied to the J/ψ candidate, and kaon momentum was corrected such that the B^+ mass matches the known [57] value. This procedure results in at most a few per mille correction. Momentum scale calibration allowed the LHCb experiment to produce the most precise mass measurements [58,61] to date for b-baryons, Σ_b^-, Λ_b^0, Ω_b^- and Ξ_b^0. Momentum scale calibration was also important to determine the mass difference between the J/ψ and η_c charmonium states, as discussed in section 4.4.

2.3.3 Particle identification

Charged hadron identification or separation between p, K^+ and π^+, and in particular rejection of pions - most abundant particles in the event - at a percent level, in the range 2-100 GeV/c is essential to reconstruct b and c-hadron decays and perform flavour tagging, in particular for *CP* asymmetries measurements.

A system of two ring imaging Cherenkov (RICH) detectors [34] is used for charged hadron separation. Aiming at identification of lower momenta particles, the RICH1 detector is installed upstream of the magnet. It covers a momentum range from 1 to about 70 GeV/c in the 25 to 250 (300) mrad vertical (horizontal) acceptance, and uses silica aerogel and C_4F_{10} as radiators. RICH2 employs CF_4 radiator, provides identification for particles of 15 to about 100 GeV/c momenta in the 15 to 100 (120) mrad vertical (horizontal) acceptance, and is positioned downstream of the magnet. Fig. 2.15 shows silica aerogel inside a gas tight box flushed with CO_2 to avoid performance degradation from exposure to C_4F_{10} (right).

Cherenkov light, produced in radiators, is guided to the photodetectors, positioned outside the LHCb acceptance in a tolerable radiation zone, using a system of large, precise and radiation resistant mirrors, adding minimum possible material to the budget in front the electromagnetic calorimeter. The precision of a few mrad resolution is preserved. The RICH1 employs lightweight carbon fibre spherical mirrors (Fig. 2.16a) adding about 1.5% X_0. The RICH2 acceptance is significantly larger, and each spherical mirror (Fig. 2.16b) combines 21 glass hexagonal segments, while flat mirrors, directing

Figure 2.15: Silica aerogel inside a gas tight box flushed with CO_2 to avoid performance degradation from exposure to C_4F_{10}

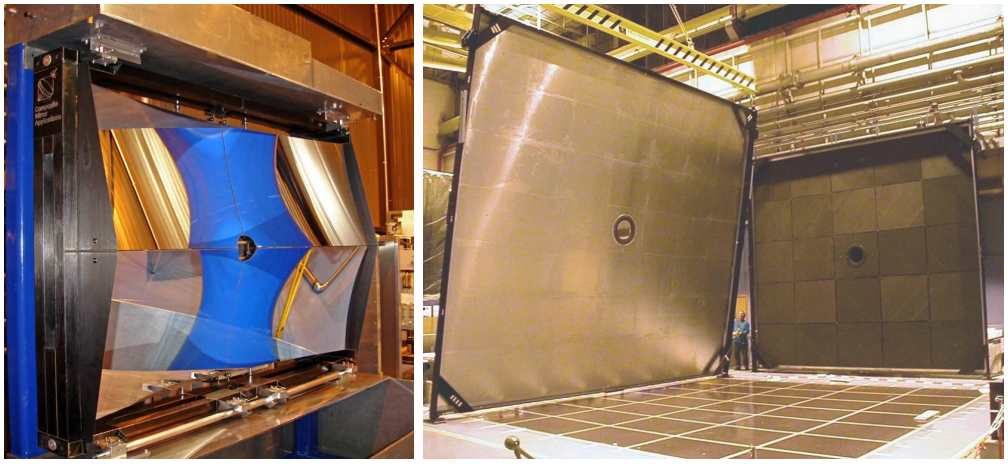

Figure 2.16: Carbon fibre mirrors of RICH1 (left) and segmented glass mirrors of RICH2 (right)

light to the photodetector planes combines 20 square glass segments.

Both RICH detectors use a dedicated photon detector, a hybrid photodiode (HPD), a tube of 8 cm diameter, with over 1000 pixels sensitive to single photoelectrons (Fig. 2.17, left). The HPD is a dedicated development for the LHCb RICH detectors and CMS HCAL. The idea of this new photon detector is to accelerate a photoelectron in a strong field, voltage of 20 kV, creating then about 5000 electron-hole pairs in the silicon sensor. Amplification in one step implies good energy resolution and a possibility to distinguish single photoelectrons. However, under high applied voltage, ion feedback can become

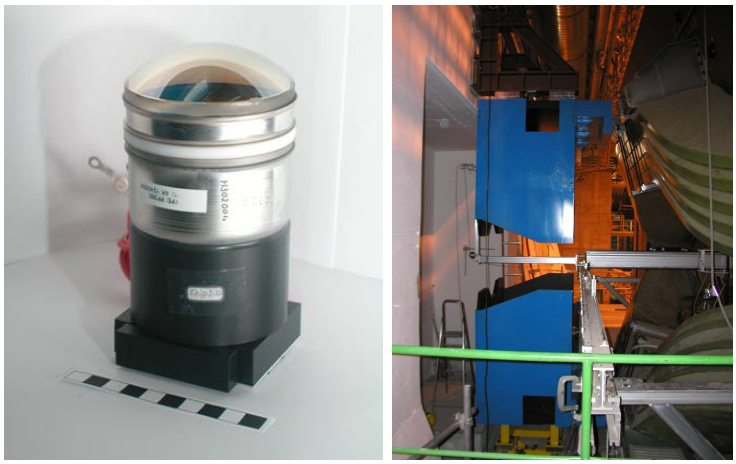

Figure 2.17: Left: hybrid photodiod; right: shielding for RICH1 photodetectors

an issue to maintain good quality vacuum. HPD detectors are enclosed in the shielding housing to suppress remaining magnetic field (Fig. 2.17, right). A 10 MHz readout electronics is embedded in the LHCb HPD detectors. In order to be able to resolve two consequtive bunch crossings, the HPD will be replaced by the MAPMT (multi-anode photon multiplier tube) for the LHCb upgrade.

Design $\sigma(\theta_C)$ resolution is achieved by taking into account contributions from radiators (radiator composition, pressure and temperature), mirror geometry (alignment down to 0.1 mrad), spatial precision (corrections for magnetic distorsion and alignment of HPDs) and tracking performance (also alignment relies on the tracking information). Using track sample from data, the RICH angular resolution was found to be $\sigma(\theta) = 1.618 \pm 0.002$ mrad for the C_4F_{10} radiator, $\sigma(\theta) = 5.0 \pm 0.2$ mrad for the aerogel in RICH1, and $\sigma(\theta) = 0.68 \pm 0.02$ mrad for the CF_4 radiator in RICH2, in agreement with the simulated resolutions.

The number of photoelentrons $N_{p.e.}$ per track was also obtained from data, using tracks from $D^0 \to K^-\pi^+$ sample (from $D^{*+} \to D^0\pi^+$) with $\beta \approx 1$, as well as muons from the $pp \to pp\mu^+\mu^-$ events. The $N_{p.e.}$ ranges from 4 to 25 depending on the radiator, and in agreement with the simulation results.

In order to quantify charged particle identification using RICH [62], a global log-likelihood algorithm was constructed, considering the integrity of pixel hits and tracks, and the three radiators. The final mass assignment is based on the differences in the log-likelihood values ΔLL, which give for each track the change in the overall event log-

likelihood when the hypothesis of that track is changed from the π hypothesis to each of the e, μ, K and p hypotheses. To determine efficiency of identification requirements and mis-identification rates, pure samples of each particle type were selected using kinematics selection criteria alone. Large samples of $K^0_S \to \pi^+\pi^-$, $\Lambda \to p\pi^-$, $D^{*+} \to D^0(\to D^0\pi^+)\pi^+$ and $\phi(1020) \to K^+K^-$ decays as well as photon conversion were exploited. The example of efficiency and mis-identification rate depending on particle momentum is shown on Fig. 2.18a, for the $\Delta LL(K-\pi) > 0$ and $\Delta LL(K-\pi) > 5$ requirements. These performance curves are consistent with those from simulation, shown on Fig. 2.18b. As expected, the RICH performance depends on particle multiplicity in the event.

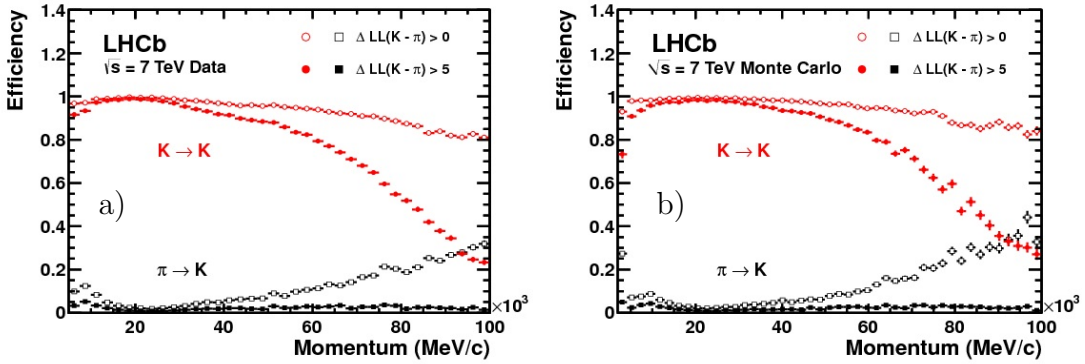

Figure 2.18: Kaon-pion separation as a function of particle momentum in data (a) and Monte Carlo simulation (b). Top curves show kaon identification efficiency, and bottom curves describe pion rejection. The two sets of curves correspond to the $\Delta LL(K-\pi) > 0$ and $\Delta LL(K-\pi) > 5$ requirements

Fig. 2.19 shows K/π separation depending on particle multiplicity (a) and number of reconstructed primary vertices (b) in the event. Excellent K/π separation is achieved averaging in the momentum range between 2 and 100 GeV/c with the average $\pi \to K$ misidentification rate of 10 % for the K identification efficiency of 95 % corresponding to the $\Delta LL(K-\pi) > 0$ requirement, and the average $\pi \to K$ misidentification rate of 3 % for the K identification efficiency of 85 % corresponding to the $\Delta LL(K-\pi) > 5$ requirement. Exact optimal requirement depends on a specific analysis performed.

For studies of charmonium production using decays to $p\bar{p}$, discussed in chapter 4, proton identification is also important. The corresponding performance curves for K/π and K/p separation are shown on Fig. 2.20a and Fig. 2.20b respectively.

Performance of charged hadron identification with the LHCb RICH system can be

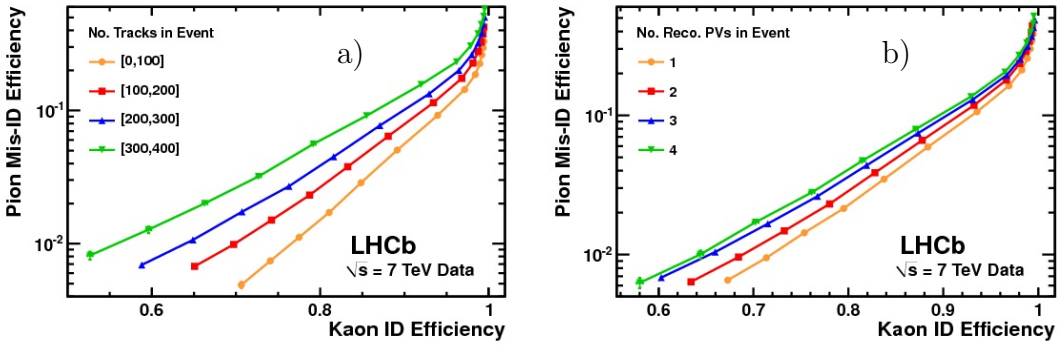

Figure 2.19: Pion misidentification fraction depending on kaon identification efficiency as measured in 7 TeV LHCb collisions as a function of track multiplicity (a) and as a function of the number of reconstructed primary vertices (b). The efficiencies are averaged over all particle momenta

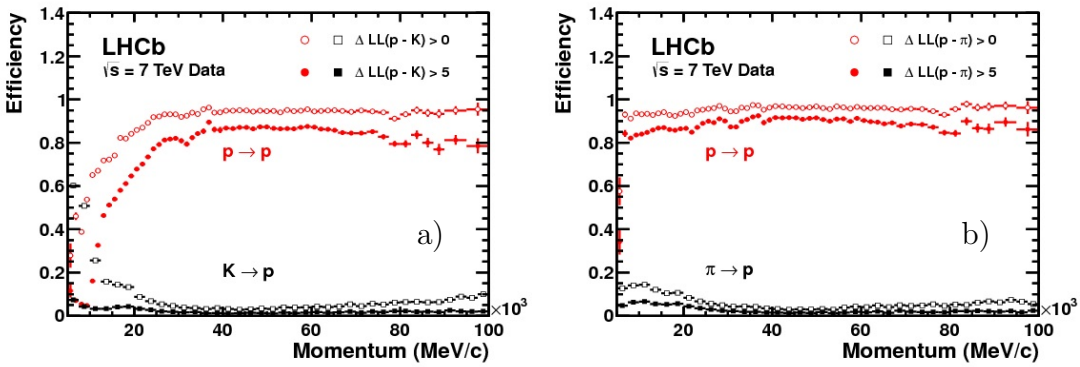

Figure 2.20: Proton-kaon (a) and proton-pion (b) separation as a function of particle momentum from data. Top curves show proton identification efficiency, and bottom curves describe kaon or pion rejection. The two sets of curves correspond to the $\Delta LL(p - K(\pi)) > 0$ and $\Delta LL(p - K(\pi)) > 5$ requirements

illustrated by the analysis of $\pi^+\pi^-$ pairs with invariant mass in the region, corresponding to b-hadron masses, in Ref. [63]. Data sample, used for this analysis, was accumulated at a center-of-mass energy of $\sqrt{s} = 7\,\text{TeV}$, and corresponds to the integrated luminosity 0.37 fb^{-1}. The selection identified a good quality decay vertex of b-hadron candidates well separated from the corresponding pp collision (*primary*) vertex, where b-hadron candidates were produced. Combinatorial background from tracks compatible with originating from primary vertex was suppressed. Further background reduction was achieved using larger transverse momentum values corresponding to the p_T spectrum in

b-hadron decays. Fig. 2.21 shows the invariant mass assuming the $\pi^+\pi^-$ hypothesis for selected b-hadron candidates, using kinematic selection criteria and without applying any PID requirement. Using the information from RICH to identify charged hadrons,

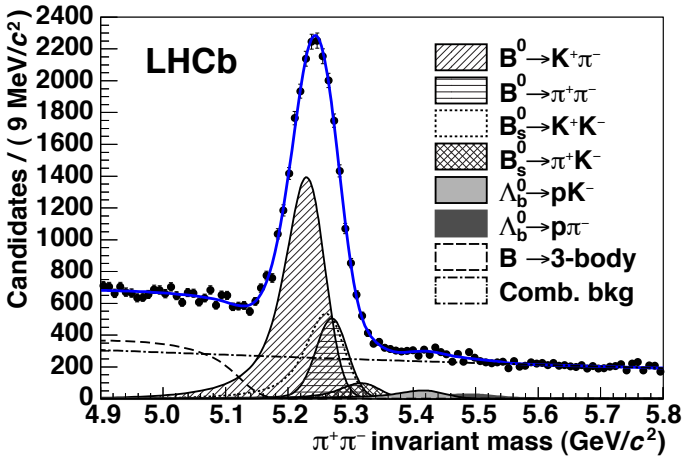

Figure 2.21: Invariant mass spectrum of the h^+h^- combinations assuming $\pi^+\pi^-$ hypothesis for kinematic-based selection of b-hadron candidates [63]. No PID requirements are applied. The main contributions to the fit model are also shown

signals from the decay modes representing core LHCb physics program are disentangled on Fig. 2.22. Prominent signal peaks are observed already with about 10% of the presently available data sample from the $B^0 \to K^+\pi^-$ mode on Fig. 2.22a, from the $B^0 \to \pi^+\pi^-$ mode on Fig. 2.22b, from the $B_s^0 \to K^+K^-$ mode on Fig. 2.22c, and from the $\Lambda_b^0 \to pK^-$ and $\Lambda_b^0 \to p\pi^-$ decay modes on Fig. 2.22d and 2.22e, respectively. Studies of charmless two-body decays of b-hadrons [63] provide access to potential contribution of new particles and/or couplings to the penguin loops, and constrain physics beyond SM. An important time-dependent study of CP-asymmetry in $B_s^0 \to K^+K^-$ decays has already been performed by LHCb [64]. A signal from the $B_s^0 \to K^+\pi^-$ decay mode is clearly visible on the right from the B^0 signal in Fig. 2.22f, with larger statistics provided a first observation of the CP-violation in B_s^0-decays [65].

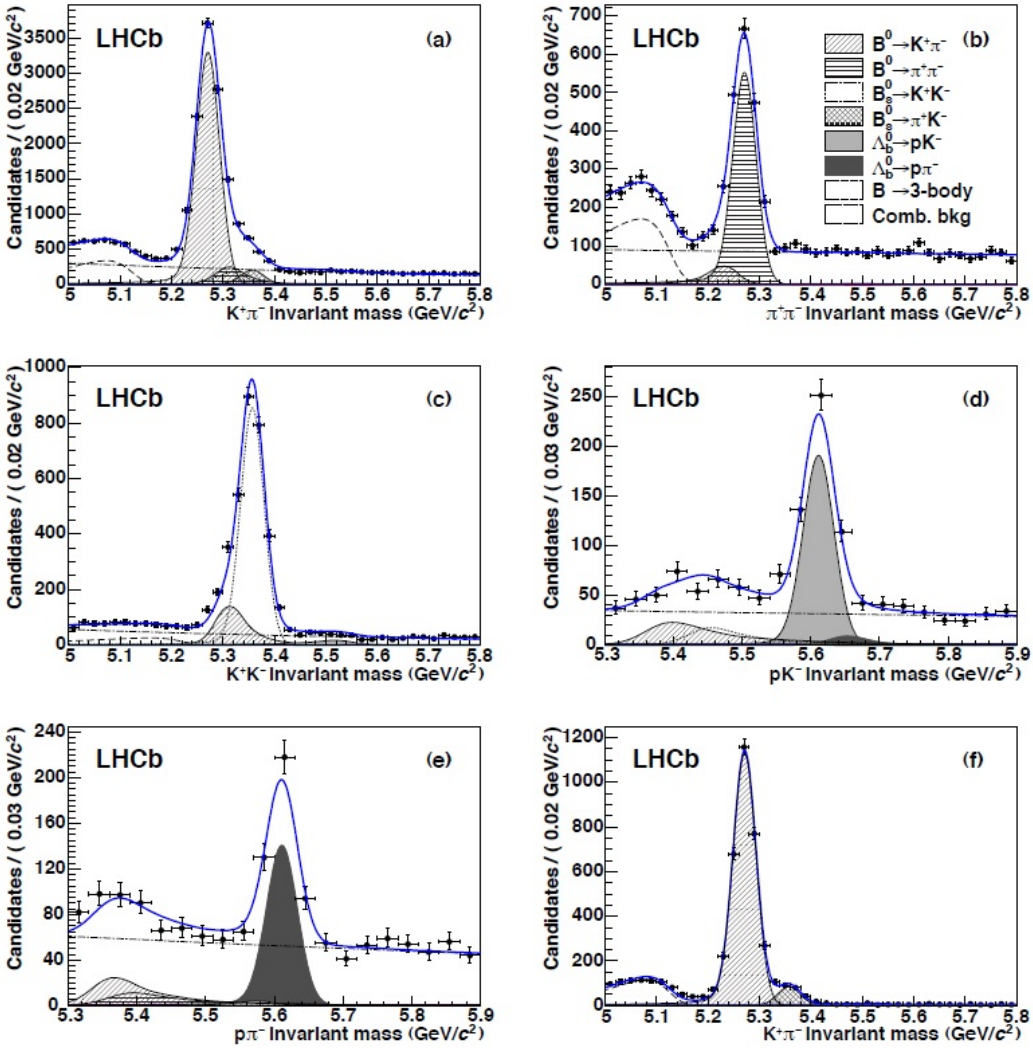

Figure 2.22: Invariant mass spectra of the h^+h^- combinations for kinematic-based selection of b-hadron candidates, using the RICH information for PID [63]. Prominent signal peaks are observed for mass hypotheses of kaon and pion with clear signal from the $B^0 \to K^+\pi^-$ mode (a) (and (f) with more selective requirements), pion mass hypotheses with clear signal from the $B^0 \to \pi^+\pi^-$ mode (b), kaon mass hypotheses with clear signal from the $B_s^0 \to K^+K^-$ mode (c), mass hypotheses of proton and kaon with clear signal from the $\Lambda_b^0 \to pK^-$ mode (d), and mass hypotheses of proton and pion with clear signal from the $\Lambda_b^0 \to p\pi^-$ mode (e). The main contributions to the fit model are also shown

Identification of electrons, photons and neutral pions as well as measurement of their energy and position is provided by the calorimeter system. The LHCb calorimeters play an essential role in the trigger, where, along with the muon detector, initiates a trigger search. In addition the electromagnetic calorimeter provides offline measurements of photons and neutral pions. The LHCb calorimeters are discussed in more detail in section 3.1.

Identification of muons is performed by muon detector [36], which is implemented in five stations, interleaved with the iron absorber. Muon detector initiates trigger search for the muon based trigger alleys, and performs offline muon identification.

The detector is composed of five stations (M1-M5) of rectangular shape, placed along the beam axis, as shown in Fig. 2.6. Station M1 is located in front of the calorimeters and is used to improve transverse momentum measurement in the first level hardware trigger. Stations M2 to M5 are placed downstream of the calorimeters and are interleaved with iron absorbers 80 cm thick to select penetrating muons. The total absorber thickness in front of station M2, including the calorimeters, is approximately 6.6 interaction lengths. More than 99% of the total area of the system is equipped with multi-wire proportional chambers (MWPC) operating with the $Ar/CO_2/CF_4$ (40:55:5) gas mixture. Only the inner part of the first station is instrumented with triple-GEM detectors filled with $Ar/CO_2/CF_4$ (45:15:40). The chambers are positioned to provide with their sensitive area a hermetic geometric acceptance to high momentum particles coming from the interaction point. In addition, the chambers of different stations form projective towers pointing to the beam crossing region.

Each muon station is designed to operate with an efficiency above 99% in a 20 ns time window with a noise rate below 1 kHz per physical channel, which was achieved during operation, as described in Ref. [66–68]. The performance of muon identification has been evaluated, using a dataset corresponding to 1 fb^{-1} recorded in 2011.

A loose binary criterium to select muons is based on the matching of hits in muon detector with the particle trajectory. For candidates satisfying this requirement, likelihoods for muon and non-muon hypotheses are built with the pattern of hits around the trajectories, which can be used to refine the selection. An additional way of rejecting fake muon candidates is provided by a variable sensitive to hit sharing by nearby particles. The muon identification efficiency was observed to be robust against the variation of

detector occupancies (Fig. 2.23a) and presents a weak dependence on momentum and

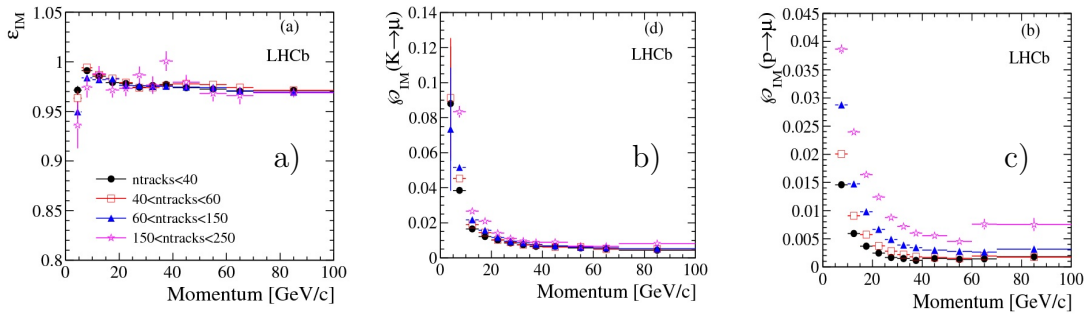

Figure 2.23: Muon efficiency (a) and kaon as muon (b) and proton as muon (c) misidentification probabilities as a function of momentum, in ranges of number of reconstructed tracks in the event

transverse momentum (Fig. 2.24a). Hadron misidentification probabilities exhibit a

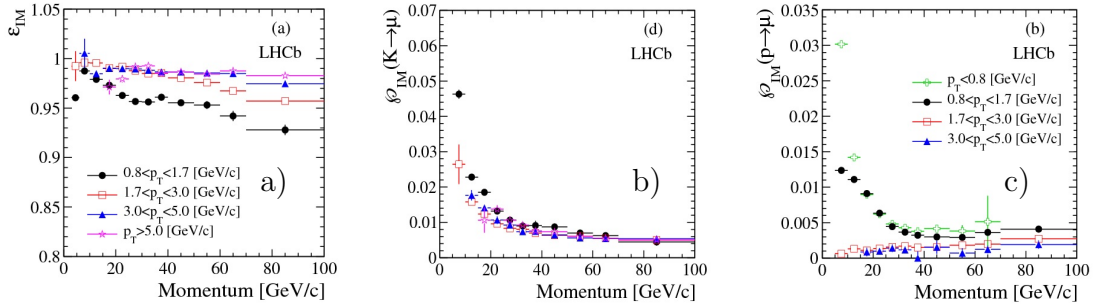

Figure 2.24: Muon efficiency (a) and kaon as muon (b) and proton as muon (c) misidentification probabilities as a function of momentum, in ranges of transverse momentum

stronger dependence on track multiplicity, however noticeable performance degradation is observed only for low momentum particles (Fig. 2.23b and 2.23c), and limited dependence on the transverse momentum (Fig. 2.24b and 2.24c). Average muon identification efficiencies at the 98% level are attainable for pion and kaon misidentification below the 1% level at high transverse momentum, using the loosest identification criterium. The performance of additional requirements based on likelihoods or on hits sharing can be tuned according to the needs of each analysis and reduce the misidentification probabilities dependence on track multiplicity. Adding a requirement on the difference of the log-likelihoods that provides a total muon efficiency at the level of 93%, the hadron misidentification probabilities are below 0.6% (Fig. 2.25).

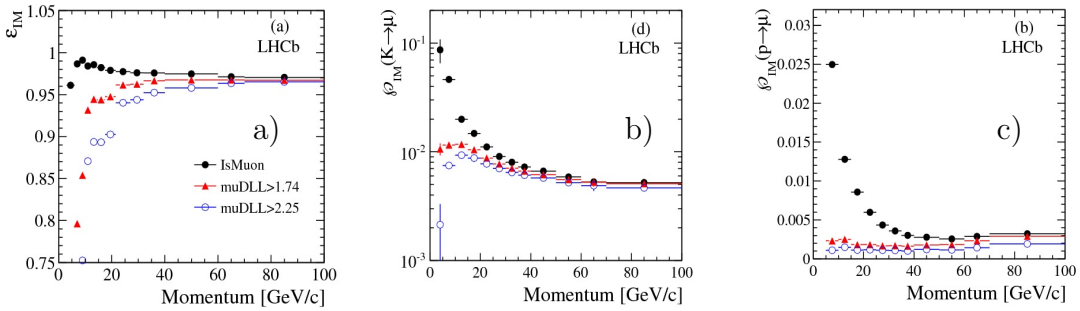

Figure 2.25: Muon efficiency (a) and kaon as muon (b) and proton as muon (c) misidentification probabilities as a function of momentum, with additinal muon DLL selection criteria

The muon identification at the trigger level is described in Ref. [69]. At the low level trigger the information from all the five stations M1-M5 is used. Providing additional point towards the magnet, the M1 station improves the muon detector based estimate of transverse momentum with the resolution going from about 35% using the information from M2-M5 stations only to about 25% where all the five stations deliver the information. The M1 information is however not useful for momentum determination at the higher level trigger or offline stage, since there direct muon track segment to the tracking system based segment matching is performed.

The offline muon identification [70] uses only the information from the four stations located downstream from the calorimeters.

2.3.4 Trigger

Heavy flavour particles are copiously produced at the LHC, with a rate of about 30 kHz $b\bar{b}$ and about 600 kHz $c\bar{c}$ pairs in the LHCb acceptance. Charm and beauty hadrons decaying via weak interactions fly on average 3 mm and 10 mm respectively in the LHCb detector. Retaining interesting charm and beauty decays requires trigger selectivity at the level of traditional physics analysis using powerful vertex reconstruction and particle identification already at the trigger level.

The LHCb trigger uses all of the detector sub-systems of LHCb. Its architecture consists of two levels, the first level trigger (L0) and the High Level Trigger (HLT). The LHCb trigger proved to be a powerful and flexible system, robust during the LHC

operation in 2010-2012 [71], can quickly react on changes in running conditions, with a recent deferred triggering that further boosts recorded physics samples.

L0 is implemented in hardware and uses the information from the calorimeter and muon systems. L0 reduces the rate of crossings with at least one inelastic pp interaction to below 1.1 MHz, at which the whole detector can be read out. This maximum rate is imposed by the front-end (FE) electronics. L0 comprises three independent triggers: the L0-Calorimeter trigger relevant to the analyses discussed in the chapter 4; the L0-Muon trigger that served majority of charmonium states studies so far; and the L0-PileUp trigger, which is not used to select flavour physics events, but aids the determination of the luminosity [72]. The L0 system is fully synchronous with the 40 MHz bunch crossing signal of the LHC. The latencies are fixed to a maximum of 4 μs and depend neither on the occupancy nor on the bunch crossing history. The trigger decisions are combined in a single L0 decision. Depending on the state of the FE buffers and the buffers in the readout boards of all sub-detectors and the availability of the PCs in the farm, a bunch crossing can be retained or throttled.

The L0-Calorimeter system computes the transverse energy deposited in clusters of 2×2 cells, using only cells located in the same zone. The ECAL and HCAL signals are read out and processed in the FE boards (FEB), each responsible for an area of 8×4 calorimeter cells with one row and column sharing information between neighbouring FEB. Each FEB selects the highest E_T cluster among its 32 clusters. From these clusters, three types of candidates are built combining information as follows:

- hadron candidate (L0Hadron), the highest E_T HCAL cluster, can be a sum of the E_T of the HCAL cluster and the matching ECAL cluster in front;
- photon candidate (L0Photon), the highest E_T ECAL cluster with PS cells hit in front of the ECAL cluster and no hit in the SPD cells corresponding to the PS cells;
- electron candidate (L0Electron), having the same requirements as for a photon candidate, with in addition at least one SPD cell hit in front of the PS cells.

The E_T of the candidates is compared to a fixed threshold and events containing at least one candidate above threshold are retained by L0.

Each quadrant of the muon detector is connected to a L0 muon processor. Each of the four L0 muon processors tries to identify the two muon tracks with the largest and second largest transverse momentum p_T in their quadrant, the search being limited to the candidates with $p_T > 0.5$ GeV/c. The position of a track in the first two stations allows the determination of its p_T with a measured resolution of 25% relative to off-line reconstructed muon tracks. The trigger sets a single threshold on either the largest p_T of the eight candidates (L0Muon), or a threshold on a product of the largest p_T and the second largest p_T of the muon candidates (L0DiMuon).

The total L0 output rate amounts to about 1 MHz, with about 40% contribution from L0 muon triggers, about 45% contribution from L0 hadron trigger, and about 15% contribution from L0 electron and photon triggers.

An event which is accepted by L0 is transferred by the on-line system from the FEB to the Event Filter Farm, where HLT software applications run. The HLT is based on the same software as used for the LHCb data processing and simulation [39]. The offline event reconstruction and selection requires about 2 s per event. During 2011 the L0 rate was about 870 kHz. Given the available resources this limits the time per event in the HLT to $\sim$ 30 ms. The HLT is thus divided into two stages. The first stage (HLT1) processes the full L0 rate and uses partial event reconstruction to reduce the rate to about 43 kHz and 80 kHz in 2011 and 2012, respectively. At this rate the second stage (HLT2) performs a more complete event reconstruction. The LHCb selectivity and trigger bandwidth constraints force essential physics analyses selection to be implemented already at the trigger level under dedicated *trigger lines*. Trigger lines are composed of a sequence of reconstruction algorithms and inclusive or exclusive selections. An event is accepted by L0, HLT1 or HLT2 if it is accepted by at least one of its trigger lines at the relevant stage. During 2011 running, the HLT contained 38 HLT1 and 131 HLT2 lines.

The HLT has evolved significantly compared to Ref. [41], in which it is assumed that the LHC machine would operate with a 25 ns bunch separation [37], and that LHCb would limit the number of visible pp interactions such that the average number of visible interactions per bunch crossing $\mu \approx 0.4$. However, the smallest bunch separation of the machine was 50 ns in the 2011 physics runs. To compensate for the loss in number of bunches, and combined with the fact that the LHCb detector performance did not degrade up to $\mu \approx 2.5$, LHCb decided to run at $\mu \approx 1.4$. Therefore the HLT had to

adapt to running conditions rather different from those described in Ref. [41]. The HLT reduces the rate of accepted events to ~ 3 kHz, and all such events are written to storage. The events written to storage are then processed offline with a more accurate alignment and calibration of the sub-detectors, and with reconstruction and selection software that is more elaborate and allows for more redundancy than is possible in the HLT.

Finally, deferred trigger was developed that allowed HLT an overcommitement by 20% to 30%. Using a 1 PB storage at the farm, the deferred trigger then runs during the LHC breaks. Using deferred trigger made it possible to lower track reconstruction thresholds.

The HLT writes about 5 kHz to storage, including about 2 kHz of inclusive B-candidates, about 2 kHz of inclusive charm candidates and about 1 kHz decay signatures with muons.

Specific selection of the $p\overline{p}$ combinations that are consistent with being charmonia decay products is performed already at the trigger level with dedicated HLT lines (sections 4.2.2 and 4.3.2). Reconstruction of charmonia or B_s^0 meson decays to ϕ mesons consider events triggered by any signal trigger line (sections 4.3.3, 5.1.2 and 5.2.2).

2.3.5 The LHCb experiment upgrade

Further LHCb detector modifications are associated with the LHCb upgrade, launched as a letter of intent [73] in 2011. During the LHC run I, the LHCb experiment achieved results that go well beyond the expectations, which will be pursued with the LHC run II. The 2010 - 2012 data taking demonstrated that the detector and the trigger system are robust and well functioning, fully operational above nominal luminosity of 2×10^{32} $\mathrm{cm}^{-2}\mathrm{s}^{-1}$. At the end of the run I data taking, the experiment was operating at the luminosity of $3 - 4 \times 10^{32}$ $\mathrm{cm}^{-2}\mathrm{s}^{-1}$, while the tests were performed at 5×10^{32} $\mathrm{cm}^{-2}\mathrm{s}^{-1}$ and beyond. Beyond the run II, the LHCb physics reach can be extended to study very rare phenomena and to search for new physics in the heavy flavor sector under the condition that the collected data will be increased much beyond the 1 fb^{-1} per year. In order to achieve this goal detector design, data acquisition and trigger must be improved, under the goal to keep the LHCb performance at least at the already

achieved level.

At the nominal LHC energy and a luminosity up to $2 \times 10^{33}\text{cm}^{-2}\text{s}^{-1}$ with then multiple interactions per beam crossing, the fake rates will drastically increase. In order to stay within the reserved bandwidth in the present trigger configuration, the requirements on the transverse energy must be increased, leading to inevitable reduction of signal yields. The solution is to deliver to lowest level trigger the information from the entire detector at 40 MHz, which transforms hardware based Level 0 trigger to the first part of the software trigger. The LHCb upgrade strategy therefore consists of reading out the entire detector at 40 MHz, with a fully software trigger keeping the luminosity levelled at $1 \times 10^{33}\text{cm}^{-2}\text{s}^{-1}$, but the experiment fully functional up to a luminosity of $2 \times 10^{33}\text{cm}^{-2}\text{s}^{-1}$. This solution will impose to all the sub-detectors not only to cope with increased occupancies, but to have their FE electronics functional at 40 MHz readout. Since the luminosity of 2×10^{33} $\text{cm}^{-2}\text{s}^{-1}$ is below already demonstrated LHC luminosity, the LHCb upgrade is in principle independent of the LHC machine upgrade.

In order to keep presently achieved performance of the track and vertex reconstruction in the new challenging conditions, VELO granularity will be increased passing from the $r-\phi$ geometry to 55×55 μm^2 pixels [74]. With also increased granularity, silicon tracker will undergo sensors replacement, and outer tracker will be re-designed from straw tube technology to scintillating fibers read out by SiPM [75]. Particle identification detector design will also be modified [76]. Hybrid photon detectors, having integrated front-end electronics will be replaced by multi-anode photon multipliers in both RICH detectors. Due to high occupancy in RICH1, the optics will be re-designed, and the aerogel radiator in RICH1 will be replaced by the CF_4 radiator. The detectors only dedicated to L0 trigger, first station of muon chambers, scintillator pad detector and preshower, will be removed. This will not affect the performance, because complete detector information will be available already at the trigger level in the upgraded LHCb trigger design. The reduced photomultiplier (PM) gains of the ECAL and HCAL will be compensated by the increased electronics gain.

The physics case of the upgraded LHCb experiment implies an order of magnitude increasing signal yields for key measurements, while keeping background level under control. Among the examples of the upgraded LHCb physics reach, improving precision of the branching fraction $\mathcal{B}(B_s^0 \to \mu^+\mu^-)$ measurement and search for $B^0 \to \mu^+\mu^-$ decay channel should be mentioned. The results of the LHCb [25] and CMS [77]

experiments already allowed excluding several theoretical models [78, 79]. With the upgraded detector $\mathcal{B}(B_s^0 \to \mu^+\mu^-)$ measurement is expected to reach 5% precision, while the error on the ratio $\mathcal{B}(B^0 \to \mu^+\mu^-)/\mathcal{B}(B_s^0 \to \mu^+\mu^-)$ is expected to be about 35%, and will allow to exclude several other models, if no deviation is found. Data taking after the LHCb upgrade can significantly increase sensitivity for another broad class of rare decays, driven by $b \to s$ transitions, *e.g.* $B^+ \to K^*(K\pi)\mu\mu$. This decay mode has been already addressed by LHCb [80, 81], comparing several observables to theoretical predictions. With the upgraded detector, the precision on all the observables is expected to increase by at least one order of magnitude. Important measurements of angle γ to search for *CP* symmetry violation effects, other than introduced by the Standard Model [82], is another key line in the program of the upgraded LHCb. The angle γ of the unitarity triangle is the least known to date, and is considered to be the most promising to compare tree mediated processes to those involving loop diagrams, in order to extract potential contribution of effects beyond the SM. The current best determination of the angle γ is obtained by LHCb [17], and with the upgraded detector a precision below 1% is expected. Finally the upgraded LHCb detector should fully exploit its capacity for precision measurements involving B_s^0 meson decays. Data from Tevatron experiments indicated potential anomalous CP violating effects [83–86], while the LHCb measurements using 1 fb^{-1} integrated luminosity are compatible with the SM expectations within uncertainties [19, 87, 88]. The upgraded LHCb experiment will be able to probe these effects to a precision of the order 10^{-3} in several decay modes, thus (discovering or) providing strong constraints on possible sources of physics beyond SM in these processes.

The upgraded version of the LHCb experiment is scheduled to enter the scene in 2019, for the LHC run 3.

In terms of detector development, the next chapter addresses more a retrospective calorimeter discussion, rather than the upgrade-related issues.

Chapter 3

Construction of the LHCb electromagnetic calorimeter detector

We can forgive a man for making a useful thing as long as he does not admire it. The only excuse for making a useless thing is that one admires it intensely.

Oscar Wilde

3.1 The LHCb calorimeter system

In this chapter the LHCb calorimeter detectors are addressed, noticing common principles and approaches to construct an integrated system of four calorimeter detectors. The LHCb calorimeters are key ingredients of the LHCb trigger (section 2.3.4). In addition, ECAL provides offline measurement of photons and neutral pions.

The LHCb calorimeter system [35,40] is located between 12.3 and 15.0 m from the pp beam crossing area, and comprises three calorimeters, preshower (PS), electromagnetic (ECAL) and hadronic (HCAL), and one threshold scintillator pad detector (SPD), all arranged in a pseudo-projective geometry.

The two halves of each calorimeter detector can be retracted separately and independently of other detectors to the left and right side of the beam to ensure service and maintenance.

The calorimeter outer dimensions match projectively those of the tracking system, $\theta_x < 300$ mrad, $\theta_y < 250$ mrad, the inner acceptance is restricted to $\theta_{x,y} > 20$ mrad around the beam pipe[1]. The sensitive area of each calorimeter detector thus covers a surface of about 50 m^2. The hit density is a steep function of the distance from the beam pipe, and varies over the active calorimeter surface by two orders of magnitude. Each detector is therefore subdivided into three sections with cell size of approximately 4×4 cm^2, 6×6 cm^2 and 12×12 cm^2. However, given the hadronic shower dimensions, the HCAL is segmented only into two zones with cell sizes a factor two bigger with respect to the values imposed by projectivity.

One of the main tasks of the calorimeter is to ensure the hardware implemented part of the high-E_T $e^{\pm}$, γ, π^0 and $h^{\pm}$ LHCb trigger alleys (section 2.3.4). The pp collisions occur every 25 ns, so that the detector response should be collected and readout within this time. This timing constraint is met by use of fast scintillating materials, and spill-over cancellation at the front-end electronics level with the signal clipping and subtraction of delayed signal for ECAL and HCAL, and with two alternating integrators for SPD and PS [89].

All four detectors follow the common principle of measuring shower energy from the light in the scintillator tiles transported to the photomultipliers by wavelength shifting (WLS) fibers.

For all detectors scintillator tiles are produced from polystyrene as a basic component with primary and secondary WLS dopants, paraterphenyl (PTP) and POPOP. A 1.75% to 2.5% of PTP and 0.01% to 0.05% of POPOP is admixed, with the individual optimal percentage for each detector. The Kuraray WLS fibers were used for all detectors, a 1 mm diameter Y11(250)MS70 for SPD and PS, and a 1.2 mm diameter Y11(250)MSJ for ECAL and HCAL. These fibers deliver the light captured in the scintillator tiles to their photodetectors.

[1]The ECAL acceptance was in addition limited by $\theta_x > 25$ mrad around the beam pipe due to the substantial radiation dose level, as discussed in section 3.2.3. The excluded region has been partly instrumented using the available FEE channels.

The ECAL and HCAL use R7899-20 phototubes, while SPD and PS employ the 64-channel R5900-M64 phototubes (MAPMT), both from Hamamatsu, with the high voltage always provided by a Cockcroft-Walton base. The photodetectors are screened with MuMetal shielding from the remaining magnetic field.

The **SPD/PS** detector consists of a 15 mm (2.5 X_0) thick lead converter sandwiched between two identical planes of 6016 high granularity scintillator pads each readout by the WLS fibers that are coupled to the 64 channels MAPMT via clear plastic fibers. Basic SPD/PS detector unit is a 15 mm thick scintillator tile, with a 3.5 loops of WLS fiber coiled and glued in a milled ring groove of the tile. The number of fiber loops in the groove is a compromize between the efficiency of light collection in the fiber and attenuation of the light during the travel inside the fiber. Each tile is then wrapped with a 0.15 mm TYVEK paper, and grouped into module units (Fig. 3.1).

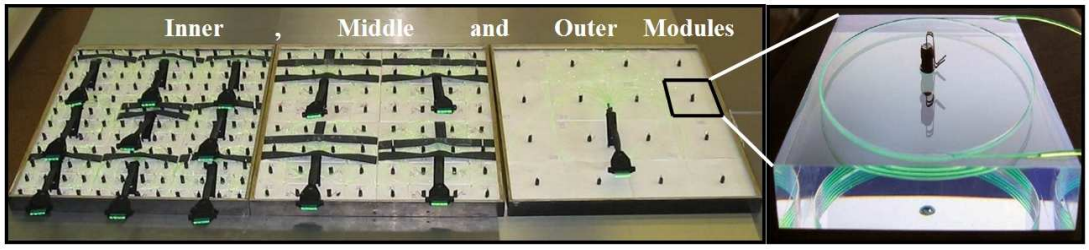

Figure 3.1: SPD/PS inner, middle and outer section modules (left to right) assembled from individually readout scintillator tiles (right)

The PS based e/π and SPD based γ/e separation was studied with the test beam. With a threshold of 4 MIPs pion rejection factors of 99.6%, 99.6% and 99.7% with electron retentions of 91%, 92% and 97% are achieved for 10, 20 and 50 GeV/c particle momenta, respectively. Fig. 3.2 shows energy deposits from 50 GeV electrons and pions. Three major processes can cause γ/e mis-identification. Dominant contribution comes from photon conversions in the material before SPD, with e.g. about 30% of photons converted before the calorimeter for photons from the $B^0 \to K^{*0}\gamma$ decay. The other two processes, producing charged particles in the SPD itself and charged back splash particles generated in the lead absorber or in the ECAL, have been studied in tagged photon beam and electron and pion beams of different energy [90, 91]. For a threshold of 0.7 MIP, mis-identification probability is $(0.8 \pm 0.3)\%$ due to interactions in the SPD scintillator, and $(0.9 \pm 0.6)\%$ and $(1.4 \pm 0.6)\%$ due to back splash for 20 and 50 GeV photons respectively. The above numbers are properly described by the simulation.

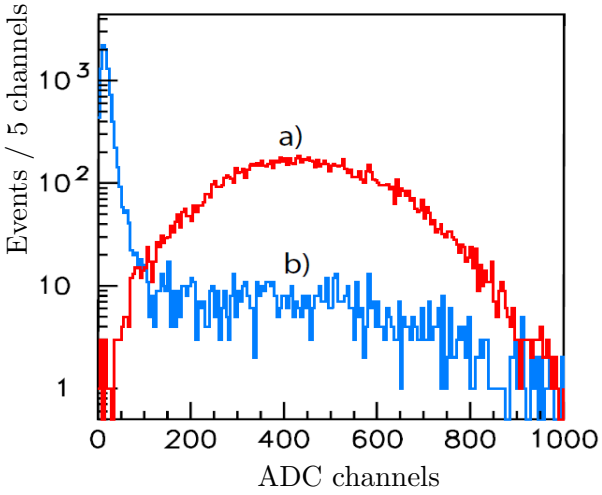

Figure 3.2: Energy deposit of 50 GeV electrons (a) and pions (b) in the PS

The detector has been pre-calibrated in horizontal position using cosmic particles. The average number of photoelectrons per MIP was measured to be 21 to 28 p.e./MIP depending on the cell size. Each cell is illuminated by individual LED monitoring light to follow detector stability and identify dead channels. A 5 Hz online event reconstruction provides monitoring with particles.

In addition, SPD provides particle multiplicity counting in low-multiplicity events, crucial for specific physics measurements [92, 93].

ECAL and HCAL are sampling calorimeters and employ the Shashlik and Tilecal technology, respectively.

The **HCAL** is an iron-scintillator tile calorimeter, $5.6\lambda_I$ deep, comprising 1488 readout cells. The scintillator tiles are positioned parallel to the beam axis (Fig. 3.3). Light from the tiles is then transferred by the WLS fibers passing along the tile edges, to the PM at the rear side of the HCAL. The Al mirror on the fiber front edge serves to increase the light yield and to partly compensate light attenuation in the fiber. Further compensation of light attenuation is achieved by the adjusted fiber-tile contact length depending on the distance to PM.

The lateral scan of the HCAL using 30 GeV electron beam provides a visual illustration of the signal propagation in the Tilecal (Fig. 3.4). Two effects have to be taken into account to explain the observed shapes, distance that light travels; and signal attenuation while the light is transported in the optical fiber and while the light is

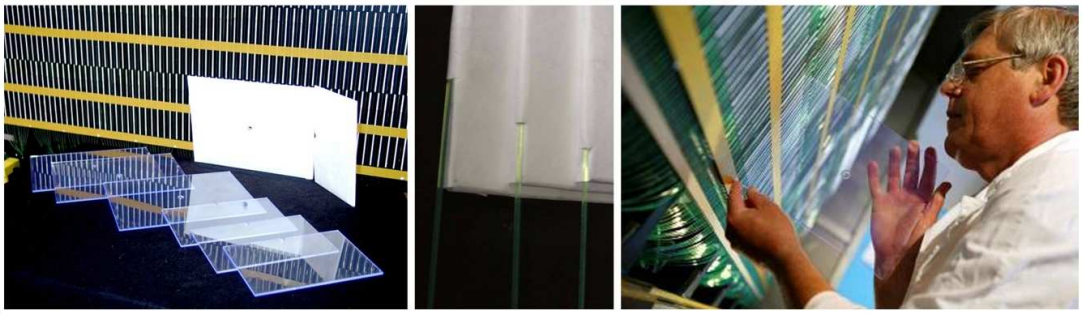

Figure 3.3: HCAL module scintillator tiles, TYVEK paper and iron profile (left), WLS fibers reading out the light from scintillator tiles with adjusted tile-fiber contact (center) and scintillator tile insertion in the module (right)

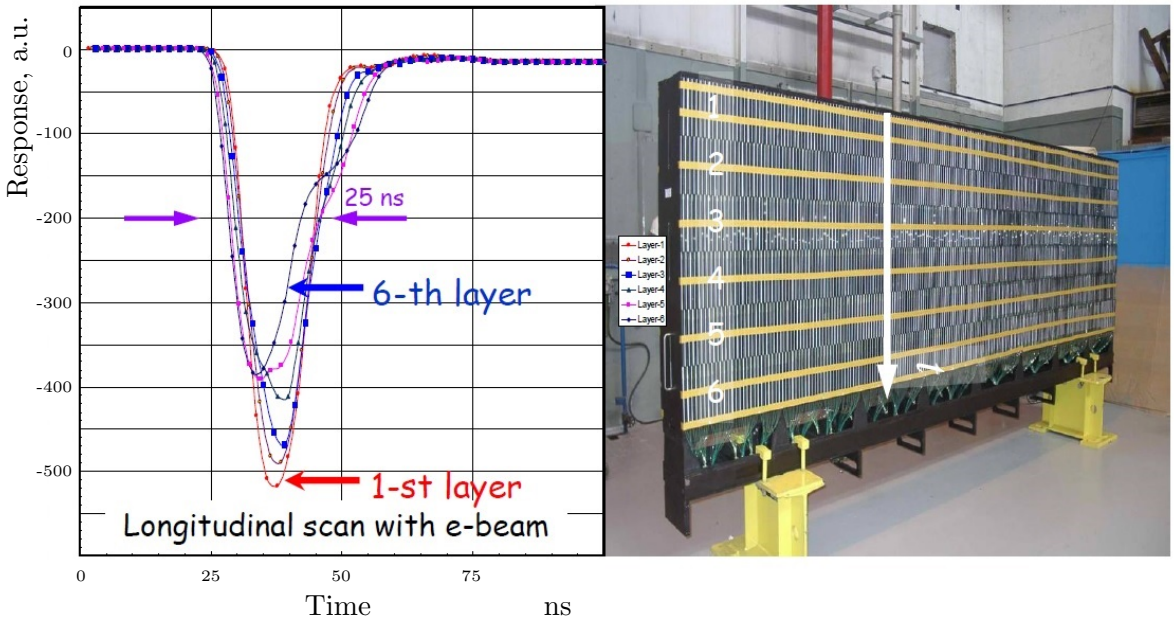

Figure 3.4: Lateral scan of the HCAL module with the electron beam. Time dependence of the signal shape is shown on the plot for different beam positions (numbers on the photo)

reflected from the mirror on the front side of the module. Each observed signal shape is composed of the part corresponding to the light directly transported to the rear (PM) side of HCAL, and of the part corresponding to the light transported to the front (mirror) side of HCAL, then reflected and passed all the depth of the HCAL towards the PM at the rear HCAL side. The first, direct, component arrives faster and is less attenuated, while second, reflected, component arrives later and is more attenuated. The difference in the arrival time and in the amplitudes between the two components

is smaller towards the front side of the HCAL. Therefore, the signal is observed as a single component with large amplitude when the first layer of the module is exposed to the beam, and as two components with most separated arrival time of the signal and different amplitudes when exposing to the beam the sixth layer of the module. In all the cases, and taking into account that HCAL primary function is the trigger search, signal is comfortably contained in the 25 ns time slot between the subsequent LHC beam crossing.

Measured energy resolution of $\sigma_E/E = (69 \pm 5)\%/\sqrt{E} \oplus (9 \pm 2)\%$ with E measured in GeV, fully meets the essentially trigger requirements to the HCAL performance. The light yield of 105 p.e./GeV requires compared to ECAL higher gain settings for the PM. About 3% angular dependence of the response at higher energies is explained by not fully shower containment in the instrumented depth of $5.6\lambda_I$.

The in-situ calibration is achieved using the dedicated ^{137}Cs source. The ^{137}Cs source can be precisely positioned inside the steel tube penetrating the center of each tile using the remotely controlled water pumping system. All cells have been measured this way before the HCAL installation in the LHCb experiment. In addition selected cells have been cross-calibrated at the test beam. The ^{137}Cs source scan showed the tiles belonging to the same HCAL readout cells to have light yield r.m.s. below 5%. This measurement also yielded a by-product verification of the light attenuation correction technique described above. The ^{137}Cs source measurements of the tile amplitude variations showed the minimum-to-maximum difference of less than 4% of the average over the two months time for 99% of the cells, proving the system to be very stable. For the remaining 1% of the cells corrections using the LED system are required. Several annual re-calibration sessions with ^{137}Cs source are performed to follow the gain evolution in HCAL cells.

The requirement to have the same physics scale over the calorimeter surface assumes the PM gain to follow the E_{max} = 15 GeV $/sin(\theta)$ distribution. PM high voltage settings adjusted to ensure this so-called physics gain distribution cause PM transit time spread. The resulting gain dependence over the calorimeter surface is illustrated by the HCAL current distribution from the ^{137}Cs source scan of each scintillator tile (Fig. 3.5). Channel-to-channel time spread of minimum-to-maximum difference of 4 ns and r.m.s. of 0.7 ns, is however dominated by time of flight variations.

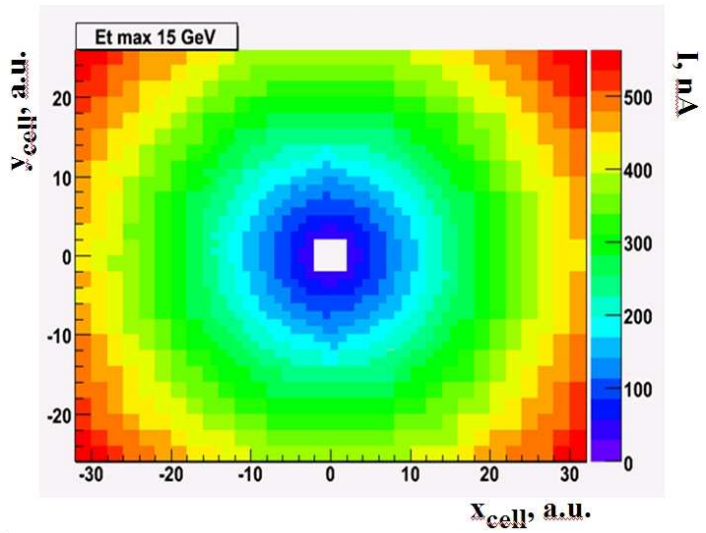

Figure 3.5: Scan of the HCAL scintillator tiles with the ^{137}Cs source. Current from PM matching the HCAL scintillator tile with the ^{137}Cs source is shown over the whole HCAL surface. The PM high voltage settings are adjusted to ensure physics gain distribution

The LHCb **ECAL** provides the reconstruction of electrons and photons, discrimination between electrons, and charged hadrons with overlapping photons, efficient π^0 and η reconstruction in a wide range of momentum. Fig. 3.6 shows pion misidentification

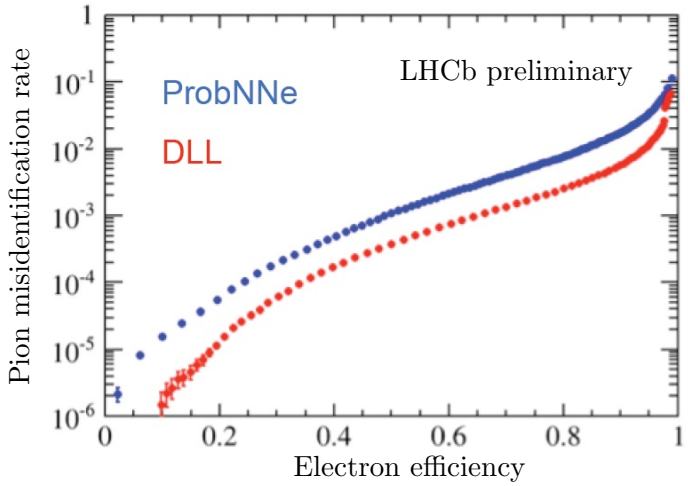

Figure 3.6: Electron identification. Pion misidentification rate is shown as a function of electron efficiency

curve depending on electron efficiency. Fig. 3.7 shows π^0 signal on the invariant mass spectrum of photon pairs. It allowed reconstruction of penguin B-decays $B^0 \to K^{*0}\gamma$ and $B_s^0 \to \phi\gamma$ with a high-E_T photon [94], reconstruction of χ_c states for numerous

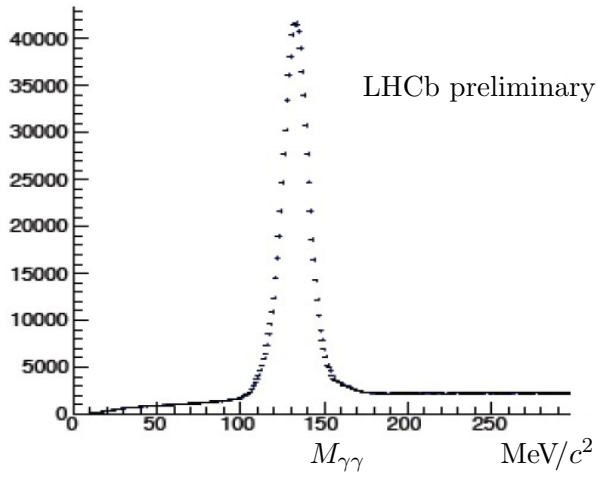

Figure 3.7: Reconstruction of neutral pions. Invariant mass spectrum of photon pairs

production analyses [9–11, 95] and $\chi_b(1\mathrm{P})$ states from $\Upsilon(1S)$ decays [11], and study of radiative transitions $B^{\pm} \to K^{\pm}\pi^{\mp}\pi^{\pm}$ [96] and $X(3872) \to \psi(2S)\gamma$ [97], with photons having lower E_T.

The ECAL detector is discussed in the next section. After presenting general concept, more details on the design, key performance issues, tests and detector construction are addressed.

3.2 Design and construction of electromagnetic calorimeter detector

3.2.1 Design of the calorimeter module

Engineering design of the electromagnetic calorimeter cells was performed together with Alexander Soldatov, Vladimir Rusinov, Evgueny Tarkovsky and others. Stanislav Malyshev provided an impressive technical support to prototypes construction. Test beam studies were performed with Vladimir Rusinov, Evgueny Tarkovsky, Ivan Korolko, Oleg Gushchin, Boris Bobchenko and others, and relied on a kind help from Lau Gatignon, Yens Spangaart and their colleagues from SPS team. Test beam studies were a subject of internship of Alexey Morozov.

The LHCb ECAL employs a sampling Shashlik technology. Shashlik technology implies a sampling scintillator-lead sandwich read out by plastic WLS fibers. This approach has been previously addressed by the RD36 project [98, 99], the PHENIX experiment [100, 101] at BNL, the HERA-B experiment [102–105] at DESY, and has therefore been chosen for LHCb ECAL and ALICE EMCAL [106, 107]. This choice was motivated by a good energy resolution, fast response time, acceptable radiation resistance and reliability of Shashlik technology, as well as the accumulated construction and operation experience. This technique offers a combination of an easy assembly, good hermeticity and a cheap solution compared to crystals or cryogenic liquid calorimeters.

The ECAL detector comprises 6016 readout cells, repartitioned between 3312 modules, comprising one, four or nine separately readout cells, depending on the distance to the beam pipe. In depth, ECAL cells (Fig. 3.8 and 3.9) are built from

Figure 3.8: Outer, middle and inner type modules

alternating layers of 2 mm thick lead, white reflecting 120 μm thick TYVEK paper and 4 mm thick scintillator tiles (Fig. 3.10, left). The 66 lead and 67 scintillator layers form a 42 cm deep stack corresponding to 25 X_0 or 1.1 λ_I. In each layer of module stack, the cells share the same lead plate abut posess individual scintillator tiles, with light isolation at the edges to prevent tile-to-tile cross talk. The Moliere radius of the stack is 3.5 cm. The stack is wrapped with black paper to ensure light tightness, pressed and fixed from the sides by welding of 100 μm steel foil.

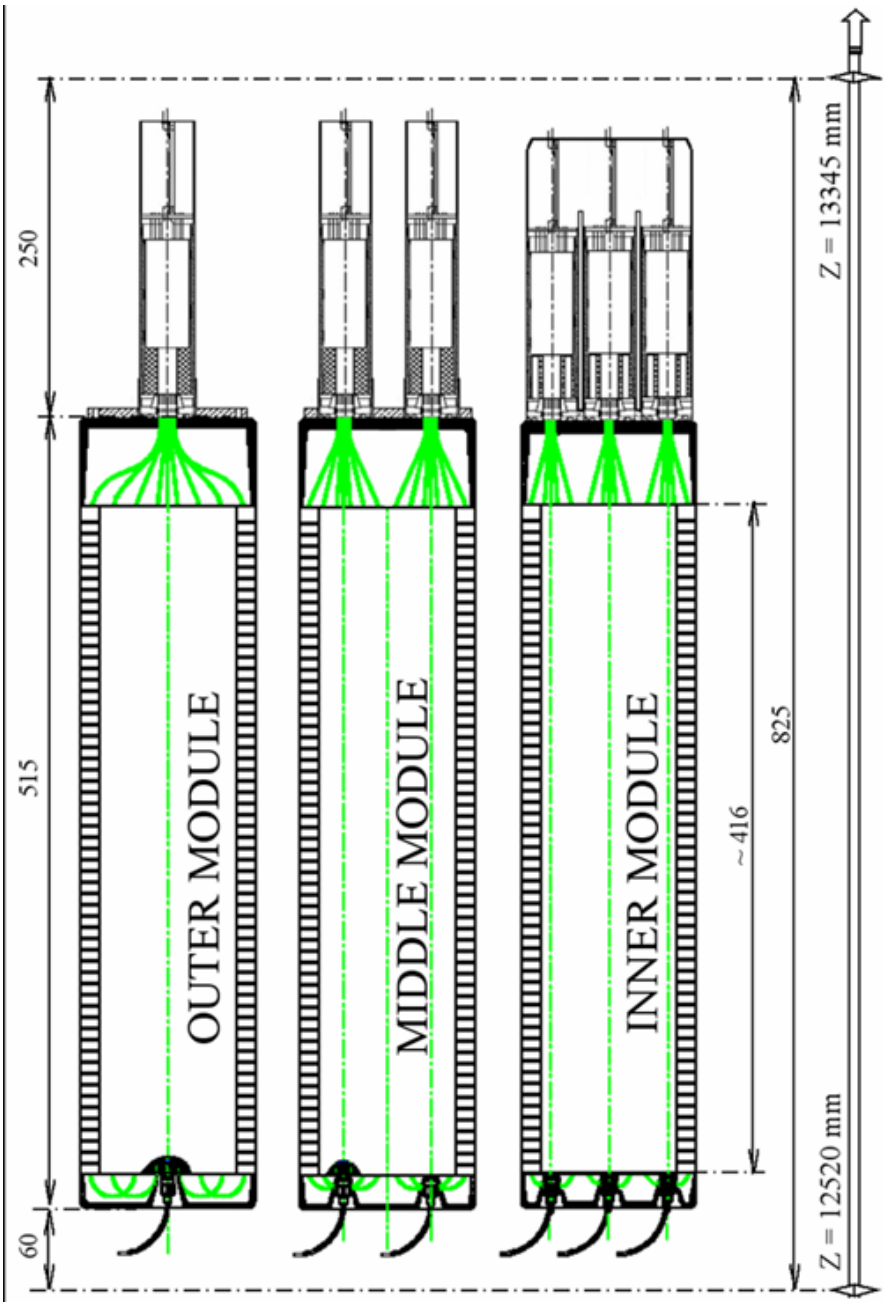

Figure 3.9: Electromagnetic calorimeter modules for inner, middle and outer sections. At the monitoring side shown are transport fibers, connectors, fiber loops and plastic covers. At the read-out side shown are fiber bundles, PMs and their bases

Module stack structure is illustrated by Fig. 3.8 and 3.9 for assembled detector, and

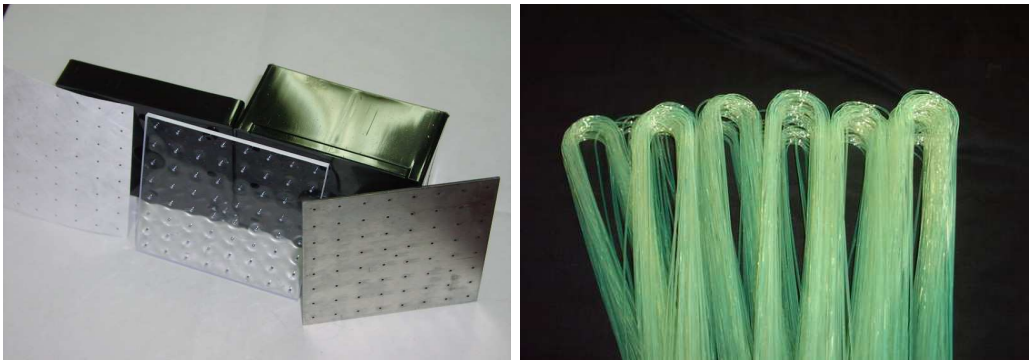

Figure 3.10: Components of the ECAL module stack, scintillator tiles, lead plates, TYVEK paper, fiber loop and fiber bundle plastic housings (left), WLS fiber loops (right)

by Fig. 3.35 and 3.34 in section 3.2.4 for open stack during module assembly.

Main parameters of the LHCb ECAL are shown in Table 3.1. Colour code on

	Inner section	Middle section	Outer section
Inner size, $x \times y$, cm^2	65×48	194×145	388×242
Outer size, $x \times y$, cm^2	194×145	388×242	776×630
Cell size, cm^2	4.04×4.04	6.06×6.06	12.12×12.12
# of modules	176	448	2688
# of channels	1536	1792	2688
# of cells per module	9	4	1
# of fibers per module	144	144	64
Fiber density, cm^{-2}	0.98	0.98	0.44

Table 3.1: Main parameters of the LHCb electromagnetic calorimeter

Fig. 3.51 in section 3.2.7 visualizes an area covered by ECAL sections with different cell size as well as the gap around the beam pipe.

Tiles were produced using the injection molding technique. Tile edges were chemically treated (section 4.1) thus providing diffusive reflection in order to improve light collection efficiency, lateral uniformity and prevent tile-to-tile light cross-talk. This way not only the tile edge inefficiency but also the effect of dead material between the modules has

been corrected, so that lateral non-uniformity does not dominate the constant term of energy resolution. Alternatively tile edges could have been aluminized (HERA-B-like solution) with the technique of Al evaporation in vacuum by HV-induced explosion. This latter method yields about 10% worse reflection efficiency, compared to the mat coating.

The light from scintillator tiles is re-emitted and transported by WLS Y-11(250)MSJ *fibers* penetrating the entire module. In addition, a clear fiber penetrates the center of each ECAL cell to deliver the LED light from the distribution system on the front side of ECAL to the PM for monitoring of the readout chain. The fibers belonging to each calorimeter cell are bundled at the end of the module and polished. Fiber density in the ECAL cell varies from $1.0\,\mathrm{cm}^{-2}$ for inner and middle type cells to $0.4\,\mathrm{cm}^{-2}$ for the outer type cell, where fiber density was reduced in order to obtain smaller fiber bundle size and thus impose reasonable requirements to the photocathode uniformity, and better lateral uniformity of response (section 3.2.2).

Kuraray Y11(200)MSJ fibers have been selected due to their high light yield; small attenuation length, matching of the absorption and emission spectra to the light coming from the scintillator tiles and registered by the photomultipliers, respectively; and tolerable radiation resistance (section 3.2.3). Y11(200)MS denotes multi-cladding (M) S-type (S) Y11 Kuraray fibers with the concentration of WLS dye of 200 *ppm*.

The fiber core is conventionally a polystyrene (PS, refraction index 1.59) based one, with the first cladding produced of Polymethylmethacrylate (PMMA, refraction index 1.49) and the second cladding (for multicladding fibers) of Fluorinated polymer (FP, refraction index 1.42) (Fig. 3.11). Using the subsequent claddings with lower refraction index, the light trapping angle is increased (Fig. 3.12). The amount of trapped light, that can be transmitted along the fiber, is thus also increased, from about 3.1% to 5.4% when adding a second cladding layer.

In order to improve light collection efficiency and lateral uniformity of response, the fibers form *loops* (Fig. 3.10, right) at the front side of the module.

The S-type fibers are produced with a molecular orientation along the fiber axis direction. They have better mechanical properties, are more resistant against cracks and can be bent to smaller angles without mechanical damage. Fig. 3.13a shows a principle of Kuraray measurements of the bending loss at the example of 1 mm diameter

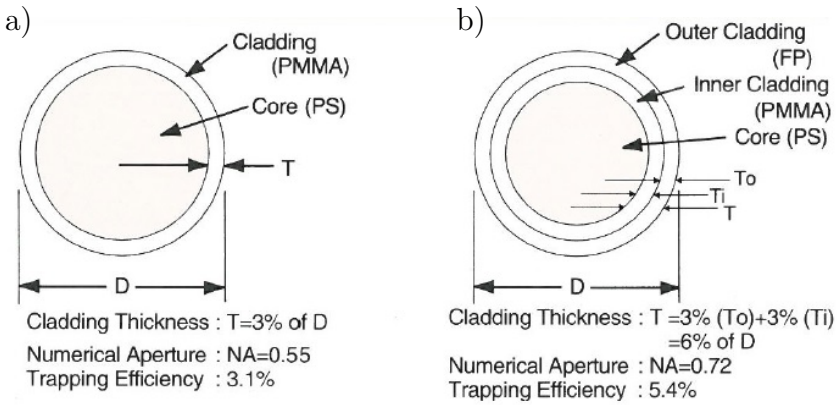

Figure 3.11: Parameters of single (a) and multi-cladding (b) optical fibers. Illustrations from booklet of Kuraray 1999

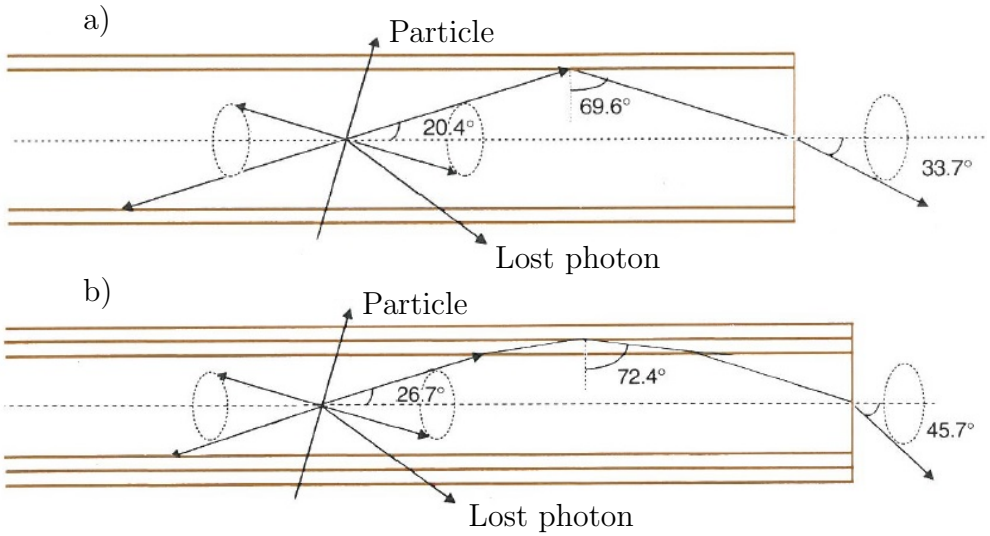

Figure 3.12: Geometrical optics scheme to explain the light trapping for single and multi-cladding optical fibers. Illustrations from booklet of Kuraray 1999

fiber, and Fig. 3.13b demonstrates a clear difference in the bending loss between S-type and non-S type fibers at small values of bending diameter. For a 1 mm diameter fiber, Kuraray recommends a minimum bending diameter of 200 mm for non-S type fibers, and of 100 mm for the fibers of S-type. However the ECAL cell design, motivated by considerations of lateral uniformity of response and aimed at reducing requirements to the PM photocathode uniformity (section 3.2.2), assumes fiber bending down to diameter values of 20 mm, which is significantly below the diameter values quoted by Kuraray. A method of fiber bending in the uniformly heated volume was developed at

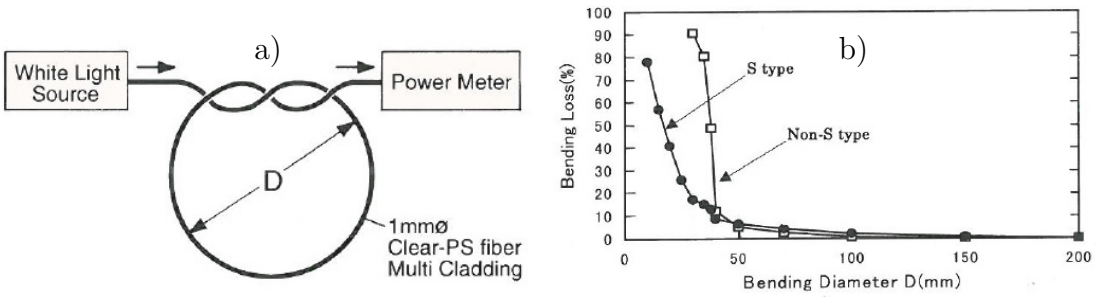

Figure 3.13: Principle of measurements of the bending loss (a) and bending loss for S-type and non-S type optical fibers (b). Illustrations from booklet of Kuraray 1999

ITEP and allowed to achieve required bending values, while the light loss is still driven mainly by the geometrical optics reflection down the loop. It is discussed in more detail in section 3.2.4.

In total, about 180 km of WLS fibers are routed inside the ECAL modules.

The light is read out with Hamamatsu R7899-20 phototubes with the high voltage provided by a Cockcroft-Walton base (Figure 3.14).

Figure 3.14: Hamamatsu R7899-20 phototube together with the light mixer, mixer housing and permalloy magnetic screen (left) and the Cockcroft-Walton multiplier soldered to the PM (right)

To further reduce the contribution from the PM cathode non-uniformity to the constant term, a quadrangular prism *light mixer* made from polystyrene, is inserted between the fiber bundle and the window of PM. The response to MIP was simulated with the light produced in scintillator, and then absorbed, re-emitted and transported by WLS fibers. Fig. 3.15 shows the distribution of the response non-uniformity versus

the length of light mixer. The non-uniformity of response is the non-uniformity at the

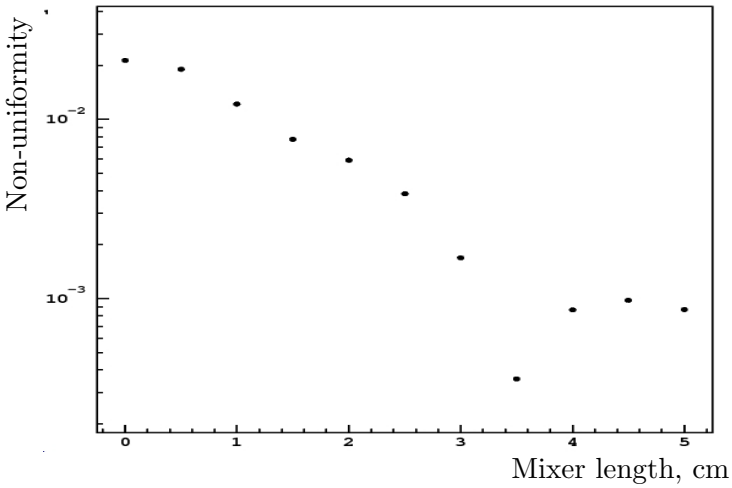

Figure 3.15: Simulation results for quadrangular light mixer. Shown is the non-uniformity of response versus the length of light mixer. The photocathode non-uniformity of 20% is assumed

mixer end, convoluted with PM cathode non-uniformity [2]. The resulting non-uniformity is small with respect to the constant term of the energy resolution.

The average light yield was measured to be between 2600 and 3500 photoelectrons per GeV, depending on the cell size [108]. The energy resolution of the ECAL cells was first measured in 2002 with an electron beam using a 3×3 matrix of outer type cells (Fig. 3.16) to be

$$\frac{\sigma_E}{E} = \frac{(9.4 \pm 0.2)\%}{\sqrt{E}} \oplus (0.83 \pm 0.02)\% \oplus \frac{(0.15 \pm 0.02)\,\mathrm{GeV}}{E} \ ,$$

well within the design value of $\sigma_E/E = 10\%/\sqrt{E} \oplus 1\%$, where E is always measured in GeV.

All ECAL cells have been pre-calibrated with cosmic particles before the installation in the LHCb detector (section 3.2.6). For further, in-situ, calibration, fluctuations of the signal from LED were used to preliminarily adjust the gain of the readout part (PM, amplifier and ADC) to better than 10%. The energy flow method, using smooth

[2] For the case illustrated in Figure 3.15 photocathode non-uniformity was taken to be 20%. The light produced in the scintillator tile by MIP, produces a green light distributed over all the WLS fibers. Typically contribution of the closest fiber is only about 15% of total light. Therefore the response non-uniformity to MIP signal is as small as $\sim 2\%$ already without the use of light mixer.

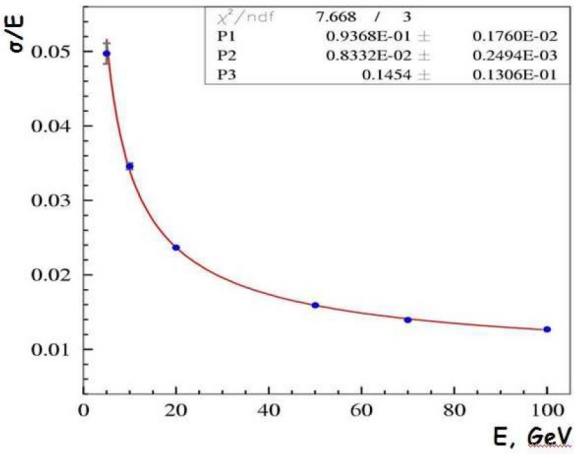

Figure 3.16: Energy resolution of the outer ECAL cell measured with electrons with the energy between 5 and 100 GeV using a 3×3 matrix of outer cells. Note the suppressed zero on the plot

distribution of energy deposition over calorimeter surface and symmetry considerations, was developed providing improvement to about 5% with possible 1-2% remaining bias. Calibration methods relying on the π^0 signal reconstruction have been proved to achieve calibration level of 1%. Finally the LED system was supposed to be used to follow eventual gain variations, while stability of LED light pulses is monitored with a system of pin diodes.

Two major effects were considered crucial for the ECAL performance, lateral uniformity of response, affecting constant term of energy resolution; and radiation resistance of scintillator materials, tiles and WLS fibers, that given sufficient amount of light produces larger effects on longitudinal uniformity of response, impacts linearity, and also affects the constant term of energy resolution.

3.2.2 Uniformity of lateral response

Exceptional expertise and a nice attitute of Vladimir Rusinov and Evgeny Tarkovsky guaranteed not just an optimisation of the calorimeter design, but a comprehension of different effects producing the observed lateral uniformity picture.

For a given cell size and sampling fraction, energy resolution, and to a lesser extent,

spatial resolution of Shashlik cell is determined by the uniformity of response.

Longitudinal uniformity can be achieved by using, over the depth of calorimeter cell, scintillator tiles with identical lateral uniformity of response, and WLS fibers with identical absorption and emission properties over their length and negligible attenuation. Alternatively, similar shower shapes for all incoming particles would make it possible to consider calorimeter as longitudinally uniform, after calibration. In any case, radiation induced degradation of plastic materials will differently damage calorimeter cell over its depth, causing different longitudinal non-uniformity effects for different energies, and requiring calorimeter re-calibration.

Lateral uniformity of the ECAL response, cell design optimisation in order to improve the ECAL uniformity, analysis of light collection and related test beam results are addressed in Ref. [108, 109]. The response was considered for particles incoming along the ECAL cell axis. For particles, inclined with respect to this direction, the effects causing non-uniformity are smeared as the shower traverses geometrical points having different response.

Lateral non-uniformity in a Shashlik detector, where WLS fibers collect light produced in the scintillator tiles, comes predominantly from two sources, the effect of non-perfect light reflection from tile edges (*global non-uniformity*), and the effect of shower position with respect to the fibers (*local or inter-fiber non-uniformity*).

Global non-uniformity shows that, because of the efficiency loss when light is reflected from the tile edges, the light originating at the tile center has higher probability to get collected by fibers than the light originating at the periphery of the tile. Thus the effect depends on the mean light path, which is a function of tile transparency, edge reflection quality and fiber density, and the efficiency exhibits a parabola-like behaviour over the tile surface.

Improving the efficiency of light reflection from tile edges serves also to prevent the tile-to-tile light cross-talk.

Local non-uniformity indicates the solid angle from which the fibers are seen from a particular point, and introduces a cosine-like term into the efficiency position dependence. Distance between fibers and fiber diameter affect local non-uniformity effect.

Following Ref. [98] the non-uniformity effect is parameterized with

$$f(x) = a \times \left[1 - A_{global} \cdot \left(\frac{x - x_0}{l_0/2}\right)^2\right] \times \left[1 - A_{local} \cdot \cos\left\{\frac{2\pi}{d} \cdot (x - x_0)\right\}\right] , \quad (3.1)$$

where x_0 is a cell center position, l_0 – cell size, d – distance between the fibers, a – normalization factor, and A_{global} and A_{local} values determine the size of global and local non-uniformity effect, respectively.

Two major approaches can be followed to reduce lateral non-uniformity effect. Using complete detector information, on-line or off-line corrections can be applied on the candidate-by-candidate basis. For electrons shower center position is then refined using parameters of matching track, with direction and momentum measured by the tracking detectors. For γ showers an iterative procedure, relying on the known uniformity distribution, improves the precision, using the expression 3.1 and cell response and shower center position as parameters. Overlapping showers, which belong to photons from π^0 or η decay, limit the improvement potential, while contribution from pile-up obscures the picture of showers from neutral particles. Global uniformity corrections do not require precise coordinate knowledge, and are easiest to apply.

Alternatively or complementarily, lateral uniformity can be improved at the stage of calorimeter cell design. Improving the reflection efficiency from the tile edges and the choice of fiber density are discussed below.

Response to a ^{90}Sr source at the tile center and close to the tile edge was compared using a test setup for 55.5×55.5 mm^2 tiles with blackened, aluminized and white painted edges. Light was read out via fibers penetrating the tile similar to ordinary module read-out. PM current at different ^{90}Sr source positions over the tile surface was measured. Table 3.2 shows response at the tile center and the difference in response between the center and the edge for tiles with different edge coating, thus comparing global non-uniformity effect and corresponding degradation of the mean light path, induced by tile edge reflection inefficiency. These results agree well with the simulation, which also predicts 2, 5 and 7 cm mean light path for blackened, aluminized and white tile edge respectively.

Another impact on the uniformity comes from the fiber density of the cell. Reducing fiber density in the outer section cell [3] improves global uniformity (tile edges are better

[3]Inner section cells suffer from substantial radiation dose. The annual dose reaches 0.25 $Mrad$ for

Table 3.2: Non-uniformity global effect, induced by tile edge reflection inefficiency. The response at the tile center and the difference in response between the center and the edge of tile are shown for blackened, aluminized and white painted edges. Directly measured was the PM current depending on the ^{90}Sr source position over the tile surface

edge coverage type	response at tile center, $[nA]$	center-edge difference, [%]
blackened	48	19
aluminized	112	7
white diffused (BC-622A)	134	4

seen from the tile center for reduced fiber density, and are effectively screened from the tile center for high fiber densities) and reduces the module cost. However, at the same time local uniformity degrades (the distance between fibers increases) and light yield reduces.

Three identical modules of 124.2×124.2 mm^2 size, similar to the size of LHCb ECAL outer cell, were assembled with 64, 100 and 144 fibers per module. Tile edges were chemically coated (section 3.2.4) to provide a diffusive reflection, relying on the test results shown above. The fiber front ends were coated with Aluminum mirrors. Nonet of modules was tested with MIP and 50 GeV electron beam at SPS. Table 3.3 shows the light yield and response uniformity parameters. Figure 3.17 shows the response, after global type uniformity correction, versus the coordinate. The response follows the fiber pattern. According to expectations, non-uniformity effect increases with the inter-fiber distance, the fit gives 0.3%, 0.5% and 0.7% for 144, 100 and 64 fiber cells, respectively. This non-uniformity, and in particular local non-uniformity, effect is further smeared when particles come at non-zero angle θ to the normal to calorimeter surface. This angle exceeds $\theta_0 = 80$ $mrad$ for photons entering outer region of calorimeter.

Simulation of light propagation in the scintillator tile with WLS fibers, illustrate the interplay between the tile transparency and the fiber density impacts on the local

the innermost region (section 3.2.3). To minimize module degradation the geometry absorption length, λ_{geom}, should be as small as possible, thus prohibiting to reduce fiber density. On the contrary, dose accumulated by the outer section modules does not exceed 0.02 $Mrad$ per year of LHCb operation, and the fiber density optimization is allowed.

Table 3.3: Response non-uniformity of modules with 144, 100 and 64 fibers per module, as measured with MIP and electron beams. Global and local non-uniformity effects are expressed in terms of A_{global} and A_{local} coefficients from parameterization (1) correspondingly. Implied is the integration over the effect along y-direction

	144 fibers	100 fibers	64 fibers
MIP beam			
light yield, $[a.u.]$	1.20	1.00	0.74
global non-uniformity, A_{global}	0.06(1)	0.03(1)	0.01(1)
local non-uniformity, A_{local}	0.004(1)	0.009(1)	0.012(1)
e^- beam			
light yield, $[a.u.]$	1.27	1.00	0.70
global non-uniformity, A_{global}	0.03(1)	0.02(1)	0.02(1)
local non-uniformity, A_{local}	0.003(1)	0.005(1)	0.007(1)

uniformity of response. Table 3.4 shows A_{local} coefficients from parameterization 3.1

Table 3.4: Scintillator transparency and fiber density impact on the local uniformity of the response to MIPs, as studied with Monte Carlo. Shown is the value of A_{local} coefficient from parameterization (1). Options with 144, 100 and 64, and $\lambda_{Sci} = 15\ cm$, 25 cm and 50 cm are considered

	Fibers per tile		
Mean light path, λ_{Sci}	144	100	64
15 cm	0.0035(5)	0.0091(4)	0.0132(3)
25 cm	0.0005(5)	0.0051(4)	0.0089(3)
50 cm	0.0004(4)	0.0022(3)	0.0063(3)

for the cells with 144, 100 and 64 fibers per tile, and mean light path of $\lambda_{Sci} = 15\,\text{cm}$, 25 cm and 50 cm. As expected, both increasing fiber density and increasing of mean light path effects improve local uniformity of response. Indeed, if photons travel long enough in the tile (due to good scintillator transparency and efficient edge reflection), they meet a fiber with high probability, and the local non-uniformity becomes small. The picture obtained is in good agreement with the local uniformity as measured with

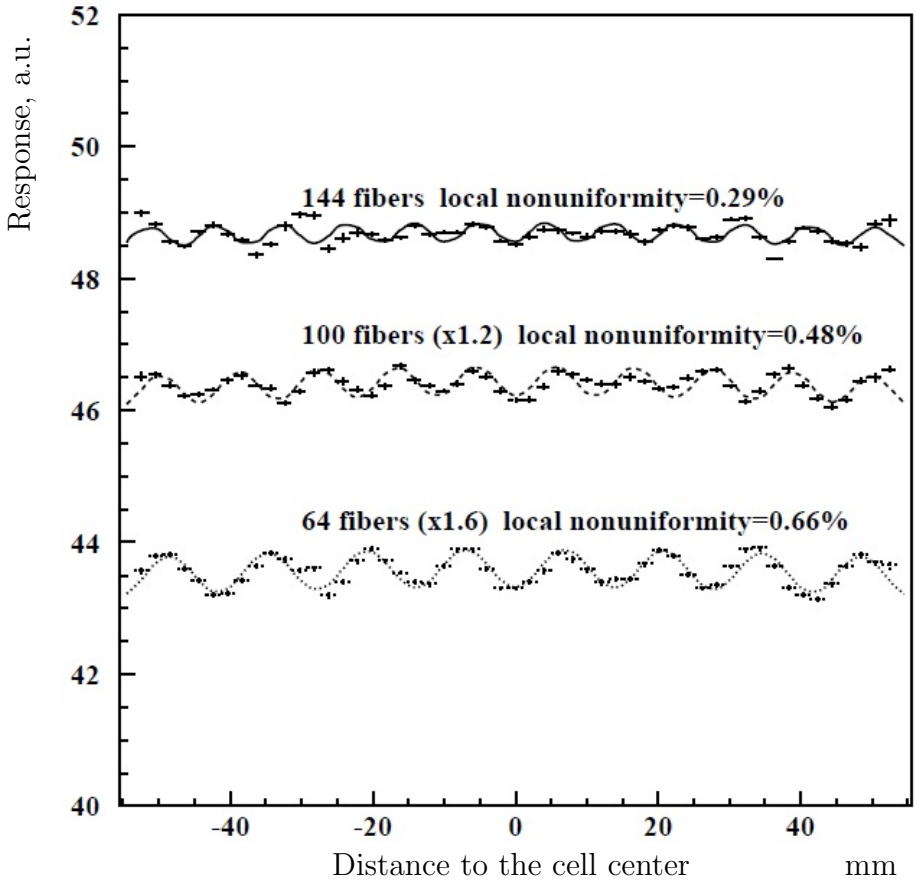

Figure 3.17: Local response uniformity measured for three modules with 64, 100 and 144 fibers per module, with 50 GeV electrons at $X7$ beam at CERN. Global type uniformity corrections are taken into account on the plot. The curves are the results of the fit

MIPs (Table 3.3), if assuming $\lambda_{Sci} \sim 15\,\text{cm}$.

The measurements shown, that about 30% of light is reflected from TYVEK paper prior to being collected by WLS fibers. Given sufficient light yield, uniformity of response can be complementarily improved by using *masks* – paper placed between tile and TYVEK, governing the reflection from tile sides. Such a mask suppresses the light at positions corresponding to maxima of cell response, thus improving the uniformity of both types.

LHCb ECAL employed the solution with 64 fibers per outer section module and with 144 fibers per module for inner or middle sections. Mat coating of tile edges allowed to achieve record lateral uniformity of response for Shashlik type calorimeters. Response variation over the cell position for outer type cell was measured with the

electron beam after corrections for energy-position dependence of the beam. Variations within ±1.3% over the cell surface were observed (Fig. 3.18). For realistic incident

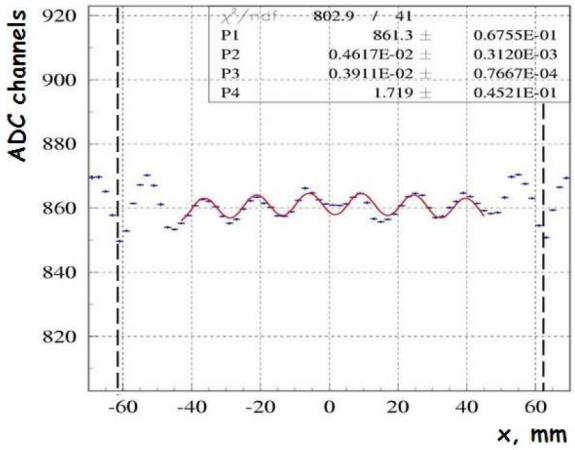

Figure 3.18: Lateral scan of outer ECAL cell with 50 GeV electrons. Dashed lines indicate borders with neighbour cells. Note the suppressed zero on the plot

angles, bigger than 200 mrad, the response varies by less than ±0.6% over the module surface. Variations seen around ±60 mm from the cell center, correspond to transition between the modules. For the inner and middle type cells fiber type non-uniformity is smaller due to higher fiber density. Results on the lateral variation of response are well described by the simulation for both e^- and μ^- lateral scans [110].

Contribution from lateral non-uniformity of response can be directly observed by comparing the energy resolution obtained in three different geometries [111]: a rectangle (full non-uniformity effect included), a strip (non-uniformity along one coordinate is eliminated) and a spot by averaging the energy resolution curves for four symmetrical $\pm 1mm \times \pm 1mm$ areas across the module surface (Fig. 3.19). The measured constant term differs for the three geometries, and its variation is consistent with corresponding lateral non-uniformities measured in terms of the A_{local} parameter (eq. 3.1).

3.2.3 Radiation resistance of scintillating materials

Choice of materials and understanding of the expected ECAL radiation resistance was possible due to a substantial number of experiments organised by Vladimir Rusinov and Evgeny Tarkovsky.

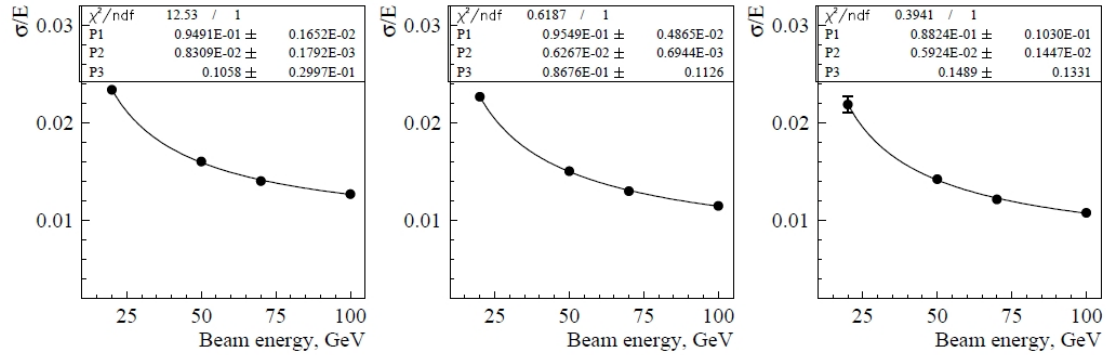

Figure 3.19: Energy resolution curves over different area on the cell surface: rectangle $(\Delta x, \Delta y) = (\pm 15mm, \pm 30mm)$), strip $(\Delta x, \Delta y) = (\pm 1mm, \pm 30mm)$) and spot $(\Delta x, \Delta y) = (\pm 1mm, \pm 1mm)$)

Calorimeter detectors experience significant radiation dose during LHCb operation. Expected radiation-induced degradation of the calorimeter resolution due to deterioration of optical components is discussed in Ref. [112, 113]. The performance degradation of the ECAL has to be compared to the performance required by physics considerations. The annual radiation dose, corresponding to 10^7 s operation and integrated luminosity $\int Ldt = 2$ fb^{-1}, reaches its maximum of 250 krad at the shower maximum position of the innermost ECAL cell, with about equal contributions from electromagnetic and hadronic components (Fig. 3.20). The dose exponentially decreases with the distance from the beam axis (Fig. 3.21), and therefore the optical components for the ECAL inner type cells are most subjected to the high dose values. Availability of spare readout channels motivated extension of instrumented ECAL volume as close to the beam as the vertical bar in horizontal direction (Fig. 3.21a) and as close to the beam as the left histogram bound in vertical direction (Fig. 3.21b). The modules of middle and outer regions do not suffer from such a dose, the maximum dose achieves there about 0.02 $Mrad$ per year of LHCb operation. Thus the reference maximum dose rate for the LHCb ECAL is taken as about 0.03 rad/s. The radiation resistance of the LHCb ECAL cells is discussed below.

As long as the photostatistics remains sufficient, ECAL energy resolution is determined by the constant term, that can be influenced by radiation induced degradation of active detector components, scintillator tiles and WLS fibers. Their radiation-induced degradation is discussed below. Radiation induced transverse and longitudinal non-uniformity makes the constant term rising. Light mixer and PM window transparency

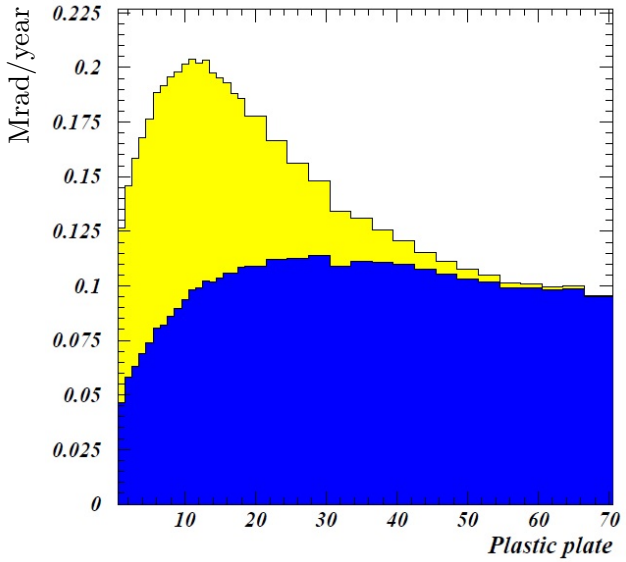

Figure 3.20: Longitudinal profile of the reference dose for the innermost module. The contributions from electromagnetic (light) and hadronic (dark) components of the shower are shown separately

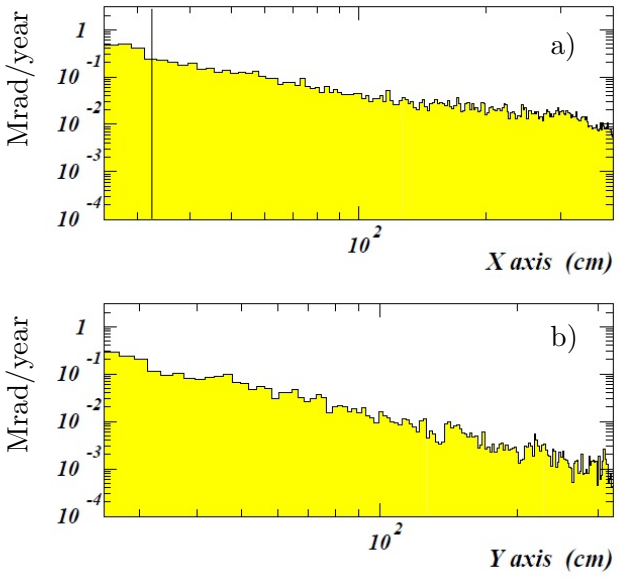

Figure 3.21: Lateral distribution of the reference annual radiation dose along x-axis in $y = 0$ slice (a) and along y-axis in $x = 0$ slice (b). Vertical line indicates the innermost position of active calorimeter volume

deterioration is not addressed. As far as plastic scintillator components are concerned, integral effect of brightness, transparency, possible tile edge coating degradation and fiber loop quality can degrade due to radiation induced structure distortion, active

radicals, radiolysis gaseous products and other effects.

At present many radiation test results are available. However, measurement conditions of each test are adapted to a specific experiment. They differ by

- dose parameters: dose value, rate and profile;
- annealing time: time intervals between irradiations and measurements;
- particles used for irradiation: photons, electrons, charged hadrons or neutrons;
- scintillator material: wide-spread are PSM-115, SCSN-81, BASF-165, and exactitude of raw material, tracked up to producer and production batch;
- fiber type: Kuraray Y11, Bicron BCF91, BCF92 and BCF99, Pol.Hi.Tech. S048 and S248, single or multi-cladding;
- geometrical features: fiber and tile size, fiber density, module geometry, etc.

This makes general comparisons difficult, and often requires dedicated tests for a given experiment.

Radiation induced damage reduces both brightness – ability to emit light for scintillator, and to re-emit light for fiber – and transparency of scintillator tiles and WLS fibers.

Brightness deterioration is first of all the property of materials themselves, and is considered to substantially depend on the irradiation method, in particular, on the dose accumulation rate and particle type. Since an annealing process proceeds in parallel with the radiation-induced degradation, one expects competing annealing process to noticeably compensate the degradation under small dose rates. Most often radiation tests are carried out with the dose rates, that are considerably higher compared to those expected in the experiment.

Similar to brightness deterioration, the change in mean path of photons depends on material and irradiation method, but also is a strong function of the pattern geometry. For scintillator this means, that the radiation induced changes increase with the mean light path. Thus, in order of Shashlik type calorimeter to operate in the highly irradiated

area, small size tiles and high fiber density (and even, probably, low reflection efficiency from tile edges) are profitable to diminish the initial mean light path.

For fiber damage studies the dose irradiation profile is important, uniform or approximated according to the expected distribution, and a presence, or not, of the reflected light, that can travel twice through the damaged area. Longer fibers effectively shift the spectrum transmitted light to bigger wavelength values. For LHCb ECAL typical fiber length is approximately 0.5 m or bigger for the light passing through fiber loop. Under irradiation transmission of small wavelength light degrades first, so that longer fibers become effectively more radiation resistance.

Major part of experiments aimed at radiation hardness studies of plastic materials used radioactive sources for irradiation. Complete module irradiation with an electron beam [114, 115] qualitatively showed the picture similar to that after irradiation with the source. Along with that, the irradiation with the proton beam [116] demonstrated possible dependence of the damage on particle type used for irradiation.

The above considerations allowed preliminary material selection as candidates for LHCb ECAL. Authors of Ref. [117] concluded that in view of brightness and radiation hardness, the combination of PSM-115 plastic and Y11 fibers is about equivalent to that of SCSN-81 plastic and the same Y11 fibers, so that the two major scintillator types, PSM-115 and SCSN-81, show similar performance. The emission spectrum of irradiated PSM-115 plastic and the degradation of scintillator transparency depending on the wavelength have been studied.

The initial choice of Y11(200)MS and BCF-91A(DC) double cladding Bicron fibers for detailed testing relies on the previous convincing measurements. The BCF99 fibers degradation dynamics relative to the degradation of BCF91 fibers under irradiation [4] up to 0.5 Mrad with a dose rate of about 0.6 rad/s at the 1.8 GeV energy ITEP proton accelerator, is shown in Fig. 3.22. The light yield from the beam induced signal was monitored for BCF-91A(DC), BCF-99 and Y11(200)MS fiber samples. Relative light yield $\frac{LY\ (BCF99)}{LY\ (BCF91)}$ follows beam current curve, and annealing effect is clearly seen without beam. Relative annealing is visible and matches the beam current evolution. Unlike evident BCF-99 fiber degradation, BCF-91A(DC) and Y11(200)MS fiber samples show

[4] Particles from interactions of 2.5 GeV/c momentum proton beam with the target were used for irradiation.

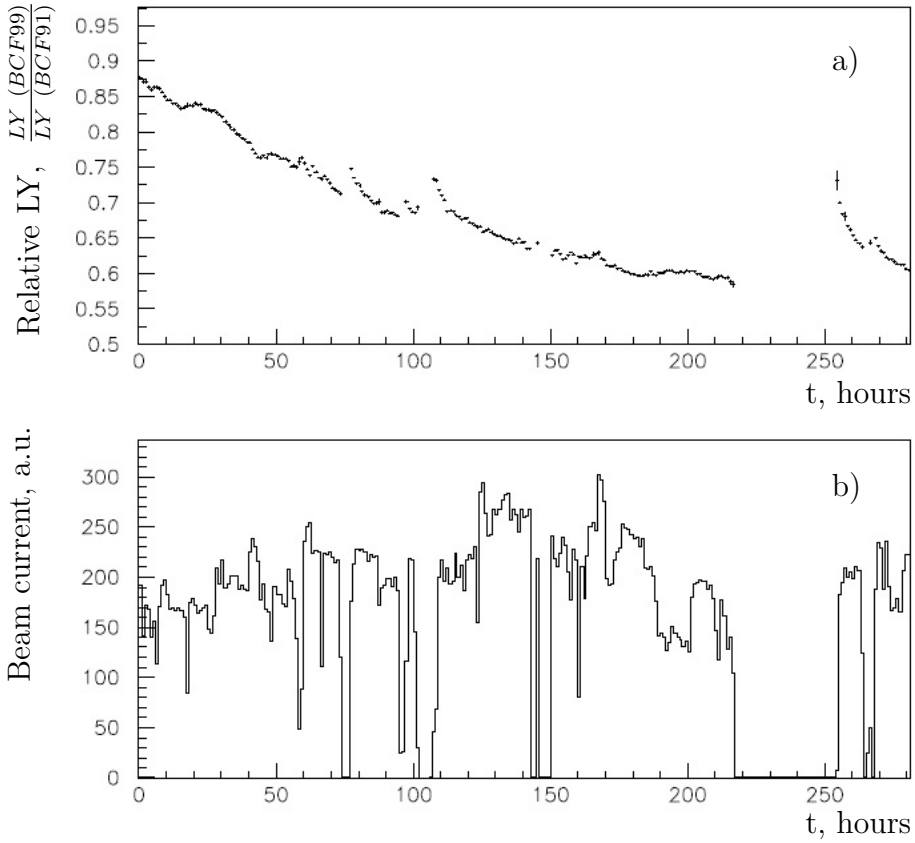

Figure 3.22: Degradation dynamics of BCF99 fibers relative to the degradation of BCF91 fibers under irradiation up to 0.5 $Mrad$ at ITEP accelerator. Time dependence of relative light yield $\frac{LY\ (BCF99)}{LY\ (BCF91)}$ (a) and the corresponding beam current (b) are shown

similar behaviour under these irradiation conditions.

Ref. [118] shows radiation resistance of Pol.Hi.Tech. fibers to be clearly worse than that of Kuraray products. Faster Bicron BCF-92A fibers also show worse radiation resistance [118, 119]. The Y11(250)MSJ and BCF-92A fiber samples were irradiated using ^{60}Co source up to 400 krad in four series of 100 krad each. The dose rate was about 0.4 rad/s. Brightness and transparency coefficients were measured before and after each irradiation period and 700 h after full irradiation dose is achieved. No visible degradation of Y11(250)MSJ fibers was observed, while BCF-92A fibers lost about 30% for each coefficient value.

Loops of BCF92 fibers with a loop diameter of 29 mm, corresponding to outer type ECAL cells, together with same type straight fibers, were irradiated with a ^{60}Co source

up to 150 krad with a dose rate of about 1 rad/s. When the effect of degradation corresponding to straight fibers is subtracted from the observed degradation for fibers forming loops, the remaining effect can be attributed to the deterioration of fiber loop quality. No significant deterioration of fiber loops was observed. Measurement error was estimated to be 5%.

Irradiation $40.2 \times 40.2\,\mathrm{mm}^2$ BASF-165 scintillator tiles with the ^{60}Co source up to doses of 100 krad and 200 krad with a dose accumulation rate of about 0.4 rad/s demonstrated similar annealing curves for the two dose values. The light yield dependence on the annealing time was measured using the hedgehog setup (section 3.2.5) starting from only about 3 h after irradiation was terminated.

The $40.2 \times 40.2\,\mathrm{mm}^2$ BASF-165 scintillator tiles and Y11(250)MSJ WLS fibers were irradiated at the ITEP proton beam, with the dose rate of 28 rad/s and a total of 1 Mrad accumulated dose. After irradiation, light yield of the tiles was measured with the ^{90}Sr source at 20 positions over the tile surface and then averaged. Reference tile measurements were used for normalization. After about 60 h of annealing process, the light yield reached a plateau at 80% of the initial light yield of the tile. Effect of brightness and transparency degradation of the fibers was studied separately and distinguished via $LY = B \cdot e^{-x/T}$ fit, where LY is the light yield, x is the distance from the PM to the tile moved along the fiber and excited with the ^{90}Sr source, and B and T are the extracted brightness and transparency coefficients. The reference fiber was used for normalization. After the 1 Mrad dose irradiation, annealing time about 100 h was observed with plateau values of 88% and 75% of the initial B and T values correspondingly.

In order to safely predict radiation damage of the designed experiment, perfectly reproduced beam energy, beam composition, expected dose rate and a full-scale detector prototype are required. Unfortunately such an experiment run into many difficulties, e.g. it takes exactly the designed project operation time. Still natural source of information mostly satisfying the above requirements could be a detector of similar design, operating in a similar accelerator environment. The HERA-B calorimeter provided some useful information that was possible to perform well-educated irradiation tests for LHCb ECAL.

An important *radiation test* has been performed *using electron beam of LIL*, LEP

Injector Linac. Three identical towers of 40×40 mm^2 size were assembled using PSM-115 plastic tiles and two species of fibers, Y11-200(MS) and BCF-91A(DC). Fibers had no treatment at their front end, so that only negligible fraction of reflected light from fiber front end, was achieving PM. Artificial sandwich of 20 layers each consistent of one 1.5 mm thick lead plate and five 4 mm thick scintillator tiles, was assembled in order to approximate combined electromagnetic and hadron dose profile [5] with 500 MeV energy electrons. Two modules were irradiated with electrons of 500 MeV energy up to 5 Mrad dose at shower maximum. The irradiation rate was approximately 10 rad/s, that is about 200 higher rate than the LHCb one.

Comparison was made between the irradiated modules with Y11-200(MS) and BCF-91A(DC) fibers, with respect to the reference non-irradiated module. Combining conventional irradiated lead/scintillator stack with reference fibers, and reference lead/scintillator stack with irradiated fibers, the damage effects of scintillator tiles and WLS fibers were separated. Each combination was longitudinally scanned with ^{90}Sr radioactive source, and the light yield was measured. The main results obtained are discussed below.

Scintillator degradation and annealing effect was studied after irradiation up to 5 Mrad dose at shower maximum. Fig. 3.23 shows light yield depending on distance to PM in 7, 55, 175 and 2000 hours after irradiation. Annealing effect is clearly seen up to $\sim$ 50 hours after irradiation. In Ref. [119] PSM-115 scintillator was irradiated with ^{137}Cs radioactive source with rate of 6 rad/s, and the observed annealing effect shows similar behaviour. However, the authors of Ref. [119] observed no remaining degradation after annealing for doses below 1 Mrad. Studying dependence of PSM-115 scintillator damage on the dose rate, authors of Ref. [120] performed irradiation ^{137}Cs source with the dose rates of 0.32 rad/s and 6 rad/s. They observed degradation to clearly increase with the dose rate. However they measured annealing effect to the same level independently on the dose rate.

Fig. 3.23 describes total signal reduction because of brightness degradation from one hand, and of light collection degradation, caused by scintillator blur, from the other. Light collection efficiency and its radiation induced degradation depend on [6]

[5] A price to pay for such a tricky sandwich is the impossibility to directly measure overall module effect from irradiation.

[6] For below discussion, scintillator material and fiber density are assumed to be predefined on the

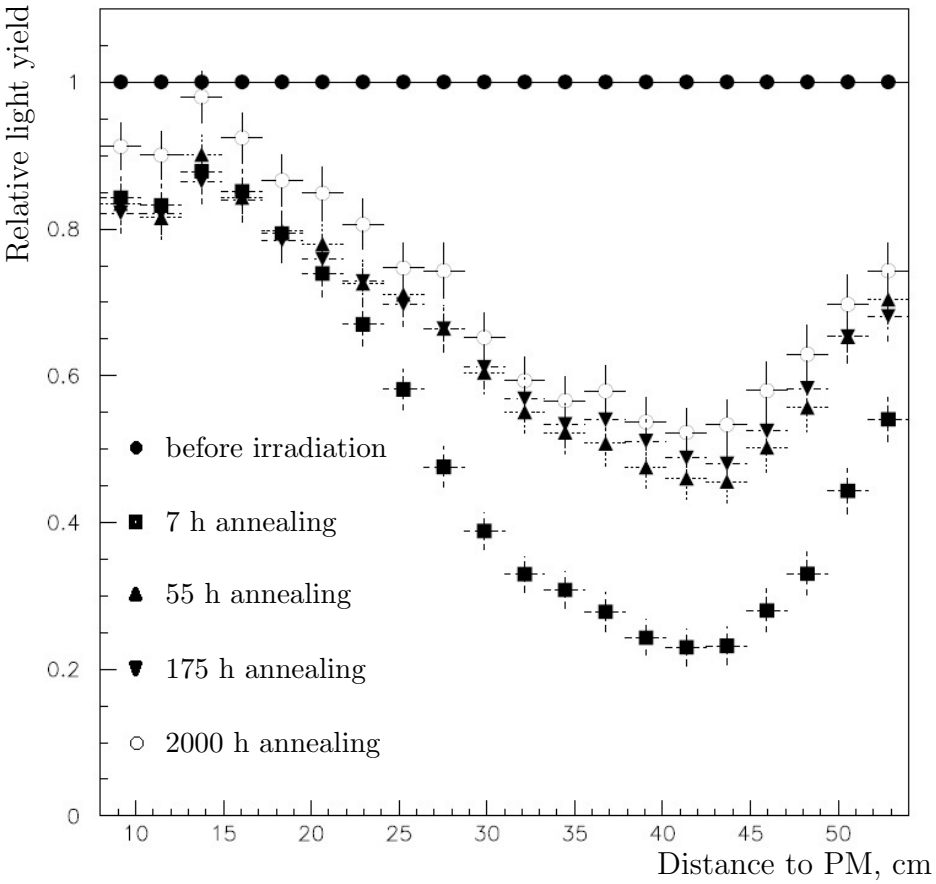

Figure 3.23: Scintillator degradation and annealing effect after irradiation at LIL up to 5 Mrad dose at shower maximum (shower maximum position corresponds to distance to PM of 42 cm). Shown is the light yield vs. distance to PM after 7, 55, 175 and 2000 hours after irradiation

the attenuation length λ_{bulk}, which reflects a property of material to be transparent to the light of a given wavelength, and on the light absorption length λ_{geom} driven by the geometry (effective fiber surface, as seen by the light, and efficiencies of reflection from the tile edges, from the fiber holes and from TYVEK, enter λ_{geom}). While λ_{bulk} worsens with the dose accumulated, the λ_{geom} is determined by the design.

The λ_{geom} reduction is profitable in a sense, that λ_{bulk} fall-off is less felt by the total scintillator tile light yield degradation. In order to decrease λ_{geom} one could shorten the mean light path of photon in non-irradiated tile. For illustration, considered is the shortening of mean light path achieved by worsening the quality of light reflection from tile edges. This would lead to lower radiation induced degradation effects from

basis of other considerations.

one hand, and to decreasing of the light yield from the other. Thus, having enough photostatistics, one would naively prefer the very poor light reflection efficiency from tile edges, if it were not for important transverse uniformity considerations [109].

To prove λ_{geom} significant impact on the performance, and to get quantitative picture, three PSM-115 tiles of 4×4 cm^2 size with clear polished edges, with aluminized edges and with mat edges respectively, were irradiated with ^{60}Co source up to 2 Mrad dose with a dose rate of about 10 rad/s. Initial light yield after irradiation was measured. Loss of the light yield depending on the accumulated dose is shown in Fig. 3.24. According to

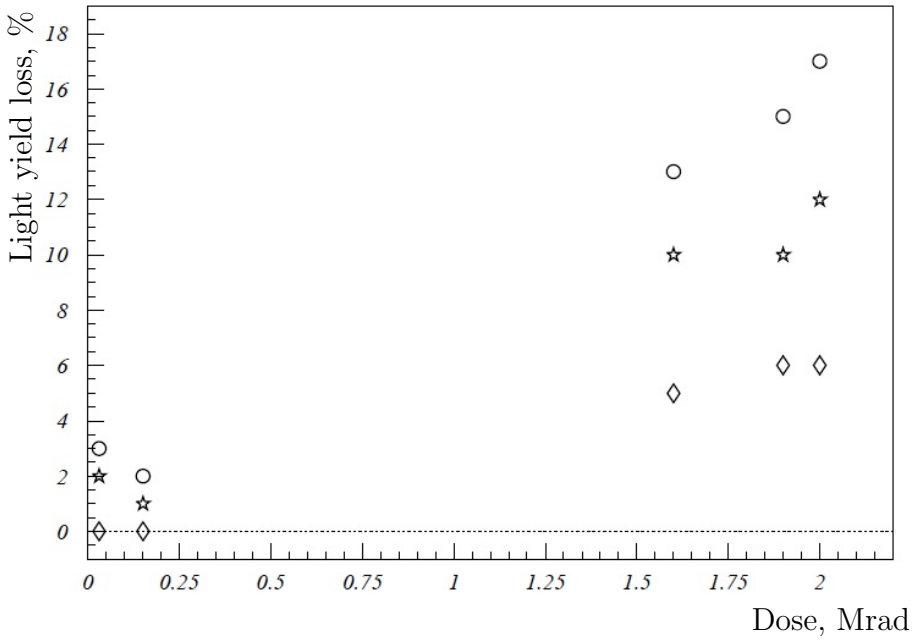

Figure 3.24: Radiation induced degradation of tiles of 4×4 cm^2 size with open (diamond), aluminized (stars) and mat (circles) edges. Light yield loss (in %) depending on accumulated dose is shown. Tiles were irradiated with ^{60}Co source up to 2 $Mrad$ dose, and read out by WLS fibers. Typical error of each measurement is $\sim 2\%$

the expectations, the tile with clear polished edges showed the least degradation, and the tile with mat edges, and consequently the largest λ_{geom}, degraded to the highest extent. Results for different λ_{geom} values obtained in Ref. [121] also support this interpretation of transparency impact on scintillator degradation. Thus small geometrical attenuation length, *i.e.* high fiber density and poor edge reflection, is advantegeous to limit radiation induced degradation effects.

Fig. 3.25 and 3.26 describe fiber degradation and annealing effect for Bicron BCF-

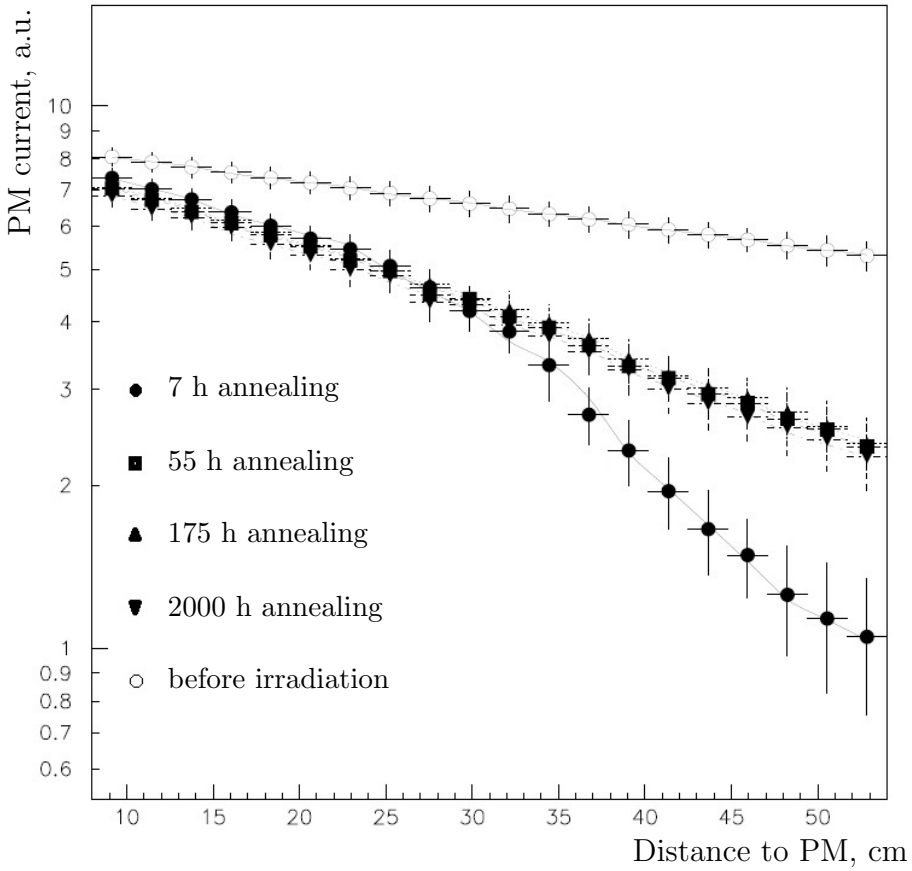

Figure 3.25: Bicron BCF-91A fiber degradation and annealing effect after irradiation at LIL up to 5 $Mrad$ dose at shower maximum. Shown is the PM current vs. distance to PM for non-irradiated fiber sample, and for irradiated fiber sample after 7, 55, 175 and 2000 *hours* after irradiation

91A and Kuraray Y11(200)MS fiber samples after irradiation up to 5 $Mrad$ dose at shower maximum. The PM current depending on the distance to PM for non-irradiated fiber sample, and for irradiated fiber sample is measured in 7, 55, 175 and 2000 *hours* after irradiation. Attenuation of signal from the largest distance for BCF-91A fiber was reduced to 20% from the initial value. Subsequent annealing improves the attenuation up to 50% in the first ~ 50 *hours* with no further improvement visible. For Y11(200)MS fibers the attenuation was reduced to less than 10% value compared to the initial measurement. Annealing effect improves attenuation up to 40% in the first ~ 50 *hours* after irradiation, and up to 70% after ~ 175 *hours* with no further improvement. Kuraray Y11(200)MS fibers behaviour appears more advantegeous, given limited realistic dose rate. For smaller fiber length, $l \approx 25\,\mathrm{cm}$, Y11(200)MS fibers were shown to have much better radiation resistance compared to that of BCF-91A

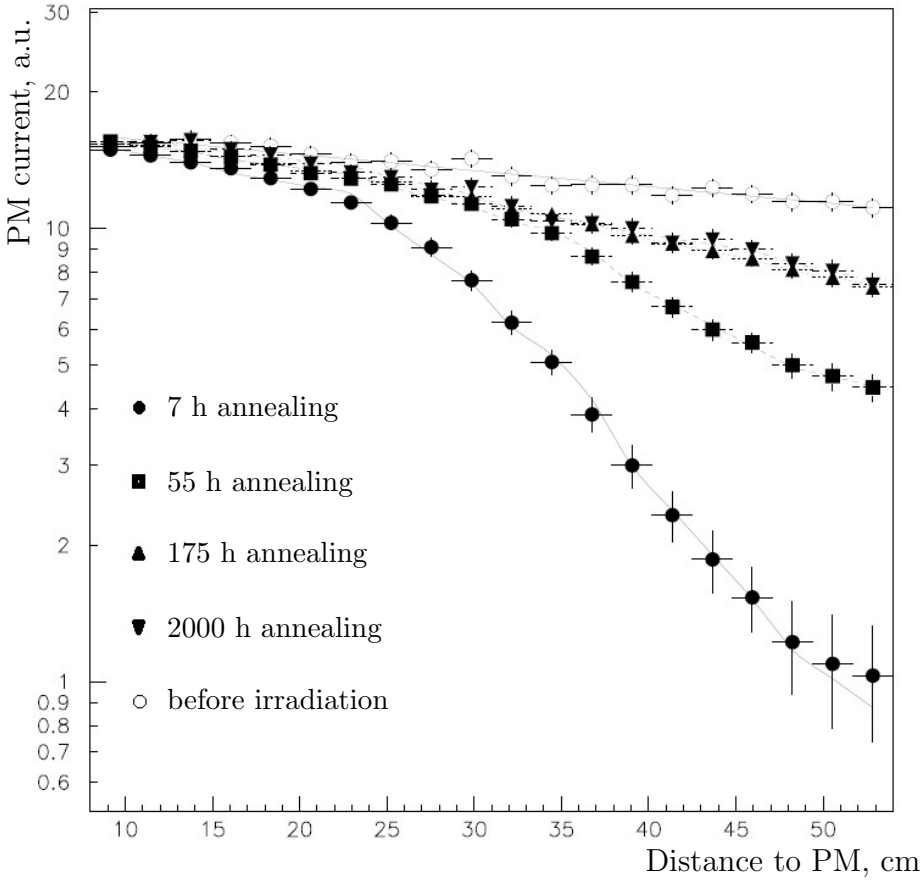

Figure 3.26: Kuraray Y11(200)MS fiber degradation and annealing effect after irradiation at LIL up to 5 *Mrad* dose at shower maximum. Shown is the PM current depending on the distance to PM for non-irradiated fiber sample, and for irradiated fiber sample after 7, 55, 175 and 2000 *hours* after irradiation

fibers [102].

Translation of the collected dose to the **actual module degradation and** to the corresponding change in the **energy resolution** is done using Monte Carlo simulation. The dose distribution along the module length was taken from Fig. 3.20. In addition, all observed radiation damage was assumed to have electromagnetic origine. Using the relation between the distance to PM from Fig. 3.25 and 3.26 and the accumulated dose, the dose dependence on the attenuation length was estimated for Bicron BCF-91A(DC) and Kuraray Y11(200)MS fiber samples. Scintillator degradation was estimated using the information from Fig. 3.23. Data distributions of scintillator brightness and fiber attenuation length depending on the dose were fit with an exponential function, assuming

B_{Sci} and λ_{Fib} dependences to be

$$B_{Sci} = B^0_{Sci} \cdot e^{-\frac{D}{D_S}} \quad and \quad \lambda_{Fib} = \lambda^0_{Fib} \cdot e^{-\frac{D}{D_F}} \ ,$$

where B^0_{Sci} and λ^0_{Fib} are the values of B_{Sci} and λ_{Fib} before irradiation, and D is the accumulated dose. The fit yielded (dose parameter estimates correspond to LHCb ECAL scintillator tile geometry and fiber length) dose parameter for scintillator $D_S = 7.3\ Mrad$, and fiber dose parameters $D_F = 4.4\ Mrad$ for BCF-91A(DC) fibers and $D_F = 7.1\ Mrad$ for Y11(200)MS fibers [7], which became the input to the simulation model.

Projected calorimeter performance degradation for the Y11(200)MS⊕PSM-115 and BCF-91A(DC)⊕PSM-115 combinations was obtained using simulation studies (Fig. 3.27 and 3.28, respectively). Peak damage depending on the energy for accumulated dose of $0; 1; 2; 3; 4; 5\ Mrad$, energy resolution degradation for energies of $5; 10; 20; 50; 100$ GeV, and radiation-induced degradation of the energy resolution constant term,

$$\frac{\sigma_{damage}}{E} = \sqrt{\left\{\frac{\sigma_E}{E}\right\}^2 - \left\{\left(\frac{\sigma_E}{E}\right)_0\right\}^2} \ ,$$

where subscript index "0" denotes non-irradiated value, are shown. For considered energies and dose values the BCF-91A(DC) and PSM-115 combination exhibits stronger degradation than the combination of Y11(200)MS and PSM-115. Horizontal lines indicate constant term of energy resolution reaching 1.5% value, considered as a limit, still accepted by physics performance criteria. This limit is reached at 1.9 $Mrad$ accumulated dose for the BCF-91A(DC)⊕PSM-115 combination and at 2.2 $Mrad$ for the Y11(200)MS⊕PSM-115 combination, respectively.

The Y11(200)MS and PSM-115 combination has been chosen for the LHCb ECAL. Fig. 3.21 predicts for the ECAL innermost cells to accumulate a dose of 2.5 $Mrad$ in 10 years of LHCb operation, corresponding to about 30% reduction in light yield. However, the ECAL energy resolution is not limited by photostatistics, and the expected induced constant term degradation of 1.5% is caused by longitudinal fluctuations, and achieved at a dose of 2.2 Mrad. Taking also into account the uncertainties, due to determination of dose values in the irradiation tests and due to predicting the dose values corresponding to LHC operation, a possibility to replace 48 innermost modules is foreseen in the calorimeter design (section 3.2.7).

[7] The λ^0_{Fib} parameters for BCF-91A(DC) and Y11(200)MS fibers have almost equal values of 105 cm and 100 cm, respectively.

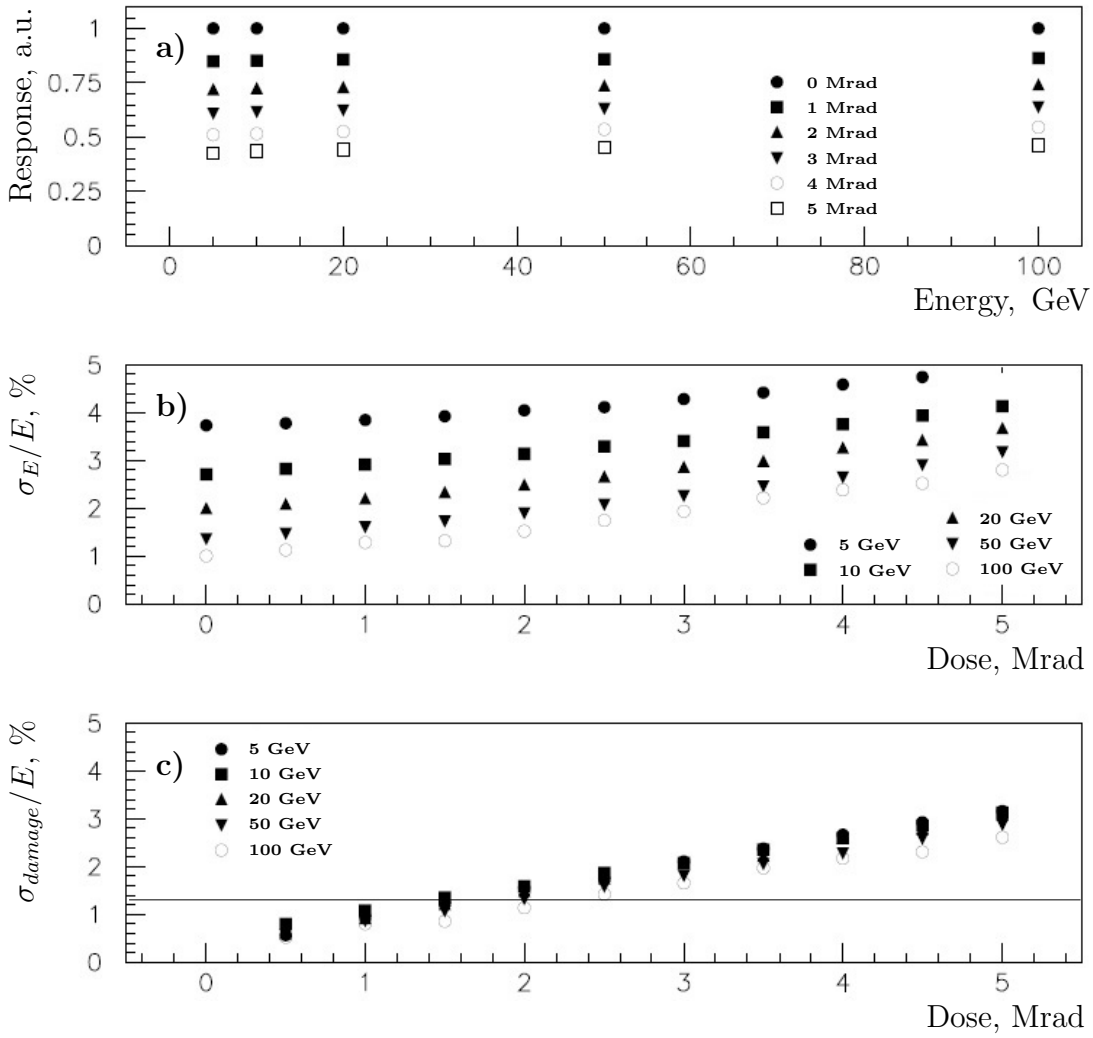

Figure 3.27: Simulation studies of radiation induced module performance degradation. The Y11(200)MS and PSM-115 combination and dose profile from Fig. 3.20 are considered. Shown are peak damage versus energy for accumulated dose of $0; 1; 2; 3; 4; 5$ *Mrad* (a); energy resolution degradation for $5; 10; 20; 50; 100$ GeV energy (b); constant term degradation or radiation induced constant term for $5; 10; 20; 50; 100$ GeV energy (c). Horizontal line corresponds to the 1.5% value of the constant term

In addition sets of comprehensive dose monitors have been distributed over calorimeter surface, in the regions close to the beam pipe, periphery and close to position of FEE. This provides not only a dose map reference, but also yields the information of scintillator materials aging for irradiating particles, corresponding to realistic environment of hadron collider, and at realistic dose accumulation rate. Only passive dose monitors, accessible for reading during long LHC stops, are used. A combination of

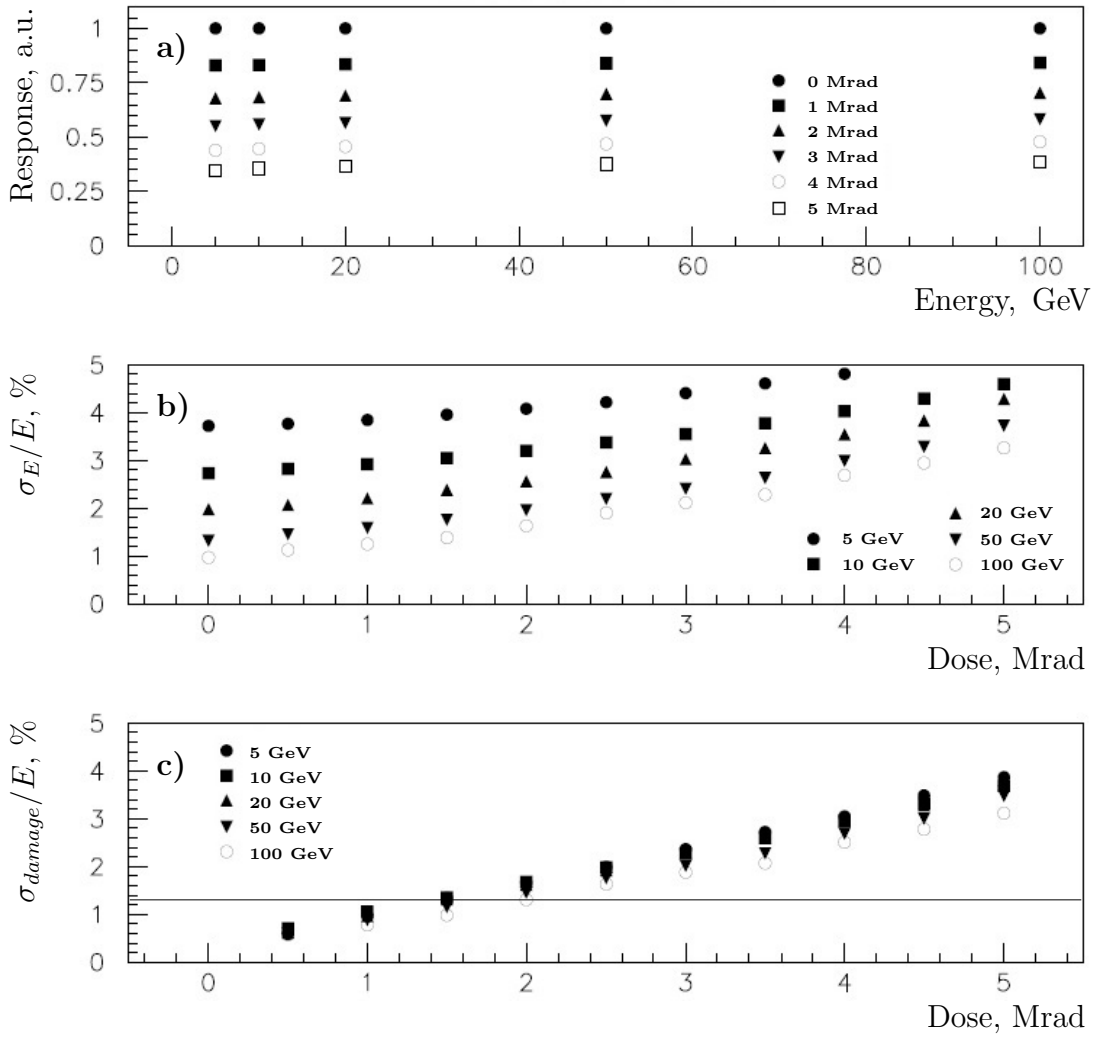

Figure 3.28: Simulation studies of radiation induced module performance degradation. The BCF-91A(DC) and PSM-115 combination and dose profile from Fig. 3.20 are considered. Shown are peak damage versus energy for accumulated dose of $0; 1; 2; 3; 4; 5$ $Mrad$ (a); energy resolution degradation for $5; 10; 20; 50; 100$ GeV energy (b); constant term degradation for $5; 10; 20; 50; 100$ GeV energy (c). Horizontal line corresponds to the 1.5% value of the constant term

polymer alanine, thermo-luminescent dosimeter and pin diode has been chosen. Having different response to different radiation types, the monitors will provide a separate dose map for electromagnetic component, charged hadrons and neutrons.

3.2.4 Module construction

Module assembly took place in Vladimir town, at Uniplast facility developed by Viktor Mayatsky, based on the experience from the ECAL construction for PHENIX and HERA-B experiments. Many nice engineering solutions were developed by Stanislav Malyshev.

Main part of the ECAL modules production [122] took place in Vladimir site, having the experience of Shashlik module construction for PHENIX and HERA-B calorimeters. Production of the scintillator and lead tiles, treatment of tile edges, preparation of WLS fiber loops, and module assembly are the important steps of LHCb ECAL module construction. Every production stage, in particular for active materials, requires quality control of produced sample.

Scintillator tiles were produced from polystyrene with 2.5% p-terphenyl and 0.01% POPOP admixtures. The concentration of scintillating dopants is tuned for the scintillator emission spectrum to match the absorption spectrum of WLS fiber. The scintillator tile production employed the high pressure injection molding technique. Tile edges were chemically treated (Fig. 3.29) thus providing diffusive reflection in order to improve

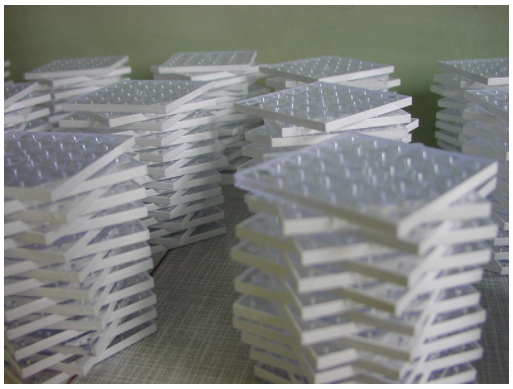

Figure 3.29: Scintillator tiles with treated edges

light collection efficiency, lateral uniformity and prevent tile-to-tile light cross-talk (section 3.2.2). A stack of tiles separated with thin spacers was put in a chemical solution that produced micro-bubbles of air in a thin layer at the tile edges. Not only the tile edges were treated, but also about 200 μm distance from the edges on the tile sides, which partially compensated the effects of global non-uniformity and dead material at the module borders. Scintillator tiles have been molded at a rate of up to

800 per day, and DMA edge treatment rate was up to 700 tiles per day. At this rate the effect from previous admixtures in the molding machine became negligible after about 20 days, and the average light yield of the produced tiles reached a plateau (Fig. 3.30).

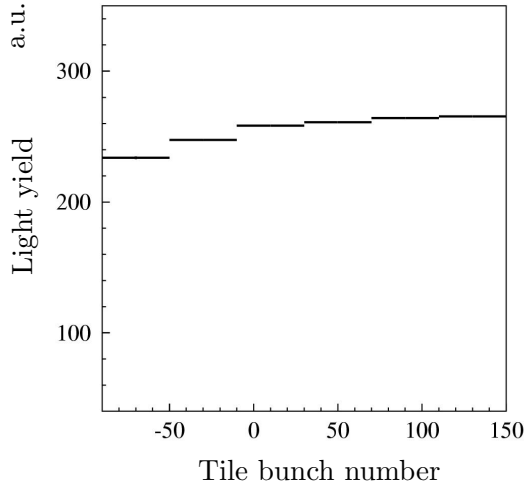

Figure 3.30: Evolution of average light yield of tile bunches

The lead plates are produced using sheet-metal stamping by the JL Goslar company, specializing on producing lead for roofs. This was the first and successful application of their equipment to HEP instrumentation. The lead plates have 2 mm thickness produced with a 10 μm tolerance, and were covered by a thin, about 5 μm, layer of tin. A matrix of the holes, corresponding to passage of the optical fibers, was produced in each lead plate, with each hole having a double-conical shape to avoid scratches on the fiber cladding.

The light from the scintillator tiles, is re-emitted and transported by 1.2 mm diameter WLS Y-11(250)MSJ fibers from Kuraray, penetrating the entire stack. In order to improve light collection efficiency and lateral uniformity of response, the WLS fibers form loops (Fig. 3.10, right) at the front side of the module. Fiber loops with radii as small as 10 mm, where the light loss is driven mainly by the geometrical optics reflection down the loop, were required. To achieve these small radius values, far below conventionally tolerated values, fibers were fixed in the frame and placed in an oven under uniformly distributed dry heat and under constant uniform mechanical load (Fig. 3.31 and 3.32).

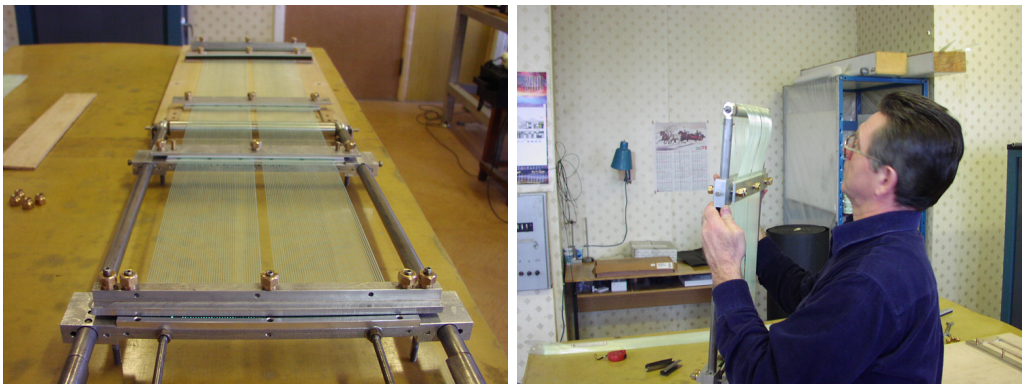

Figure 3.31: Preparation of fiber loops. Attaching fibers to the frame (left) and bending fibers to the loop shape before placing them in the oven (right)

Figure 3.32: Preparation of fiber loops. Placing the frame in the oven, delivering uniformly distributed heat (left), and extraction of bent fibers from the frame (right)

Bending of the fiber at small curvature radii leads to light losses both due to mechanical degradation because of fiber cracking, and due to the change of light reflection angles, governed by the geometrical optics. The latter effect dependence on the bending radius, has been simulated for 1.2 mm diameter fibers. Simulation results are plotted in Fig. 3.33.

A production rate of fiber loops of up to 1.5k per day was achieved.

The module assembly is discussed below for the most complicated case of inner module, comprising nine cells. It started from the lead-scintillator stack assembly in the vertical position using well-like tooling (Fig. 3.35a). Then the assembled stack was pressed with 500 kg force. This procedure was repeated 5 times, which made possible

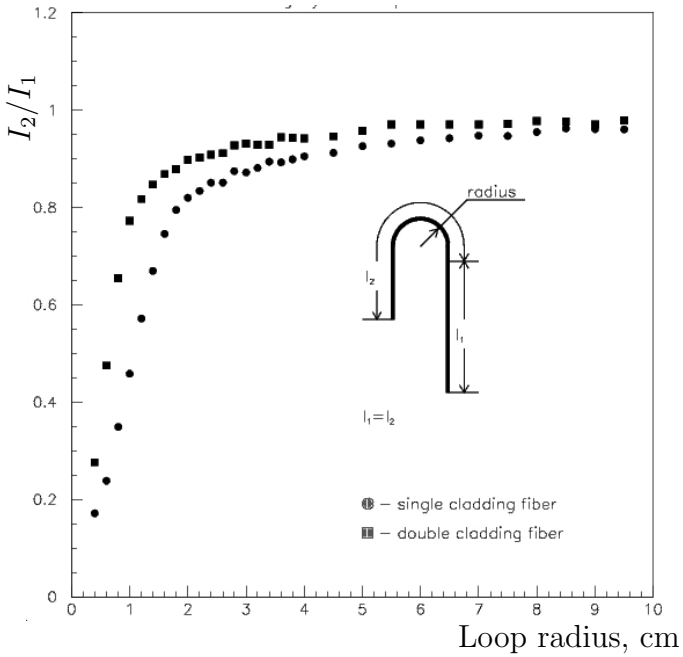

Figure 3.33: Simulation results of light yield efficiency dependence on the fiber bending radius, I_1 and I_2 are the light intensities measured at the straight and looped ends, respectively

Figure 3.34: Assembly of the outer section module, first stage. Lead-scintillator stack during assembly (left) and pressing the stack and preparing steel tapes for welding (right) are shown

structure deformations stable, and after that the stainless steel side tapes of 100 μ thickness were welded to the steel matrix plate. For the outer type modules, stack assembly is shown on Fig. 3.34.

Next WLS and calibration fibers were inserted into the stack structure (Fig. 3.35b).

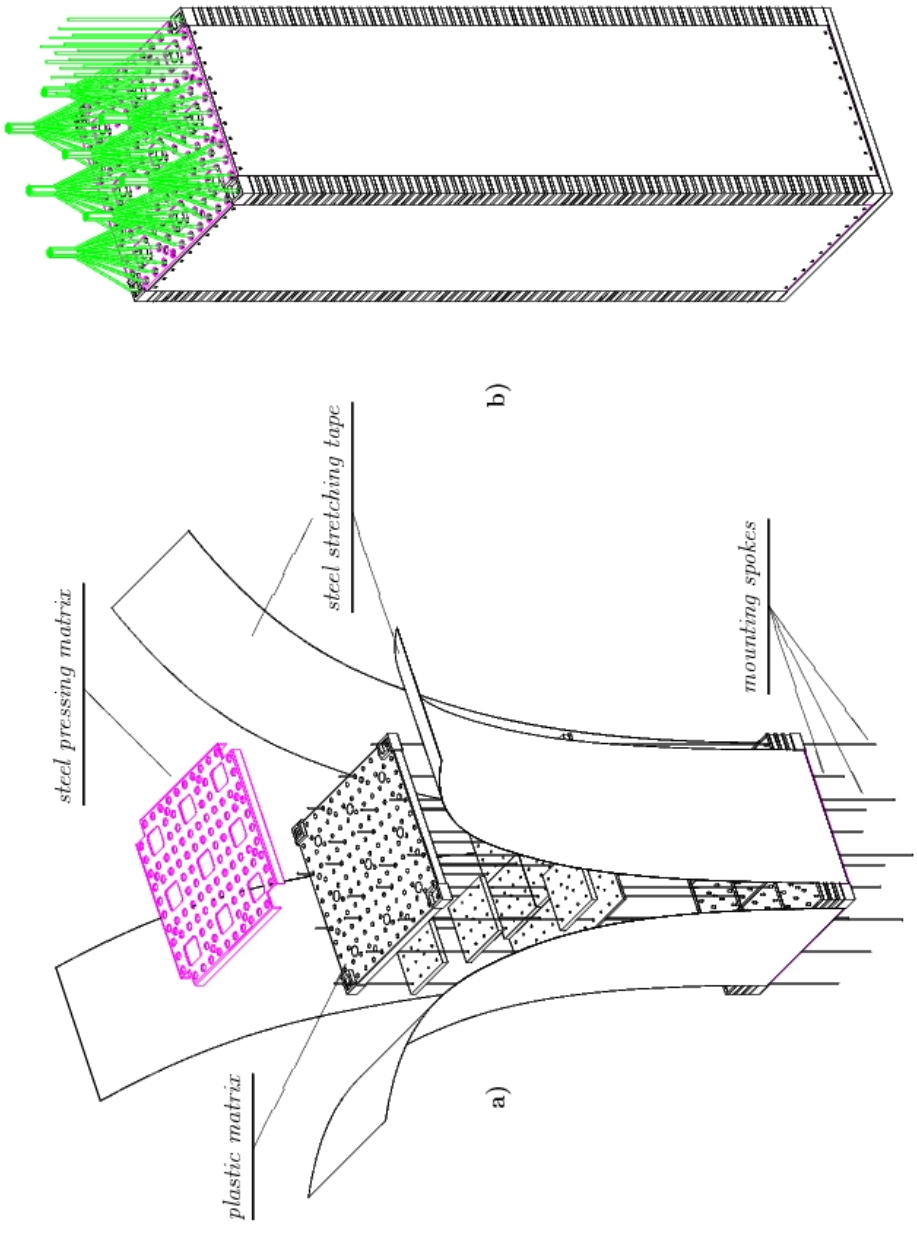

Figure 3.35: Assembly of the inner section module, first stage. Lead-scintillator stack during assembly (a) and the assembled stack with welded tape and inserted fibers (b) are shown

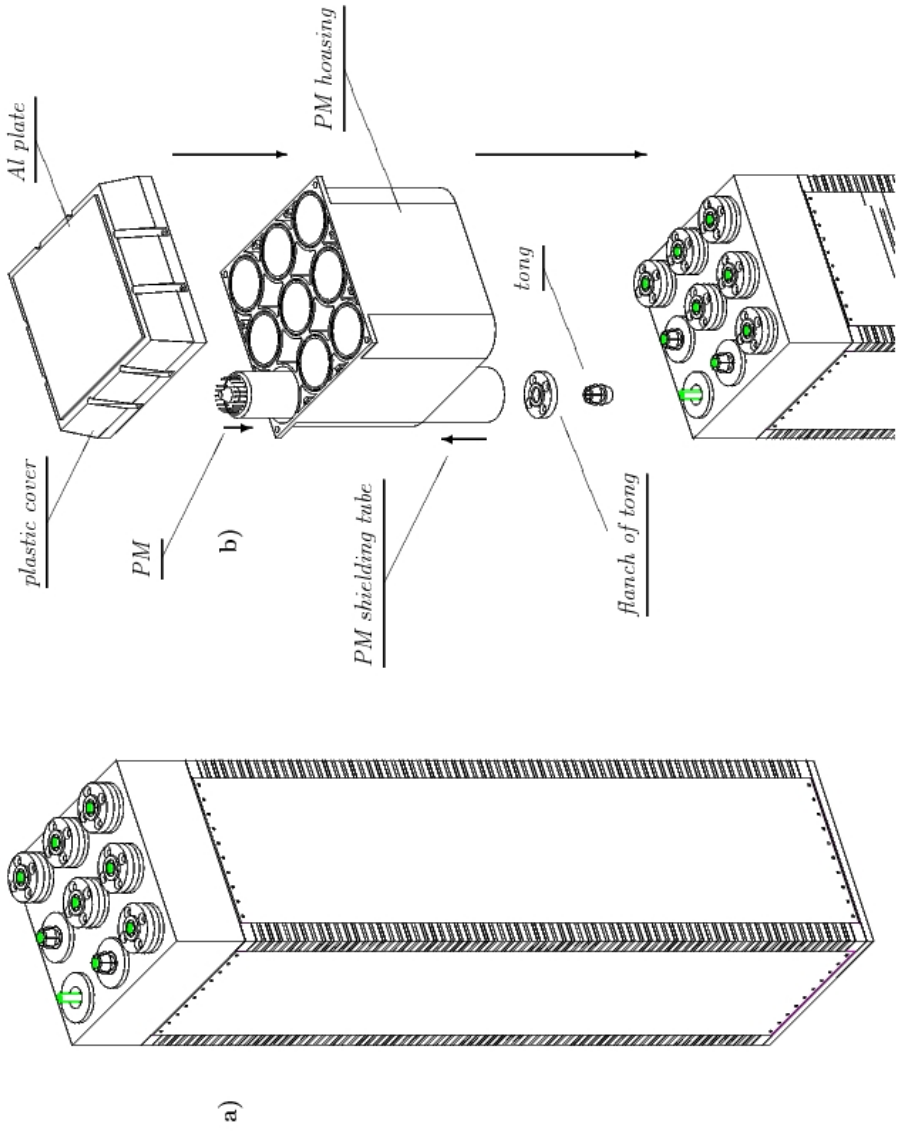

Figure 3.36: Assembly of the inner section module, second stage. Assembled stack with 6 from 9 formed fiber bundles (a), and the read-out part assembly (b) are shown

Fibers belonging to each calorimeter cell were bundled at the end of the module and polished. In order to form a fiber bundle, a fiber housing was mounted, and fibers were fixed with the tongs (Fig. 3.36a). Flay-cut of fiber ends ensured fibers to be collinear and perpendicular to the cut.

Then mounting of the read-out system followed (Fig. 3.36b).

PM is placed in the housing with insertion of 2.5 mm thick steel screen and three layers of 0.05 mm thick permalloy protection [8]. Finally mounted is the module end-cup cover, which guarantees the light isolation.

Assembly rate of up to 10 outer section modules per day has been achieved. Though the production rate was 2-3 times lower for small cell size inner modules, their amount of 176 is small, compared to the total number of 3312 modules.

Quality control was ensured at all stages of module production, starting from tile raw materials control and until assembled modules tests.

3.2.5 Quality control

Quality control was performed at the production facility in Vladimir and ITEP, and was efficient due to major contribution of Vladimir Rusinov and Evgueny Tarkovsky.

Quality control comprised on-site measurements, starting from the input control of raw material and up to characteristics studies of the assembled module, full-scale prototype studies with the test beam facilities, and pre-calibration of all the ECAL cells using cosmic rays upon arrival at CERN [122].

The idea of the on-site control measurements is to compare the result of measurement to that obtained for the working standard, which performance has been proved by the extensive studies from spectroscopy analysis and up to the beam tests.

The most important at the stage of *raw material* treatment was the polystyrene and p-terphenyl quality control. For tile production polystyrene-based PSM-115 plastic, which shows similar radiation hardness [123], was used instead of pure polystyrene.

[8] The length of this screening is determined by the longitudinal component of the magnetic field.

Two tests were used to control the polystyrene quality.

First test relied on infrared spectroscopy technique, which was developed to analyze composition of organic substances. Different chemical bonds correspond to different resonance frequencies, and the frequency spectrum was compared to the standard one. Fig. 3.37 shows the infrared spectra for two samples of PSM-115 plastic, where only minor differences are seen. The pure polystyrene spectrum shows no peak in the region

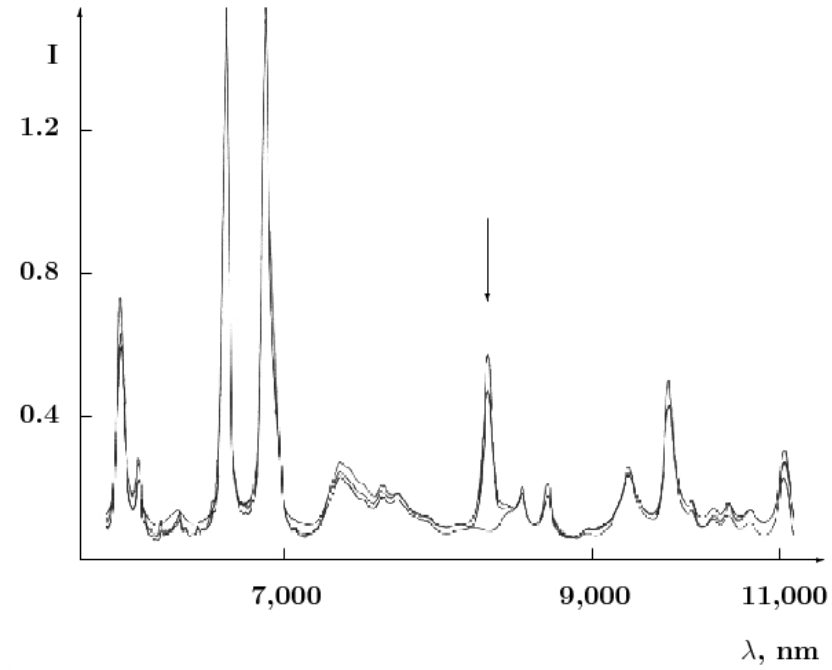

Figure 3.37: Infrared spectra for two samples of PSM-115 plastic. The pure polystyrene spectrum shows no peak in the region indicated by arrow

indicated by arrow. Another application of the technique consists in identification of the extraneous admixture present in polystyrene sample. The specimen is taken out mechanically and dissolved in the e.g. chloroform. The spectrum of this solution is compared to the standard spectrum of polystyrene, and to other standard spectra.

The other test was the control of *transparency*, i.e. the response from polystyrene, measured with a spectrophotometer, depending on the wavelength of incoming light. The MPS-500 spectrophotometer was used for the measurements with the two-beams method. High apparatus sensitivity allowed the measurements with either a single tile or rouleau of tiles.

Each tile was measured in 10 points distributed along its surface. Special attention

has been paid to the transparency for the light with $\lambda = 420\,\text{nm}$, corresponding to the light emitted by the scintillator. To account for losses due to the partial reflection, the reference value measured at $\lambda = 590\ nm$ was subtracted [9].

Quality control of p-terphenyl sample began from the infrared spectroscopy test, similar to the polystyrene control. It was followed by gas and liquid chromatography quantative tests, probing chemical composition and concentration of the components using the measurements of time delay and amplitude of separated chemical compounds. Finally, p-terphenyl sample was subjected to transparency studies with the spectrophotometer, as for polystyrene control, to search for any difference between the spectra of test and reference samples.

A technique to determine the dye dopant concentration in the produced *scintillator tile*, with spectrophotometer, has also been elaborated. However, it appeared to be time- and work-consuming, and was used only to cross-check performance of other control methods. Routinely scintillator tiles were controlled in three steps. Fluctuations of the tile-to-tile light yield had an R.M.S. smaller than 2.5%.

Spectrophotometer control ensured the transparency for the blue (420 nm) light. Fig. 3.38 shows the tile-to-tile transparency variations. The individual value $\hat{\mu}$ is the

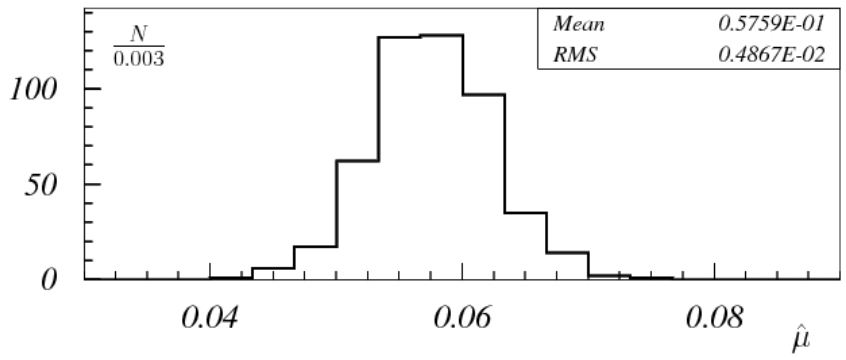

Figure 3.38: Tile transparency measurements accomplished with spectrophotometer. The $\hat{\mu}$ variable is an average over the values $\frac{I_{590}-I_{420}}{I_{590}}$, as measured at 5 points distributed over the tile surface

average over the values $\frac{I_{590}-I_{420}}{I_{590}}$, as measured at 5 different points laterally distributed over the tile, where I_{420} and I_{590} is the transparency of a tile for 420 and 590 nm light,

[9] At this wavelength the absorption is considered to be negligible.

respectively. About 5.8% of the 420 nm light is lost with respect to 590 nm. The r.m.s. of this distribution is 0.5%. Transparency variations over a tile surface could be estimated by the $\sqrt{\hat{\sigma}^2}/\hat{\mu}$ value (Fig. 3.39), where $\hat{\sigma}^2$ is the variance of one tile measurements.

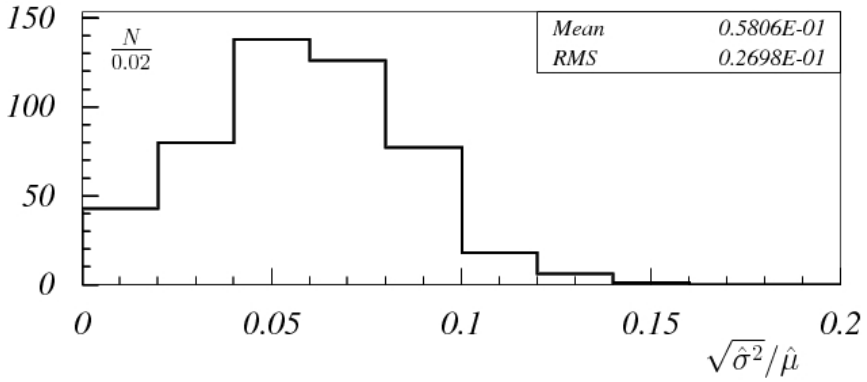

Figure 3.39: Tile transparency measurements accomplished with spectrophotometer. The $\hat{\mu}$ and $\hat{\sigma}^2$ variables are the average and variance over the values $\frac{I_{590}-I_{420}}{I_{590}}$, as measured at 5 points distributed over the tile surface

The setup of the next test resembled a hedgehog, represented by a scintillator tile and fibers coming through its holes. The tile was irradiated with ^{90}Sr radioactive source, and the response from fibers (via PM) was measured.

An individual measurement comprised the measurement of dark current, i.e. noise plus fiber response to the irradiation, and the measurement of current from complete *hedgehog* (scintillator tile and fibers). The result of the test was the difference between the two measured values, compared then to the reference tile. Tiles with the difference of less than 5% from the standard value, were accepted for further control. Tile-to-tile spread with the RMS of 1.5% was observed.

Scintillator tiles were subjected to the same hedgehog test after DMA treatment of tile edges. This test provided a quality control of the tile edge coating, and verified the light yield of the tiles before stack assembly. Fig. 3.40 shows the light yield relative to that of a reference tile, measured with the hedgehog test, and averaged for groups of three tiles. The tiles with $LY > 0.93 \cdot LY_{ref}$ (region to the right from the arrow) were then used for module assembly. The r.m.s. for the retained sample was ≈ 0.09. Since the photostatistics of the LHCb ECAL is sufficient, control of tile light yield is only important to limit tile-to-tile spread inside a cell, thus improving longitudinal

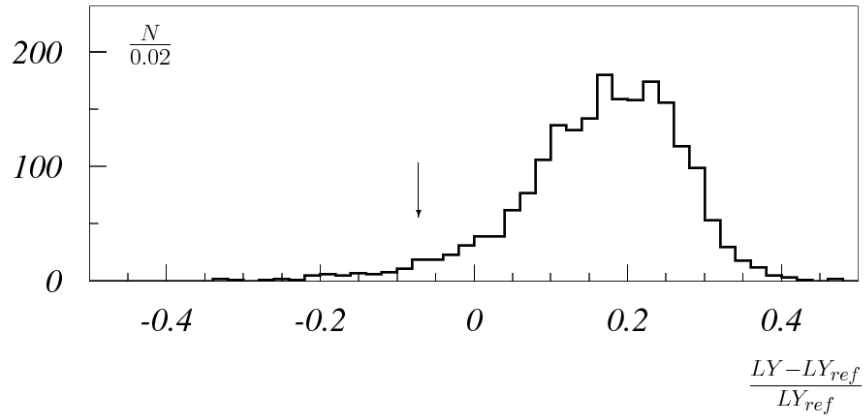

Figure 3.40: Results of the hedgehog test for groups of three tiles. Shown is the light yield relative to that of a reference tile. The r.m.s. for the tiles used for module assembly ($LY > 0.93 \cdot LY_{ref}$, corresponding region is to the right from arrow) is ≈ 0.09

uniformity of response. After the edge treatment tile-to-tile spread with the RMS of 2.5% was observed. When convoluted with the longitudinal shower development, this spread produces negligible impact on the constant term of energy resolution.

The analysis showed that tile quality crucially depends on tile edge coating quality, and there is only a minor dependence on the transparency properties.

Principle of bent *WLS fibers* control was similar to the one shown on Fig. 3.33, where the light initiated in the scintillator tile using ^{90}Sr source, was readout via the tested fiber loop. When measured after the fiber loop, the light yield loop-to-loop variations due to fiber bending were measured to have an R.M.S. of the spread of 1.6%, and the spread of 2.0% including straight fiber-to-fiber variations. These values produce negligible impact to the constant term of energy resolution, when considering realistic shower size and light collection mechanism, discussed in section 3.2.2.

Clear fibers penetrating cell centers have been tested using LED light inside the assembled modules to account for possible mechanical damage during module assembly. They have found to be identical to better than 3%. This value does not enter the performance of the calorimeter as long as clear fibers deliver sufficient amount of LED light to measure PM gain.

The control of the *assembled module* with cosmic particles along with the lead-scintillator stack control, covers the test of fibers and bundle quality. On-site test

with cosmic rays of horizontally positioned modules with the same calibrated PM has been performed. The precision of this test was limited, since all the crossing particles, independently of their exact trajectories, have been used, and spectrum qualitative agreement was required. When subtracting measurement reproducibility, cell-to-cell spread were estimated to be better than about 6%. Significantly better precision was achieved with the test of modules in vertical position with cosmic rays, upon their arrival at CERN.

3.2.6 Cosmic ray test

Cosmic ray measurements at CERN have been accomplished during the summer 2004, with Oleg Gushchin, Boris Bobchenko, Leslie Camilleri and others, and were subject of the internships of K. A. Koopmans and K. Voronchev.

As a final stage of module quality control and as a tool of pre-calibration, response of ECAL cells to the cosmic particles has been measured before the installation in the LHCb detector. After the arrival of the detector at CERN and without unpacking the ECAL modules, all the ECAL cells, including spare modules, have been measured.

The ECAL modules were delivered in wooden boxes in vertical position, with each box comprising 30 modules (Fig. 3.41, left). The transportation box was positioned

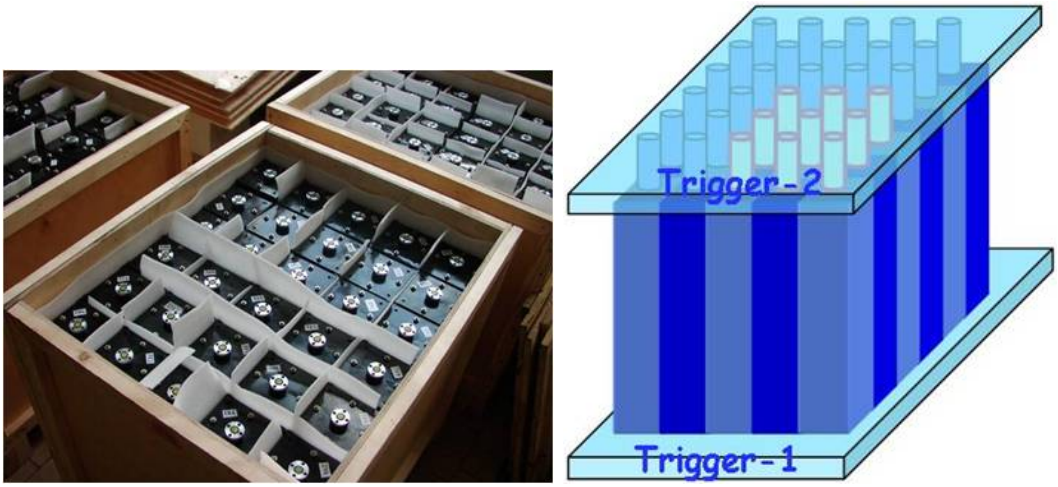

Figure 3.41: Delivery of the modules to CERN in matrices 6×5 (left) and triggering of cosmic muons (right)

between the two planes of scintillator trigger counters in order to select muons traversing longitudinally the 6×5 matrix of the ECAL modules.

The same PM gain, the gain value chosen at 10^6, is required for calibration purposes. In order to determine the gain, each PM was illuminated by the LED light, and the LED peak position and Gaussian width were measured. The LED light was delivered by clear transport fiber arriving from the readout side of the module, and reflected from the fiber bundle tong to the PM window. The same set of PM, readout chain and LED and PIN diode system were used for measurements of each module box. In order to be sensitive for MIPs higher PM gains were set.

In order to obtain peaking distribution and thus a good estimate of the ECAL cell response, muon trajectories entirely comprised in one cell were selected. Since the scintillator trigger counters did not posess any granularity and thus did not provide a position information for the entering or exiting cosmic muon candidate, this was achieved offline by vetoing any energy deposit in the neighboring cells. This procedure works well for all the cells having neightbours on each side, where veto procedure transformed a typical ADC spectrum shown on Fig. 3.42a to the spectrum shown on Fig. 3.42b, where MIP peak position can be properly determined. For the border cells

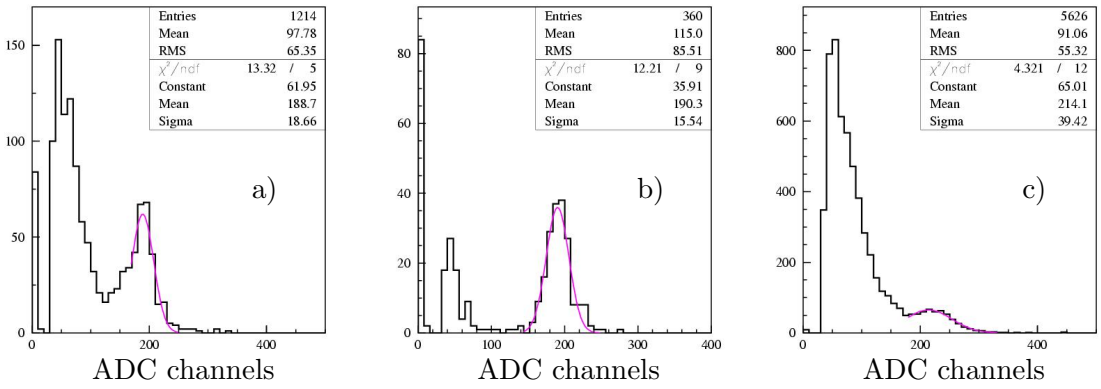

Figure 3.42: Typical ADC spectra from cosmic rays in the matrix of ECAL modules. Spectra in the cell having neighbors without (a) and with (b) veto on the signal presence in the neighbour cells, and in the corner cell in the matrix (c) are shown

and in particular for the corner cells (Fig. 3.42c) in the matrix, signals from the muons with only part of the trajectory inside the cell were also collected. In this latter case, peak position was essentially defined by the high energy shoulder, and more statistics, that is more exposition time, was needed to achieve similar accuracy in the peak position

determination. Time needed to determine peak position to a precision of about 1%, varied from about 1 hour for outer type cells to about 30 hours for cells of inner type.

The cell response values are shown on Fig. 3.43 for the inner, middle and outer ECAL cells. Number of measured cells and number of cells, that did not pass quality

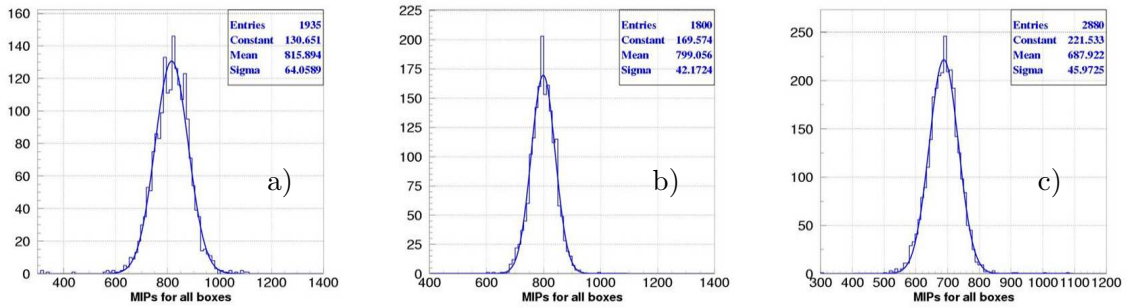

ADC channels ADC channels ADC channels

Figure 3.43: Cell response measurements using cosmic rays for (a) inner, (b) middle and (c) outer ECAL cells

control requirements, the spread of cell-to-cell response, and the spread of cell-to-cell response with quadratically subtracted measurement error, are shown in Table 3.5. Reproducibility of the measurements was found to be about 3%. This value was

	Inner section	Middle section	Outer section
Number of cells	1935	1798	2790
Number of disqualified cells	12	2	4
Spread of MIP signal position	8.0%	5.3%	6.7%
Spread of MIP signal position with measurement error subtracted	7.4%	4.4%	6.0%

Table 3.5: Number of measured cells and number of cells, that did not pass quality control requirements, the spread of cell-to-cell response, and the spread of cell-to-cell response with quadratically subtracted measurement error

quadratically subtracted from the measured cell-to-cell spread value for each type of the ECAL modules, in order to determine actual cell-to-cell response spread. The cell-to-cell variations were found to be 8% for the inner, 5% for the middle and 7% for the outer type modules. Note, that the calibration of the complete readout chain had

to be added to the detector cell calibration, as well as the effect of the spread in the LED signal attenuation in the clear transport fibers.

Cosmic particles have also been reconstructed with the assembled LHCb detector. Horizontally oriented LHCb detector positioned a 100 m underground is not ideal for cosmic particles reconstruction. However, while waiting for the pp collisions in 2009, the LHCb detector exploited cosmic particles to better understand the detector. More than one million calorimeter triggered tracks was collected. In order to obtain measurable signal from MIP, calorimeter detectors gain was increased similar to the pre-calibration measurements. The transverse projection of the typical cosmic particle track reconstructed in the calorimeter is shown on Fig. 3.44, left, and a very rare track fully contained in the thin SPD is shown on Fig. 3.44, center. The sample of

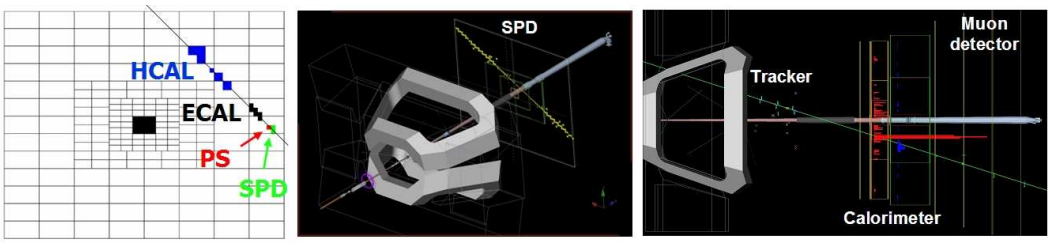

Figure 3.44: Projection of the cosmic particle track reconstructed in the calorimeter detectors (left), a rare cosmic particle track fully contained in SPD (center) and the example of the track triggered with calorimeter and reconstructed in the tracking system and muon detector stations (right)

the reconstructed MIP tracks was used to commission the calorimeter detectors, and also large surface tracking detectors (Fig. 3.44, right), to verify efficiencies and time alignment.

Time alignment between different channels of a given calorimeter and between the calorimeter detectors, and minimizing the spill-over effect with cosmic rays, were achieved by reading out consecutive 25 ns samplings. Due to different signal and LED paths a time adjustment between different calorimeter detectors is required. Most sensitive for a channel-to-channel alignment and for the spill-over optimization was proven to be a comparison between amplitudes from the two subsequent samplings when the timing is shifted by 12.5 ns with respect to the best guess initial setting in order to probe the region with highest possible signal derivative. For the time alignment between the two different detectors time difference was plot versus the estimated flight

path between the detectors. For the perfect alignment the distribution line, smeared by the detector cell sizes and estimate of the MIP signal collection, points to zero. With the collected cosmic rays sample, time alignment of ± 2 ns was achieved between the ECAL and HCAL.

3.2.7 Assembly of the ECAL modules in LHCb

The initial engineering design of the ECAL modules and the calorimeter wall was performed by Alexander Soldatov. The design of all the calorimeter structures in the LHCb cavern was then taken over by the Annecy team, Claude Girard, Bruno Lieunard, Marie-Noelle Minard and others, including detailed design of the calorimeter platforms, beam plugs and simulation of potential earthquake effects. This design corresponds to present calorimeter assembly in LHCb and is shown in Fig. 3.45. Many

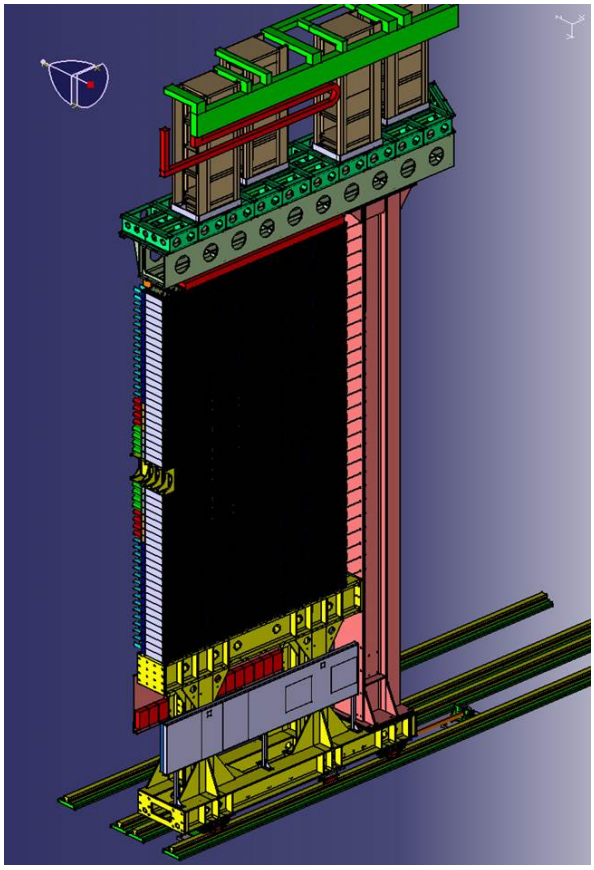

Figure 3.45: Design of half ECAL wall

nice engineering solutions, including stretching system design and technical solution for

replacing modules in the region around the beam pipe, came from Alexander Arefiev. Principal characteristics of photomultipliers, including linearity and stability, were checked at three test benches by Bernard Jean-Marie, Anatoliy Konopliannikov, Oleg Gushchin, Evgueni Tarkovski and Tengiz Kvaratskheliia. Cockcroft-Walton bases were designed by Yuri Gilitskiy, produced in IHEP Protvino, tested by Oleg Gushchin, Tatiana Zakoryuchkina and Olga Zhiryakova, and soldered to photomultipliers by Nikolai Filimonov, Maria Filimonova and Tatiana Zakoryuchkina. Signal cables were prepared by Jacques Lefrançois together with the engineers at LAL, while power and control cables prepared by Valery Dolgoshein, Yuri Kuznetsov and Olga Zhiryakova, who also mounted them on the cable-holding bands. Monitoring system was developed by Ivan Korolko, Evgeny Melnikov and Oleg Gushchin. Preparation and bundling of clear transport fibers was done by Stanislav Malyshev, Elena Mayatskaya and Olga Zhiryakova. Monitoring fibers distribution and tests were done together with Kirill Voronchev and K. A. Koopmans. The modules have been assembled in a wall, with their position controlled, in about 6 weeks, togeher with Alexander Arefiev, Tengiz Kvaratskheliia and Alexander Lukyanov, and with efficient help of Robert Kristic and engineers of the LHC point 8, Bernard Chadaj, Gerard Decreuse, Bernard Corajod, Patrick Vallet, Frank Lamour, Cedric Fournier and others. The front-end and trigger electronics, readout and control was the responsibility of the LAL team, Christophe Beigbeder, Dominique Breton, Olivier Callot, Daniel Charlet, Olivier Duarte, Jacques Lefrançois, Frederic Machefert, Patrick Robbe, Vanessa Tocut, Ioanna Videau and others.

Electromagnetic calorimeter wall is mounted on two main platforms, on each side of the beam. Platforms are placed on rails, and can be moved out, in order to allow calorimeter maintenance, and access the beam pipe. Beam plugs (Fig. 3.46) replace the ECAL modules around the beam pipe, where the radiation level exceeds tolerable values (section 3.2.3).

Modules of each platform are grouped in two-row module structures, by being constricted with horizontal stainless steel tapes of 0.1 mm thickness and 400 mm width (Fig. 3.47). The same size steel tape is put inbetween the two rows inside the double row structure, to ensure the uniform load distribution. Each group is stretched with a dedicated mechanical tooling to ensure a dense (adjusted) packing, and positioned in x-coordinate as a unit structure, in order to precisely align the edge at $x = 0$.

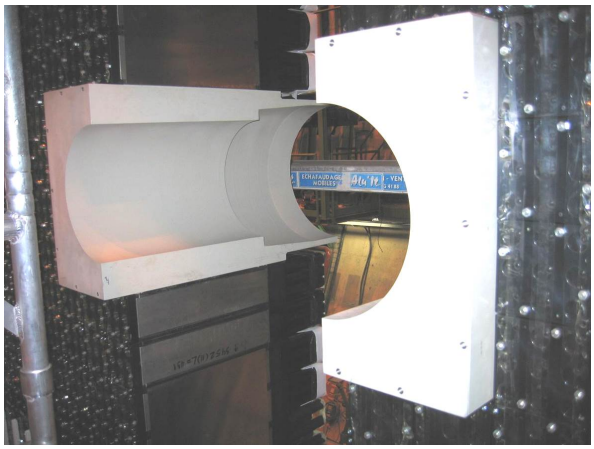

Figure 3.46: Beam plugs replacing ECAL modules around the beam pipe

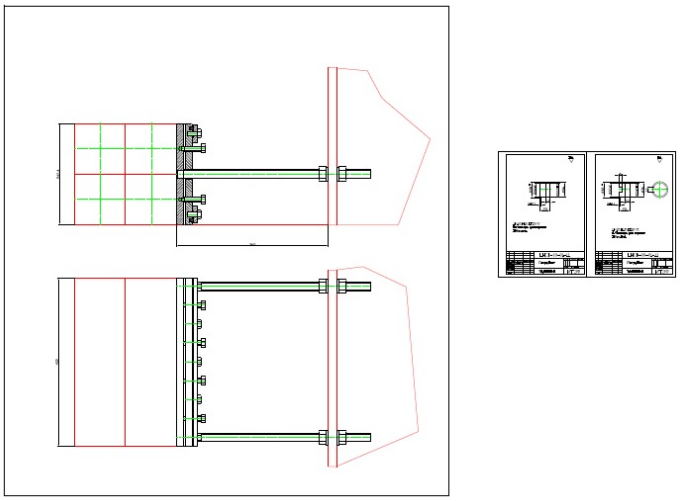

Figure 3.47: Principal design of stainless steel tape used to group the double row of modules in the dense structure

The innermost modules (up to 48 modules) exposed to the highest radiation dose, can be replaced during a long LHC shutdown, if the radiation induced degradation significantly affects the detector performance. To allow the replacement the design of the four vertical columns is different. The modules belonging to this area as well as the modules on top of them, are grouped in two double columns, and each is stretched vertically similar to the treating of horizontal double rows. The grouping of modules into double rows and double columns for the central part of the half calorimeter wall is illustrated on Fig. 3.48. The disassembly of double columns is done module by

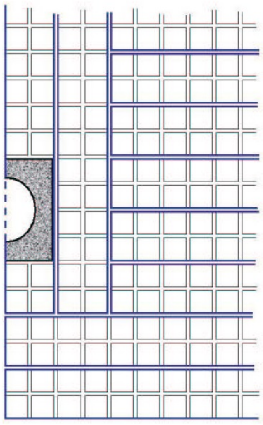

Figure 3.48: Grouping of modules into double rows and double columns for the central part of the half calorimeter wall

module, starting from the top, in the sequence opposite to the assembly procedure. Implementation of the stretching system is shown on Fig. 3.49 for double rows and

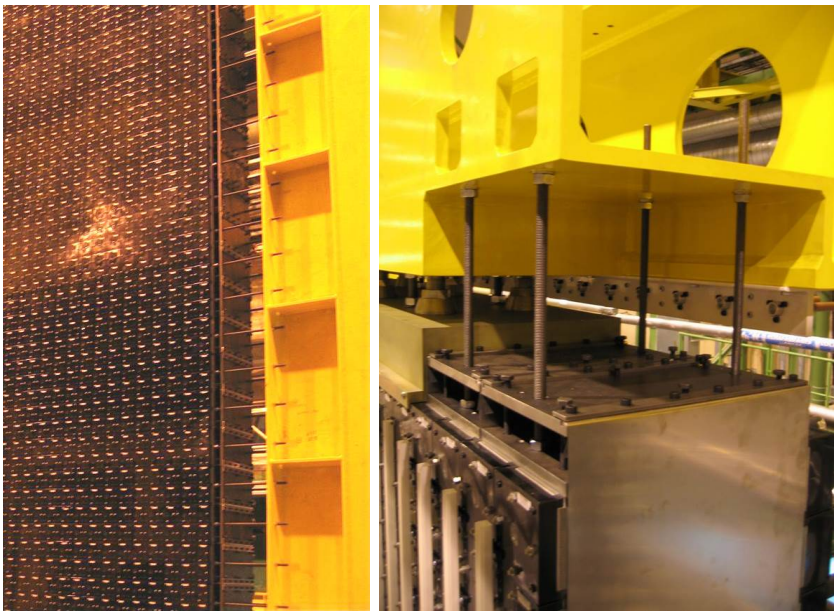

Figure 3.49: Stretching system to position double rows (a) and double columes (b) of modules

double columns of modules.

Electronics platforms are positioned at the top of calorimeter wall. Each electronic platform hosts 4 racks with the ECAL and PS/SPD FEE. The weight of individual module amounts to 30 kg, from which the Pb/Sc stack weights of about 27.5 kg, and

the read-out part and housing mechanics contribute another 2 kg. In addition, module structure of each half a platform is pressed from the top with 1.4 t load distributed over the surface with the pressing plate. Electronics platform load is carried by the calorimeter wall and partially by the side columns. The integrated load on each main platform amounts to about 51 t.

Monitoring signals from light emission diodes (LED) are distributed during the empty beam crossing, at the front side of the calorimeter wall (Fig. 3.50). Signals are

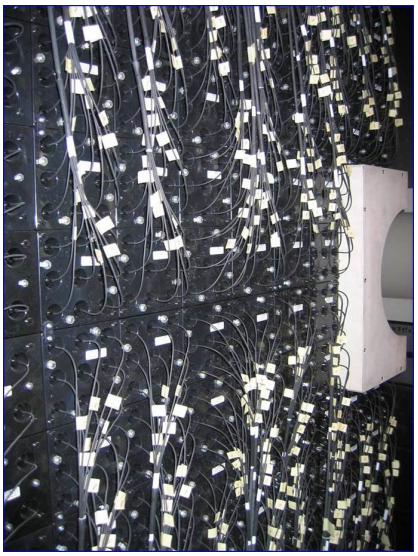

Figure 3.50: Distribution of monitoring signals from LED to the ECAL cells

delivered to the clear fiber penetrating each cell, which is bundled together with the WLS fibers in front of the light mixer and PM. LED light is split to 16 or 25 clear transport fibers, with an additional clear fiber to deliver the light to a pin diode and monitor stability of each LED.

The monitoring side of the ECAL is mechanically protected as shown on Fig. 3.51.

At the downstream side of ECAL, cables are distributed over the detector via dedicated steel cabling tapes of 210 mm width, which drive signal cables from the detector to the electronics platform, and power supply and voltage control cables from the control electronics positioned under the supporting platform to the CW bases on the detector. Cable routing and connections are shown on Fig. 3.52. Cabling tapes are mechanically attached to both the electronics and the supporting platforms. Signal cables of C-50-2-1 type and 2.85 mm external diameter have been attached to the cabling

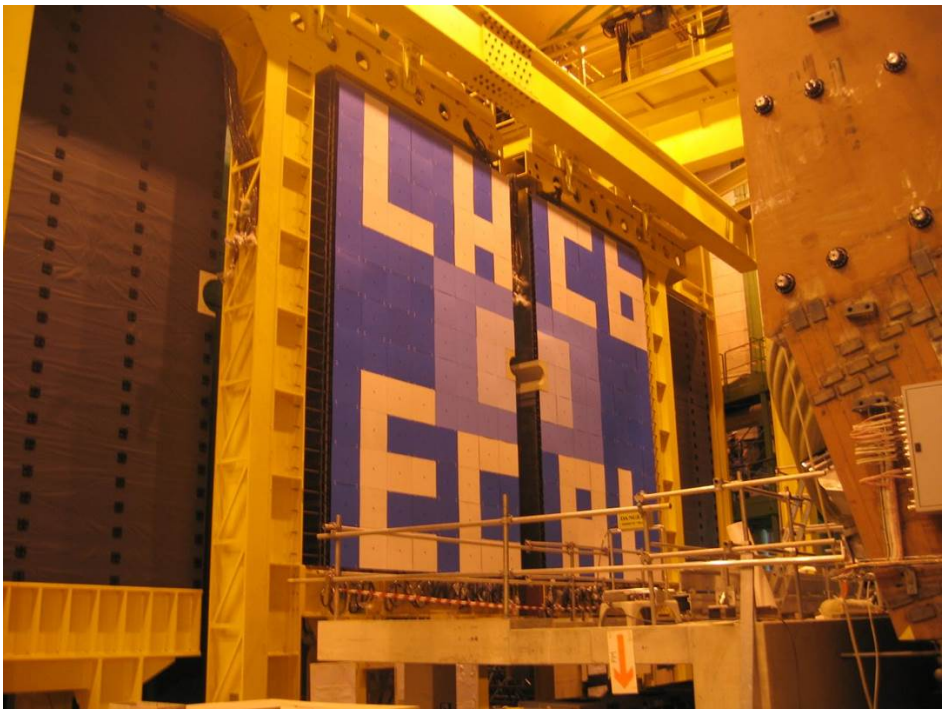

Figure 3.51: Protection of the ECAL monitoring side. The three sections with different cell size are distinguishable by colour

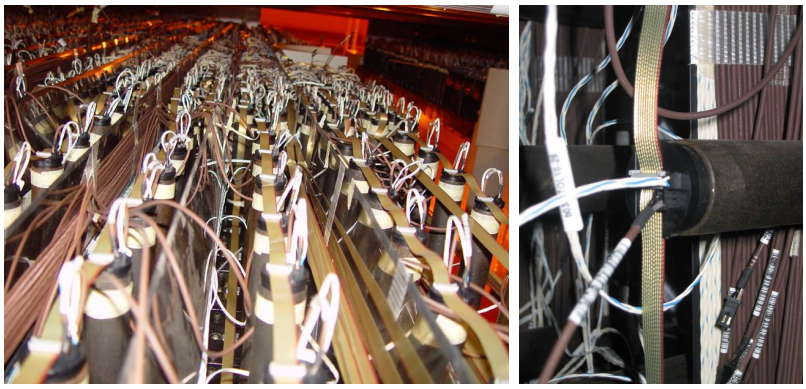

Figure 3.52: Cable routing (left) and connections to ECAL modules (right)

tape in two layers before installing in the detector. From the cabling tape, they are routed in bunches to the FEE cards [124] located on the electronics platform through the holes on the bar under the electronics platform. Each signal cable bunch serves the corresponding neighboring columns of modules. Its cross section is maximal for the central region columns and is estimated to be $\sim 20\,\mathrm{cm}^2$. Since all the signal cables have the same length of 12 m, the total extra cable length of about $\sim 24\,\mathrm{km}$ or $\sim 0.17\,\mathrm{m}^3$ has

been stored inside the electronics platform. Power supply and voltage control employ flat cables, which go from the control electronics under the main platform through the slots. In order to route the cabling, that serve four module columns from each side of the beam axis, a dedicated groove of at least 20 cm (width) × 2.2 cm (depth) in the external surface around the beam plug was produced.

Both supporting and electronics platform design implements the slots from the readout side for cabling tape and cables attached to it, signal cables go to racks on the electronics platform from underneath, and power supply and voltage control cables and monitoring fibers go through the supporting platform to the distribution boards.

Nominal transverse dimension of the assembled stack, 121.7 mm × 121.7 mm, is important since it drives the total size of calorimeter module wall and the overall projectivity. Measurements of ten modules at various cross sections gave the value of (121.78 ± 0.06) mm, which is translated into extra-size of (2.6 ± 0.3) mm for each half calorimeter wall in horizointal and (4.2 ± 0.4) mm for the calorimeter wall in vertical direction. Vertical pile of 13 modules, corresponding to a 1/4 of the ECAL wall height, was directly measured, and translated to a single module dimension of (121.8 ± 0.1) mm, which is in a good agreement with the first result. Taking into account the thickness of steel tape, used to make the structure dense, and also to properly position double rows of modules, this gave the dimension of $x = 3898$ mm and $y = 6344$ mm for each half calorimeter wall.

From the upstream side 60 mm was allocated for the monitoring system and its protection. The module stack together with the pressing plates and the front and rear fiber housings was measured to be 515 mm long for selected outer and middle section modules. For the inner section modules this length is a 5 mm shorter because it requires less space to collect fibers together to form a bundle. The R/O part of the module is 250 mm long, where the last 35 mm space is taken by the connectors and the turned signal cable. For the inner section modules the R/O part takes a 5 mm less space by accommodating a shorter light mixer. The choice of a Cockcroft-Walton base with small, typically less than 0.1 W per base, power consumption, made it possible to avoid supplementary cooling of the base. The whole static z-envelope of ECAL adds up to 825 mm.

The calorimeter module wall was assembled on each platform separately. First, the

supporting platform and the side frame were installed and surveyed. The assembly of the module wall began with positioning the pre-shaped steel stretching tape, followed by the two module rows, interspaced with the 200 μm thick steel tape. Then loop of stretching tape closed, and appropriate tension tooling ensure the double row to be dense, and moved to the precise x position. Positioning of the structure and individual modules were controled with theodolite. Adding up the double rows, the half wall is being assembled. Then the electronics platform was mounted on the top, aligned and fixed, double-module columns were installed.

The second survey took place after installation of the beam plug. The fully loaded supporting structure undergoes the third survey, as well as the module half wall.

Mounting of the monitoring system comprised routing of fibers over the wall surface, installation of LEDs, pin-diods and light splitters, checking of the connections. Visual check of the fibers connectivity was performed from the readout side, using a light injected at the splitter level.

At the module readout side, light mixers and mixer housings, PM housings, steel covers and permalloy screenings, PM and PM bases, and the external covers, have been mounted. Steel tapes with the pre-mounted cables have been installed, adjusted, and the cables were connected to the cells. At the FEE side extra cabling length was stored, and connectors were plugged into FEE. Also connected is the control electronics underneath the main platform.

After the ECAL wall assembly, a survey performed over all the module positions showed their actual positions to be identical to their calculated positions to better than 0.5 mm.

3.2.8 Discussion

LHCb ECAL detector was designed, constructed, tested, pre-calibrated and installed in the experiment. The Shashlik cell design inherited essential experience from the previous constructions, and in particular PHENIX and HERA-B calorimeters. In addition, LHCb ECAL triggered several new successful developments. Effects influencing lateral uniformity of response were better understood, while record lateral uniformity for

Shashyk type calorimeters was demonstrated. Among other developments, a new technique of S-type fiber bending allowed to achieve bending radii of 10 mm for a fiber diameter of 1.2 mm, more than five times lower with respect to fiber specifications, without any mechanical damage. Important studies of radiation resistance of plastic scintillators have been performed. Scintillator tile and WLS fiber combination was selected for the LHCb ECAL. Taking into account a substantial radiation dose close to the beam pipe, the ECAL design provides the possibility to replace 48 modules, which are most exposed to radiation. In addition sets of comprehensive dose monitors have been distributed over calorimeter surface, that will allow not only a dose map reference, but will also provide information of scintillator materials aging for irradiating particles, corresponding to realistic environment of hadron collider, and at realistic dose accumulation rate. Having different response to different radiation types, the monitors will provide a separate dose map for electromagnetic component, charged hadrons and neutrons. During the LHCb data taking, the calorimeter demonstrated reliable operation with less than 0.2% dead channels. However, long clear transport fibers, distributing LED monitoring pulses, appeared to be sensitive to radiation. Online degradation and annealing effects following the beam crossing pattern have been observed. This increases the importance of the online monitoring using reconstructed π^0 signal.

Upgrade-related calorimeter challenges comprise the front-end electronics modification, potential performance degradation of the π^0 containing decay modes due to increased pileup, and radiation resistance of the inner ECAL detector under a 10 times increased annual dose. The solution of this latter problem could be to compromise the physics case with inner ECAL, or to consider a different technology for inner region ECAL, e.g. $PbWO_4$ crystals using the CMS and PANDA developments, or preserving the existing Shashlik technology but searching for new, more radiation resistant materials.

Comparison with other Shashlik calorimeters, and in particular attemps to ultimatly reduce the effect of sampling, are discussed below.

It is interesting to mention an old development of the sampling calorimeter using spiral arrangement of the wavelength shifting (WLS) fibers, aimed at improving uniformity of ECAL response [125]. A 2% lateral uniformity has been demonstrated.

Shashlik calorimeter with longitudinal segmentation has been proposed [126] for

barrel ECAL at Linear Collider. Longitudinal segmentation was proposed in two different ways, either using thin vacuum photodiodes inserted between the adjacent towers in the front part of the calorimeter, or using two scintillator types with different decay times inserted in the first and second longitudinal part of the calorimeter, respectively. Both solutions have been implemented in the prototypes and studied with a test beam.

The ALICE EMCAL [107] is a later addition to the ALICE detector, aiming at triggering on high energy gamma-rays and jets. The detector implemented a design similar to that of LHCb ECAL, however barrel implementation assumes dead zones between the neighbour modules, increasing in the direction of shower development. The EMCAL energy resolution was measured to be $\sigma_E/E = (11.1 \pm 0.4)\%/\sqrt{E} \oplus (1.7 \pm 0.3)\%$, where E is measured in GeV.

Looking at later developments, several technological improvements have been developed, which allowed to demonstrate what is the almost ultimate performance of Shashlik technology. The sampling fraction – relation between thickness of lead and scintillator tiles – dominates energy resolution of Shashlik calorimeter at intermediate energies. Decreasing the thickness of the lead will increase the length of the module, while proportional decreasing thickness of both lead and scintillator tiles will reduce light collection efficiency. The number of projects considering Shashlik approach for ECAL shows it to be among the best choice for wide range of physics goals where sampling calorimeters can be considered.

Among later developments, an interesting example of ECAL for KOPIO experiment [127] at BNL should be mentioned. Electromagnetic calorimeter is important to precisely measure photons from π^0 decays to reconstruct $K^0_{\mathrm{L}} \to \pi^0 \nu \overline{\nu}$, which is on of the key processes for *CP*-violation studies [128]. The energy of the photons ranges between 50 and 1000 MeV. A proposed Shashlik calorimeter [129, 130] is built out of 300 sampling layers comprising 1.5 mm scintillator tiles and 0.275 mm lead plates to develop a shower. The detector is a $15.9 X_o$ deep. Its density of about 0.9 cm^{-2} is similar to the fiber density of the LHCb cells in middle and outer regions. Design of this detector is very similar to the LHCb Shashlik, employing for example similar fiber routing with loops at the front calorimeter. Scintillator tiles posess lego-type locks which simplify stack assembly and precise tile positioning. Wrapping the module with TYVEK paper, a difference of 2.3% in the light collection efficiency between the center and the edge of the tile was achieved. The achieved energy resolution of

$\sigma_E/E = (2.74 \pm 0.05)\%/\sqrt{E} \oplus (1.96 \pm 0.10)\%$ is within the KOPIO requirements.

Shashlik technology has also been proposed for the forward ECAL of PANDA experiment, where the energy measurements are required in the range between 1 and 19 GeV. The same design and sampling as for KOPIO experiment, but deeper, $20X_o$, Shashlik prototype was tested with the electron beam [131]. Measured energy resolution of $\sigma_E/E = (2.8 \pm 0.2)\%/\sqrt{E} \oplus (1.3 \pm 0.1)\%$ was found to be consistent with the simulation and previous results [129, 130]. In addition position resolution was measured to be $\sigma_x = 13.1/\sqrt{E} \oplus 4.0(\,\mathrm{mm})$, where E is in GeV, in agreement with the simulation. Reconstruction of π^0 will be studied at different energies to make a decision on lateral segmentation.

Another Shashlik ECAL with micropixel avalanche photodiodes readout has been proposed for COMPASS II [132]. Each Shashlik stack comprises 109 sampling layers, each layer consisting of a 0.8 mm thick lead plate and nine 1.5 mm thick scintillator tiles with dimensions close to those of LHCb inner region ECAL. Total depth of the calorimeter amounts to about $15X_o$. 1.2 mm diameter thick BCF 91A WLS fibers readout the light from the scintillator tiles. The fiber density of about 0.9 cm^{-2} is similar to the fiber density of the LHCb cells in middle and outer regions. Energy resolution with a stochastic term of $7.8\%/\sqrt{E}$ was obtained with the electron test beam.

LHCb-like Shashlik has been proposed for the development of the SHIP experiment at CERN.

Finally, along with Si/W sandwich, Shashlik is one of the two candidates for the upgrade of the CMS forward region electromagnetic calorimeter. Being cheaper solution, a Shashlik technology, employing radiation resistant scintillating materials, and being able to operate in the forward region of high luminosity CMS experiment, is still to be demonstrated.

Chapter 4

Charmonium states production at LHCb using decays to $p\overline{p}$ and $\phi\phi$

Imagination is the only weapon
in the war against reality.

Lewis Carroll

Precision studies of J/ψ and $\psi(2S)$ states production have been performed using decays of these charmonium states to the $\mu^+\mu^-$ final state, which is efficiently triggered and reconstructed by experiments. Production of the χ_c family can be studied using χ_c radiative decays to J/ψ meson. However low-energy photons have to be reconstructed. The analysis of charmonia production in using hadronic decays finds its place as a possibility to access production of other charmonia, and to complement χ_c production studies by alternative method, which does not require reconstruction of low-energy photons and thus improves reconstruction efficiency and simplifies separation of χ_c states. Studies of charmonia production are addressed in section 4.1. Reconstruction of η_c (1S) meson via its decay to the $p\overline{p}$ final state is used to measure the η_c (1S) prompt production in section 4.2. Charmonia production in b-hadron decays using charmonia decays to the $p\overline{p}$ and $\phi\phi$ final states, is studied in section 4.3. Section 4.4 addresses determination of mass and natural width of the η_c (1S) meson. The results presented in this chapter are preliminary LHCb results.

4.1 Production of charmonium states

Experimental results on the properties of charmonium states come from both e^+e^- and hadron colliders. Charmonia properties, including precise determination of their mass and width, verification of their quantum numbers and study of their decay modes, are coming from all experiments, where charmonia are copiously produced. The charm factories, CLEO-c and now BES, operating at $D\bar{D}$ threshold, collected large data samples at energies around the charmonium production region. Clean data samples are available, for example up to few $\times 10^7$ $\psi(3770)$ at CLEO-c, and more than 2×10^6 D-mesons in the 2010-2011 data sample accumulated by the BES experiment [133]. Charmonium production in b-hadron decays is only accessible at B-factories and higher energy machines. The B-factories, BaBar and Belle, provide a clean environment, with often only two B mesons produced in the event in a $\Upsilon(4S) \to B\overline{B}$ process, and a possibility to fully reconstruct the event. They accumulated large samples of charmonium states from B meson decays with more than 10^9 $B\bar{B}$ pairs produced.

The pp or $p\bar{p}$ colliders operate in a more challenging environment, however they deliver larger statistical samples of reconstructed charmonia states, and provide a unique instrument to study charmonium hadroproduction. The results are delivered by the CDF and D0 experiments at Tevatron, and ATLAS, CMS and LHCb experiments at LHC. High production cross-section at small rapidities at CDF, and at forward LHCb rapidities, *e.g.* $\sigma(c\bar{c})_{\mathrm{LHCb},7TeV} \sim 1400$ μb [2], provides large samples of reconstructed charmonia.

At the LHC centre-of-mass energy $\sqrt{s} = 7\,\mathrm{TeV}$ and LHCb luminosity of 4×10^{32} cm^{-2}s^{-1}, the experiment exploits the high $c\bar{c}$ production cross section $\sigma(pp \to c\bar{c}X) \sim 6$ mb, which is however an order of magnitude lower than the inelastic cross section. The $b\bar{b}$ production cross section is suppressed by another factor 20, $\sigma(pp \to b\bar{b}X) \sim 0.3$ mb. However, tolerable storage rate of about 5 kHz does not allow accumulating all the $c\bar{c}$ or $b\bar{b}$ candidates and requires futher selectivity. This is achieved by the trigger system, hardware at the L0 stage, reducing a 10 MHz input rate to about 1 MHz entering HLT, and HLT implemented at the farm, further reducing the rate to about 5 kHz, stored and subject to further treatment by data stripping procedure (section 2.3.4).

The LHCb experiment performed a wide range of charmonium production studies,

and in particular production studies of charmonia with $J^{PC} = 1^{--}$ quantum numbers, where decays to dimuon final state, having high trigger and reconstruction efficiency, as well as powerful background rejection due to excellent muon identification capabilities, can be used. In addition to the J/ψ and $\psi(2S)$ production [11, 134, 135], the χ_c states production has been studied [136], using radiative decays of the χ_c states to J/ψ. In order to explore other states than those having 1^{--} quantum numbers, and avoiding reconstruction of radiative decays with low energy photons, hadronic final states should be investigated [137]. Reconstruction of charmonia decays to hadrons rely on hadronic trigger alleys (section 2.3.3), and hadron identification capabilities (section 2.3.4). In the remaining sections of this chapter the decays to the $p\overline{p}$ final state [138] as well as decays to ϕ mesons are employed for the studies of charmonium production, prompt production and inclusive charmonium production in b-hadron decays. All known charmonium states decay to $p\overline{p}$, though with different probabilities, while decays of $J^{PC} = 1^{--}$ states to two vector mesons ($\phi\phi$) are forbidden. Table 4.1 shows masses of known charmonium states, and the branching fractions of charmonia decays to $p\overline{p}$ and $\phi\phi$ pairs [57]. The branching fraction of h_c meson decay to $p\overline{p}$ final state is estimated as

	Mass, MeV/c^2	$\mathcal{B}(c\overline{c} \to p\overline{p})$, $\times 10^{-3}$	$\mathcal{B}(c\overline{c} \to \phi\phi)$, $\times 10^{-3}$
η_c (1S)	2980.5 ± 1.47	1.51 ± 0.16	1.76 ± 0.20
J/ψ (1S)	3096.916 ± 0.011	2.120 ± 0.029	forbidden
χ_{c0} (1P)	3414.75 ± 0.31	0.213 ± 0.012	0.79 ± 0.08
χ_{c1} (1P)	3510.66 ± 0.07	0.073 ± 0.004	0.44 ± 0.06
h_c(1P)	3525.67 ± 0.32	not seen	not seen
χ_{c2} (1P)	3556.20 ± 0.09	0.071 ± 0.004	1.16 ± 0.10
η_c (2S)	3638.9 ± 1.3	< 0.29 at 90% CL	not seen
$\psi(2S)$	3686.09 ± 0.04	0.275 ± 0.012	forbidden
$\psi(3770)$	3773.15 ± 0.33	not seen	forbidden

Table 4.1: Masses of charmonium states and branching fractions of their decays to the $p\overline{p}$ and $\phi\phi$ final states [57]

$\mathcal{B}(h_c \to p\overline{p}) = (3.2 \pm 0.5) \times 10^{-3}$ [137], where only uncertainty of the experimental input is shown.

In the clean environment of the e^+e^- machine, decays to $p\overline{p}$, $\phi\phi$ and final states with kaons and pions have been used to reconstruct η_c state in the $J/\psi \to \gamma\eta_c$ decay mode by

the BES experiment [139]. The LHCb experiment reconstructed η_c via decays to the $p\overline{p}$ final state to study the η_c (1S) prompt production and inclusive production in b-hadron decays. In addition the η_c family, η_c (1S) and η_c (2S), and the χ_c family, χ_{c0}, χ_{c1} and χ_{c2}, are reconstructed using decays to $\phi\phi$ in the inclusive decays of b-hadrons. The inclusive analysis using decays to hadronic final states is performed for the first time at a hadron machine environment. Owing to powerful charged-hadron identification and high luminosity, the LHCb experiment is well-positioned for these studies. The η_c production measurements, using decays to $p\overline{p}$ final state, are performed using the topologically and kinematically similar $J/\psi \to p\overline{p}$ normalization channel, which allows systematic uncertainties to partially cancel in the ratio.

In the following quarkonium states are defined as being promptly produced when they are directly produced in parton interactions or originate from the decays of heavier quarkonium states, which are in turn produced in parton interactions. We distinguish promptly produced quarkonia from those originating from b-hadron decays. Experimentally, discrimination between prompt quarkonia and quarkonia produced in the b-hadron decays is achieved by reconstructing a (b-hadron and) charmonium decay vertex that is well distinguished from the corresponding pp collision vertex where b-hadron is born (*primary vertex*). On average b-hadron travels about 1 cm in the LHCb detector before its decay. This is illustrated by the LHCb event display of the $B_s^0 \to \mu^+\mu^-$ candidate on Fig. 2.5.

4.2 Prompt production of charmonium states

The idea to study prompt charmonium production using charmonia decays to hadronic final states with LHCb originated from the brainstorming discussion with Emi Kou, and further interesting discussions with Jibo He, Emi Kou and Benoit Viaud. Trigger lines and stripping of corresponding LHCb data was performed by Jibo He. This analysis became a subject of the Ph.D. thesis of Maksym Teklishyn. The results discussed in this section are preliminary LHCb results.

4.2.1 Landscape for charmonia prompt production studies

Heavy quarkonium states are particularly interesting systems to test our understanding of strong interactions, both at perturbative and non-perturbative regimes. This explains why theoretical and experimental groups are attracted by studying production and decays of charmonium states. Majority of the current theoretical activity is inspired by establishing of the original effective field theory, non-relativistic QCD (NRQCD) [140, 141], providing the ground for further developments. NRQCD factorises the production of heavy quarkonium in two stages, first, a heavy quark-antiquark pair is created at short distances and then it evolves non-perturbatively into quarkonium at long distances.

At the LHC, $c\bar{c}$ pairs are expected to be produced at leading order (LO) through gluon-gluon interactions, followed by the formation of bound charmonium states [141]. The production of the $c\bar{c}$ pair is described by perturbative QCD, while non-perturbative QCD is used for the description of the evolution of the $c\bar{c}$ pair to the bound state. Several models have been developed for the non-perturbative part, such as the Colour Singlet (CS) model [142–145] and important developments in the framework of NRQCD [12, 141, 146–149]. The CS model assumes the $c\bar{c}$ pair to be created in a hard scattering reaction as a colour singlet with the same quantum numbers as the final charmonium state. The NRQCD model includes, in addition to the colour singlet mechanism, the production of $c\bar{c}$ pairs as colour octets (CO), and in this case the CO state evolves to the final charmonium state via soft gluon emission. In the NRQCD calculations, CS and CO amplitudes account for the probability of a heavy quark-antiquark pair in a particular colour state to evolve into a heavy quarkonium state. Initially, the CS model was proposed to describe experimental data. However, it underestimates the observed cross-section for single J/ψ production at high transverse momentum (p_{T}). To resolve this discrepancy, the CO mechanism was introduced. More recent higher-order calculations to the CS predictions raise substantially the cross-sections at large p_{T} bringing them closer to the experimental data. However, none of these approaches can reproduce in a consistent way the available experimental results on both production cross-section and polarisation [5].

Following the Tevatron era, LHC energies provide additional powerful tests for models describing charmonium production. The measurements of the J/ψ and $\psi(2S)$ production rate at the LHC [7, 134, 135, 150–152], are in general successfully described by NLO

calculations [153]. Results of the LHC experiments, measuring quarkonia production rate are consistent, and complementary in rapidity region. This is illustrated by rapidity dependence of the J/ψ, $\psi(2S)$, $\Upsilon(1S)$, $\Upsilon(2S)$ and $\Upsilon(3S)$ quarkonia production rate is shown on Fig. 4.1 prepared by H. Woehri for LHCP conference in 2013, based on the results from Refs. [6, 134, 136, 150–152, 154]. The plot also demonstrates how

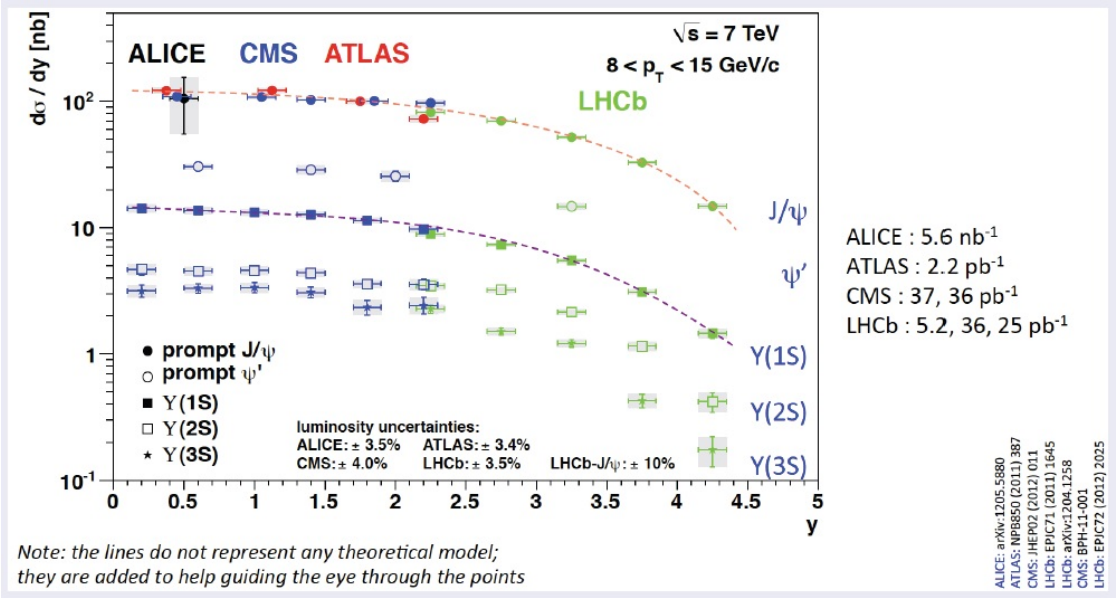

Figure 4.1: Rapidity dependence of the J/ψ, $\psi(2S)$, $\Upsilon(1S)$, $\Upsilon(2S)$ and $\Upsilon(3S)$ quarkonia production rate measured by the LHC experiments. Plot of H. Woehri shown at the LHCP conference in 2013

LHCb rapidity coverage complements the rapidity range covered by ATLAS and CMS. However the observation of small or no polarization for the J/ψ production [135] remains unexplained within the available theoretical framework.

In the high-p_{T} region, where the quarkonium transverse momentum is much larger than its mass (in natural units), the CS model underestimates significantly the measured prompt J/ψ and $\psi(2S)$ production cross-sections [134,136,155], while the NRQCD model provides a good description of the p_{T}-dependent J/ψ and $\psi(2S)$ cross-sections measured by LHCb [134,136] and CMS [150]. The CS model predicts large longitudinal polarisation for J/ψ and $\psi(2S)$ mesons. On the other hand, in the NRQCD model, where quarkonium production is dominated by the gluon fragmentation process in the high-p_{T} region, the gluon is almost on-shell, leading to predictions of large transverse polarisations [146]. Precise measurements of the J/ψ polarisation at both the Tevatron [156] and the

LHC [135, 157, 158], show no significant longitudinal or transverse polarisations, while at HERA, polarization at small p_{T} values has been reported [159]. The measurements do not support neither the CSM nor NRQCD predictions. Studies of polarisation for promptly produced $\psi(2S)$ mesons have been performed by the CDF [156], CMS [158] and LHCb [160] experiments. No significant polarisation was observed. Although a direct comparison between the results of different experiments is not possible due to the different kinematic ranges, all results disfavour large polarisation in the high-p_{T} region. The prompt $\psi(2S)$ polarisation measured at LHCb disagrees with the CSM predictions [161] both in the size of the polarisation parameters and the p_{T} dependence. While the NRQCD models at NLO [161–163] provide a good description of the LHCb data in the low-p_{T} region, the predicted transverse polarisation at high-p_{T} is not observed.

The production of χ_{cJ} states at the LHC energies has been studied using their radiative decays to J/ψ meson $\chi_{cJ} \to J/\psi\gamma$, using converted or non-converted photons [9–11]. Reconstruction of low-energy photons reduces the experimental precision. The study of χ_{cJ} prompt production provides another test of the CS and CO models. In addition, the measurement of the χ_{cJ} prompt production is important since these resonances give a substantial feed-down contribution to prompt J/ψ production through their radiative decay $\chi_c \to J/\psi\gamma$ and can have a significant impact on the J/ψ polarization measurements. Measurements of χ_{c1} and χ_{c2} production cross-section for various particle beams and energies have been reported in Refs. [9, 11, 164–167]. In addition, LHCb reported the first evidence of the χ_{c0} production [11] at high-energy hadron colliders. The p_{T} dependence of ratio of the χ_{c2} and χ_{c1} productions [11] was found to be generally consistent with both LO [168] and NLO NRQCD [12] predictions.

Another potentially powerful approach to better understand prompt charmonium production mechanism is provided by studies of the central exclusive production. LHCb recently measured [6] the differential cross-section of the J/ψ and $\psi(2S)$ exclusive production as a function of rapidity, with a precision better than 10% for the J/ψ exclusive production. In addition χ_{cJ} exclusive production was observed. The LHCb result is an update of the Ref. [169] and a continuation of the J/ψ exclusive production measurements performed at HERA [170–172] and Tevatron [173], and $\psi(2S)$ measurements performed at HERA [174] and Tevatron [173]. Exclusive J/ψ and $\psi(2S)$ meson production in hadron collisions are diffractive processes that can be calculated in

perturbative quantum chromodynamics (QCD) [175]. At leading order (LO) they are thought to proceed via the exchange of a photon and a pomeron, which at sufficiently hard scales can be described by two gluons. Measurements of this class of processes thus provide a test of QCD and shed light on the pomeron, which plays a critical role in the description of diffraction and soft processes. In the exclusive processes, the J/ψ and $\psi(2S)$ mesons cannot be produced as colour octets, thus providing a useful tool to distinguish between the CS and CO contributions.

The investigation of the lowest-state, the η_c meson, can provide important additional information to the global fit of the long-distance matrix elements [161,163]. In particular, heavy quark spin-symmetry relation between the η_c and J/ψ matrix elements can be tested for the first time. Furthermore, the NLO computations lead to a different p_{T} dependence of the production rates for spin singlet (η_c) and triplet (J/ψ , χ_{cJ}) states [176]. Thus, a measurement of the p_{T} dependence of the η_c production rate, in particular in the low p_{T} region, can have important implications. Recent LHCb results on χ_c states production [11] allow extracting information on the production of the P-wave states χ_{c0} and χ_{c2} at low p_{T} using the well understood χ_{c1} production as a reference. A measurement of the cross-section of the η_c production, direct in parton interactions or in the decays of heavier resonance states, which are in turn produced in parton interactions, may allow an important comparison with the χ_{c0} production results and yield indirect information on the properties of heavier states production, in particular access to the η_c (2S) production cross section multiplied by the branching fraction of η_c (2S) decays to η_c (1S) $\sigma_{\eta_c(2S)} \times \mathcal{B}(\eta_c(2S) \to \eta_c(1S)X)$.

Finally, measured quarkonia production associated to the pp collision vertex, i.e. the vertex of prompt quarkonia production, comprises direct production in the hard scattering, and the production through feed-down from higher-mass quarkonia states. In the case of $\psi(2S)$ mesons, the contribution from feed-down is negligible, allowing a straightforward comparison between measurements of prompt production and predictions for direct contributions. For other charmonia, production of heavier states, that potentilly decay to the charmonium state under study, should be performed to determine the feed-down contribution.

The LHCb experiment reported a first measurement of the prompt η_c production cross-section in pp collisions at $\sqrt{s} = 7\,\mathrm{TeV}$ and $\sqrt{s} = 8\,\mathrm{TeV}$ centre-of-mass energy [138], that is addressed in section 4.2.2.

4.2.2 Measurement of the η_c prompt production cross-section using decays to the $p\bar{p}$ final state

The analysis of the η_c prompt production using decays to the $p\bar{p}$ final state used the pp collision data recorded by the LHCb experiment at $\sqrt{s} = 7\,\text{TeV}$, corresponding to an integrated luminosity of $0.7\,\text{fb}^{-1}$ [1], and at $\sqrt{s} = 8\,\text{TeV}$, corresponding to an integrated luminosity of $2.0\,\text{fb}^{-1}$.

Events enriched in signal decays, $\eta_c, J/\psi \to p\bar{p}$, are selected by the hardware trigger based on the presence of a single high-energy deposition in the calorimeter. The subsequent software trigger specifically rejects high-multiplicity events and selects p and $\overline{p}$ candidates that exhibit good track-fit quality, $\chi^2/\text{ndf} < 4$, and have transverse momentum larger than $1.9\,\text{GeV}/c$. Proton candidates are positively identified using the information from RICH and other relevant detectors in LHCb combined into differences between the logarithms of the particle identification likelihoods under different mass hypotheses (DLL). Selected proton candidates are required to have $\text{DLL}_{pK} \equiv \ln\mathcal{L}_p - \ln\mathcal{L}_K > 15$ and $\text{DLL}_{p\pi} \equiv \ln\mathcal{L}_p - \ln\mathcal{L}_\pi > 20$. Selected p and $\overline{p}$ candidates are required to form a good quality common vertex fit, $\chi^2 < 9$. In order to further suppress the dominant background from accidental combinations of random tracks (combinatorial background), charmonium candidates are also required to have high transverse momentum, $p_\text{T} > 6.5\,\text{GeV}/c$.

Offline analysis in addition requires the transverse momentum of p and $\overline{p}$ to be $p_\text{T} > 2.0\,\text{GeV}/c$, and restricts charmonium candidates to the rapidity range $2 < y < 4.5$, corresponding to the rapidity of the J/ψ production analysis.

We see from above that signal selection criteria for the analysis of charmonium decays to $p\overline{p}$ are largely implemented already at the level of trigger. This is a consequence of the fact, that in order to achieve tolerable trigger rate, substantial combinatorial background can only be suppressed using limited number of handles, kinematical variables - transverse momentum, and particle identification. In order to select charmonium produced in the inclusive b-hadron decays, reconstructed charmonium decay vertex, well-distinguished from the vertex of pp interaction, yields additional tool to suppress

[1] The dataset corresponding to $\sqrt{s} = 7\,\text{TeV}$ is reduced with respect to the overall integrated luminosity collected at this centre-of-mass energy due to the fact, that corresponding trigger alleys were not operational at the beginning of the data taking.

combinatorial background.

In order to distinguish between promptly produced charmonium candidates and charmonium candidates from b-hadron decays, the pseudo-proper lifetime $\tau_z = \Delta z \cdot M/p_z$, where Δz is the distance along the beam between charmonium candidate production and decay vertices, M is the reconstructed mass of charmonium candidate and p_z is the longitudinal component of its momentum, is required to be below and above 80 fs, respectively. In addition for charmonium candidates from b-hadron decays the large impact parameter of the proton tracks with respect to charmonium candidate production vertex is required, $\chi^2_{\rm IP}/{\rm ndf} > 16$. Fig. 4.2 shows the t_z distribution from the simulation of $J/\psi \to p\overline{p}$ signal, with all selection criteria applied, including separation requirements. The results are stable under variation of the discriminating t_z requirement

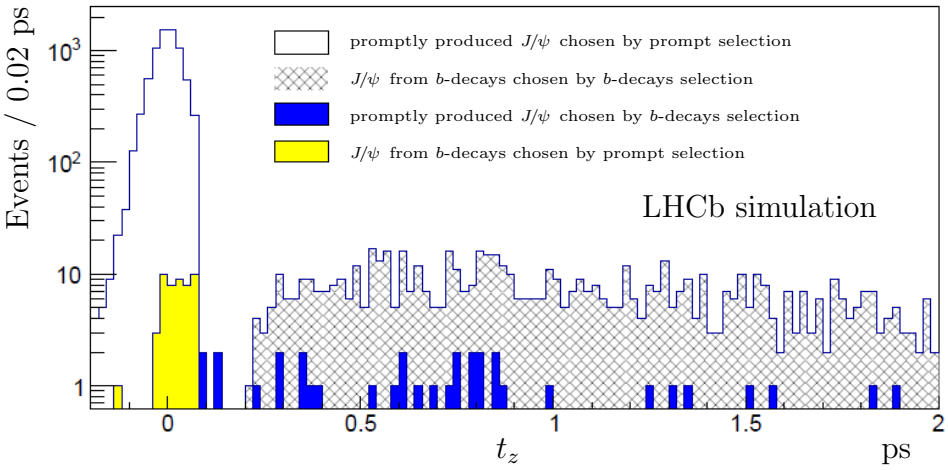

Figure 4.2: Distribution of t_z variable from the simulation of the $J/\psi \to p\overline{p}$ signal with all selection criteria applied. Empty and hatched histograms correspond to prompt J/ψ production and J/ψ production from b-hadron decays, selected by prompt production and production from b-hadron decays analyses, respectively. Blue and yellow filled histograms correspond to the cross-talk between the samples, that is J/ψ from prompt production and production from b-hadron decays, selected by production from b-hadron decays and prompt production analyses, respectively

value.

Thus selected samples of promptly produced charmonium candidates and charmonium candidates from b-hadron decays, have some events in common (*cross-talk*), *i.e.* small contribution of prompty produced charmonium enters selected sample containing

charmonium candidates from b-hadron decays, and vice versa. The cross-talk probability was estimated using Monte-Carlo (MC) simulation, scaled using the observed event yields, and was subtracted to obtain the ratio of produced η_c and J/ψ, decaying to $p\overline{p}$. Corrections range from 2% to 3% for the ratio of promptly produced charmonia, and from 8% to 10% for the ratio of charmonia produced in b-hadron decays.

The ratios of obtained signal event yields are translated to the ratios of production cross-sections multiplied by the relevant decay branching fractions as

$$\frac{N^P_{\eta_c}}{N^P_{J/\psi}} = \frac{\sigma(\eta_c) \times \mathcal{B}_{\eta_c \to p\overline{p}}}{\sigma(J/\psi) \times \mathcal{B}_{J/\psi \to p\overline{p}}} ,$$
$$\frac{N^S_{\eta_c}}{N^S_{J/\psi}} = \frac{\mathcal{B}_{b\to\eta_c X} \times \mathcal{B}_{\eta_c \to p\overline{p}}}{\mathcal{B}_{b\to J/\psi X} \times \mathcal{B}_{J/\psi \to p\overline{p}}} ,$$

where N^P and N^S are the numbers of produced charmonium for prompt production and for charmonia from b-hadron decays, respectively. Similar efficiencies are assumed for the η_c and J/ψ meson reconstruction and selection criteria. The MC simulation reasonably describes the kinematics-related differences between the η_c and J/ψ decay modes and predicts the efficiencies for selecting and reconstructing η_c and J/ψ mesons to differ by less than 0.5%. Prompt J/ψ production efficiency is also corrected for polarisation effects, as a function of rapidity and p_{T}, according to Ref. [135].

The number of reconstructed η_c and J/ψ candidates is extracted from an extended maximum likelihood fit of the unbinned $p\overline{p}$ invariant mass distribution.

The J/ψ peak position $M_{J/\psi}$ and the mass difference $\Delta M_{J/\psi,\eta_c}$ are fitted in the sample of charmonia from b-hadron decays, where the signal is more prominent owing to the reduced background level due to charmonium decay-vertex displacement requirements. The results are then used to apply Gaussian constraints in the fit to the $p\overline{p}$ invariant mass spectrum in the prompt production analysis, where the signal-to-background ratio is worse, due to large combinatorial backgrounds.

The signal shape is defined by the detector response, and the natural width in the case of the η_c resonance. The detector response is described using two Gaussian functions with a common mean value. Identical shape to account for the detector resolution is essential for description of both η_c and J/ψ signal peaks reconstructed in both prompt charmonia production and charmonia produced in b-hadron decays. Choice of this shape is motivated by MC studies and large candidate samples in signal

peaks. In the description of each resonance, the ratio of the two Gaussian widths, $\sigma^a_{J/\psi}/\sigma^b_{J/\psi} = \sigma^a_{\eta_c}/\sigma^b_{\eta_c}$, and the fraction of the "narrow" Gaussian component, as well as the ratio of Gaussian widths corresponding to the η_c and J/ψ decay kinematic properties, $\sigma^a_{\eta_c}/\sigma^a_{J/\psi}$, are fixed in the fit to the values observed in simulation. The only resolution parameter left free in the fit in the analysis of charmonium production from b-hadron decays, $\sigma^a_{J/\psi}$, is then fixed to its central value in the fit to the prompt sample. The natural width Γ_{η_c} of the η_c resonance is also extracted from the fit of the b-hadron decays sample, and is then fixed to that value in the prompt production analysis.

The combinatorial background is parametrized by a sum of Chebychev polynomials up to the third order in the fit to the prompt sample.

Combinations $p\overline{p}$ from the decay $J/\psi \to p\overline{p}\pi^0$ potentially affect the region close to the η_c peak position; hence this reflection is specifically included in the background description. The reflection produces a non-peaking contribution, and is described by a square-root shape to account for the phase space available to the $p\overline{p}$ system from the $J/\psi \to p\overline{p}\pi^0$ decay, convoluted with the two Gaussian functions to account for the detector resolution. In the fit to the $p\overline{p}$ invariant mass spectrum, the normalization of this reflection is fixed using the number of events found in J/ψ signal peak, the ratios of branching fractions and efficiencies for the $J/\psi \to p\overline{p}\pi^0$ and $J/\psi \to p\overline{p}$ decay modes.

In the fit to the proton-antiproton invariant mass spectrum for prompt production candidates, the η_c natural width in the prompt production analysis fit is fixed to the average value of 25.8 MeV from the analysis of charmonium production in b-hadron decays, signal resolutions are extracted from the fit of the low-background sample from b-hadron decays, and Gaussian constraints on the J/ψ meson mass and the $\Delta M_{J/\psi\,,\eta_c}$ mass difference, from that fit are applied. The fit with free mass values gives consistent results.

The result of the unbinned maximum likelihood fit of the $p\overline{p}$ invariant mass spectrum for the prompt charmonium production analysis is shown on Fig. 4.3 and Fig. 4.4 for the data samples corresponding to a centre-of-mass energy $\sqrt{s} = 7\,\text{TeV}$ and $\sqrt{s} = 8\,\text{TeV}$, respectively. The fit yields 13370 ± 2260 η_c and 11052 ± 1004 J/ψ candidates, and 22416 ± 4072 η_c and 20217 ± 1403 J/ψ candidates, in the signal peaks, for the data samples corresponding to a centre-of-mass energy $\sqrt{s} = 7\,\text{TeV}$ and $\sqrt{s} = 8\,\text{TeV}$, respectively. These numbers have then been corrected for the cross-talk effect.

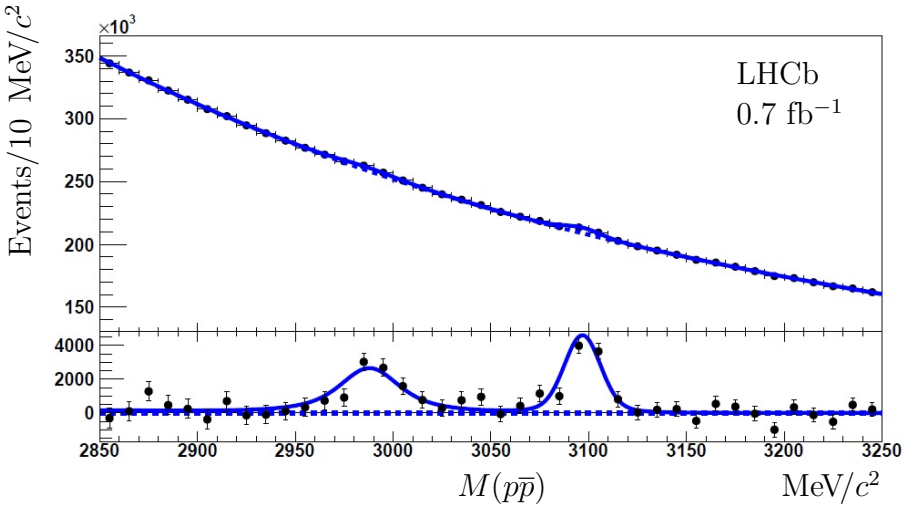

Figure 4.3: Proton-antiproton invariant mass spectrum for candidates coming from a primary vertex (top), and residual plot with respect to the fitted background curve (bottom) in the data sample, corresponding to a centre-of-mass energy $\sqrt{s} = 7\,\text{TeV}$. The J/ψ signal is described by a double-Gaussian function, the η_c signal is described by a double-Gaussian function convoluted with a Breit-Wigner function, the contribution from $J/\psi \to p\bar{p}\pi^0$ decay with non-reconstructed pion is taken into account. Gaussian constraints on the J/ψ mass and the difference $\Delta M_{J/\psi,\eta_c} = M_{J/\psi} - M_{\eta_c}$, from the fit of the sample corresponding to charmonium candidates from b-hadron decays, are applied

Systematic uncertainties due to detector resolution, background description, feed-down from $J/\psi \to p\bar{p}\pi^0$ decays, possible differences of the prompt charmonium production spectra in data and simulation, and cross-talk between the prompt charmonium sample and the charmonium sample from b-hadron decays, are considered. Uncertainties due to detector resolution are estimated by assigning the same σ^a value to the η_c and J/ψ signal description for charmonium production from b-hadron decays, and by varying the σ^a parameters within uncertainties from the b-hadron decays production fit in the prompt production analysis. Uncertainties associated with the background description are estimated by using an alternative parametrisation and varying the fit range. The uncertainty due to the contribution from the $J/\psi \to p\bar{p}\pi^0$ decay is dominated by the modelling of the $p\bar{p}$ invariant mass shape, and is estimated by using an alternative parametrisation, linear with the energy release. Possible differences of the prompt charmonium production spectra in data and simulation are estimated by correcting the efficiency derived from simulation according to the observed p_{T} distribution. The uncertainty related to the cross-talk is estimated by varying the event yields according

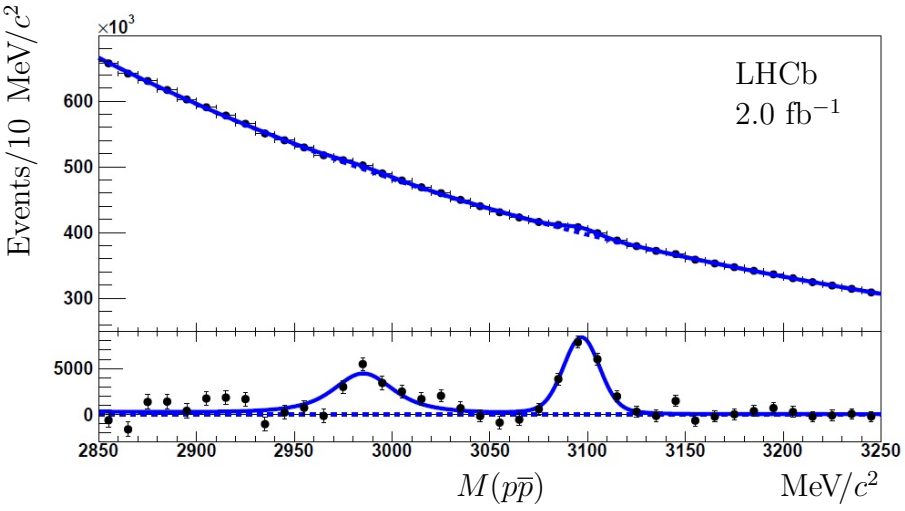

Figure 4.4: Proton-antiproton invariant mass spectrum for candidates coming from a primary vertex (top), and residual plot with respect to the fitted background curve (bottom) in the data sample, corresponding to a centre-of-mass energy $\sqrt{s} = 8\,\text{TeV}$. The J/ψ signal is described by a double-Gaussian function, the η_c signal is described by a double-Gaussian function convoluted with a Breit-Wigner function, the contribution from $J/\psi \to p\bar{p}\pi^0$ decay with non-reconstructed pion is taken into account. Gaussian constraints on the J/ψ mass and the difference $\Delta M_{J/\psi,\eta_c} = M_{J/\psi} - M_{\eta_c}$, from the fit of the sample corresponding to charmonium candidates from b-hadron decays, are applied

1

to their statistical and systematic uncertainties in the samples that causes the cross-talk. In order to estimate the systematic uncertainty associated with the η_c natural width, which enters the results for prompt production analysis, the alternative Γ_{η_c} value of 32.0 MeV from Ref. [57] is used. The total systematic uncertainty is dominated by the uncertainty associated with the natural η_c width Γ_{η_c} for the prompt production measurement.

The prompt production yield ratios at the different centre-of-mass energies are obtained as

$$\left(N^P_{\eta_c}/N^P_{J/\psi}\right)_{7\,\text{TeV}} = 1.24 \pm 0.21 \pm 0.20\ ,$$
$$\left(N^P_{\eta_c}/N^P_{J/\psi}\right)_{8\,\text{TeV}} = 1.14 \pm 0.21 \pm 0.18\ .$$

By correcting them with the ratio of branching fractions [57], $\mathcal{B}_{J/\psi\to p\bar{p}}/\mathcal{B}_{\eta_c\to p\bar{p}} = 1.40 \pm 0.15$, the relative η_c to J/ψ prompt production rate in the kinematic regime $2.0 < y < 4.5$

[2]

and $p_{\mathrm{T}}(J/\psi\,,\eta_c) > 6.5\,\mathrm{GeV}/c$ is found to be

$$\left(\sigma_{\eta_c}/\sigma_{J/\psi}\right)_{\sqrt{s}=7\,\mathrm{TeV}} = 1.75 \pm 0.30 \pm 0.28 \pm 0.19_{\mathcal{B}_{J/\psi\to p\overline{p},\eta_c\to p\overline{p}}}$$

for the data sample, collected at $\sqrt{s} = 7\,\mathrm{TeV}$, and

$$\left(\sigma_{\eta_c}/\sigma_{J/\psi}\right)_{\sqrt{s}=8\,\mathrm{TeV}} = 1.60 \pm 0.29 \pm 0.25 \pm 0.17_{\mathcal{B}_{J/\psi\to p\overline{p},\eta_c\to p\overline{p}}}$$

for the data sample, collected at $\sqrt{s} = 8\,\mathrm{TeV}$. The third contribution to the uncertainty in the above results is due to the uncertainty in the $J/\psi \to p\overline{p}$ and $\eta_c \to p\overline{p}$ branching fractions.

The absolute η_c prompt production cross section is calculated using the J/ψ prompt production cross section, measured in Refs. [135] and [7], and integrated in the kinematic range of the present analysis, $2.0 < y < 4.5$ and $p_{\mathrm{T}}(J/\psi\,,\eta_c) > 6.5\,\mathrm{GeV}/c$. The corresponding J/ψ prompt production cross section is determined to be

$$\left(\sigma_{J/\psi}\right)_{\sqrt{s}=7\,\mathrm{TeV},\ 2.0<y<4.5,\ p_{\mathrm{T}}>6.5\,\mathrm{GeV}/c} = 296.9 \pm 1.8 \pm 5.5\ \ \mathrm{nb}$$

for a centre-of-mass energy $\sqrt{s} = 7\,\mathrm{TeV}$, and

$$\left(\sigma_{J/\psi}\right)_{\sqrt{s}=8\,\mathrm{TeV},\ 2.0<y<4.5,\ p_{\mathrm{T}}>6.5\,\mathrm{GeV}/c} = 371.4 \pm 1.4 \pm 2.7\ \ \mathrm{nb}$$

for a centre-of-mass energy $\sqrt{s} = 8\,\mathrm{TeV}$. The J/ψ meson is assumed to be produced unpolarized. The prompt η_c production cross-section for this kinematic regime is determined to be

$$\left(\sigma_{\eta_c}\right)_{\sqrt{s}=7\,\mathrm{TeV},\ 2.0<y<4.5,\ p_{\mathrm{T}}>6.5\,\mathrm{GeV}/c} = 0.52 \pm 0.09 \pm 0.08 \pm 0.06_{\sigma_{J/\psi}\,,\mathcal{B}_{J/\psi\to p\overline{p},\eta_c\to p\overline{p}}}\ \ \mu\mathrm{b}$$

for $\sqrt{s} = 7\,\mathrm{TeV}$, and

$$\left(\sigma_{\eta_c}\right)_{\sqrt{s}=8\,\mathrm{TeV},\ 2.0<y<4.5,\ p_{\mathrm{T}}>6.5\,\mathrm{GeV}/c} = 0.59 \pm 0.11 \pm 0.09 \pm 0.06_{\sigma_{J/\psi}\,,\mathcal{B}_{J/\psi\to p\overline{p},\eta_c\to p\overline{p}}}\ \ \mu\mathrm{b}$$

for $\sqrt{s} = 8\,\mathrm{TeV}$. Uncertainties associated with the $J/\psi \to p\overline{p}$ and $\eta_c \to p\overline{p}$ branching fractions, and with the J/ψ cross-section measurement, are combined into the last uncertainty component, dominated by the knowledge of the branching fractions. This is the first measurement of prompt η_c production in pp collisions. The obtained cross-section of the η_c prompt production is in agreement with the colour-singlet leading order (LO) calculations, while taking into account colour-octet LO contribution predicted cross-section exceeds the observed one by two orders of magnitude [177]. However the NLO contribution is expected to significantly modify the LO result [176].

4.2.3 The $p_{\rm T}$ dependence of the η_c state production

The η_c production as a function of $p_{\rm T}$, is obtained by fitting the $p\overline{p}$ invariant mass spectrum in three of four bins of $p_{\rm T}$. The J/ψ $p_{\rm T}$ spectrum [7, 134, 135] is used to access the η_c $p_{\rm T}$ spectrum for both prompt production and inclusive η_c production in b-hadron decays. Figs. 4.5a and 4.5b show the obtained differential cross-sections for η_c and J/ψ meson production as a function of transverse momentum for the $\sqrt{s} = 7\,\text{TeV}$ and $\sqrt{s} = 8\,\text{TeV}$ data samples, respectively. The J/ψ cross section $p_{\rm T}$

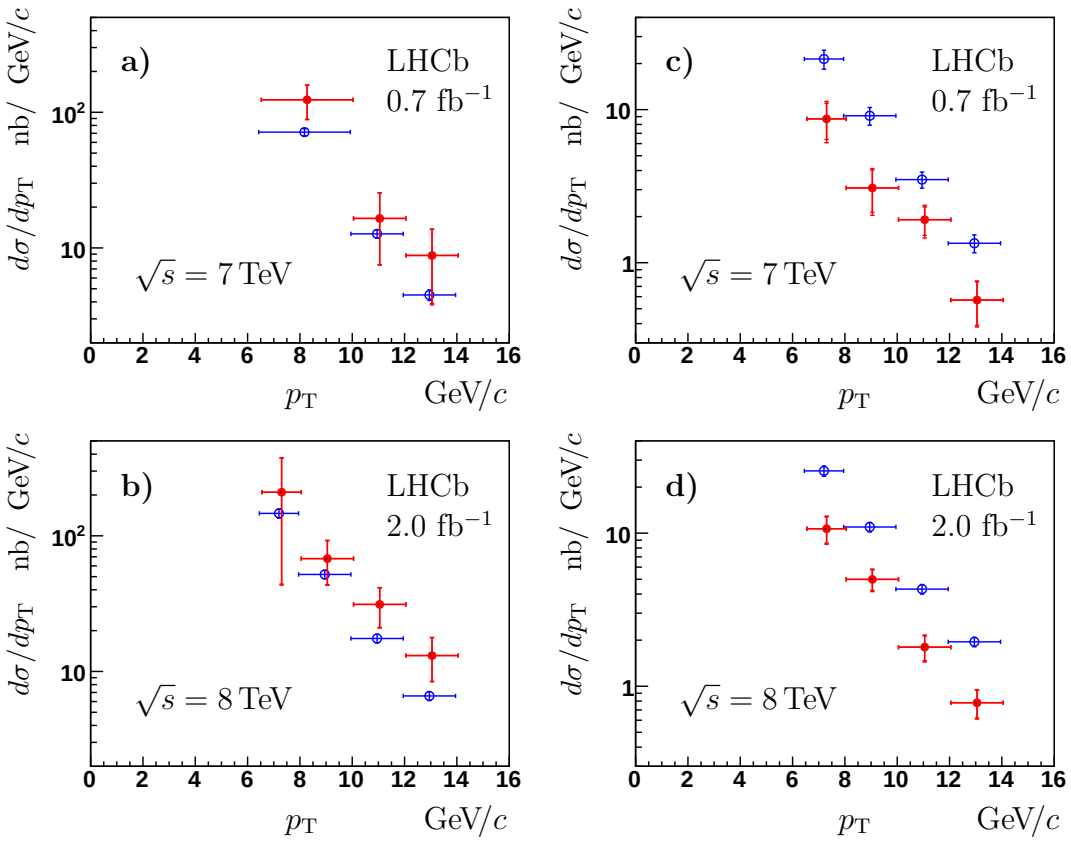

Figure 4.5: Differential cross-section for η_c meson production (empty circles) from the present analysis and J/ψ meson production (filled circles) from Refs. [7, 134, 135] as a function of transverse momentum $p_{\rm T}$. Prompt production spectra are shown on a) and b) for the data, corresponding to the centre-of-mass energy $\sqrt{s} = 7\,\text{TeV}$ and $\sqrt{s} = 8\,\text{TeV}$, respectively. The spectra, corresponding to inclusive charmonium production in b-hadron decays, are shown on c) and d) for the data, corresponding to the centre-of-mass energy $\sqrt{s} = 7\,\text{TeV}$ and $\sqrt{s} = 8\,\text{TeV}$, respectively

dependence [7, 134, 135] is also shown for reference. The $p_{\rm T}$ dependence of the η_c

and J/ψ production exhibits a similar behaviour in the studied kinematical regime, though with significantly larger η_c production uncertainties. Calculations of the NLO contribution to the cross-section are important to compare the observed p_{T} dependence to the theoretical predictions [178, 179].

4.2.4 Discussion and outlook

The prompt η_c production at $\sqrt{s} = 7\,\mathrm{TeV}$ and at $\sqrt{s} = 8\,\mathrm{TeV}$ centre-of-mass energy is measured for the first time. The relative η_c to J/ψ prompt production rate in the kinematic range $2.0 < y < 4.5$ and $p_{\mathrm{T}}(J/\psi, \eta_c) > 6.5\,\mathrm{GeV}/c$ is found to be

$$\begin{aligned}\left(\sigma_{\eta_c}/\sigma_{J/\psi}\right)_{\sqrt{s}=7\,\mathrm{TeV}} &= 1.75 \pm 0.30 \pm 0.28 \pm 0.19_{\mathcal{B}_{J/\psi\to p\overline{p},\eta_c\to p\overline{p}}}\ ,\\ \left(\sigma_{\eta_c}/\sigma_{J/\psi}\right)_{\sqrt{s}=8\,\mathrm{TeV}} &= 1.60 \pm 0.29 \pm 0.25 \pm 0.17_{\mathcal{B}_{J/\psi\to p\overline{p},\eta_c\to p\overline{p}}}\end{aligned}$$

for the data collected at $\sqrt{s} = 7\,\mathrm{TeV}$ and $\sqrt{s} = 8\,\mathrm{TeV}$, respectively. The absolute η_c prompt production cross section is determined using the J/ψ prompt production cross section in the same kinematic range to be

$$\begin{aligned}(\sigma_{\eta_c})_{\sqrt{s}=7\,\mathrm{TeV},\ 2.0<y<4.5,\ p_{\mathrm{T}}>6.5\,\mathrm{GeV}/c} &= 0.52 \pm 0.09 \pm 0.08 \pm 0.06_{\sigma_{J/\psi},\mathcal{B}_{J/\psi\to p\overline{p},\eta_c\to p\overline{p}}}\ \mu\mathrm{b}\ ,\\ (\sigma_{\eta_c})_{\sqrt{s}=8\,\mathrm{TeV},\ 2.0<y<4.5,\ p_{\mathrm{T}}>6.5\,\mathrm{GeV}/c} &= 0.59 \pm 0.11 \pm 0.09 \pm 0.06_{\sigma_{J/\psi},\mathcal{B}_{J/\psi\to p\overline{p},\eta_c\to p\overline{p}}}\ \mu\mathrm{b}\end{aligned}$$

for $\sqrt{s} = 7\,\mathrm{TeV}$ and $\sqrt{s} = 8\,\mathrm{TeV}$, respectively. The obtained cross-section of the η_c prompt production is in agreement with the colour-singlet leading order (LO) calculations, while taking into account colour-octet LO contribution predicted cross-section exceeds the observed one by two orders of magnitude [177]. However the NLO contribution is expected to significantly modify the LO result [176]. The theory-experiment comparison requires major efforts from both parts. The η_c prompt production cross section is shown on Fig. 4.6 with the statistical and systematic uncertainties, and the uncertainty associated to the $J/\psi \to p\overline{p}$ and $\eta_c \to p\overline{p}$ branching fractions and the J/ψ cross-section measurement, shown separately. Measurements at higher centre-of-mass energies, $\sqrt{s} = 13\,\mathrm{TeV}$ in 2015 and eventually full LHC energy of $\sqrt{s} = 14\,\mathrm{TeV}$, will allow to study energy dependence of the η_c prompt production.

The p_{T} dependence of the η_c and J/ψ production are found to exhibit a similar behaviour in the studied kinematical regime, though with significantly larger η_c production uncertainties. Calculations of the NLO contribution to the cross-section are important

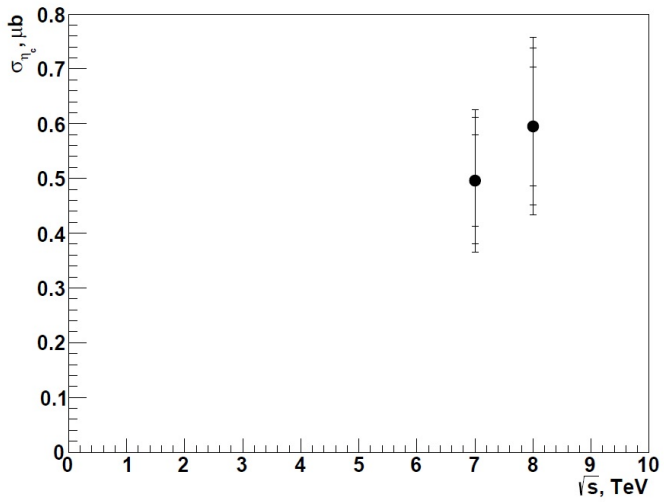

Figure 4.6: Prompt η_c production cross section as a function of collision energy. The cross section corresponds to the kinematic range $2.0 < y < 4.5$ and $p_{\rm T}(\eta_c) > 6.5\,{\rm GeV}/c$. Statistical and systematic uncertainties, and the uncertainty associated to the $J/\psi \to p\overline{p}$ and $\eta_c \to p\overline{p}$ branching fractions and the J/ψ cross-section measurement, are shown separately

to compare the observed $p_{\rm T}$ dependence to the theoretical predictions [178, 179]. The NLO calculations of the η_c production rate in the same $p_{\rm T}$ intervals are being performed by K.T. Chao *et al.* from Beijing university. Their calculations will allow the first direct comparison between the theoretical calculations and the LHCb experimental results for $p_{\rm T}$ dependence of the η_c production. A possible future improvement of the efficiency of the LHCb trigger line selecting $p\overline{p}$ combinations consistent with being produced in charmonium decays, should make it possible to extend η_c production studies to lower $p_{\rm T}$-values, and to explore heavier charmonium and charmonium-like states.

Considering other decays of the η_c meson, e.g. decays to $\phi\phi$ exploited to study charmonia production in inclusive b-decays in section 4.3.3, and possible future adjustment of the LHCb trigger lines can provide improved precision for the studies of the η_c production with the next LHCb data taking period at a centre-of-mass energy $\sqrt{s} = 13\,{\rm TeV}$.

Jacques Lefrançois proposed to study charmonium production via decays to baryon-antibaryon pairs, $\Lambda\overline{\Lambda} \to (p\pi^-)(\overline{p}\pi^+)$ or $\Xi\overline{\Xi} \to (\overline{\Lambda}\pi^+)(\Lambda\pi^-) \to ((\overline{p}\pi^+)\pi^+)((p\pi^-)\pi^-)$. The measured branching ratios for charmonia decays to $\Lambda\overline{\Lambda}$ and $\Xi\overline{\Xi}$ are similar to the

ones for the $p\overline{p}$ final state. Experimentally, reconstruction efficiency reduces because of the 4 (6) tracks in the final state, and trigger efficiencies reduce because of lower particle momenta. On the other hand, 2 or 4 secondary vertices in the event provide a clean signature that allows to strongly suppress combinatorial background. Developing challenging dedicated trigger line, optimized to efficiently capture charmonium decays to baryon-antibaryon pairs, could provide clean samples of prompt charmonia, other than having $J^{PC} = 1^{--}$ quantum numbers.

Finally, decays to hadronic final states open a possibility of studies of central exclusive production (CEP) of other charmonia than those having $J^{PC} = 1^{--}$ quantum numbers, or those decaying to them. This study has been started as an extension of the CEP measurements of the J/ψ and $\psi(2S)$ production, and requires a dedicated trigger to select low multiplicity events [6, 169].

4.3 Charmonium state inclusive production in b-hadron decays

The idea to study charmonium production from b-hadron decays using charmonia decays to hadronic final states with LHCb originated from the brainstorming discussion with Emi Kou, and further interesting discussions with Jibo He, Emi Kou and Benoit Viaud. Trigger lines and stripping of corresponding LHCb data were performed by Jibo He. This analysis became a subject of the internships of Nazar Stefanyuk, Andrii Usachov and Ph.D. thesis of Maksym Teklishyn. The results discussed in this section are preliminary LHCb results.

4.3.1 Landscape for charmonia inclusive production in b-hadron decays

Charmonium states are also produced in b-hadron decays. Experimentally, charmonium candidates from b-hadron decays are distinguished from prompt charmonia by exploiting the b-hadron finite decay time and reconstructing a b-hadron (and charmonium) decay vertex well-distinguished from the primary vertex where the b-hadron candidate was produced.

Numerous measurements of the branching fractions of exclusive B-meson decays to charmonium states, in particular J/ψ and $\psi(2S)$, have been performed. Such decays probe charmonium properties and have important implications in the CP-asymmetry studies and studies of mixing in neutral B-systems [180]. Using decays of J/ψ and $\psi(2S)$ to di-muon final state, ratios of B^0 meson exclusive decay branching fractions have been studied for $B^0 \to \psi(2S)K^{*0}$ and $B^0 \to J/\psi\, K^{*0}$, and $B^0 \to \psi(2S)\pi^+\pi^-$ and $B^0 \to J/\psi\,\pi^+\pi^-$, decay modes [181–183], ratios of B_s^0 exclusive decay branching fractions have been studied for $B_s^0 \to \psi(2S)\phi$ and $B_s^0 \to J/\psi\,\phi$, $B_s^0 \to \psi(2S)\eta$ and $B_s^0 \to J/\psi\,\eta$, and $B_s^0 \to \psi(2S)\pi^+\pi^-$ and $B_s^0 \to J/\psi\,\pi^+\pi^-$ decay modes [182, 184, 185], and ratios of the exclusive decay branching fractions for charged B^+-meson have been studied for $B^+ \to \psi(2S)K^+$ and $B^+ \to J/\psi\, K^+$ channels [181, 182, 185]. These decay modes are used or are promising to be used for systematic study of CP-asymmetry effects. Exclusive analysis of η_c and J/ψ production in b-hadron decays using the $B^+ \to K^+ p\overline{p}$

and $B^+ \to \pi^+ p\overline{p}$ decay modes has been performed by the Belle experiment [186, 187], by the BaBar experiment [188] and recently by the LHCb experiment [189]. Ratio of the branching fractions of charmonium yield using charmonium states decaying to $p\overline{p}$ have been measured for B^+ exclusive decays $B^+ \to p\overline{p}K^+$ [190]. The measurements have been performed for η_c, J/ψ and $\psi(2S)$ states, while upper limits obtained for η_c (2S) and charmonium-like X(3872) and X(3915) states.

The available results on inclusive charmonium production from b-hadron decays are limited and are shown in Table 4.2. These measurements involve different admixtures

	$B^-/\overline{B}^0$ admixture	$B^-/\overline{B}^0/\overline{B}^0_s$/$b$-baryon admixture
η_c (1S)	$< 0.9@90\%CL$	–
J/ψ (1S)	1.094 ± 0.032	1.16 ± 0.10
χ_{c0} (1P)	–	–
χ_{c1} (1P)	0.386 ± 0.027	1.4 ± 0.4
h_c(1P)	–	–
χ_{c2} (1P)	0.13 ± 0.04	–
η_c (2S)	–	–
$\psi(2S)$	0.307 ± 0.021	0.283 ± 0.029

Table 4.2: Branching fractions (in %) of the inclusive b-hadron decays into charmonium states [57]. Admixture of light B^+ and $\overline{B}^0$ mesons is shown for the measurements of the e^+e^- experiments operating at a centre-of-mass energy around $\Upsilon(4S)$resonance, while admixtures of B^-, $\overline{B}^0$, $\overline{B}^0_s$ and b-baryons are considered for measurements from experiments at LEP, Tevatron and LHC

of b-hadron species. At the time, where majority of b-physics results were coming from the experiments operating around $\Upsilon(4S)$ resonance energy, ARGUS, CLEO, Belle and BaBar, the b-hadrons studied were B^- and $\overline{B}^0$ mesons. The results from the CLEO and Belle experiments operating around $\Upsilon(5S)$ resonance energy, involved in addition $\overline{B}^0_s$ meson. At the energies of the LEP experiments, operating at Z resonance, and the Tevatron and LHC TeV scale energies, all the b-hadron species are produced, including weakly decaying B^-, $\overline{B}^0$, $\overline{B}^0_s$, B^-_c mesons and b-baryons.

The world average for charmonium branching fractions in the inclusive decays of admixture of light B-mesons is dominated by CLEO [191, 192], Belle [193] and BaBar [194] results from 2001-2003 years. While for J/ψ, $\psi(2S)$ and χ_{c1} branching

fractions these results are consistent, yielding the average of better than 10% precision, the CLEO [192] result on the χ_{c2} branching fraction is significantly smaller with respect to those by Belle [193] and BaBar [194], and PDG gives a 3σ precise average [57]. A previous study of inclusive η_c meson production in b-hadron decays by the CLEO experiment yielded the following upper limit on the combined inclusive branching fraction of B^- and $\overline{B}^0$ meson decays into final states containing an η_c meson, $\mathcal{B}(B^-, \overline{B}^0 \to \eta_c X) < 9 \times 10^{-3}$ at the 90% confidence level [195].

The world average for the branching fraction of the J/ψ and $\psi(2S)$ inclusive production in b-hadron decays, where all the b-species are involved, are known at a 10% level, with the results dominated by the measurements at LEP [196–198]. The ratio of $\psi(2S)$ and J/ψ yields has been measured at the LHC, by the LHCb and CMS experiments, to a 5% level [136, 150]. However, the only PDG result for the χ_c family, χ_{c1} inclusive production in the b-hadron decays, is a 3.5σ value, averaging DELPHI and L3 measurements [196, 197]. This reflects a difficulty to reconstruct low-energy photons in the high multiplicity events, and in particular in a hadron machine environment.

While experimentally the reconstruction of charmonium from inclusive b-hadron decays allows to drastically reduce combinatorial background with respect to reconstruction of promptly produced charmonium candidates, theoretically inclusive b-hadron decays to charmonium are less clean, and in particular require delicate NLO calculations of the singlet contribution. The QCD predictions are based on the Fixed-Order-Next-to-Leading-Log (FONLL) formalism [4, 199], which combines a Fixed-Order calculation with an all-order resummation of Leading and Next-to-Leading logarithms. In order to explain experimental data, the authors of Ref. [200] included colour octet contribution in the calculations of inclusive b-hadron decays into charmonium. The measurement of the momentum dependence in the $b \to J/\psi X$ decays by BaBar [194] showed clear octet matrix elements contribution qualitatively consistent with the theoretical description in Ref. [201]. The remaining difference of the observed J/ψ spectrum with respect to that from Ref. [201] can be attributed to contributions from intermediate charmonium-like XYZ particles [202].

While the branching fraction of b-hadron inclusive decays into J/ψ [57] is in a reasonable agreement with theoretical calculations, taking into account the large theoretical uncertainties, the experimental upper limit on the branching fraction of b-hadron inclusive decays into η_c [57] is below numerous predictions [200, 203–205].

In the following, the inclusive b-hadron decays, studied by the LHCb experiment, are addressed. First, using decays to $p\bar{p}$, the ratio of branching fractions for inclusive b-hadron decays to η_c and J/ψ is measured in section 4.3.2. Thus, the branching fraction of the inclusive b-hadron decays to η_c mesons is precisely determined and can be used as a reference in the measurements exploiting charmonia decays to $\phi\phi$. Then, using charmonia decays to $\phi\phi$, ratios of inclusive yields within η_c and χ_c families are obtained in section 4.3.3. Decays of 1^{--} state to two vector mesons are forbidden, so that J/ψ, $\psi(2S)$ and $\psi(3770)$ states cannot be accessed. Two narrow ϕ peaks and four charged kaons in the final state provide a clean signature, so that branching fractions down to a few $\times 10^{-4}$ can be probed for other charmonia. Finally, production dependence on the transverse momentum is mentioned in section 4.3.4 and mass and width of the $\eta_c(1S)$ meson are determined in section 4.4.

4.3.2 Production studies using charmonia decays to $p\bar{p}$

Using an integrated luminosity of $\int \mathcal{L}dt \approx 0.7$ fb^{-1} accumulated at a centre-of-mass energy $\sqrt{s} = 7$ TeV in 2011 and an integrated luminosity of $\int \mathcal{L}dt \approx 2.0$ fb^{-1} accumulated at a centre-of-mass energy $\sqrt{s} = 8$ TeV in 2012, and powerful charged hadron identification capabilities, the LHCb experiment measures inclusive branching fraction of the η_c meson in b-hadron decays with respect to the J/ψ meson inclusive production.

Selection of charmonium candidates from b-hadron decays is similar to that for prompt production sample, described in section 4.2.2, and profits in addition from a charmonium decay vertex well-distinguished from the corresponding primary vertex.

Signal parametrization is identical to that, described in section 4.2.2, and delivers detector resolution, mass and width measurements to the prompt production fit. The combinatorial background is parametrized by an exponential function in the fit of the sample from b-decays.

The $p\bar{p}$ invariant mass spectrum for charmonium candidates from b-hadron decays shows good agreement between the data accumulated at a center-of-mass energy of 7 TeV and 8 TeV for the η_c and J/ψ signal shapes, as well as for the background description. The two data samples are therefore combined and the corresponding $p\bar{p}$ invariant mass spectrum is shown in Fig. 4.7 with fit overlaid. The dashed red line corresponding

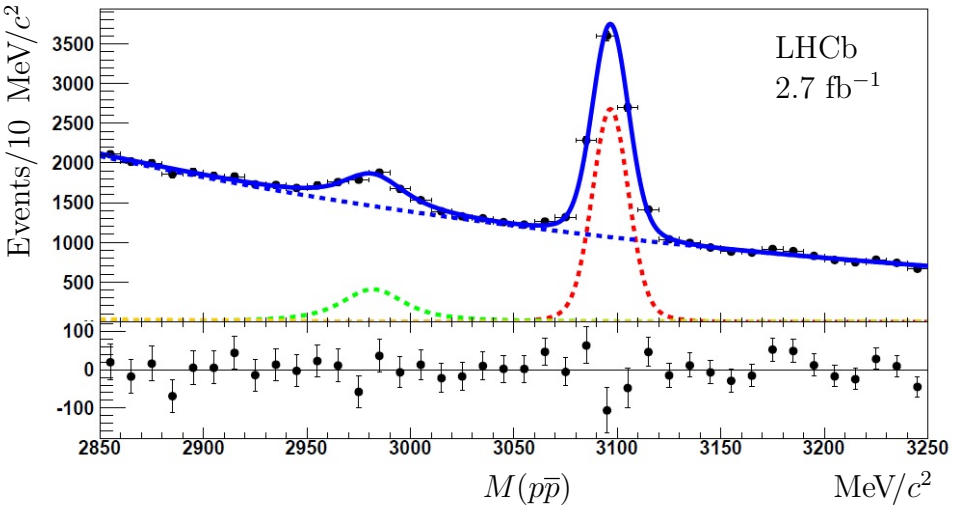

Figure 4.7: Proton-antiproton invariant mass spectrum for candidates coming from a secondary vertex. The solid blue line represents the best-fit curve, the dashed red line corresponds to double-Gaussian function for the J/ψ signal, the dashed green line corresponds to the double-Gaussian function convoluted with a Breit-Wigner function for the η_c signal, the dashed yellow line corresponds to the $J/\psi \to p\bar{p}\pi^0$ spectrum with non-reconstructed pion. The data accumulated at a centre-of-mass energy of 7 TeV and 8 TeV are combined

to the J/ψ signal is described using a double-Gaussian function. The dashed green line corresponds to the η_c signal and is described using a double-Gaussian function, convoluted with a relativistic Breit-Wigner function. The background component, comprising the contribution from the $J/\psi \to p\bar{p}\pi^0$ decay with the pion not reconstructed is described by the dashed yellow line. The unbinned likelihood fit yields 2020 ± 230 and 6110 ± 116 candidates in the η_c and J/ψ peaks respectively. These numbers have then been corrected for the cross-talk effect.

Systematic uncertainties are estimated in a similar way as in section 4.2.2. The total systematic uncertainty is dominated by the fit range variation for the measurement of inclusive charmonium production in b-hadron decays.

The yield ratio for charmonium production in b-hadron decays is obtained as

$$N^S_{\eta_c}/N^S_{J/\psi} = 0.302 \pm 0.039 \pm 0.015 \ .$$

By correcting it with the ratio of branching fractions [57], $\mathcal{B}_{J/\psi\to p\bar{p}}/\mathcal{B}_{\eta_c\to p\bar{p}} = 1.40 \pm 0.15$, the ratio of the η_c and J/ψ inclusive branching fractions from b-hadron decays, for

charmonium transverse momentum $p_{\rm T} > 6.5\,{\rm GeV}/c$ is written as

$$\mathcal{B}_{b\to\eta_c X}/\mathcal{B}_{b\to J/\psi X} = 0.424 \pm 0.055 \pm 0.021 \pm 0.045_{\mathcal{B}_{J/\psi\to p\overline{p},\eta_c\to p\overline{p}}} \ ,$$

where the third uncertainty is due to the uncertainty on the $J/\psi \to p\overline{p}$ and $\eta_c \to p\overline{p}$ branching fractions [57]. Assuming that the $p_{\rm T}(\eta_c, J/\psi) > 6.5\,{\rm GeV}/c$ requirement does not bias the distribution of charmonium momentum in the b-hadron rest frame, and using the branching fraction of b-hadron inclusive decays into J/ψ mesons from Ref. [57] $\mathcal{B}(b \to J/\psi X) = (1.16 \pm 0.10)\%$, the inclusive branching fraction of η_c from b-hadron decays is derived as

$$\mathcal{B}(b \to \eta_c X) = (4.92 \pm 0.64 \pm 0.25 \pm 0.67_{\mathcal{B}(J/\psi\to p\overline{p},\eta_c\to p\overline{p}),\mathcal{B}(b\to J/\psi X)}) \times 10^{-3} \ ,$$

where the third uncertainty component includes also the uncertainty on the J/ψ inclusive branching fraction from b-hadron decays. This is the first measurement of the inclusive branching fraction of b-hadrons into a η_c meson. It is consistent with a previous 90% confidence level upper limit restricted to B^- and $\overline{B}^0$ decays, $\mathcal{B}(B^-, \overline{B}^0 \to \eta_c X) < 9 \times 10^{-3}$ at the 90% confidence level [195]. A direct determination of the ratio $\mathcal{B}(J/\psi \to p\overline{p})/\mathcal{B}(\eta_c \to p\overline{p})$, which may be accessible by the BES experiment, can significantly reduce the systematic uncertainty of the result.

4.3.3 Production studies using charmonia decays to $\phi\phi$

Studies of charmonia inclusive production in b-hadron decays using charmonia decays to $\phi\phi$ have been performed with the LHCb experiment.

Similar to production studies using charmonia decays to $p\overline{p}$ in section 4.3.2, relative inclusive yields are determined. The precisely measured production of $\eta_c(1S)$ state in inclusive b-hadron decays is often chosen as a reference, allowing partial cancellation of systematic uncertainties. Also relative inclusive yield in the χ_c family is determined to compare to theoretical predictions.

This analysis is based on the pp collision data recorded by the LHCb experiment at $\sqrt{s} = 7\,{\rm TeV}$ in 2011 and at $\sqrt{s} = 8\,{\rm TeV}$ in 2012. The data correspond to an integrated luminosity $\int \mathcal{L}dt \approx 1.0\ {\rm fb}^{-1}$ accumulated in 2011 and an integrated luminosity of $\int \mathcal{L}dt \approx 2.2\ {\rm fb}^{-1}$ accumulated in 2012.

Kaon candidates were required to have a good track fit quality $\chi^2/\text{ndf} < 4$, be positively identified against charged pion hypothesis $\text{DLL}_{K\pi} > 5$, and have transverse momentum larger than 0.5 GeV/c. The ϕ candidates are reconstructed from oppositely charged particles identified as kaons by the LHCb detector. Two ϕ mesons system was considered as a charmonium candidate if forming a good vertex quality $\chi^2 < 16$. In order to suppress combinatorial background associated with primary vertex particles, charmonium candidates from inclusive b-hadron decays are required to form a vertex well distinguished from the corresponding primary vertex, with a significant distance between the two vertices $\chi^2 > 100$.

A relative production of states A and B in the inclusive b-hadron decays is calculated from the ratio of observed event yields, efficiency ratio and ratio of branching fractions of A or B decays to $\phi\phi$,

$$\frac{\mathcal{B}(b \to AX) \times \mathcal{B}(A \to \phi\phi)}{\mathcal{B}(b \to BX) \times \mathcal{B}(B \to \phi\phi)} = \frac{N_A}{N_B} \times \frac{\varepsilon_B}{\varepsilon_A} \,, \tag{4.1}$$

where $\varepsilon_{A,B}$ are the corresponding efficiencies. For the states with similar kinematics, for example for the ratio of the production of χ_c states, efficincies are similar, and their ratio is close to 1.

In a similar way, the ratio between the η_c and J/ψ inclusive production in b-hadron decays, using their decays to $p\overline{p}$,

$$\frac{\mathcal{B}(b \to \eta_c X) \times \mathcal{B}(\eta_c \to p\overline{p})}{\mathcal{B}(b \to J/\psi\, X) \times \mathcal{B}(J/\psi \to p\overline{p})} = \frac{N_{\eta_c}}{N_{J/\psi}} \times \frac{\varepsilon_{J/\psi}}{\varepsilon_{\eta_c}} \,, \tag{4.2}$$

where ε_{η_c} and $\varepsilon_{J/\psi}$ have similar values, and N_{η_c} and $N_{J/\psi}$ are the η_c and J/ψ event yields, was discussed in section 4.3.2.

In order to extract a pure $\phi\phi$ component, the two-dimensional unbinned maximum likelihood fit corresponding to the two K^+K^- combinations, in the bins of the $K^+K^-K^+K^-$ invariant mass, was performed. The two-dimensional fit accounts for the $\phi\phi$, ϕK^+K^- and $K^+K^-K^+K^-$ components, taking into account also the phase space factor. In the 2D fit of the K^+K^- invariant masses, ϕ signal is described by the convolution of the Breit-Wigner function to describe natural width of the ϕ resonance, and Gaussian function to describe the detector resolution. Combinatorial background is described by the first order polynomial. A threshold factor to describe phase space difference is introduced in both signal and combinatorial background shapes. The

two-dimensional fit function as well as the projections on the two axes, for the complete event sample is shown on Fig. 4.8. The obtained sample contains two-ϕ combinations,

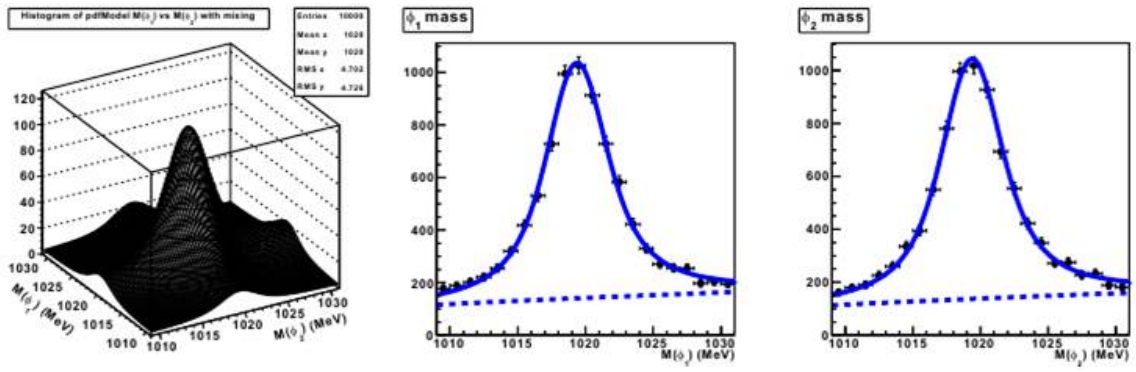

Figure 4.8: A 2D fit to extract pure $\phi\phi$ combinations (left) and fit projections on the two ϕ candidate planes (center and right)

that are either random combinations or originate from the decay of mother particles.

The invariant mass distribution of the $\phi\phi$ candidates is fit to the sum of the signal shapes for all the known charmonium and charmonium-like states with the mass in the range of the histogram, and the background shape. The η_c family, η_c (1S) and η_c (2S), and χ_c family, χ_{c0}, χ_{c1} and χ_{c2}, as well as charmonium-like $X(3872)$ and $X(3915)$ states are taken into account in the fit. These states are parametrized by the convolution of Breit-Wigner function to describe natural width of the ϕ resonance, and Gaussian function to describe the effects of detector resolution. Masses of all the described states, heavier than χ_{c2}, are related between them, so that a single mass value, $M_{\chi_{c2}}$, was left free parameter in the fit. Natural width of the χ_c states were fixed to their known values [57]. Gaussian constraints were applied on the mass and natural width parameters of the η_c (2S) meson, using the average values from Ref. [57], $M_{\eta_c(2S)} = 3639.4 \pm 1.3\,\mathrm{MeV}/c^2$ and $\Gamma_{\eta_c(2S)} = 11.3^{+3.2}_{-2.9}\,\mathrm{MeV}$. The detector resolution is a free parameter of the fit in the η_c (1S) signal shape description, and is scaled according to energy release for higher mass states. The combinatorial background is described by a first order polynomial, multiplied with an exponential function. Threshold factor to describe phase space difference is also introduced.

Fig. 4.9 shows the fit to the spectrum of invariant mass of the $\phi\phi$ combinations, for combined data sample, accumulated at $\sqrt{s} = 7\,\mathrm{TeV}$ and $\sqrt{s} = 8\,\mathrm{TeV}$, and corresponding to an integrated luminosity 3 fb^{-1}. Signals from η_c (1S), χ_{c0}, χ_{c1}, χ_{c2} and η_c (2S)

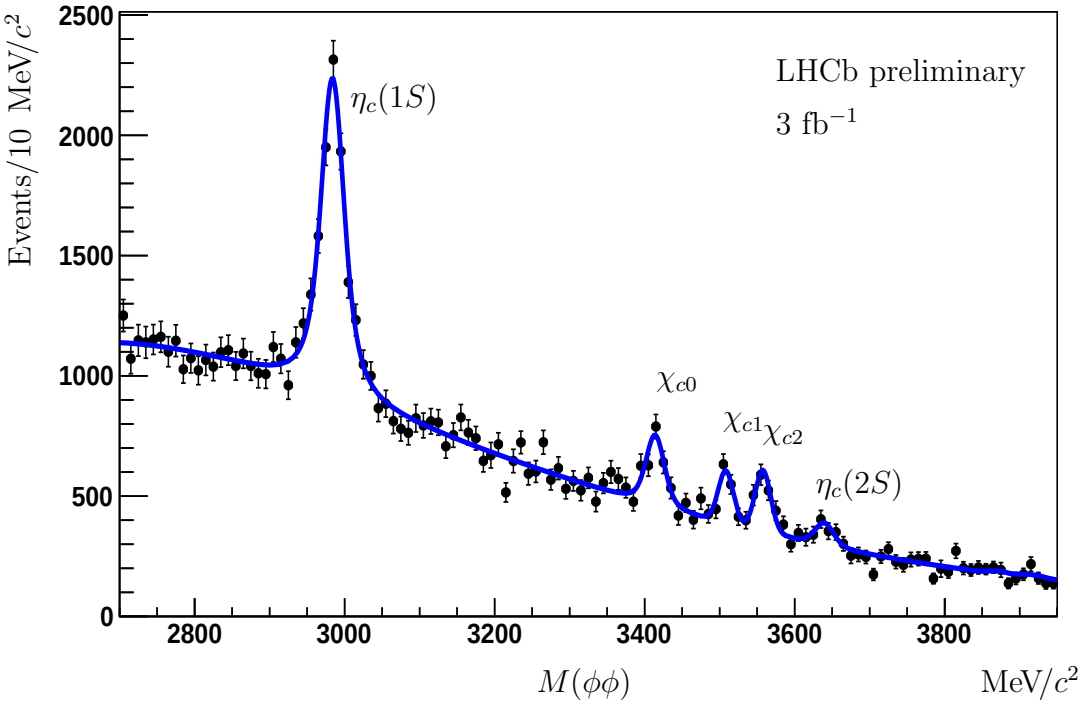

Figure 4.9: Distribution of the $\phi\phi$ invariant mass for combined data sample, accumulated at $\sqrt{s} = 7\,\text{TeV}$ and $\sqrt{s} = 8\,\text{TeV}$. The number of candidates in each bin comes from the 2D fit, as decribed in the text. Masses of the $c\bar{c}$ resonances decaying to $\phi\phi$ are indicated on the plot. The results of the fit are shown in Table 4.3

decays into $\phi\phi$ are clearly visible. The results of the fit are summarized in Table 4.3. Numbers of signal candidates are consistent between the data samples collected at a

Resonance	Event yield
η_c (1S)	6810 ± 175
χ_{c0} (1P)	1059 ± 66
χ_{c1} (1P)	560 ± 50
χ_{c2} (1P)	696 ± 48
η_c (2S)	343 ± 73

Table 4.3: Results of the fit to the spectrum of the $\phi\phi$ invariant mass

centre-of-mass energy of $\sqrt{s} = 7\,\text{TeV}$ and $\sqrt{s} = 8\,\text{TeV}$, and with the combined data sample.

The observed decays of the η_c and χ_c family into $\phi\phi$ common final states allowed to obtain relative inclusive inclusive yield of these charmonia from b-hadron decays.

Assuming negligible difference in the trigger, reconstruction and selection efficiency for decays of the χ_c states into $\phi\phi$, relative yields of the χ_c states in b-hadron inclusive decays are derived as

$$\frac{\mathcal{B}(b \to \chi_{c1}X) \times \mathcal{B}(\chi_{c1} \to \phi\phi)}{\mathcal{B}(b \to \chi_{c0}X) \times \mathcal{B}(\chi_{c0} \to \phi\phi)} = 0.53 \pm 0.06 \pm 0.02 \ ,$$
$$\frac{\mathcal{B}(b \to \chi_{c2}X) \times \mathcal{B}(\chi_{c2} \to \phi\phi)}{\mathcal{B}(b \to \chi_{c0}X) \times \mathcal{B}(\chi_{c0} \to \phi\phi)} = 0.66 \pm 0.06 \pm 0.05 \ .$$

The systematic uncertainty comprises contributions from background shape description and uncertainty of the natural width values in Ref. [57]. The systematic uncertainty is smaller than the statistical one, so that precision will improve with more data accumulated by LHCb.

Using branching fractions of the χ_c decays to $\phi\phi$ from Ref. [57], relative branching fractions of b-hadron decays to χ_c states can be derived as

$$\frac{\mathcal{B}(b \to \chi_{c1}X)}{\mathcal{B}(b \to \chi_{c0}X)} = 0.95 \pm 0.10 \pm 0.17 \ ,$$
$$\frac{\mathcal{B}(b \to \chi_{c2}X)}{\mathcal{B}(b \to \chi_{c0}X)} = 0.45 \pm 0.04 \pm 0.07 \ ,$$

where systematic uncertainty is dominated by the uncertainty of the branching fractions $\mathcal{B}(\chi_c \to \phi\phi)$.

This is the first or most precise determination of the χ_c relative yields in b-hadron decays. These results are in agreement with the PDG average values [57] for the B^0/B^+ branching fractions into χ_{c1} and χ_{c2} mesons measured by CLEO [191, 192], Belle [193] and BaBar [194] experiments. However, the average value for the branching fraction $\mathcal{B}(B \to \chi_{c2}X) = (1.3 \pm 0.4) \times 10^{-3}$ [57] has limited precision and is different from zero by a three standard deviations. This is a result of a descrepancy between the results of the Belle [193] and BaBar [194] experiments on one side and the CLEO result [192] on the other side (Fig. 4.10), which calls for another measurement.

To derive absolute values of the χ_c yields from b-hadron decays, the result of the η_c inclusive yield using decay to $p\overline{p}$ in section 4.3.2 was used. Taking into account the difference in trigger, reconstruction and selection efficiencies for η_c and χ_c mesons,

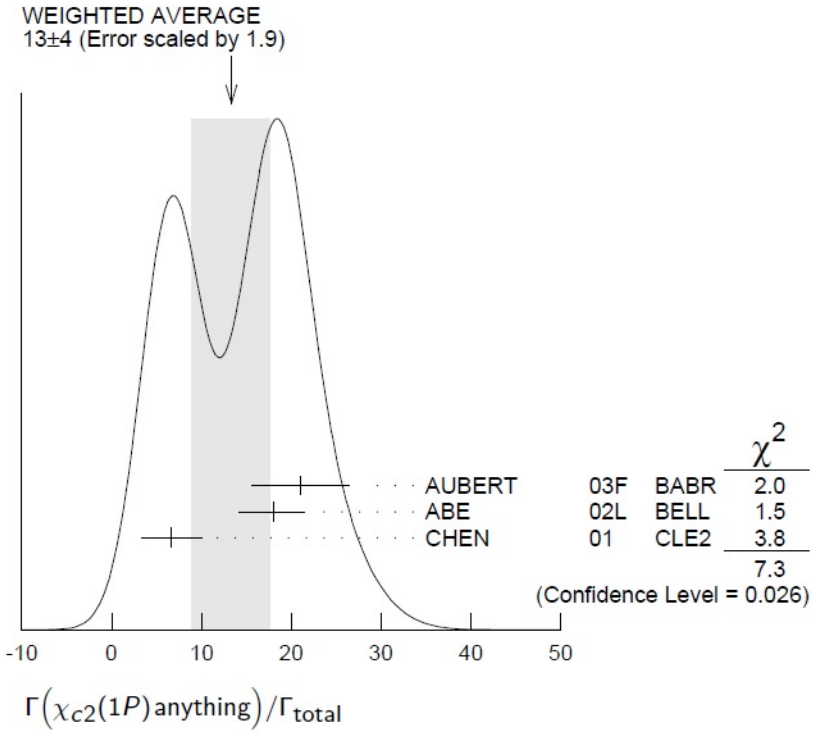

Figure 4.10: Measurements of the branching fraction of B^0/B^+ decays into χ_{c2} meson [57]

$\varepsilon_{\chi_c}/\varepsilon_{\eta_c} \approx 1.03$, the yield ratios relative to the η_c yield were constructed as

$$\frac{\mathcal{B}(b \to \chi_{c0}X) \times \mathcal{B}(\chi_{c0} \to \phi\phi)}{\mathcal{B}(b \to \eta_c X) \times \mathcal{B}(\eta_c \to \phi\phi)} = 0.151 \pm 0.010 \pm 0.005 \ ,$$
$$\frac{\mathcal{B}(b \to \chi_{c1}X) \times \mathcal{B}(\chi_{c1} \to \phi\phi)}{\mathcal{B}(b \to \eta_c X) \times \mathcal{B}(\eta_c \to \phi\phi)} = 0.080 \pm 0.007 \pm 0.002 \ ,$$
$$\frac{\mathcal{B}(b \to \chi_{c2}X) \times \mathcal{B}(\chi_{c2} \to \phi\phi)}{\mathcal{B}(b \to \eta_c X) \times \mathcal{B}(\eta_c \to \phi\phi)} = 0.099 \pm 0.007 \pm 0.003 \ .$$

Using branching fractions of the η_c and χ_c decays to $\phi\phi$ from Ref. [57], relative branching fractions of b-hadron decays to χ_c states can be derived as

$$\frac{\mathcal{B}(b \to \chi_{c0}X)}{\mathcal{B}(b \to \eta_c X)} = 0.336 \pm 0.023 \pm 0.052 \ ,$$
$$\frac{\mathcal{B}(b \to \chi_{c1}X)}{\mathcal{B}(b \to \eta_c X)} = 0.319 \pm 0.030 \pm 0.057 \ ,$$
$$\frac{\mathcal{B}(b \to \chi_{c2}X)}{\mathcal{B}(b \to \eta_c X)} = 0.151 \pm 0.011 \pm 0.022 \ ,$$

where systematic uncertainty is dominated by the uncertainty of the branching fractions $\mathcal{B}(\eta_c, \chi_c \to \phi\phi)$.

With the branching fraction of η_c production in b-hadron decays $\mathcal{B}(b \to \eta_c X) = (4.92 \pm 0.96) \times 10^{-3}$ (section 4.3.2), the absolute branching fractions of χ_c production in b-hadron decays are obtained as

$$\mathcal{B}(b \to \chi_{c0} X) = (1.66 \pm 0.11 \pm 0.41) \times 10^{-3} ,$$
$$\mathcal{B}(b \to \chi_{c1} X) = (1.57 \pm 0.15 \pm 0.42) \times 10^{-3} ,$$
$$\mathcal{B}(b \to \chi_{c2} X) = (0.74 \pm 0.05 \pm 0.18) \times 10^{-3} ,$$

where systematic uncertainty is dominated by the uncertainty of the branching fraction of the b-hadron decays to η_c meson $\mathcal{B}(b \to \eta_c X)$.

The branching fraction of b-hadron decays into χ_{c0} is measured for the first time, and is above the values predicted in Ref. [200].

The result for b-decays into χ_{c1} is the most precise measurement for the admixture of B^0, B^+, B_s^0 and b-baryons. Central value of the result for b-decays into χ_{c1} is lower than the value measured by DELPHI [196] and L3 [197] experiments at LEP, however, taking into account the LEP results limited precision, the LHCb result is consistent with them. The obtained value is lower than the branching fraction of b-decays into χ_{c1} measured by CLEO [191], Belle [193] and BaBar [194] using the admixture of B^0 and B^+. Finally, the LHCb result for b-decays into χ_{c1} is consistent with the prediction in Ref. [200].

The branching fraction of b-hadron decays into χ_{c2} is measured for the first time with the B^0, B^+, B_s^0 and b-baryons admixture. The result is consistent with the average, corresponding to the B^0, B^+ admixture, from Ref. [57], given large PDG uncertainty. The obtained value has higher precision than the results from CLEO [192], Belle [193] and BaBar [194], is close to the CLEO result of $(0.67 \pm 0.34 \pm 0.03) \times 10^{-3}$ and is different by more than 2σ from the results of Belle, $(1.80^{+0.23}_{-0.28} \pm 0.26) \times 10^{-3}$, and BaBar, $(2.10 \pm 0.45 \pm 0.31) \times 10^{-3}$. The obtained value is below the range predicted in Ref. [200].

It should be mentioned, that the measured branching fractions of b-hadron decays to charmonia comprise also decays via intermediate higher-mass charmonium resonance, contrary to the theory calculations, which consider only direct b-hadron to the considered charmonium state transitions.

Another goal was to quantify the observed signal of 343 ± 73 η_c (2S) meson candidates in b-hadron inclusive decays. Taking into account the difference in trigger, reconstruction

and selection efficiencies for η_c (1S) and η_c (2S) mesons, $\varepsilon_{\eta_c(2S)}/\varepsilon_{\eta_c(1S)} \approx 1.03$, the yield ratio relative to the η_c (1S) yield was constructed as

$$\frac{\mathcal{B}(b \to \eta_c(2S)X) \times \mathcal{B}(\eta_c(2S) \to \phi\phi)}{\mathcal{B}(b \to \eta_c(1S)X) \times \mathcal{B}(\eta_c(1S) \to \phi\phi)} = 0.049 \pm 0.010 \pm 0.007 \ ,$$

where systematic uncertainty is dominated by the background description. Since the decay of η_c (2S) meson to $\phi\phi$ has not been observed neither, the product of the branching fraction of b-hadron decays to η_c (2S) and the branching fraction of the $\eta_c(2S) \to \phi\phi$ decay mode, can only be determined. Using $\mathcal{B}(b \to \eta_c(1S)X) = (4.92 \pm 0.96) \times 10^{-3}$ obtained in section 4.3.2, and $\mathcal{B}(\eta_c(1S) \to \phi\phi) = (1.76 \pm 0.20) \times 10^{-3}$ from Ref. [57], the result is derived as

$$\mathcal{B}(b \to \eta_c(2S)X) \times \mathcal{B}(\eta_c(2S) \to \phi\phi) = (4.2 \pm 0.9 \pm 1.1) \times 10^{-7} \ ,$$

where systematic uncertainty is dominated by the uncertainty of the η_c production in b-decays. This is the first indication of the $\eta_c(2S)$ production in b-decays, as well as the decay of $\eta_c(2S)$ meson to the $\phi\phi$ pair.

4.3.4 The p_{T} dependence of the η_c state production

The η_c production as a function of p_{T} is obtained by fitting the $p\overline{p}$ invariant mass spectrum in four bins of p_{T}. The J/ψ p_{T} spectrum [7, 134, 135] is used to access the η_c p_{T} spectrum. Figs. 4.5c and 4.5d show the obtained cross section dependence on the transverse momentum for the $\sqrt{s} = 7\,\mathrm{TeV}$ and $\sqrt{s} = 8\,\mathrm{TeV}$ data samples, respectively. The J/ψ cross section p_{T} dependence [7, 134, 135] is also shown for reference. The p_{T} dependence of the η_c and J/ψ production cross section exhibits a similar behaviour in the studied kinematical regime, though with significantly larger η_c production uncertainties.

4.3.5 Discussion and outlook

In this section charmonium decays to hadronic final states, $p\overline{p}$ and $\phi\phi$, are used to study charmonia inclusive production in b-hadron decays. These are the first charmonium inclusive production measurements, using charmonia decays to hadronic final state, in the high-multiplicity environment of a hadron machine.

The $p_{\rm T}$ dependence of the η_c and J/ψ production cross section exhibits a similar behaviour in the studied kinematical regime, though with significantly larger η_c production uncertainties. The NLO calculations of the η_c production rate in the same $p_{\rm T}$ intervals are being performed by K.T. Chao *et al.* from Beijing university. Their calculations will allow the first direct comparison between the theoretical calculations and the LHCb experimental results for the η_c production.

The relation of the η_c production to that of J/ψ, using their decays to the $p\overline{p}$ final states, was important to relate production of charmonia, other than having $J^{PC} = 1^{--}$ quantum numbers, and reconstructed using final states, that are forbidden for $J^{PC} = 1^{--}$ charmonia, e.g. $\phi\phi$ final state, to the now precisely determined η_c production.

Reconstructing charmonium candidates via their decays to $\phi\phi$ in b-hadron decays, signals corresponding to the η_c family and χ_c states have been observed on a low level of combinatorial background. Furthermore, using a 2D fit in bins of the $\phi\phi$ combinations invariant mass, the spectrum, containing only true $\phi\phi$ pairs, originating from heavier state decay, or random $\phi\phi$ combinations, has been extracted. From the fit to this spectrum, yield ratios of different charmonium states in b-hadron decays have been derived. This is the first or most precise determination of the production ratios for η_c and χ_c states in b-hadron decays.

It is interesting to compare the ratio of branching fractions of inclusive b-hadron decays to η_c and J/ψ measured as

$$\mathcal{B}_{b\to\eta_c X}/\mathcal{B}_{b\to J/\psi\, X} = 0.424 \pm 0.055 \pm 0.021 \pm 0.045_{\mathcal{B}_{J/\psi\to p\overline{p},\eta_c\to p\overline{p}}} \ ,$$

with the ratio of the branching fractions of the η_c and J/ψ yields using exclusive charmonia decays to $p\overline{p}$ measured for B^+ exclusive decays $B^+ \to p\overline{p}K^+$ in Ref. [190]. The ratio obtained in the exclusive analysis,

$$\frac{\mathcal{B}(B^+ \to \eta_c(1S)K^+ \to p\overline{p}K^+)}{\mathcal{B}(B^+ \to J/\psi\, K^+ \to p\overline{p}K^+)} = 0.578 \pm 0.035 \pm 0.025 \ ,$$

is translated to the ratio $\mathcal{B}(B^+ \to \eta_c(1S)K^+)/\mathcal{B}(B^+ \to J/\psi\, K^+)$, which is almost twice as large with respect to the ratio of the corresponding inclusive branching fractions.

Emi Kou proposed to compare data on the η_c and J/ψ yields from inclusive b-hadron decays to extract information on the octet matrix elements, and test matrix element universality. This analysis requires more work to interpret the measured values.

A possibility of translation of the η_c and J/ψ $p_{\rm T}$ range to the estimated momentum dependence in the b-hadron rest frame can allow better comparison with the BaBar measurement [194] of the production of these states in b-hadron decays and following theoretical speculations [200–202].

A possible future improvement of the efficiency of the involved LHCb trigger lines, should make it possible to extend η_c production studies to lower $p_{\rm T}$-values, and exploring heavier charmonium and charmonium-like states, using charmonia decays to both $p\overline{p}$ and $\phi\phi$ final states.

As an extension of the charmonium production studies using decays to $\phi\phi$, to other two-body decays, leading to final states with four charged kaons, can be addressed at LHCb. Decays to ϕf_x final states, where f_x is a resonance with defined quantum numbers decaying to K^+K^-, are interesting not only because they can increase the precision, if combined with the study using decays to $\phi\phi$, but also they can provide direct normalization to production of the states with $J^{PC} = 1^{--}$ quantum numbers [137].

The proposal of Jacques Lefrançois to reconstruct charmonia via decays to baryon-antibaryon pairs, discussed in view of prompt production measurements in section 4.2.4 is also applicable for charmonia from b-hadron decays. However b-hadron production rates multiplied by the branching fractions of the involved decays do not allow by now to observe corresponding signals.

Finally, Emi Kou proposed to compare angular dependences in the $J/\psi \to p\overline{p}$ to those in the decay $J/\psi \to \mu^+\mu^-$ in order to extract further information on the spin-selection rules breaking [206], as well as the $J/\psi \to p\overline{p}$ transition mechanism. A low-background sample of J/ψ mesons from b-hadron decays, with well-known polarizarion, will be exposed to this study.

4.4 Mass and natural width of the η_c (1S) state

4.4.1 Landscape for studies of mass and natural width of the η_c states

By the time of issueing the printed version of the PDG 2012 [57], the measurements of even the simplest parameters, mass and natural width, of the ground $c\bar{c}$ state, η_c (1S), exhibited large consistency problems. Fig. 4.11 shows the PDG fit of the η_c mass measurements available by the time of issueing of the PDG 2012 book. The majority of

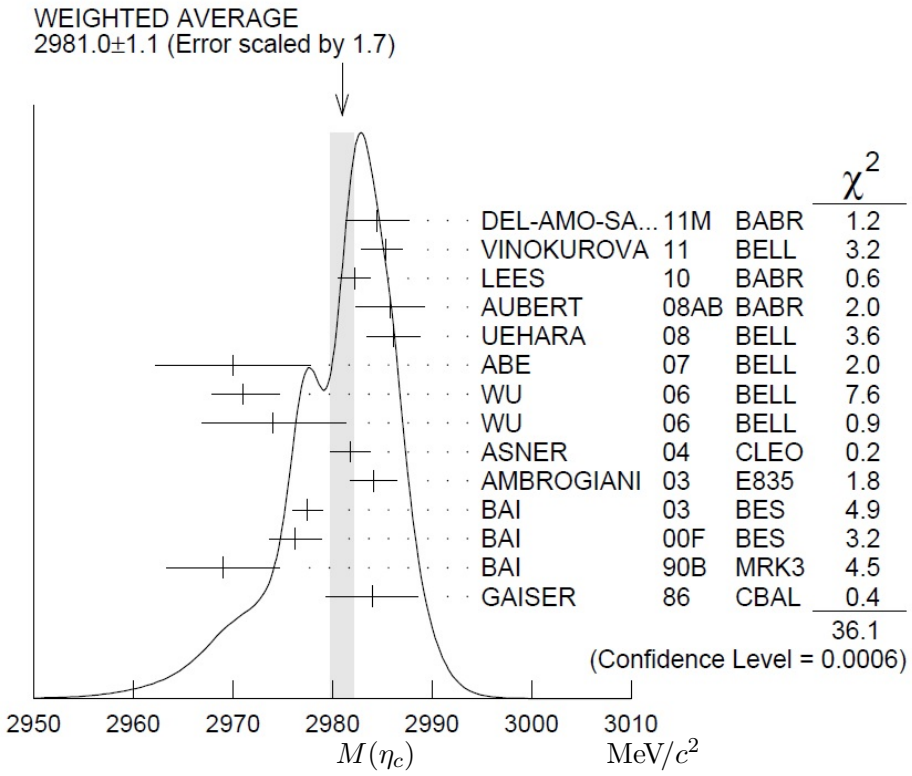

Figure 4.11: Measurements of the η_c mass from the printed version of PDG 2012 [57]. Confidence level of the fit is 0.0006

the measurements, taken into account in the fit, come from the $\gamma\gamma \to \eta_c \to hadrons$, radiative decays $J/\psi\,(\psi(2S)) \to \eta_c\gamma$, $p\overline{p} \to \eta_c \to \gamma\gamma$, and exclusive B-decays at B-factories, yielding the average of $2981.0 \pm 1.1\,\mathrm{MeV}/c^2$. The only measurement, involving η_c reconstruction via its decay to $p\overline{p}$, was performed by Belle in 2006 [207]. The analysis was based on 195 η_c candidates, and yielded a measurement with moderate accuracy and

the central value shifted with respect to the present PDG average, $2971 \pm 3^{+2}_{-1}\,\mathrm{MeV}/c^2$. In 1990 MARKIII experiment performed another measurement [208] with the technique close to the one employed in LHCb, reconstructing η_c candidates via the $K^+K^-K^+K^-$ final state, in the radiative decays of J/ψ. The MARKIII analysis was based on 80 η_c candidates, and yielded a measurement of $2969 \pm 4 \pm 4\,\mathrm{MeV}/c^2$. Finally, in 2009 CLEO observed a significant asymmetry in the lineshapes of radiative $J/\psi \to \gamma\eta_c$ and $\psi(2S) \to \gamma\eta_c$ transitions [209]. If ignored, this asymmetry could lead to significant bias whenever the mass and width are measured in J/ψ or $\psi(2S)$ radiative decays. The new precise BES results, $M_{\eta_c} = 2984.49 \pm 1.16 \pm 0.52$ [210] and $M_{\eta_c} = 2984.3 \pm 0.6 \pm 0.6$ [211], obtained using radiative decays of $\psi(2S)$, positioned the actual PDG average [57] to $2983.7 \pm 0.7\,\mathrm{MeV}/c^2$. This change of more than 2σ calls for an improving precision of the η_c mass measurement using a different technique.

Similar situation occurs with the η_c natural width determination. Fig. 4.12 shows the PDG fit of the η_c natural width measurements available by the time of issueing of the PDG 2012 book. The new BES results $M_{\eta_c} = 36.4 \pm 3.2 \pm 1.7$ [210] and

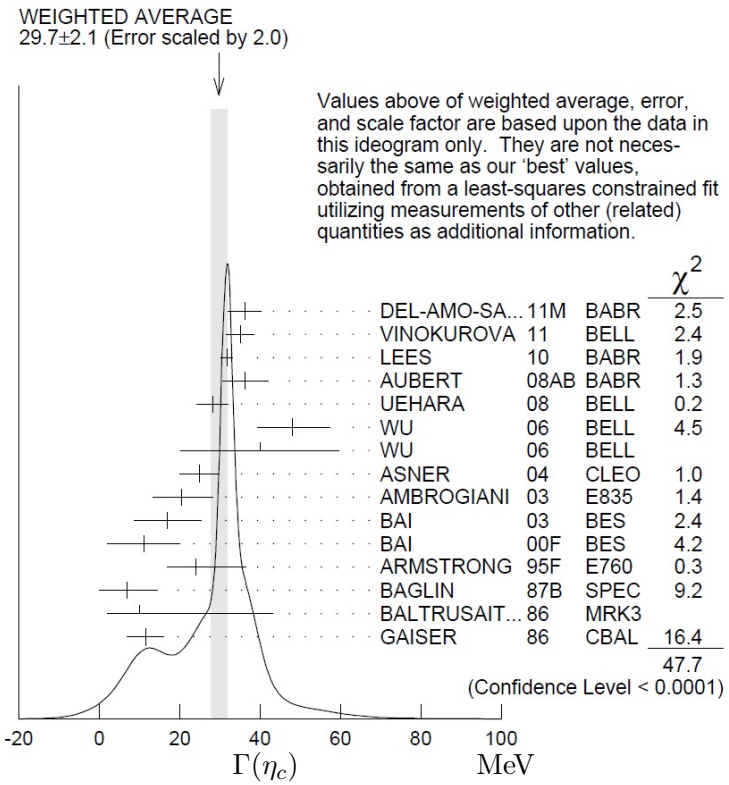

Figure 4.12: Measurements of the η_c natural width from the printed version of PDG 2012 [57]. Confidence level of the fit is less than 0.0001

$\Gamma_{\eta_c} = 32.0 \pm 1.2 \pm 1.0$ [211], obtained using radiative decays of $\psi(2S)$, shifted the actual PDG average [57] from $29.7 \pm 1.0\,\text{MeV}$ to $32.0 \pm 0.9\,\text{MeV}$.

The properties of the η_c (2S) state is by far less investigated. Measurements of CLEO [212], BaBar [213, 214], Belle [215, 216] and BES [217, 218] experiments, using $\gamma\gamma \to hadrons$, double charmonium production in e^+e^-, exclusive B-decays and radiative transitions of $\psi(2S)$, contribute to the PDG averages [57] of $3639.4 \pm 1.3\,\text{MeV}/c^2$ for the η_c (2S) mass, and $11.3^{+3.2}_{-2.9}\,\text{MeV}$ for its natural width. The recent results from BES are consistent with the previous measurements and improved the uncertainty. The comparison between the results for the η_c (2S) natural width should take into account large uncertainty from first measurements. Uncertainty for the η_c (2S) measurements are larger, and the number of delivered results is smaller, as compared to the η_c (1S) studies.

A more than 2σ difference between the recent BES results [210, 211] and earlier measurements [57] motivates the determination of the mass difference $\Delta M_{J/\psi\,,\eta_c} = M_{J/\psi} - M_{\eta_c}$ and the η_c natural width Γ_{η_c} using a different technique or final state.

4.4.2 Measurements of the $\eta_c(1S)$ mass and natural width

The LHCb experiment measured the mass difference $\Delta M_{J/\psi\,,\eta_c} = M_{J/\psi} - M_{\eta_c}$ and the η_c natural width Γ_{η_c}, using η_c and J/ψ decay to $p\overline{p}$ and $\phi\phi$ final states.

The excellent performance of the LHCb tracking system and the usage of the same final state for both J/ψ and η_c decays allows a precise measurement of the mass difference between the two mesons. In order to measure the η_c mass relative to the well-reconstructed and well-known J/ψ mass, a momentum scale calibration [219] is performed on data, and validated with the J/ψ mass measurement. The $M_{J/\psi}$ and $\Delta M_{J/\psi\,,\eta_c}$ values are extracted from the fit to the $p\overline{p}$ invariant mass in the low-background sample of charmonium candidates produced in b-hadron decays (Fig. 4.7). The J/ψ mass measurement, $M_{J/\psi} = 3096.66 \pm 0.19 \pm 0.02\ \text{MeV}/c^2$, agrees well with the average from Ref. [57]. The $\Delta M_{J/\psi\,,\eta_c}$ measurement,

$$\Delta M_{J/\psi\,,\eta_c} = 114.7 \pm 1.5 \pm 0.1\ \text{MeV}/c^2\ ,$$

is dominated by the statistical uncertainty. The systematic uncertainty is dominated by the $J/\psi \to p\overline{p}\pi^0$ reflection description. The mass difference also agrees with the

average from Ref. [57]. Its precision improves upon that of the measurements in e^+e^- collisions at the $\Upsilon(4S)$ resonance and provides an independent check of the recent BES results [210, 211]. In addition, the η_c natural width is obtained from the fit to the $p\bar{p}$ invariant mass (Fig. 4.7) to be $\Gamma_{\eta_c} = 25.8 \pm 5.2 \pm 1.9\,\text{MeV}$. The systematic uncertainty is significantly smaller than the statistical one, and is dominated by the detector resolution. The obtained Γ_{η_c} value is in a good agreement with the average from Ref. [57]. However it is less precise than previous measurements. Fig. 4.13 shows the Γ_{η_c}, $\Delta M_{J/\psi,\eta_c}$ contour plot, obtained from the analysis of b-hadron decays into η_c

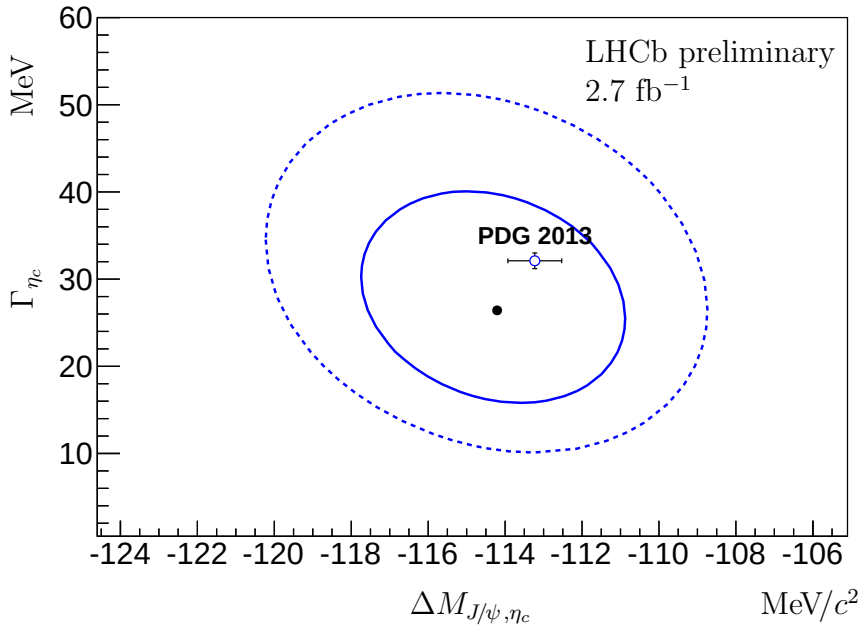

Figure 4.13: Contour plot of Γ_{η_c} and $\Delta M_{J/\psi,\eta_c}$ using $\eta_c \to p\bar{p}$ decay for the combined data sample. The two curves indicate 68.3 C.L. (one-sigma) and 95.5 C.L. (two-sigma) contours. Only statistical uncertainties are shown. The PDG [57] value is indicated as a point with error bars

meson, where the η_c candidates are reconstructed in the $\eta_c \to p\bar{p}$ decay. The $\sqrt{s} = 7\,\text{TeV}$ and $\sqrt{s} = 8\,\text{TeV}$ results are consistent with each other, so that contour plot for combined data sample is shown. The results are consistent with the PDG values [57].

Similar measurements were performed using the η_c mesons reconstructed in the $\eta_c \to \phi\phi$ decay mode, using 5×10^3 η_c candidates in the signal peak (section 4.3.3). Momentum scale calibration was also performed on the data sample. The η_c mass was

measured to be

$$M_{\eta_c} = 2984.0 \pm 0.5 \pm 0.2 \text{ MeV}/c^2 \ .$$

The precision of the result is dominated by the statistical uncertainty, while background shape parameterization uncertainty yields a dominant contribution to the systematic uncertainty. This measurement is consistent with the LHCb result from the η_c production analysis using $\eta_c \to p\overline{p}$ decays, with the recent BES results [210, 211], with the average value in Ref. [57], and has a precision comparable to that of the average in Ref. [57]. Fig. 4.14 shows the Γ_{η_c}, M_{η_c} contour plot, obtained from the analysis of b-hadron decays into η_c meson, where the η_c candidates are reconstructed via the $\eta_c \to \phi\phi$ decay, for the combined data sample. Measurements of the η_c mass using η_c meson decays to $p\overline{p}$

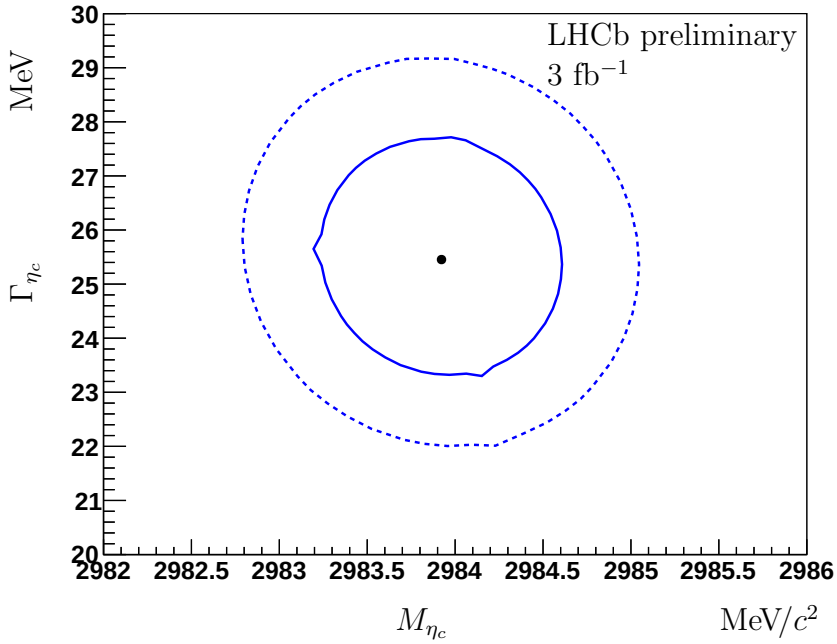

Figure 4.14: Contour plots of Γ_{η_c} and M_{η_c} using $\eta_c \to \phi\phi$ decay for the combined data sample. The two curves indicate 68.3 C.L. (one-sigma) and 95.5 C.L. (two-sigma) contours. Only statistical uncertainties are shown. The PDG [57] value is indicated as a point with error bars

and decays to $\phi\phi$, are consistent with each other and with the PDG average [57].

4.4.3 Discussion and outlook

Using low-level background samples of charmonia candidates produced in inclusive b-hadron decays, and a momentum scale calibration [219] performed on data, mass and natural width of the η_c (1S) state have been measured using decays to $p\overline{p}$ and to $\phi\phi$ final states. These measurements used another method, compared to the most precise to date recent results of the BES experiment [210, 211], and provided an important consistency check.

Measurements of the η_c mass and natural width using η_c meson decays to $p\overline{p}$ and decays to $\phi\phi$, are consistent with each other and with the PDG average [57]. Precision of the η_c mass measurement using $\eta_c \to p\overline{p}$ decays improves upon that of the measurements in e^+e^- collisions at the $\Upsilon(4S)$ resonance and is compatible to the BES results. The η_c mass measurement using $\eta_c \to \phi\phi$ decays is the most precise η_c mass determination with the precision exceeding that quoted in Ref. [57].

The difference between the masses in η_c family, $\eta_c(2S)$ and $\eta_c(1S)$, and in χ_c family, will be studied using larger event samples expected from the operation in 2015.

Chapter 5

Decays of B_s^0 to ϕ mesons

Throwing pebbles into the water, look at the ripples
they form on the surface.
Otherwise this activity will be an empty amusement.

Kozma Prutkov

The analysis of B_s^0 decays to ϕ mesons historically appeared as an extention of the analysis of charmonium production using charmonia decays to $\phi\phi$ (section 4.3.3). Clean B_s^0 signal is observed in the $\phi\phi$ invariant mass spectrum, and corresponds to $B_s^0 \to \phi\phi$ decays. Simulteneous reconstruction of B_s^0 and η_c mesons in the same decay mode to $\phi\phi$ (sections 5.1.2 and 4.3.3) allows determination of the $B_s^0 \to \phi\phi$ branching fraction (section 5.1.3). In addition, decays of B_s^0 meson to three ϕ mesons, $B_s^0 \to \phi\phi\phi$, were observed (section 5.2.2), and branching fraction of the $B_s^0 \to \phi\phi\phi$ transition was derived (section 5.2.3). This decay can proceed via intermediate resonances, e.g. $B_s^0 \to \eta_c\phi$ followed by $\eta_c \to \phi\phi$ decay, or as a three-body decay (section 5.2.4). The latter one corresponds to a rare quark diagram with gluonic penguin and additional creation of $s\bar{s}$ pair. The results presented in this chapter are preliminary LHCb results.

5.1 Decays of B_s^0 to two ϕ mesons, $B_s^0 \to \phi\phi$

The idea to measure the branching fraction of the $B_s^0 \to \phi\phi$ decay mode via normalization to $\eta_c \to \phi\phi$, $\eta_c \to p\overline{p}$ and $J/\psi \to p\overline{p}$ modes originated from the brainstorming discussion with Emi Kou, and further interesting discussions with Emi Kou and Jibo He. Stripping of corresponding LHCb data was performed by Jibo He. This analysis became a subject of Master thesis of Nazar Stefanyuk, internships of Maksym Teklishyn and Andrii Usachov. The results discussed in this section are preliminary LHCb results.

5.1.1 Landscape for the $B_s^0 \to \phi\phi$ decay mode

In the SM the decay $B_s^0 \to \phi\phi$ is forbidden at the tree level and proceeds via a gluonic penguin process, $b \to s\bar{s}s$, with four strange quarks in the final state. Its quark diagram is shown on Fig. 5.1. Being induced by a purely loop quark diagram, this

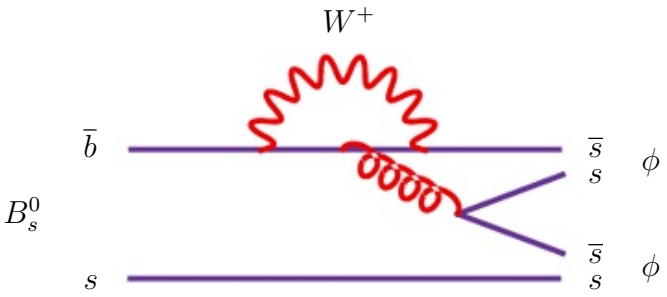

Figure 5.1: Quark diagram describing $B_s^0 \to \phi\phi$ decay

rare decay provides an excellent probe of new heavy particles entering the penguin quantum loop [220–222]. Measurements of the polarization amplitudes and triple product asymmetries in the $B_s^0 \to \phi\phi$ decay mode were pointed out to provide important probes of the non-factorizable penguin-annihilation effects [223], final state interactions [224], and NP contributions to the penguin loops [225, 226]. Recently, the LHCb experiment performed a measurement of the time-dependent *CP*-violating asymmetry in $B_s^0 \to \phi\phi$ decays [18], and probed the *CP*-violating phase ϕ_s for the first time. The branching fraction $\mathcal{B}(B_s^0 \to \phi\phi)$ has been calculated using pertubative QCD approach (Ref. [227] and references therein) and QCD factorization (Ref. [221, 222] and references therein). However, experimental knowledge of the branching fraction for this mode remains

limited, with measurements from CDF [228, 229] and upper limit set by the SLD experiment [230]. In the recent CDF result [229], $\mathcal{B}(B_s^0 \to \phi\phi) = (17.7 \pm 2.4^{+5.7}_{-3.2}) \times 10^{-6}$, the systematic uncertainty is dominated by the precision of the branching fraction for the normalization channel $B_s^0 \to J/\psi\,\phi$. This measurement is limited by large systematic uncertainties and calls for the $\mathcal{B}(B_s^0 \to \phi\phi)$ determination using alternative approach. Reconstructing the B_s^0 meson via its decay to $\phi\phi$, and comparing the η_c and B_s^0 event yields, the branching fraction $\mathcal{B}(B_s^0 \to \phi\phi)$ can be obtained.

5.1.2 Reconstruction of the $B_s^0 \to \phi\phi$ decay mode

The $B_s^0 \to \phi\phi$ candidates were reconstructed using selection criteria similar to those applied for charmonia reconstruction via decays to $\phi\phi$ in the production analysis, as discussed in section 4.3.3. Charged kaon separation against pions, $\mathrm{DLL}_{K\pi} > 5$, and kaon transverse momentum $p_\mathrm{T} > 0.5\,\mathrm{GeV}/c$ were required. Two ϕ candidates were required to form good quality common vertex, $\chi^2/\mathrm{ndf} < 16$, well distinguished from the corresponding primary vertex with a significant distance between the two vertices, $\chi^2 > 100$. The two-dimensional fit selected true $\phi\phi$ combinations, suppressing a significant reflection from $B^0 \to \phi K^{*0}$. Separate analysis of the data samples, corresponding to $\sqrt{s} = 7\,\mathrm{TeV}$ and $\sqrt{s} = 8\,\mathrm{TeV}$, shown consistent results for signal and background models and event yields, so that the combined data sample was considered. A fit to the $\phi\phi$ invariant mass spectrum in the region of the B_s^0 mass is shown in Fig. 5.2. Gaussian function was used to describe the B_s^0 signal shape, while an exponential function modelled combinatorial background. The fit yielded 2564 ± 59 candidates in the B_s^0 signal peak, and the B_s^0 mass value $M_{B_s^0} = 5366.8 \pm 0.3\,\mathrm{MeV}/c^2$, in agreement with the PDG average of $5366.77 \pm 0.24\,\mathrm{MeV}/c^2$ [57].

5.1.3 Branching fraction $\mathcal{B}(B_s^0 \to \phi\phi)$

Having reconstructed the η_c and B_s^0 mesons in the $\eta_c \to \phi\phi$ and $B_s^0 \to \phi\phi$ decay modes, comparing the η_c and B_s^0 event yields, and accounting for the efficiency difference, the branching fraction $\mathcal{B}(B_s^0 \to \phi\phi)$ can be obtained.

In the ratio of the B_s^0 production, where B_s^0 is reconstructed via the $B_s^0 \to \phi\phi$ decay, to the η_c production in b-hadron inclusive decays, the B_s^0 fragmentation from

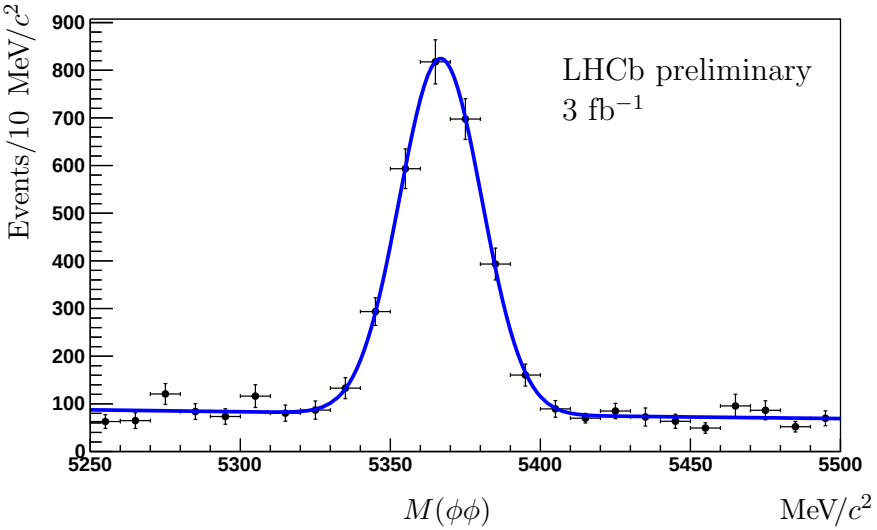

Figure 5.2: Invariant mass spectrum of the $\phi\phi$ combinations in the region of the B_s^0 mass for combined data sample. The number of candidates in each bin comes from the 2D fit, decribed in section 4.3.3

the b-quark has to be taken into account,

$$\frac{\mathcal{B}(\bar{b} \to B_s^0) \times \mathcal{B}(B_s^0 \to \phi\phi)}{\mathcal{B}(b \to \eta_c X) \times \mathcal{B}(\eta_c \to \phi\phi)} = \frac{N_{B_s^0}}{N_{\eta_c}} \times \frac{\varepsilon_{\eta_c}}{\varepsilon_{B_s^0}} \,, \tag{5.1}$$

where N_{η_c} and $N_{B_s^0}$ are the event yields for η_c and B_s^0 signals, respectively, and the efficiency ratio is estimated using MC simulation to be $\varepsilon_{\eta_c}/\varepsilon_{B_s^0} = 0.56 \pm 0.02$. The ratio of B_s^0 production to the η_c inclusive production in b-hadron decays is thus obtained to be

$$\frac{\mathcal{B}(\bar{b} \to B_s^0) \times \mathcal{B}(B_s^0 \to \phi\phi)}{\mathcal{B}(b \to \eta_c X) \times \mathcal{B}(\eta_c \to \phi\phi)} = 0.211 \pm 0.007 \pm 0.012 \,. \tag{5.2}$$

Using the above ratio, together with the ratio $\mathcal{B}(b \to \eta_c X)/\mathcal{B}(b \to J/\psi X)$ in the same $p_{\rm T}$ region, allows to extract the branching fraction $\mathcal{B}(B_s^0 \to \phi\phi)$ as

$$\begin{aligned}\mathcal{B}(B_s^0 \to \phi\phi) = \frac{N_{B_s^0}}{N_{\eta_c}} \times \frac{\varepsilon_{\eta_c}}{\varepsilon_{B_s^0}} \times \\ \times \frac{\mathcal{B}(b \to \eta_c X) \times \mathcal{B}(\eta_c \to p\bar{p})}{\mathcal{B}(b \to J/\psi X) \times \mathcal{B}(J/\psi \to p\bar{p})} \times \\ \times \frac{\mathcal{B}(\eta_c \to \phi\phi)}{\mathcal{B}(\eta_c \to p\bar{p})} \times \mathcal{B}(b \to J/\psi X) \times \mathcal{B}(J/\psi \to p\bar{p})/\mathcal{B}(\bar{b} \to B_s^0) \,.\end{aligned}$$

In the above expression, the ratio on the second line has been measured in Ref. [138] to be $\frac{\mathcal{B}(b\to\eta_c X)\times\mathcal{B}(\eta_c\to p\bar{p})}{\mathcal{B}(b\to J/\psi X)\times\mathcal{B}(J/\psi\to p\bar{p})} = 0.302\pm0.039\pm0.015 = 0.302\pm0.042$ for $p_{\rm T}(\eta_c, J/\psi) > 6.5\,\text{GeV}$,

and can be used as an estimate for the present calculations; the ratio of the η_c branching fractions to the $\phi\phi$ and $p\overline{p}$ final states $\mathcal{B}(\eta_c \to \phi\phi)/\mathcal{B}(\eta_c \to p\overline{p}) = 1.17 \pm 0.18$ [57], and is dominated by the accuracy of BES measurements; the inclusive branching fraction of b-hadrons into J/ψ final states $\mathcal{B}(b \to J/\psi X) = (1.16 \pm 0.10)\%$, where decays of the admixture of $B^{\pm}$, B^0, B_s^0 and b baryons are considered [57]; and the branching fraction of the J/ψ meson decay to the $p\overline{p}$ final state $\mathcal{B}(J/\psi \to p\overline{p}) = (2.120 \pm 0.029) \times 10^{-3}$ [57].

The fragmentation of the $\overline{b}$ to B_s^0 is driven by strong dynamics in the nonperturbative regime, and no reliable theoretical prediction can be made. Thus the f_s has also to be determined experimentally. The LHCb experiment determined $\frac{f_s}{f_d}$ via semileptonic [231] and hadronic [232] decays, and found it consistent with being independent on the rapidity and transverse momentum. The two measurements agree to each other, and yield the average of

$$\frac{f_s}{f_d} = 0.256 \pm 0.020 \ .$$

Though $\frac{f_s}{f_d}$ is not a priori a "universal" number, the LHCb result is similar to those obtained by the experiments at LEP and Tevatron. Assuming universality, the Ref. [57] proposes a value of $f_s = \mathcal{B}(\overline{b} \to B_s^0) = 0.107 \pm 0.014$.

From the above input, the branching fraction $\mathcal{B}(B_s^0 \to \phi\phi)$ is obtained to be

$$\mathcal{B}(B_s^0 \to \phi\phi) = (1.71 \pm 0.06 \pm 0.45) \times 10^{-5} \ ,$$

where the systematic uncertainty dominates the measurement precision. The largest contribution to the systematic uncertainty comes from the uncertainty in the ratio of the η_c branching fractions $\frac{\mathcal{B}(\eta_c \to \phi\phi)}{\mathcal{B}(\eta_c \to p\overline{p})}$, and the knowledge of the f_s parameter.

5.1.4 Discussion and outlook

The branching ratio $\mathcal{B}(B_s^0 \to \phi\phi) = (1.71 \pm 0.06 \pm 0.45) \times 10^{-5}$ was measured with a different technique with respect to previous results [228–230]. The measurement is consistent with the previous CDF results and has a precision similar to that of the PDG value [57]. The result is also consistent with theoretical calculations [221, 222, 227].

Precision of the measured branching fraction $\mathcal{B}(B_s^0 \to \phi\phi)$ is fully dominated by the systematic uncertainty, which is in turn dominated by the uncertainty in the ratio of the

η_c branching fractions $\frac{\mathcal{B}(\eta_c \to \phi\phi)}{\mathcal{B}(\eta_c \to p\overline{p})}$, and the knowledge of the f_s parameter. Averages [57] of the branching fractions $\mathcal{B}(\eta_c \to \phi\phi)$ and $\mathcal{B}(\eta_c \to p\overline{p})$ rely on the so far most precise measurements by DM2 [233], and BES [139, 211, 234] experiments. Precision of all the above measurements is dominated by the systematic uncertainty. And none of the experiments directly performed measurement of the ratio of the two branching fractions, which would allow partial cancellation of systematic uncertainty, and would consequently reduce the systematic uncertainty of the branching fraction $\mathcal{B}(B_s^0 \to \phi\phi)$ measured by LHCb. Contacts with the BES collaboration have started in order to motivate them to revisit their analysis and yield the measurement of the ratio with improved precision.

5.2 Decays of B_s^0 to three ϕ mesons, $B_s^0 \to \phi\phi\phi$

The idea to search for the $B_s^0 \to \phi\phi\phi$ decay mode originated from the LHCb working group discussion with Mathew Needham and Vanya Belyaev, and further interesting discussions with Jibo He. Stripping of corresponding LHCb data was performed by Jibo He. This analysis became a subject of the internship of Andrii Usachov. The results discussed in this section are preliminary LHCb results.

5.2.1 Landscape for the $B_s^0 \to \phi\phi\phi$ decay mode

Adding another reconstructed ϕ candidate to the $\phi\phi$ system, allows to search for the $B_s^0 \to \phi\phi\phi$ decay. The transition $B_s^0 \to \phi\phi\phi$ can proceed via two-body decay involving intermediate resonances, or via three-body $B_s^0 \to \phi\phi\phi$ decay.

The three-body $B_s^0 \to \phi\phi\phi$ decay can be described by a quark diagram shown on Fig. 5.3. This is a penguin diagram, similar to the diagram describing the $B_s^0 \to \phi\phi$ decay mode (Fig. 5.1), and involves a creation of an additional $s\overline{s}$ pair. The transition thus leads to the final state with six strange quarks.

The $B_s^0 \to \eta_c\phi$ decay mode followed by the $\eta_c \to \phi\phi$ decay, is an example of the decay via intermediate resonance, yielding three-ϕ system. The $B_s^0 \to \eta_c\phi$ decay is described by the internal emission of W boson. This decay has not been observed

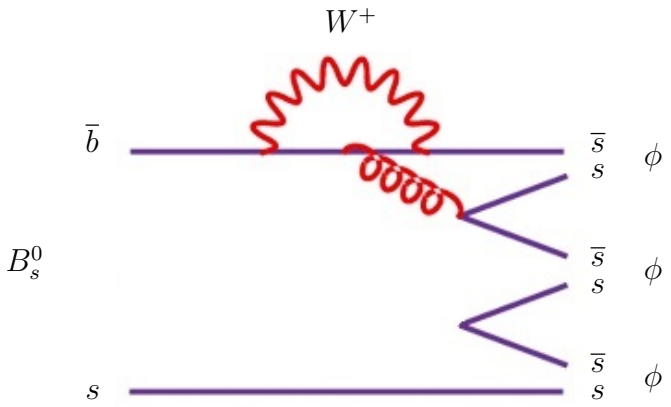

Figure 5.3: Quark diagram describing three-body $B_s^0 \to \phi\phi\phi$ decay

so far. However, the similar $B_s^0 \to J/\psi\,\phi$ decay occurs with a branching fraction of $\mathcal{B}(B_s^0 \to J/\psi\,\phi) = (1.09^{+0.28}_{-0.23}) \times 10^{-3}$ [57]. The difference between the branching fractions for the $B_s^0 \to \eta_c\phi$ and $B_s^0 \to J/\psi\,\phi$ decays can however be expected due the fact, that the latter decay is a $P \to VV$ transition. For example, branching fractions of light B-meson decays to $J/\psi\,K^*$ exceed those of light B-meson decays to $\eta_c K^*$ by a factor 2, where only neutral B-decays are measured precisely enough to draw this conclusion at a quantitative level [57]. In addition, in order to make a comparison between the $B_s^0 \to \eta_c\phi$ and three-body contributions to the $B_s^0 \to \phi\phi\phi$ decay, the $\eta_c \to \phi\phi$ branching fraction, $BR(\eta_c \to \phi\phi) = (1.94 \pm 0.30) \times 10^{-3}$ [57] should be taken into account. Comparing the considerations above for the branching fraction of the $B_s^0 \to \eta_c\phi$ decay to the branching fraction of the $B_s^0 \to \phi\phi$ decay mode, and neglecting any possible interference effects, the $\mathcal{B}(B_s^0 \to \eta_c\phi)$ can be expected to be below the branching fraction of the three-body $B_s^0 \to \phi\phi\phi$ transition.

5.2.2 Reconstruction of the $B_s^0 \to \phi\phi\phi$ decay mode

Reconstruction of the $B_s^0 \to \phi\phi\phi$ decay mode employs selection criteria, that are similar to those used for the analysis of the $B_s^0 \to \phi\phi$ decay. In the $B_s^0 \to \phi\phi\phi$ analysis, in order to extract true $\phi\phi\phi$ combinations a maximum likelihood unbinned 3D fit is used, similar to the 2D fit used to extract true $\phi\phi$ combinations for selection of charmonia or B_s^0 decays to $\phi\phi$, as was discussed in sections 4.3.3 and 5.1.2. The fit shape accounts

for $\phi\phi\phi$, $\phi\phi K^+K^-$, $\phi K^+K^-K^+K^-$ and $K^+K^-K^+K^-K^+K^-$ contributions and takes into account the available phase space. Projections of the 3D fit for the entire sample of candidates on each ϕ candidate are shown on Fig. 5.4. On the left of each ϕ projection,

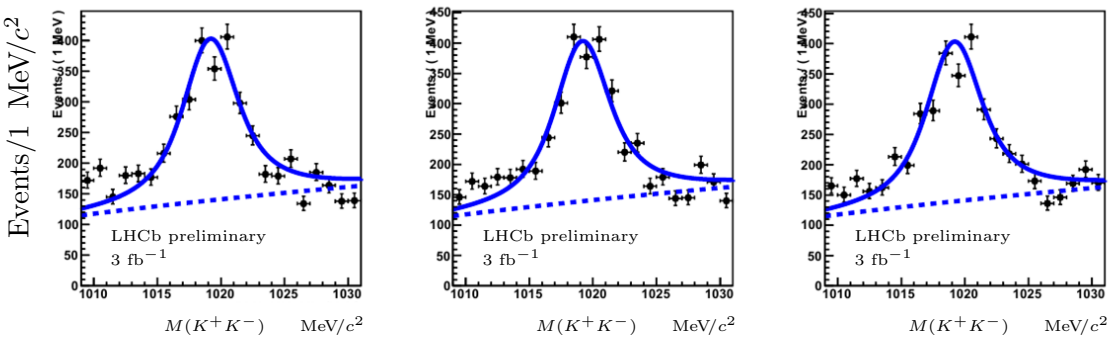

Figure 5.4: Projections of the entire sample of the $\phi\phi\phi$ candidates 3D fit on each ϕ candidate

a possible contribution from $f_0(980)$ resonance is visible. Fig. 5.5 shows invariant mass distribution of the $\phi\phi\phi$ system. A fit to the invariant mass spectrum, using a Gaussian

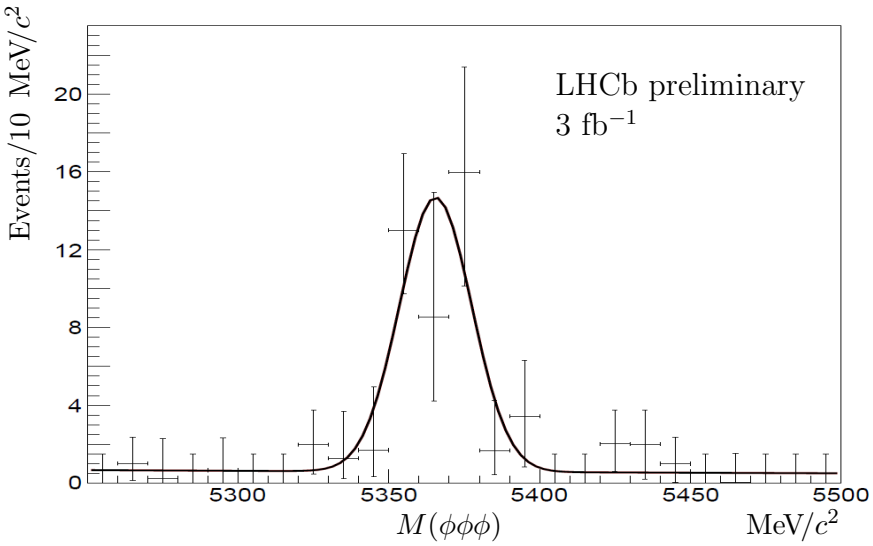

Figure 5.5: Distribution of the $\phi\phi\phi$ invariant mass for combined data sample accumulated at $\sqrt{s} = 7\,\text{TeV}$ and $\sqrt{s} = 8\,\text{TeV}$

function to describe a clear B_s^0 signal corresponding to the transition $B_s^0 \to \phi\phi\phi$, and an exponential to describe combinatorial background, yielded 42.3 ± 13.4 B_s^0 candidates over a low level background.

5.2.3 Branching fraction $\mathcal{B}(B_s^0 \to \phi\phi\phi)$

Reconstructing the decays of B_s^0 meson to two ϕ mesons, $B_s^0 \to \phi\phi$, and three ϕ mesons, $B_s^0 \to \phi\phi\phi$, with similar selection criteria, allows a determination of the ratio of their branching fractions to be

$$\frac{\mathcal{B}(B_s^0 \to \phi\phi\phi)}{\mathcal{B}(B_s^0 \to \phi\phi)} = \frac{N_{B_s^0 \to \phi\phi\phi}}{N_{B_s^0 \to \phi\phi}} \times \frac{\varepsilon_{B_s^0 \to \phi\phi}}{\varepsilon_{B_s^0 \to \phi\phi\phi}} \times \frac{1}{\mathcal{B}(\phi \to K^+K^-)} \ .$$

In the above expression, the event yields are measured in the present analysis, and the efficiency ratio is estimated using MC simulation to be $\varepsilon_{B_s^0 \to \phi\phi}/\varepsilon_{B_s^0 \to \phi\phi\phi} = 1.10 \pm 0.06$, assuming that the $B_s^0 \to \phi\phi\phi$ transition proceeds as a three-body decay. The ratio of the branching fraction is thus obtained as

$$\frac{\mathcal{B}(B_s^0 \to \phi\phi\phi)}{\mathcal{B}(B_s^0 \to \phi\phi)} = 0.038 \pm 0.012 \pm 0.004 \ ,$$

where the systematic uncertainty is dominated by the uncertainty due to background description. Using the branching fraction of the $B_s^0 \to \phi\phi$ decay $\mathcal{B}(B_s^0 \to \phi\phi) = (1.71 \pm 0.06 \pm 0.45) \times 10^{-5}$ from section 5.1.3, the branching fraction for the B_s^0 meson decay to three ϕ mesons is derived as

$$\mathcal{B}(B_s^0 \to \phi\phi\phi) = (6.4 \pm 2.0 \pm 1.8) \times 10^{-7} \ ,$$

The systematic uncertainty is dominated by the uncertainty of the branching fraction $\mathcal{B}(B_s^0 \to \phi\phi)$ measurement.

In order to search for possible contributions from intermediate resonances the invariant mass of $\phi\phi$ pairs is looked at. Fig. 5.6 shows the invariant mass distribution of $\phi\phi$ pairs from the $B_s^0 \to \phi\phi\phi$ candidates. Though the event sample is too small to conclude, no indication of a dominating resonance contribution is visible for the $\eta_c(1S)$, χ_{c0}, χ_{c1}, χ_{c2} or $\eta_c(2S)$ contribution. In addition, there is no indication of the $f_2(2300)$ or $f_2(2340)$ presence.

5.2.4 Discussion and outlook

The branching fraction of the transition $B_s^0 \to \phi\phi\phi$ is measured to be $\mathcal{B}(B_s^0 \to \phi\phi\phi) = (6.4 \pm 2.0 \pm 1.8) \times 10^{-7}$. This decay can proceed via two-body decay involving intermediate

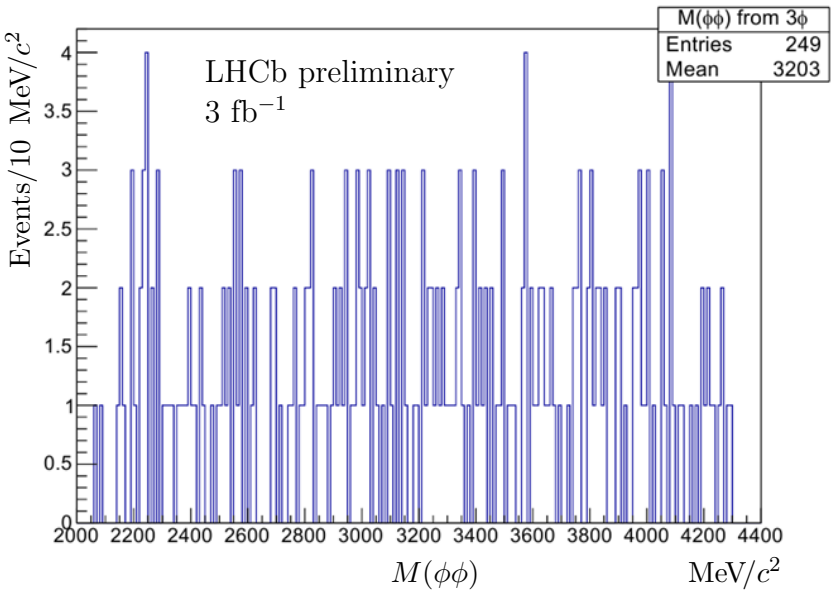

Figure 5.6: Invariant mass distribution of the $\phi\phi$ pair from the $B_s^0 \to \phi\phi\phi$ candidates for combined data sample accumulated at $\sqrt{s} = 7\,\text{TeV}$ and $\sqrt{s} = 8\,\text{TeV}$

resonances, e.g. $B_s^0 \to \eta_c\phi$ with $\eta_c \to \phi\phi$ yielding three-ϕ system or via three-body $B_s^0 \to \phi\phi\phi$ decay.

No clear resonant structure is observed in the $\phi\phi$ invariant mass distribution. This suggests to use the measured branching fraction, $\mathcal{B}(B_s^0 \to \phi\phi\phi) = (6.4 \pm 2.0 \pm 1.8) \times 10^{-7}$, as un upper limit for the branching fraction of the three-body transition. At the same time, comparison between the $\eta_c\phi$ and the three-body contributions (section 5.2.1) allows also to consider this value as an estimate of the upper limit on the branching fraction of the $B_s^0 \to \eta_c\phi$ decay mode.

Despite the fact, that no dominant resonance contribution has been observed, a Dalitz plot analysis should be performed to further study resonance structure of the $B_s^0 \to \phi\phi\phi$ transition. The technique developed in Ref. [235] for three-body decays to identical particles will be used in the future analysis.

Chapter 6

Summary

What the caterpillar calls the end of the world,
the master calls a butterfly.

Richard Bach

In summary, present writing addresses two major subjects, design, construction and tests of the LHCb electromagnetic calorimeter detector, and charmonia production studies, using decays to hadronic final states, and measurement of branching fractions of B_s^0-decays to ϕ mesons, in the LHCb experiment.

LHCb ECAL detector was designed, constructed, tested, pre-calibrated and installed in the experiment. The Shashlik cell design inherited essential experience from the previous constructions, and in particular PHENIX and HERA-B calorimeters. Complementary to existed experience, LHCb ECAL triggered several new successful developments. Effects influencing lateral uniformity of response were better understood, while record lateral uniformity for Shashyk type calorimeters was demonstrated. Among other developments, a new technique of S-type fiber bending allowed to achieve bending radii of 10 mm for fiber diameter of 1.2 mm, more than five times lower with respect to fiber specifications, without a mechanical damage. Important studies of radiation resistance of plastic scintillators have been performed. The optimal scintillator tile and WLS fiber combination was selected for the LHCb ECAL. Taking into account a substantial radiation dose close to the beam pipe, the ECAL design provides a possibility to replace 48 modules, that are most exposed to radiation. In addition sets of comprehensive dose

monitors have been distributed over the calorimeter surface, that will allow not only a dose map reference, but will also provide information of scintillator materials aging for irradiating particles, corresponding to realistic environment of hadron collider, and at realistic dose accumulation rate. Having different response to different radiation types, the monitors will provide a separate dose map for electromagnetic component, charged hadrons and neutrons. During the LHCb data taking, the calorimeter demonstrated reliable operation with less than 0.2% dead channels. However, long clear transport fibers, distributing LED monitoring pulses, appeared to be sensitive to radiation. On-line degradation and annealing effects following the beam crossing pattern have been observed. This increases the importance of the online monitoring using reconstructed π^0 signal.

Charmonia production was studied, using charmonia decays to $p\overline{p}$ and $\phi\phi$ pairs.

The η_c production is studied using pp collisions with an integrated luminosity of 0.7 fb^{-1} and 2.0 fb^{-1}, collected at a centre-of-mass energy $\sqrt{s} = 7\,\text{TeV}$ and $\sqrt{s} = 8\,\text{TeV}$, respectively. The inclusive branching fraction of b-hadron decays into η_c mesons for $p_{\text{T}}(\eta_c, J/\psi) > 6.5\,\text{GeV}/c$, relative to the corresponding J/ψ meson quantity, is measured for the first time to be

$$\mathcal{B}(b \to \eta_c X)/\mathcal{B}(b \to J/\psi\, X) = 0.424 \pm 0.055 \pm 0.015 \pm 0.045_{\mathcal{B}(J/\psi \to p\overline{p}, \eta_c \to p\overline{p})}\ .$$

The first uncertainty is statistical, the second is systematic, and the third is due to uncertainties in the branching fractions of the η_c and J/ψ meson decays to the $p\overline{p}$ final state. The η_c prompt production cross-section in the kinematic regime $2.0 < y < 4.5$ and $p_{\text{T}}(\eta_c, J/\psi) > 6.5\,\text{GeV}/c$, relative to the corresponding J/ψ meson cross-section, is measured for the first time, yielding

$$\begin{aligned}\left(\sigma_{\eta_c}/\sigma_{J/\psi}\right)_{\sqrt{s}=7\,\text{TeV}} &= 1.75 \pm 0.30 \pm 0.28 \pm 0.19_{\mathcal{B}(J/\psi \to p\overline{p}, \eta_c \to p\overline{p})}\ ,\\ \left(\sigma_{\eta_c}/\sigma_{J/\psi}\right)_{\sqrt{s}=8\,\text{TeV}} &= 1.60 \pm 0.29 \pm 0.25 \pm 0.17_{\mathcal{B}(J/\psi \to p\overline{p}, \eta_c \to p\overline{p})}\ ,\end{aligned}$$

at a centre-of-mass energy $\sqrt{s} = 7\,\text{TeV}$ and $\sqrt{s} = 8\,\text{TeV}$, respectively. From these measurements, absolute η_c meson prompt production cross sections are derived, yielding

$$\begin{aligned}\left(\sigma_{\eta_c}\right)_{\sqrt{s}=7\,\text{TeV}} &= 0.52 \pm 0.09 \pm 0.08 \pm 0.06_{\sigma_{J/\psi},\, \mathcal{B}(J/\psi \to p\overline{p}, \eta_c \to p\overline{p})}\ \mu\text{b}\ ,\\ \left(\sigma_{\eta_c}\right)_{\sqrt{s}=8\,\text{TeV}} &= 0.59 \pm 0.11 \pm 0.09 \pm 0.06_{\sigma_{J/\psi},\, \mathcal{B}(J/\psi \to p\overline{p}, \eta_c \to p\overline{p})}\ \mu\text{b}\ ,\end{aligned}$$

at a centre-of-mass energy $\sqrt{s} = 7\,\text{TeV}$ and $\sqrt{s} = 8\,\text{TeV}$, respectively. The third uncertainty comprises in addition the uncertainty in the J/ψ meson production cross

section. The above results assume that the J/ψ is unpolarized. The obtained η_c cross-section is in a qualitative agreement to colour-singlet LO calculations, while the NLO contribution is expected to significantly modify the LO result. The p_{T} dependence of the η_c production rate exhibits similar behaviour to the J/ψ meson rate in the studied kinematic regime, though with significantly larger uncertainties. The NLO calculations of the η_c production rate in the same p_{T} intervals are being performed by K.T. Chao *et al.* from Beijing university. Their calculations will allow the first direct comparison between the theoretical calculations and the LHCb experimental results for the η_c production.

The relation of the η_c production to that of J/ψ, using their decays to $p\overline{p}$ final states, was important to relate production of charmonia, other than having $J^{PC} = 1^{--}$ quantum numbers, and reconstructed using final states, that are forbidden for $J^{PC} = 1^{--}$ charmonia, e.g. $\phi\phi$ final state, to the now precisely determined η_c production.

Charmonia production in b-hadron decays was also studied using charmonia decays to $\phi\phi$ with the full available LHCb data sample of $3\,fb^{-1}$. Relative production of the states from η_c and χ_c families was measured. Using a 2D fit in bins of the $\phi\phi$ invariant mass, the spectrum, containing only true $\phi\phi$ pairs, originating from heavier state decay, or random $\phi\phi$ combinations, has been extracted. From the fit to this spectrum, yield ratios of different charmonium states in b-hadron decays have been derived. These are the first or most precise determination of the production ratios for η_c and χ_c states in b-hadron inclusive decays.

Among further developments, Emi Kou proposed a comparison of the η_c and J/ψ production in b-hadron decays to extract information on the octet matrix elements, and test matrix element universality. A translation of the η_c and J/ψ p_{T} spectra to the p^* dependence will allow better comparison with the BaBar measurement [194] of the production of these states in b-hadron decays and following theoretical speculations [200–202]. A possible future improvement of the efficiency of the involved LHCb trigger lines, should make it possible to extend η_c production studies to lower p_{T}-values, and exploring heavier charmonium and charmonium-like states, using charmonia decays to both $p\overline{p}$ and $\phi\phi$ final states. Other promising decay modes to be considered comprise decays to ϕf_x final states, where f_x is a resonance with defined quantum numbers decaying to K^+K^-, that can also the states with $J^{PC} = 1^{--}$ quantum numbers [137]; and decays to baryon-antibaryon pairs, proposed by Jacques Lefrançois. Emi Kou proposed to

compare angular dependences in the $J/\psi \to p\overline{p}$ to those in the decay $J/\psi \to \mu^+\mu^-$ in order to extract further information on the spin-selection rules breaking [206], as well as the $J/\psi \to p\overline{p}$ transition mechanism. A low-background sample of J/ψ mesons from b-hadron decays, with well-known polarization, will be exposed to this study. Finally, decays to hadronic final states open a possibility of studies of central exclusive production of other charmonia than those having $J^{PC} = 1^{--}$ quantum numbers, or those decaying to them.

Using low-level background samples of charmonia candidates produced in inclusive b-hadron decays, and a momentum scale calibration performed on data, mass and natural width of the η_c (1S) state have been measured. These measurements used another method, compared to the most precise to date recent results of the BES experiment [210, 211], and provided an important consistency check. Using decays to $p\overline{p}$ final state, the difference between the J/ψ and η_c meson masses was measured to be $\Delta M_{J/\psi\,,\eta_c} = 114.7 \pm 1.5 \pm 0.1\,\mathrm{MeV}/c^2$. Using decays to $\phi\phi$ pairs the η_c mass was measured to be $M_{\eta_c} = 2984.0 \pm 0.5 \pm 0.2\,\mathrm{MeV}/c^2$. The results are consistent with each other and with the average from Ref. [57]. Precision of the η_c mass measurement using $\eta_c \to p\overline{p}$ decays improves upon that of the measurements in e^+e^- collisions at the $\Upsilon(4S)$ resonance and is compatible to the BES results. The η_c mass measurement using $\eta_c \to \phi\phi$ decays is the most precise η_c mass determination with the precision exceeding that quoted in Ref. [57]. The difference between the masses in η_c family, $\eta_c(2S)$ and $\eta_c(1S)$, and in χ_c family, will be studied using larger event samples expected from the operation in 2015.

Finally, B_s^0-decays to ϕ mesons, $B_s^0 \to \phi\phi$ and $B_s^0 \to \phi\phi\phi$, have been studied. Using 2D or 3D unbinned maximum likelihood fit, true $\phi\phi$ and $\phi\phi\phi$ systems have been obtained.

Relating the observed branching fraction of the $B_s^0 \to \phi\phi$ decay to the branching fraction of the η_c inclusive production in b-hadron decays, allowed to extract the value of $\mathcal{B}(B_s^0 \to \phi\phi)$ with a precision, compatible to that of the average in Ref. [57], using an however alternative technique, to be

$$\mathcal{B}(B_s^0 \to \phi\phi) = (1.71 \pm 0.06 \pm 0.45) \times 10^{-5}\ .$$

This measurement is consistent with the previous CDF results. The result is also consistent with theoretical calculations [221, 222, 227]. Dominating systematic uncertainty

can be reduced if the ratio of the η_c branching fractions $\frac{\mathcal{B}(\eta_c \to \phi\phi)}{\mathcal{B}(\eta_c \to p\bar{p})}$ is determined directly. Contacts with the BES collaboration have started in order to motivate them to revisit their analysis and yield the measurement of the ratio with improved precision.

The $B_s^0 \to \phi\phi\phi$ decay mode has been observed for the first time. No single dominating intermediate resonance is found in the $B_s^0 \to \phi\phi\phi$ transition. Using the measured branching fraction of the $B_s^0 \to \phi\phi$ decay mode, the branching fraction for the B_s^0 meson decay to three ϕ mesons was obtained to be

$$\mathcal{B}(B_s^0 \to \phi\phi\phi) = (6.4 \pm 2.0 \pm 1.8) \times 10^{-7} \ .$$

If this transition proceeds via several different intermediate two-body decays, the above value becomes an upper limit on the penguin transition and pickup of the $s\overline{s}$ pair, with six strange quarks in the final state. The above value is also an estimated upper limit on the branching fraction for the $B_s^0 \to \eta_c\phi$ mode. A Dalitz plot analysis will be performed to further study resonance structure of the $B_s^0 \to \phi\phi\phi$ transition, using the technique developed in Ref. [235] for three-body decays to identical particles.

Acknowledgements

I am particularly pleased to fill this section of the book.

First of all, I am highly indebted to Yuanning Gao, Valery Khoze, Jacques Lefrançois, Andreas Schopper, Joachim Spengler, Achille Stocchi and Isabelle Wingerter-Seez, who accepted to be members of the jury, and to come in person for the HDR session. In addition, Andreas Schopper, Joachim Spengler and Isabelle Wingerter-Seez kindly accepted to be the referees, and had the courage to read this document in advance, commenting it and writing reports. Contacting the jury members triggered some interesting discussions, which reminded me a bright part of the calorimetry and LHCb analysis on top of the background of paper work to prepare the HDR, and I am happy to acknowledge a kind support of the jury.

I am very pleased to thank all the LAL-LHCb group for the nice atmosphere in the group, friendly and supportive, and I would like to thank present and past group members, Yasmine Amhis, Martino Borsato, Olivier Callot, Bernard D´Almagne, Benoit Delcourt, Frédéric Fulda-Quenzer, Jibo He, Bernard Jean-Marie, Olga Kochebina, Jacques Lefrançois, Frédéric Machefert, Aurelien Martens, Alexandra Martin-Sanchez, Michelle Nicol, Wenbin Qian, Patrick Robbe, Marie-Hélène Schune, Maksym Teklishyn, Benoit Viaud, Ioanna Videau, Guy Wormser, and others. I am highly indebted to Jacques, who proposed me to come to LAL, and to Olivier, who introduced me to LAL and LAL to me, on the first day of my arrival. During my first year at LAL, I had a privilege to learn electronics from Jacques, and a pleasure performing calorimeter FEE tests with Christophe Beigbeder, Dominique Breton, Daniel Charlet, Beng Ky, Jacques, Frédéric, Patrick, and others. I was sharing the office at LAL with Benoit Delcourt and I appreciated discussing with Benoit physics, French culture and his grandchildren from all over the world. After LHCb group was moved to 208, for several years I was sharing

the office with Wenbin, and I was happy to learn dozens of Chinese words and a course on principles of writing Chinese.

It is my pleasure to particularly acknowledge a continuous help and support of Marie-Hélène and Achille since my arrival at LAL. We had a good time teaching in Ukraine, and launching TESHEP, successful annual summer school. Looking at Achille and Marie-Hélène, who are rapidly learning Russian and Ukrainian languages, traditions and culture, I am trying to catch up with my understanding of France. A collection of vocabulary, having French origin and accommodated by Russian and Ukrainian languages and vice versa, grown to a size of small published dictionaries of this profile. And I highly appreciated a possibility to teach at the M2 NPAC for four years.

Idea to measure charmonia production using hadronic final states and eventually extending this activity to reconstruct decays of B_s^0 meson to ϕ mesons, using LHCb data, was launched during the discussions with Emi Kou. I highly appreciate a possibility to discuss and brainstorm with Emi on any emerging ideas or questions. It was a pleasure to work on this bunch of studies together with Jibo He and Benoit Viaud. I am very pleased to thank Jibo for his kind help during his stay at LAL and later, when he moved to CERN. Jibo still finds time to share Chinese food for lunch or to talk around a coffee. I am also happy to acknowledge an important contribution from the new generation of young physicists, Maksym Teklishyn, Nazar Stefanyuk and Andrii Usachov. Many shown results have been obtained by them. The analysis of the prompt η_c production was, in addition, motivated by some LHCb colleagues, who did not believe it to be feasible in the challenging environment of hadron machine, and I would like to thank them. These studies progressed also thanks to the WG conveners, Vanya Belyaev, Giulia Manca and Zhenwei Yang, and I appreciate their kind help.

The results reported in this document are the results of the team work. I would like to mention the LHCb ECAL group, uniting CERN, ITEP and LAL people. Calorimeter group was led by Jacques and then Andreas during the period, corresponding to the discussion of chapter 3. They knew to ensure a nice and friendly atmosphere in the group, and it was a pleasure being integrated in this community for years. I would like to particularly thank Andreas Schopper for the help and extremely kind attitude when working on the calorimeter project, it was just a pleasure working with Andreas.

I would like to express my gratitude to Andrey Golutvin who proposed me to join

LHCb in 1998, and who was the ITEP-LHCb group leader for many years. At the early stage of the work on the ECAL module and wall design, I had a great pleasure working with Alexander Soldatov, Vladimir Rusinov and Evgueny Tarkovsky. Alexander with a famous Lenin profile, combining highest probe professional engineer and extreme enthusiast of wise engineering solutions, shown how a motivated person with ultimate qualification can provide a fully elaborated solution for a problem at the scale of a day. His engineering skills were complemented by a talent of cooking delicious plates during the evenings in Saint-Genis. Vladimir and Evgueny were the motors of the ECAL modules tests and production. Their exceptional experience, feeling of an apparatus, and methodical approach taught me a lot on how to approach a calorimeter. Moments of discussing with them, or spent in the control room in the West area, or around the test setups or a traditional tea in their ITEP workshop, are among the nicest moments over the years of the ECAL construction. Stas Malyshev is another person to be absolutely mentioned in relation with a calorimeter construction. Stas joined the group soon after prototyping was started, and was a key person in all the work related to optical fibers, in particular created a technical solution for WLS fiber bending. Yuri Guilitski was the person, who proposed and designed the Cockcroft-Walton bases for the ECAL. We met first in HERA-B, and worked closely around the LHCb ECAL. Yuri was bringing not only his exceptional expertise, but also his unique animated and friendly attitude. Oleg Gushchin, Boris Bobchenko, and Tengiz Kvaratskheliia were also in the core of the ECAL team, and in particular for the Cockcroft-Walton base tests and development of the test with cosmic rays. A remarkable period of mounting of the ECAL wall in the LHC together with Alexander Arefiev, Tengiz Kvaratskheliia and Alexander Lukyanov, mounting of the cables and monitoring system, marked the end of the production stage. The activities in the point 8 were always efficiently assisted by the local team of engineers, and in particular Bernard Chadaj, Gerard Decreuse, Bernard Corajod, Frank Lamour, Cedric Fournier, Patrick Vallet, and others. This was an example of a team combining exceptional professional qualities and always positive spirit. In addition, they were among my first teachers of French. A kind help on many technical issues was also received from Robert Kristic. During the preparation and installation work, we regularly interacted with Rolf Lindner, who was also coordinating the point 8 work. Besides the efficient help from Rolf, I enjoyed boxing discussions, in particular qualifications of Klichko brothers. I am particularly lucky to have worked with Alexander Arefiev on the production of HERA-B muon detector and then on the production and installation of the LHCb ECAL. As a physicist, Alexander combines a rich experience over the

whole HEP range and impressive competence on the engineering questions, and fully investing himself in the work. And as a person, he is just somebody, who you are happy to communicate with. I leant from Alexander an impressive ability to solve any kind of problem on the A4 format graph paper, and a rare example of a person for whom kind and honest human behaviour is always above professional or career considerations. It is my pleasure to thank other colleagues and friends from the LHCb calorimeter group. The final design of all the calorimeter structures in the LHCb cavern was made by the LAPP team, Claude Girard, Bruno Lieunard, Marie-Noëlle Minard, and others, with famous Catia. During two years we had many animated discussions at CERN and in their laboratory above the beautiful Annecy lake. I appreciated discussing with Leslie Camilleri, with whom I was working on the cosmic rays setup and also jointly following two CERN summer students, Yuri Gouz, who welcomes everybody around his famous 24/7 tea table, Evgueny Gushchin, Olivier Deschamps, Stephane Monteil, and others. I would like also to mention a nice time spent in the LHCb control room doing the shifts, a time-consuming activity that could have become boring, if it would not be for nice spirit in the control room. Richard Jacobsson, Alessandro Cardini, Antonio Papanestis, Dirk Wiedner and many others are fully responsible for that.

Since many years I had (and still have) a pleasure to share the office at CERN and to discuss and sometimes (now, unfortunately, not anymore) play soccer with Tengiz. I appreciated a lot numerous brainstormings with Vanya, and working together on several express feasibility-studies in LHCb, including π^0 identification, $B_s^0 \to \phi\phi$, early studies of D-mesons reconstruction in LHCb, and others. Inheriting from the KAL developed in ARGUS by Hartwig Albrecht, Vanya developed a physicist-friendy LoKi language in LHCb, and then Bender tool. I had many other nice moments shared with Vanya, as regular sessions in the Cotton club in Hamburg, discovering together Berlin, or wine club in Moscow. I would also like to thank my other (ITEP at the time being) colleagues and friends, whom I had not a chance to mention explicitly above, for their help and support. It is my pleasure to thank Vladik Balagura, Ruslan Chistov, Mikhail Danilov, Victor Egorychev, Roman Kagan, Ivan Korolko, Roman Mizuk, Pavel Pakhlov, Galina Pakhlova, Sergey Semenov, Igor Tikhomirov, Maxim Titov, Kirill Voronchev, Yuri Zaitsev and Olga Zhiryakova.

I would also like to mention a small and very nice community developed around the LEETECH project at LAL, which inherited its principle from the old setup of

Bernard Jean-Marie, and I am really pleased to work on it with Vladik Balagura, Philip Bambade, Oleg Bezshyyko, Leonid Burmistrov, Vlad Krylov, Roberto Lopez, Hugues Monard, Veronique Puill, Maxim Titov, Alessandro Variola, and others.

Finally, I have to acknowledge, that this writing has been produced only due to the persisting efforts and support of Achille, Marie-Hélène and many of my colleagues and friends. This was also possible thanks to a permanent support of my family. This is fully their merit, that the document is produced, administrative procedures passed, and I am having the honour to present the results on September 2, 2014.

Bibliography

[1] LHCb collaboration, R. Aaij *et al.*, *Measurement of B meson production cross-sections in proton-proton collisions at* $\sqrt{s} = 7$ *TeV*, JHEP **08** (2013) 117, arXiv:1306.3663.

[2] LHCb collaboration, R. Aaij *et al.*, *Prompt charm production in pp collisions at* $\sqrt{s} = 7$ *TeV*, Nucl. Phys. **B871** (2013) 1, arXiv:1302.2864.

[3] LHCb collaboration, R. Aaij *et al.*, *Measurements of* B_c^+ *production and mass with the* $B_c^+ \to J/\psi\pi^+$ *decay*, Phys. Rev. Lett. **109** (2012) 232001, arXiv:1209.5634.

[4] M. Cacciari *et al.*, *Theoretical predictions for charm and bottom production at the LHC*, JHEP **1210** (2012) 137, arXiv:1205.6344.

[5] N. Brambilla *et al.*, *Heavy quarkonium: progress, puzzles, and opportunities*, Eur. Phys. J. **C71** (2011) 1534, arXiv:1010.5827.

[6] LHCb collaboration, R. Aaij *et al.*, *Updated measurements of exclusive* J/ψ *and* $\psi(2S)$ *production cross-sections in pp collisions at* $\sqrt{s} = 7$ *TeV*, J. Phys. **G40** (2014) 055002, arXiv:1401.3288.

[7] LHCb collaboration, R. Aaij *et al.*, *Production of* J/ψ *and* Υ *mesons in pp collisions at* $\sqrt{s} = 8$ *TeV*, JHEP **06** (2013) 064, arXiv:1304.6977.

[8] LHCb collaboration, R. Aaij *et al.*, *Study of* J/ψ *production and cold nuclear matter effects in pPb collisions at* $\sqrt{s_{NN}} = 5$ *TeV*, JHEP **02** (2014) 072, arXiv:1308.6729.

[9] LHCb collaboration, R. Aaij *et al.*, *Measurement of the cross-section ratio* $\sigma(\chi_{c2})/\sigma(\chi_{c1})$ *for prompt* χ_c *production at* $\sqrt{s} = 7$ *TeV*, Phys. Lett. **B714** (2012) 215, arXiv:1202.1080.

[10] LHCb collaboration, R. Aaij *et al.*, *Measurement of the ratio of prompt χ_c to J/ψ production in pp collisions at $\sqrt{s} = 7$ TeV*, Phys. Lett. **B718** (2012) 431, arXiv:1204.1462.

[11] LHCb collaboration, R. Aaij *et al.*, *Measurement of the relative rate of prompt χ_{c0}, χ_{c1} and χ_{c2} production at $\sqrt{s} = 7$ TeV*, JHEP **10** (2013) 115, arXiv:1307.4285.

[12] Y.-Q. Ma, K. Wang, and K.-T. Chao, *QCD radiative corrections to χ_{cJ} production at hadron colliders*, Phys. Rev. **D83** (2011) 111503, arXiv:1002.3987.

[13] LHCb collaboration, R. Aaij *et al.*, *Measurement of Υ production in pp collisions at $\sqrt{s} = 7$ TeV*, Eur. Phys. J. **C72** (2012) 2025, arXiv:1202.6579.

[14] LHCb collaboration, R. Aaij *et al.*, *Measurement of Υ production in pp collisions at $\sqrt{s} = 2.76$ TeV*, Eur. Phys. J. **C74** (2014) 2835, arXiv:1402.2539.

[15] LHCb collaboration, R. Aaij *et al.*, *Study of Υ production and cold nuclear effects in pPb collisions at $\sqrt{s_{NN}} = 5$ TeV*, JHEP **07** (2014) 094, arXiv:1405.5152.

[16] P. Artoisenet *et al.*, *Υ production at Fermilab Tevatron and LHC energies*, Phys. Rev. Lett. **101** (2008) 152001, arXiv:0806.3282.

[17] LHCb collaboration, R. Aaij *et al.*, *A measurement of the CKM angle γ from a combination of $B^\pm \to Dh^\pm$ analyses*, Phys. Lett. **B726** (2013) 151, arXiv:1305.2050.

[18] LHCb collaboration, R. Aaij *et al.*, *First measurement of the CP-violating phase in $B_s^0 \to \phi\phi$ decays*, Phys. Rev. Lett. **110** (2013) 241802, arXiv:1303.7125.

[19] LHCb collaboration, R. Aaij *et al.*, *Measurement of the CP-violating phase ϕ_s in $\bar{B}_s^0 \to J/\psi\pi^+\pi^-$ decays*, Phys. Lett. **B736** (2014) 186, arXiv:1405.4140.

[20] LHCb collaboration, R. Aaij *et al.*, *Effective lifetime measurements in the $B_s^0 \to K^+K^-$, $B^0 \to K^+\pi^-$ and $B_s^0 \to \pi^+K^-$ decays*, arXiv:1406.7204, to appear in Phys. Lett. B.

[21] LHCb collaboration, R. Aaij *et al.*, *Measurement of CP asymmetry in $D^0 \to K^-K^+$ and $D^0 \to \pi^-\pi^+$ decays*, JHEP **07** (2014) 041, arXiv:1405.2797.

[22] A. J. Buras, J. Girrbach, D. Guadagnoli, and G. Isidori, *On the Standard Model prediction for $\mathcal{B}$ ($B_{s,d} \to \mu^+\mu^-$)*, Eur. Phys. J. **C72** (2012) 2172, arXiv:1208.0934.

[23] A. J. Buras, R. Fleischer, J. Girrbach, and R. Knegjens, *Probing new physics with the $B_s^0 \to \mu\mu$ time-dependent rate*, JHEP **1307** (2013) 77, arXiv:1303.3820.

[24] Heavy Flavor Averaging Group, Y. Amhis *et al.*, *Averages of b-hadron, c-hadron, and tau-lepton properties as of early 2012*, arXiv:1207.1158.

[25] LHCb collaboration, R. Aaij *et al.*, *Measurement of the $B_s^0 \to \mu^+\mu^-$ branching fraction and search for $B^0 \to \mu^+\mu^-$ decays at the LHCb experiment*, Phys. Rev. Lett. **111** (2013) 101805, arXiv:1307.5024.

[26] LHCb collaboration, R. Aaij *et al.*, *Search for the rare decay $D^0 \to \mu^+\mu^-$*, Phys. Lett. **B725** (2013) 15, arXiv:1305.5059.

[27] BTeV Collaboration, A. Santoro *et al.*, *BTeV: An expression of interest for a heavy quark program at C0*, FERMILAB-PROPOSAL-0897 (1999).

[28] LHCb Collaboration, H. Dijkstra, H. J. Hilke, T. Nakada, and T. Ypsilantis, *LHCb Letter of Intent*, LHCb-95-001, CERN-LHCb-95-001 (1995).

[29] LHCb Collaboration, S. Amato *et al.*, *LHCb technical proposal*, CERN-LHCC-98-04, CERN-LHCC-P-4 (1998).

[30] LHCb Collaboration, P. R. Barbosa-Marinho *et al.*, *LHCb VELO TDR: Vertex locator. Technical design report*, CERN-LHCC-2001-011 (2001).

[31] LHCb Collaboration, P. R. Barbosa-Marinho *et al.*, *LHCb: Outer tracker technical design report*, CERN-LHCC-2001-024 (2001).

[32] LHCb Collaboration, P. R. Barbosa-Marinho *et al.*, *LHCb: Inner tracker technical design report*, CERN-LHCC-2002-029 (2002).

[33] LHCb Collaboration, S. Amato *et al.*, *LHCb magnet: Technical design report*, CERN-LHCC-2000-007 (2000).

[34] LHCb Collaboration, S. Amato *et al.*, *LHCb: RICH technical design report*, CERN-LHCC-2000-037 (2000).

[35] LHCb Collaboration, S. Amato *et al.*, *LHCb calorimeters: Technical design report*, CERN-LHCC-2000-036 (2000).

[36] LHCb Collaboration, P. R. Barbosa-Marinho *et al.*, *LHCb muon system technical design report*, CERN-LHCC-2001-010 (2001).

[37] LHCb Collaboration, R. Antunes-Nobrega *et al.*, *LHCb trigger system technical design report*, CERN-LHCC-2003-031 (2003).

[38] LHCb Collaboration, P. Barbosa-Marinho *et al.*, *LHCb online system technical design report: Data acquisition and experiment control*, CERN-LHCC-2001-040 (2001).

[39] LHCb Collaboration, R. Antunes-Nobrega *et al.*, *LHCb computing technical design report*, CERN-LHCC-2005-019 (2005).

[40] LHCb Collaboration, R. Antunes-Nobrega *et al.*, *LHCb technical design report: Reoptimized detector design and performance*, CERN-LHCC-2003-030 (2003).

[41] LHCb collaboration, A. A. Alves Jr. *et al.*, *The LHCb detector at the LHC*, JINST **3** (2008) S08005.

[42] R. Aaij *et al.*, *Measurement of the track reconstruction efficiency at LHCb*, LHCb-DP-2013-002, in preparation.

[43] LHCb collaboration, R. Aaij *et al.*, *Measurement of the effective* $B^0_s \to K^+K^-$ *lifetime*, Phys. Lett. **B716** (2012) 393, arXiv:1207.5993.

[44] LHCb collaboration, R. Aaij *et al.*, *Measurement of the* $\bar{B}^0_s$ *effective lifetime in the* $J/\psi f_0(980)$ *final state*, Phys. Rev. Lett. **109** (2012) 152002, arXiv:1207.0878.

[45] LHCb collaboration, R. Aaij *et al.*, *Measurement of the effective* $B^0_s \to J/\psi K^0_S$ *lifetime*, Nucl. Phys. **B873** (2013) 275, arXiv:1304.4500.

[46] LHCb collaboration, R. Aaij *et al.*, *Precision measurement of the* Λ^0_b *baryon lifetime*, Phys. Rev. Lett. **111** (2013) 102003, arXiv:1307.2476.

[47] LHCb collaboration, R. Aaij *et al.*, *Measurement of the* $\bar{B}^0_s \to D^-_s D^+_s$ *and* $\bar{B}^0_s \to D^- D^+_s$ *effective lifetimes*, Phys. Rev. Lett. **112** (2014) 111802, arXiv:1312.1217.

[48] LHCb collaboration, R. Aaij *et al.*, *Measurement of the* B^+_c *meson lifetime using* $B^+_c \to J/\psi\mu^+\nu_\mu X$ *decays*, Eur. Phys. J. **C74** (2014) 2839, arXiv:1401.6932.

[49] LHCb collaboration, R. Aaij *et al.*, *Measurements of the B^+, B^0, B_s^0 meson and Λ_b^0 baryon lifetimes*, JHEP **04** (2014) 114, arXiv:1402.2554.

[50] A. Affolder *et al.*, *Radiation damage in the LHCb vertex locator*, JINST **8** (2013) P08002, arXiv:1302.5259.

[51] G. Aad *et al.*, *ATLAS pixel detector electronics and sensors*, JINST **3** (2008) P07007.

[52] A. Ahmad *et al.*, *The Silicon microstrip sensors of the ATLAS semiconductor tracker*, Nucl. Instrum. Meth. **A578** (2007) 98.

[53] CMS Collaboration, S. Chatrchyan *et al.*, *The CMS experiment at the CERN LHC*, JINST **3** (2008) S08004.

[54] CMS Collaboration, V. Khachatryan *et al.*, *CMS tracking performance results from early LHC operation*, Eur. Phys. J. **C70** (2010) 1165, arXiv:1007.1988.

[55] D. van Eijk *et al.*, *Radiation hardness of the LHCb Outer Tracker*, Nucl. Instrum. Meth. **A685** (2012) 62.

[56] R. Arink *et al.*, *Performance of the LHCb Outer Tracker*, JINST **9** (2014) P01002, arXiv:1311.3893.

[57] Particle Data Group, J. Beringer *et al.*, *Review of particle physics*, Phys. Rev. **D86** (2012) 010001, and 2013 partial update for the 2014 edition.

[58] LHCb collaboration, R. Aaij *et al.*, *Measurements of the Λ_b^0, Ξ_b^-, and Ω_b^- baryon masses*, Phys. Rev. Lett. **110** (2013) 182001, arXiv:1302.1072.

[59] LHCb collaboration, R. Aaij *et al.*, *Precision measurement of the $B_s^0 - \bar{B}_s^0$ oscillation frequency in the decay $B_s^0 \to D_s^+\pi^-$*, New J. Phys. **15** (2013) 053021, arXiv:1304.4741.

[60] J. Amoraal *et al.*, *Application of vertex and mass constraints in track-based alignment*, Nucl. Instrum. Meth. **A712** (2013) 48, arXiv:1207.4756.

[61] LHCb collaboration, R. Aaij *et al.*, *Precision measurement of the mass and lifetime of the Ξ_b^0 baryon*, Phys. Rev. Lett. **113** (2014) 032001, arXiv:1405.7223.

[62] M. Adinolfi *et al.*, *Performance of the LHCb RICH detector at the LHC*, Eur. Phys. J. **C73** (2013) 2431, arXiv:1211.6759.

[63] LHCb collaboration, R. Aaij *et al.*, *Measurement of b-hadron branching fractions for two-body decays into charmless charged hadrons*, JHEP **10** (2012) 037, arXiv:1206.2794.

[64] LHCb collaboration, R. Aaij *et al.*, *First measurement of time-dependent CP violation in $B_s^0 \to K^+K^-$ decays*, JHEP **10** (2013) 183, arXiv:1308.1428.

[65] LHCb collaboration, R. Aaij *et al.*, *First observation of CP violation in the decays of B_s^0 mesons*, Phys. Rev. Lett. **110** (2013) 221601, arXiv:1304.6173.

[66] J. Alves, A.A. *et al.*, *Performance of the LHCb muon system*, JINST **8** (2013) P02022, arXiv:1211.1346.

[67] M. Anelli *et al.*, *Performance of the LHCb muon system with cosmic rays*, JINST **5** (2010) P10003, arXiv:1009.1963.

[68] A. A. Alves Jr. *et al.*, *Performance of the LHCb muon system*, JINST **8** (2013) P02022, arXiv:1211.1346.

[69] R. Aaij and J. Albrecht, *Muon triggers in the High Level Trigger of LHCb*, Tech. Rep. LHCb-PUB-2011-017. CERN-LHCb-PUB-2011-017, CERN, Geneva, Sep, 2011.

[70] F. Archilli *et al.*, *Performance of the muon identification at LHCb*, JINST **8** (2013) P10020, arXiv:1306.0249.

[71] R. Aaij *et al.*, *The LHCb trigger and its performance in 2011*, JINST **8** (2013) P04022, arXiv:1211.3055.

[72] LHCb collaboration, R. Aaij *et al.*, *Absolute luminosity measurements with the LHCb detector at the LHC*, JINST **7** (2012) P01010, arXiv:1110.2866.

[73] LHCb Collaboration, R. Aaij *et al.*, *LHCb upgrade, Letter of Intent*, CERN-LHCC-2011-001 (2011).

[74] LHCb Collaboration, I. Bediaga *et al.*, *LHCb VELO upgrade*, CERN-LHCC-2013-021 (2013).

[75] LHCb Collaboration, A. A. Alves Jr. *et al.*, *LHCb tracker upgrade*, CERN-LHCC-2014-001 (2014).

[76] LHCb Collaboration, I. Bediaga *et al.*, *LHCb particle identification upgrade*, CERN-LHCC-2013-022 (2013).

[77] CMS Collaboration, S. Chatrchyan *et al.*, *Measurement of the $B_{(s)} \to \mu^+\mu^-$ branching fraction and search for $B^0 \to \mu^+\mu^-$ with the CMS Experiment*, Phys. Rev. Lett. **111** (2013) 101804, arXiv:1307.5025.

[78] D. M. Straub, *New physics correlations in rare decays*, arXiv:1012.3893.

[79] D. M. Straub, *Overview of Constraints on New Physics in Rare B Decays*, arXiv:1205.6094.

[80] LHCb collaboration, R. Aaij *et al.*, *Differential branching fraction and angular analysis of the decay $B^0 \to K^{*0}\mu^+\mu^-$*, JHEP **08** (2013) 131, arXiv:1304.6325.

[81] LHCb collaboration, R. Aaij *et al.*, *Measurement of form-factor-independent observables in the decay $B^0 \to K^{*0}\mu^+\mu^-$*, Phys. Rev. Lett. **111** (2013) 191801, arXiv:1308.1707.

[82] N. Cabibbo, *Unitary Symmetry and Leptonic Decays*, Phys. Rev. Lett. **10** (1963) 531.

[83] CDF Collaboration, T. Aaltonen *et al.*, *First flavor-tagged determination of bounds on mixing-induced CP violation in $B_s^0 \to J/\psi\phi$ decays*, Phys. Rev. Lett. **100** (2008) 161802, arXiv:0712.2397.

[84] D0 Collaboration, V. Abazov *et al.*, *Measurement of B_s^0 mixing parameters from the flavor-tagged decay $B_s^0 \to J/\psi\phi$*, Phys. Rev. Lett. **101** (2008) 241801, arXiv:0802.2255.

[85] CDF Collaboration, T. Aaltonen *et al.*, *Measurement of the CP-violating phase $\beta_s^{J/\Psi\phi}$ in $B_s^0 \to J/\Psi\phi$ decays with the CDF II detector*, Phys. Rev. **D85** (2012) 072002, arXiv:1112.1726.

[86] D0 Collaboration, V. M. Abazov *et al.*, *Measurement of the CP-violating phase $\phi_s^{J/\psi\phi}$ using the flavor-tagged decay $B_s^0 \to J/\psi\phi$ in 8 fb^{-1} of $p\bar{p}$ collisions*, Phys. Rev. **D85** (2012) 032006, arXiv:1109.3166.

[87] LHCb collaboration, R. Aaij *et al.*, *Measurement of the CP-violating phase ϕ_s in the decay $B_s^0 \to J/\psi\phi$*, Phys. Rev. Lett. **108** (2012) 101803, arXiv:1112.3183.

[88] LHCb collaboration, R. Aaij *et al.*, *Measurement of the CP violating phase ϕ_s in $\bar{B}_s^0 \to J/\psi f_0(980)$*, Phys. Lett. **B707** (2012) 497, arXiv:1112.3056.

[89] C. Abellan Beteta *et al.*, *Time alignment of the front end electronics of the LHCb calorimeters*, JINST **7** (2012) P08020.

[90] E. Aguilo *et al.*, *Backsplash testbeam results for the SPD subdetector of LHCb*, Nucl. Instrum. Meth. **A546** (2005) 438.

[91] L. Garrido, D. Gascon, R. Miquel, and D. Peralta, *Results of a tagged photon test beam for the scintillator pad detector*, CERN-LHCb-2000-032 (2000).

[92] LHCb collaboration, R. Aaij *et al.*, *Updated measurements of exclusive J/ψ and $\psi(2S)$ production cross-sections in pp collisions at $\sqrt{s} = 7$ TeV*, J. Phys. **G41** (2014) 055002, arXiv:1401.3288.

[93] LHCb collaboration, R. Aaij *et al.*, *Observation of charmonium pairs produced exclusively in pp collisions*, arXiv:1407.5973, submitted to J. Phys. G.

[94] LHCb collaboration, R. Aaij *et al.*, *Measurement of the ratio of branching fractions $\mathcal{B}(B^0 \to K^{*0}\gamma)/\mathcal{B}(B_s^0 \to \phi\gamma)$ and the direct CP asymmetry in $B^0 \to K^{*0}\gamma$*, Nucl. Phys. **B867** (2013) 1, arXiv:1209.0313.

[95] LHCb collaboration, R. Aaij *et al.*, *Observation of $B_s^0 \to \chi_{c1}\phi$ decay and study of $B^0 \to \chi_{c1,2}K^{*0}$ decays*, Nucl. Phys. **B874** (2013) 663, arXiv:1305.6511.

[96] LHCb collaboration, R. Aaij *et al.*, *Observation of photon polarization in the $b \to s\gamma$ transition*, Phys. Rev. Lett. **112** (2014) 161801, arXiv:1402.6852.

[97] LHCb collaboration, R. Aaij *et al.*, *Evidence for the decay $X(3872) \to \psi(2S)\gamma$*, Nucl. Phys. **B886** (2014) 665, arXiv:1404.0275.

[98] RD36 Collaboration, P. Aspell *et al.*, *Energy and spatial resolution of a Shashlik calorimeter and a silicon preshower detector*, Nucl. Instrum. Meth. **A376** (1996) 17.

[99] J. Badier *et al.*, *Shashlik calorimeter: Beam test results*, Nucl. Instrum. Meth. **A348** (1994) 74.

[100] PHENIX Collaboration, L. Aphecetche *et al.*, *PHENIX calorimeter*, Nucl. Instrum. Meth. **A499** (2003) 521.

[101] G. David *et al.*, *Performance of the PHENIX EM calorimeter*, IEEE Trans. Nucl. Sci. **43** (1996) 1491.

[102] E. Tarkovsky, *The HERA-B electromagnetic calorimeter*, Nucl. Instrum. Meth. **A379** (1996) 515.

[103] HERA-B Collaboration, A. Zoccoli, *The electromagnetic calorimeter of the HERA-B experiment*, Nucl. Instrum. Meth. **A446** (2000) 246.

[104] G. Avoni *et al.*, *The electromagnetic calorimeter of the HERA-B experiment*, Nucl. Instrum. Meth. **A461** (2001) 332.

[105] G. Avoni *et al.*, *The electromagnetic calorimeter of the HERA-B experiment*, Nucl. Instrum. Meth. **A580** (2007) 1209.

[106] ALICE EMCal Collaboration, J. Allen *et al.*, *Performance of prototypes for the ALICE electromagnetic calorimeter*, Nucl. Instrum. Meth. **A615** (2010) 6, `arXiv:0912.2005`.

[107] ALICE Collaboration, T. C. Awes, *The ALICE electromagnetic calorimeter*, Nucl. Instrum. Meth. **A617** (2010) 5.

[108] A. Arefev *et al.*, *Beam test results of the LHCb electromagnetic calorimeter*, CERN-LHCb-2007-149 (2008).

[109] S. Barsuk *et al.*, *Fiber density and uniformity of response of LHCb electromagnetic calorimeter*, CERN-LHCb-2000-034 (2000).

[110] A. Arefev *et al.*, *A study of light collection in Shashlik calorimeters*, Instrum. Exp. Tech. **51** (2008) 511.

[111] S. Barsuk, *The Shashlik electro-magnetic calorimeter for the LHCb experiment*, World Scientific Publishing, Proceedings of the conference on calorimetry in particle physics (2004) 61.

[112] S. Barsuk *et al.*, *Radiation damage of LHCb electromagnetic calorimeter*, CERN-LHCb-2000-033 (2000).

[113] S. Barsuk, *The LHCb calorimeter performance and its expected radiation-induced degradation*, IEEE Trans. Nucl. Sci. **57** 1447.

[114] S. Funaki *et al.*, *Beam test of radiation hardness of a scintillating tile / fiber calorimeter*, Nucl. Instrum. Meth. **A317** (1992) 123.

[115] S. Han *et al.*, *Radiation hardness tests of scintillating tile / WLS fiber calorimeter modules*, Nucl. Instrum. Meth. **A365** (1995) 337.

[116] G. Britvich *et al.*, *The HCAL optics radiation damage study*, CERN-LHCb-2000-037 (2000).

[117] CMS Collaboration, *CMS, the Compact Muon Solenoid: Technical proposal*, CERN-LHCC-94-38 (1994).

[118] ATLAS Collaboration, *ATLAS tile calorimeter: Technical design report*, CERN-LHCC-96-42 (1996).

[119] Y. P. V.G. Vasilchenko, *Study of radiation hardness of polimer scintillators and optical fibers*, Pribory i Tech. Exp. **1** (1994) 86.

[120] V. Vasilchenko *et al.*, *Study of radiation hardness of plastic scintillators*, Pribory i Tech. Exp. **5** (1995) 85.

[121] B. Semenov, *Results of gamma-ray irradiation of the scintillator materials for Shashlyk type electromagnetic calorimeters*, Pribory i Tech. Exp. **5** (1994) 58.

[122] A. Arefev *et al.*, *Design, construction, quality control and performance study with cosmic rays of modules for the LHCb electromagnetic calorimeter*, CERN-LHCb-2007-148 (2007).

[123] CMS Collaboration, *CMS: The hadron calorimeter technical design report*, .

[124] C. Beigbeder-Beau *et al.*, *The front-end electronics for LHCb calorimeters*, CERN-LHCb-2000-028 (2000).

[125] S. Akimenko *et al.*, *Characteristics of electromagnetic calorimeter module with wave shifting fiber spiral light collection*, IFVE-87-132 (1987).

[126] CALEIDO Collaboration, A. Benvenuti *et al.*, *A shashlik calorimeter with longitudinal segmentation for a linear collider*, Nucl. Instrum. Meth. **A461** (2001) 373.

[127] A. K. Mann *et al.*, *Long baseline neutrino oscillation experiment at the AGS: Proposal*, BNL-PROPOSAL-889 (1993).

[128] L. S. Littenberg, *The CP violating decay* $K_L^0 \to \pi^0\nu\overline{\nu}$, Phys. Rev. **D39** (1989) 3322.

[129] G. Atoian *et al.*, *Development of Shashlyk calorimeter for KOPIO*, Nucl. Instrum. Meth. **A531** (2004) 467, arXiv:physics/0310047.

[130] G. Atoian *et al.*, *An improved Shashlyk calorimeter*, Nucl. Instrum. Meth. **A584** (2008) 291, arXiv:0709.4514.

[131] D. Morozov *et al.*, *Test beam study of the PANDA shashlyk calorimeter prototype*, J. Phys. Conf. Ser. **160** (2009) 012021.

[132] N. Anfimov *et al.*, *Shashlyk EM calorimeter prototype readout by MAPD with superhigh pixel density for COMPASS II*, Nucl. Instrum. Meth. **A718** (2013) 75.

[133] BESIII Collaboration, M. Ablikim *et al.*, *Measurement of the integrated luminosities of the data taken by BESIII at* $\sqrt{s} = 3.650$ *and* 3.773 GeV, arXiv:1307.2022.

[134] LHCb collaboration, R. Aaij *et al.*, *Measurement of* J/ψ *production in pp collisions at* $\sqrt{s} = 7$ *TeV*, Eur. Phys. J. **C71** (2011) 1645, arXiv:1103.0423.

[135] LHCb collaboration, R. Aaij *et al.*, *Measurement of* J/ψ *polarization in pp collisions at* $\sqrt{s} = 7$ *TeV*, Eur. Phys. J. **C73** (2013) 2631, arXiv:1307.6379.

[136] LHCb collaboration, R. Aaij *et al.*, *Measurement of* $\psi(2S)$ *meson production in pp collisions at* $\sqrt{s} = 7$ *TeV*, Eur. Phys. J. **C72** (2012) 2100, arXiv:1204.1258.

[137] S. Barsuk, J. He, E. Kou, and B. Viaud, *Investigating charmonium production at LHC with the* $p\bar{p}$ *final state*, Phys. Rev. **D86** (2012) 034011, arXiv:1202.2273.

[138] LHCb collaboration, R. Aaij *et al.*, *Measurement of* $\eta_c(1S)$ *production via the decay* $\eta_c \to p\bar{p}$, LHCb-PAPER-2014-029, in preparation.

[139] BES Collaboration, J. Bai *et al.*, *Measurement of branching ratios for* η_c *hadronic decays*, Phys. Lett. **B578** (2004) 16, arXiv:hep-ex/0308073.

[140] W. Caswell and G. Lepage, *Effective Lagrangians for bound state problems in QED, QCD, and other field theories*, Phys. Lett. **B167** (1986) 437.

[141] G. T. Bodwin, E. Braaten, and G. P. Lepage, *Rigorous QCD analysis of inclusive annihilation and production of heavy quarkonium*, Phys. Rev. **D51** (1995) 1125, arXiv:hep-ph/9407339.

[142] V. Kartvelishvili, A. Likhoded, and S. Slabospitsky, *D meson and ψ meson production in hadronic interactions*, Sov. J. Nucl. Phys. **28** (1978) 678.

[143] E. L. Berger and D. L. Jones, *Inelastic photoproduction of J/ψ and Υ by gluons*, Phys. Rev. **D23** (1981) 1521.

[144] R. Baier and R. Ruckl, *Hadronic collisions: a quarkonium factory*, Z. Phys. **C19** (1983) 251.

[145] J. Lansberg, *J/ψ production at $\sqrt{s} = 1.96$ and 7 TeV: Color-Singlet Model, NNLO* and polarisation*, J. Phys. **G38** (2011) 124110, arXiv:1107.0292.

[146] M. Beneke and . Kramer, Michael, *Direct J/ψ and ψ' polarization and cross-sections at the Tevatron*, Phys. Rev. **D55** (1997) 5269, arXiv:hep-ph/9611218.

[147] M. Cacciari, M. Greco, M. L. Mangano, and A. Petrelli, *Charmonium production at the Tevatron*, Phys. Lett. **B356** (1995) 553, arXiv:hep-ph/9505379.

[148] P. L. Cho and A. K. Leibovich, *Color octet quarkonia production*, Phys. Rev. **D53** (1996) 150, arXiv:hep-ph/9505329.

[149] E. Braaten and S. Fleming, *Color octet fragmentation and the ψ' surplus at the Tevatron*, Phys. Rev. Lett. **74** (1995) 3327, arXiv:hep-ph/9411365.

[150] CMS Collaboration, S. Chatrchyan *et al.*, *J/ψ and $\psi(2S)$ production in pp collisions at $\sqrt{s} = 7$ TeV*, JHEP **1202** (2012) 011, arXiv:1111.1557.

[151] ATLAS Collaboration, G. Aad *et al.*, *Measurement of the differential cross-sections of inclusive, prompt and non-prompt J/ψ production in proton-proton collisions at $\sqrt{s} = 7$ TeV*, Nucl. Phys. **B850** (2011) 387, arXiv:1104.3038.

[152] ALICE Collaboration, B. Abelev *et al.*, *Measurement of prompt J/ψ and beauty hadron production cross sections at mid-rapidity in pp collisions at $\sqrt{s} = 7$ TeV*, JHEP **1211** (2012) 065, arXiv:1205.5880.

[153] Y.-Q. Ma, K. Wang, and K.-T. Chao, *J/ψ (ψ') production at the Tevatron and LHC at $O(\alpha_s^4 v^4)$ in nonrelativistic QCD*, Phys. Rev. Lett. **106** (2011) 042002, arXiv:1009.3655.

[154] CMS Collaboration, S. Chatrchyan *et al.*, *Measurement of the $\Upsilon(1S), \Upsilon(2S)$, and $\Upsilon(3S)$ cross sections in pp collisions at $\sqrt{s} = 7$ TeV*, Phys. Lett. **B727** (2013) 101, arXiv:1303.5900.

[155] CDF Collaboration, F. Abe *et al.*, *Inclusive J/ψ, $\psi(2S)$ and b quark production in $\bar{p}p$ collisions at $\sqrt{s} = 1.8$ TeV*, Phys. Rev. Lett. **69** (1992) 3704.

[156] CDF Collaboration, A. Abulencia *et al.*, *Polarization of J/ψ and $\psi(2S)$ mesons produced in $p\bar{p}$ collisions at $\sqrt{s} = 1.96$ TeV*, Phys. Rev. Lett. **99** (2007) 132001, arXiv:0704.0638.

[157] ALICE Collaboration, B. Abelev *et al.*, *J/ψ polarization in pp collisions at $\sqrt{s} = 7$ TeV*, Phys. Rev. Lett. **108** (2012) 082001, arXiv:1111.1630.

[158] CMS Collaboration, S. Chatrchyan *et al.*, *Measurement of the prompt J/ψ and $\psi(2S)$ polarizations in pp collisions at $\sqrt{s} = 7$ TeV*, Phys. Lett. **B727** (2013) 381, arXiv:1307.6070.

[159] HERA-B Collaboration, I. Abt *et al.*, *Angular distributions of leptons from J/ψ produced in* 920 GeV *fixed-target proton-nucleus collisions*, Eur. Phys. J. **C60** (2009) 517, arXiv:0901.1015.

[160] LHCb collaboration, R. Aaij *et al.*, *Measurement of $\psi(2S)$ polarisation in pp collisions at $\sqrt{s} = 7$ TeV*, Eur. Phys. J. **C74** (2014) 2872, arXiv:1403.1339.

[161] M. Butenschoen and B. A. Kniehl, *J/ψ polarization at Tevatron and LHC: Nonrelativistic-QCD factorization at the crossroads*, Phys. Rev. Lett. **108** (2012) 172002, arXiv:1201.1872.

[162] B. Gong, L.-P. Wan, J.-X. Wang, and H.-F. Zhang, *Polarization for prompt J/ψ, $\psi(2S)$ production at the Tevatron and LHC*, Phys. Rev. Lett. **110** (2013) 042002, arXiv:1205.6682.

[163] K.-T. Chao *et al.*, *J/ψ Polarization at Hadron Colliders in Nonrelativistic QCD*, Phys. Rev. Lett. **108** (2012) 242004, arXiv:1201.2675.

[164] Y. Lemoigne *et al.*, *Measurement of hadronic production of the χ 1++ (3507) and the χ 2++ (3553) through their radiative decay to J/ψ*, Phys. Lett. **B113** (1982) 509.

[165] HERA-B Collaboration, I. Abt *et al.*, *Production of the charmonium states χ_{c1} and χ_{c2} in proton nucleus interactions at $\sqrt{s} = 41.6\,\text{GeV}$*, Phys. Rev. **D79** (2009) 012001, arXiv:0807.2167.

[166] CDF Collaboration, A. Abulencia *et al.*, *Measurement of $\sigma_{\chi_{c2}}\mathcal{B}(\chi_{c2} \to J/\psi\gamma)/\sigma_{\chi_{c1}}\mathcal{B}(\chi_{c1} \to J/\psi\gamma)$ in $p\bar{p}$ collisions at $\sqrt{s} = 1.96\ TeV$*, Phys. Rev. Lett. **98** (2007) 232001, arXiv:hep-ex/0703028.

[167] CMS Collaboration, S. Chatrchyan *et al.*, *Measurement of the relative prompt production rate of χ_{c2} and χ_{c1} in pp collisions at $\sqrt{s} = 7\ TeV$*, Eur. Phys. J. **C72** (2012) 2251, arXiv:1210.0875.

[168] A. Likhoded, A. Luchinsky, and S. Poslavsky, *Hadronic production of χ_c-mesons at LHC*, arXiv:1305.2389.

[169] LHCb collaboration, R. Aaij *et al.*, *Exclusive J/ψ and $\psi(2S)$ production in pp collisions at $\sqrt{s} = 7\ TeV$*, J. Phys. **G40** (2013) 045001, arXiv:1301.7084.

[170] ZEUS Collaboration, S. Chekanov *et al.*, *Exclusive photoproduction of J/ψ mesons at HERA*, Eur. Phys. J. **C24** (2002) 345, arXiv:hep-ex/0201043.

[171] H1 Collaboration, A. Aktas *et al.*, *Elastic J/ψ production at HERA*, Eur. Phys. J. **C46** (2006) 585, arXiv:hep-ex/0510016.

[172] H1 Collaboration, C. Alexa *et al.*, *Elastic and proton-dissociative photoproduction of J/ψ mesons at HERA*, Eur. Phys. J. **C73** (2013) 2466, arXiv:1304.5162.

[173] CDF Collaboration, T. Aaltonen *et al.*, *Observation of exclusive charmonium production and $\gamma\gamma \to \mu^+\mu^-$ in $p\bar{p}$ collisions at $\sqrt{s} = 1.96\ TeV$*, Phys. Rev. Lett. **102** (2009) 242001, arXiv:0902.1271.

[174] H1 Collaboration, C. Adloff *et al.*, *Diffractive photoproduction of $\psi(2S)$ mesons at HERA*, Phys. Lett. **B541** (2002) 251, arXiv:hep-ex/0205107.

[175] M. Ryskin, *Diffractive J/ψ electroproduction in LLA QCD*, Z. Phys. **C57** (1993) 89.

[176] F. Maltoni and A. Polosa, *Observation potential for η_b at the Tevatron*, Phys. Rev. **D70** (2004) 054014, arXiv:hep-ph/0405082.

[177] S. S. Biswal and K. Sridhar, *η_c production at the Large Hadron Collider*, J. Phys. **G39** (2012) 015008, arXiv:1007.5163.

[178] A. Petrelli *et al.*, *NLO production and decay of quarkonium*, Nucl. Phys. **B514** (1998) 245, arXiv:hep-ph/9707223.

[179] J. H. Kuhn and E. Mirkes, *QCD corrections to toponium production at hadron colliders*, Phys. Rev. **D48** (1993) 179, arXiv:hep-ph/9301204.

[180] I. I. Bigi and A. Sanda, *Notes on the observability of CP violations in B decays*, Nucl. Phys. **B193** (1981) 85.

[181] CDF Collaboration, F. Abe *et al.*, *Observation of $B^+ \to \psi(2S)K^+$ and $B^0 \to \psi(2S)K^{*0}(892)$ decays and measurements of B meson branching fractions into J/ψ and $\psi(2S)$ final states*, Phys. Rev. **D58** (1998) 072001, arXiv:hep-ex/9803013.

[182] LHCb collaboration, R. Aaij *et al.*, *Measurement of relative branching fractions of B decays to $\psi(2S)$ and J/ψ mesons*, Eur. Phys. J. **C72** (2012) 2118, arXiv:1205.0918.

[183] LHCb collaboration, R. Aaij *et al.*, *Observations of $B^0_s \to \psi(2S)\eta$ and $B^0_{(s)} \to \psi(2S)\pi^+\pi^-$ decays*, Nucl. Phys. **B871** (2013) 403 , arXiv:1302.6354.

[184] CDF Collaboration, A. Abulencia *et al.*, *Observation of $B^0_s \to \psi(2S)\phi$ and measurement of ratio of branching fractions $\mathcal{B}(B^0_s \to \psi(2S)\phi)/\mathcal{B}(B^0_s \to J/\psi\,\phi)$*, Phys. Rev. Lett. **96** (2006) 231801, arXiv:hep-ex/0602005.

[185] D0 Collaboration, V. Abazov *et al.*, *Relative rates of B meson decays into $\psi(2S)$ and J/ψ mesons*, Phys. Rev. **D79** (2009) 111102, arXiv:0805.2576.

[186] Belle Collaboration, K. Abe *et al.*, *Study of charmonium decays into baryon-antibaryon pairs*, arXiv:hep-ex/0509020.

[187] BELLE Collaboration, J. Wei *et al.*, *Study of $B^+ \to p\bar{p}K^+$ and $B^+ \to p\bar{p}\pi^+$*, Phys. Lett. **B659** (2008) 80, arXiv:0706.4167.

[188] BaBar Collaboration, B. Aubert *et al.*, *Measurement of the $B^+ \to p\bar{p}K^+$ branching fraction and study of the decay dynamics*, Phys. Rev. **D72** (2005) 051101, arXiv:hep-ex/0507012.

[189] LHCb collaboration, R. Aaij *et al.*, *Studies of the decays $B^+ \to p\bar{p}h^+$ and observation of $B^+ \to \bar{\Lambda}(1520)p$*, Phys. Rev. **D88** (2013) 052015, arXiv:1307.6165.

[190] LHCb collaboration, R. Aaij *et al.*, *Measurements of the branching fractions of $B^+ \to p\bar{p}K^+$ decays*, Eur. Phys. J. **C73** (2013) 2462, arXiv:1303.7133.

[191] CLEO Collaboration, S. Anderson *et al.*, *Measurements of inclusive $B \to \psi$ production*, Phys. Rev. Lett. **89** (2002) 282001, arXiv:hep-ex/0207059.

[192] CLEO Collaboration, S. Chen *et al.*, *Study of χ_{c1} and χ_{c2} meson production in B meson decays*, Phys. Rev. **D63** (2001) 031102, arXiv:hep-ex/0009044.

[193] Belle Collaboration, K. Abe *et al.*, *Observation of χ_{c2} production in B meson decay*, Phys. Rev. Lett. **89** (2002) 011803, arXiv:hep-ex/0202028.

[194] BaBar Collaboration, B. Aubert *et al.*, *Study of inclusive production of charmonium mesons in B decay*, Phys. Rev. **D67** (2003) 032002, arXiv:hep-ex/0207097.

[195] CLEO Collaboration, R. Balest *et al.*, *Inclusive decays of B mesons to charmonium*, Phys. Rev. **D52** (1995) 2661.

[196] DELPHI Collaboration, P. Abreu *et al.*, *J/ψ production in the hadronic decays of the Z*, Phys. Lett. **B341** (1994) 109.

[197] L3 Collaboration, O. Adriani *et al.*, *χ_c production in hadronic Z decays*, Phys. Lett. **B317** (1993) 467.

[198] ALEPH Collaboration, D. Buskulic *et al.*, *Measurements of mean lifetime and branching fractions of b hadrons decaying to J/ψ*, Phys. Lett. **B295** (1992) 396.

[199] M. Cacciari, M. Greco, and P. Nason, *The P(T) spectrum in heavy flavor hadroproduction*, JHEP **9805** (1998) 007, arXiv:hep-ph/9803400.

[200] M. Beneke, F. Maltoni, and I. Rothstein, *QCD analysis of inclusive B decay into charmonium*, Phys. Rev. **D59** (1999) 054003, arXiv:hep-ph/9808360.

[201] M. Beneke, G. Schuler, and S. Wolf, *Quarkonium momentum distributions in photoproduction and B decay*, Phys. Rev. **D62** (2000) 034004, arXiv:hep-ph/0001062.

[202] T. Burns *et al.*, *The momentum distribution of J/ψ in B decays*, Phys. Rev. **D83** (2011) 114029, arXiv:1104.1781.

[203] Y. Fan, J.-Z. Li, C. Meng, and K.-T. Chao, *B-meson semi-inclusive decay to 2^{-+} charmonium in NRQCD and X(3872)*, Phys. Rev. **D85** (2012) 034032, arXiv:1112.3625.

[204] B. A. Kniehl and G. Kramer, *Inclusive J/ψ and ψ_{2S} production from B decay in $p\bar{p}$ collisions*, Phys. Rev. **D60** (1999) 014006, arXiv:hep-ph/9901348.

[205] P. Bolzoni, B. A. Kniehl, and G. Kramer, *Inclusive J/ψ and $\psi(2S)$ production from b-hadron decay in $p\bar{p}$ and pp collisions*, Phys. Rev. **D88** (2013), no. 7 074035, arXiv:1309.3389.

[206] S. J. Brodsky and G. P. Lepage, *Helicity selection rules and tests of gluon spin in exclusive QCD processes*, Phys. Rev. **D24** (1981) 2848.

[207] Belle Collaboration, C.-H. Wu *et al.*, *Study of J/ψ to $p\overline{p}$, $\Lambda\overline{\Lambda}$ and observation of $\eta(c) \to \Lambda\overline{\Lambda}$ at Belle*, Phys. Rev. Lett. **97** (2006) 162003, arXiv:hep-ex/0606022.

[208] MARK-III Collaboration, R. Baltrusaitis *et al.*, *Observation of the decay $\eta_c \to \phi\phi$ and determination of the η_c spin parity*, Phys. Rev. Lett. **52** (1984) 2126.

[209] CLEO Collaboration, R. Mitchell *et al.*, *J/ψ and $\psi(2S)$ radiative decays to $\eta_{(c)}$*, Phys. Rev. Lett. **102** (2009) 011801, arXiv:0805.0252.

[210] BESIII Collaboration, M. Ablikim *et al.*, *Measurements of the mass and width of the η_c using $\psi' \to \gamma\eta_c$*, Phys. Rev. Lett. **108** (2012) 222002, arXiv:1111.0398.

[211] BESIII Collaboration, M. Ablikim *et al.*, *Study of $\psi(3686) \to \pi^0 h_c, h_c \to \gamma\eta_c$ via η_c exclusive decays*, Phys. Rev. **D86** (2012) 092009, arXiv:1209.4963.

[212] CLEO Collaboration, D. Asner *et al.*, *Observation of η_c' production in gamma gamma fusion at CLEO*, Phys. Rev. Lett. **92** (2004) 142001, arXiv:hep-ex/0312058.

[213] BaBar Collaboration, B. Aubert *et al.*, *Measurement of double charmonium production in e^+e^- annihilations at $\sqrt{s} = 10.6\,\text{GeV}$*, Phys. Rev. **D72** (2005) 031101, arXiv:hep-ex/0506062.

[214] BaBar Collaboration, P. del Amo Sanchez *et al.*, *Observation of $\eta_c(1S)$ and $\eta_c(2S)$ decays to $K^+K^-\pi^+\pi^-\pi^0$ in two-photon interactions*, Phys. Rev. **D84** (2011) 012004, arXiv:1103.3971.

[215] Belle Collaboration, K. Abe *et al.*, *Observation of a new charmonium state in double charmonium production in e^+e^- annihilation at $\sqrt{s} \sim 10.6\,\text{GeV}$*, Phys. Rev. Lett. **98** (2007) 082001, arXiv:hep-ex/0507019.

[216] Belle collaboration, A. Vinokurova *et al.*, *Study of $B^\pm \to K^\pm(K^0_S K\pi)^0$ decay and determination of η_c and $\eta_c(2S)$ parameters*, Phys. Lett. **B706** (2011) 139, arXiv:1105.0978.

[217] BESIII Collaboration, M. Ablikim *et al.*, *Evidence for $\eta_c(2S)$ in $\psi(3686) \to \gamma K^0_S K^\pm\pi^\mp\pi^+\pi^-$*, Phys. Rev. **D87** (2013), no. 5 052005, arXiv:1301.1476.

[218] BES Collaboration, M. Ablikim *et al.*, *First observation of the M1 transition $\psi(3686) \to \gamma\eta_c(2S)$*, Phys. Rev. Lett. **109** (2012) 042003, arXiv:1205.5103.

[219] LHCb collaboration, R. Aaij *et al.*, *Measurement of the Λ_b^0, Ξ_b^- and Ω_b^- baryon masses*, Phys. Rev. Lett. **110** (2013) 182001, arXiv:1302.1072.

[220] M. Bartsch, G. Buchalla, and C. Kraus, *$B \to V(L)V(L)$ decays at Next-to-Leading Order in QCD*, arXiv:0810.0249.

[221] M. Beneke, J. Rohrer, and D. Yang, *Branching fractions, polarisation and asymmetries of $B \to VV$ decays*, Nucl. Phys. **B774** (2007) 64, arXiv:hep-ph/0612290.

[222] H.-Y. Cheng and C.-K. Chua, *QCD factorization for charmless hadronic B_s^0 decays revisited*, Phys. Rev. **D80** (2009) 114026, arXiv:0910.5237.

[223] A. L. Kagan, *Polarization in $B \to VV$ decays*, Phys. Lett. **B601** (2004) 151, arXiv:hep-ph/0405134.

[224] A. Datta *et al.*, *Testing explanations of the $B \to \phi K^*$ polarization puzzle*, Phys. Rev. **D76** (2007) 034015, arXiv:0705.3915.

[225] C.-H. Chen and C.-Q. Geng, *Scalar interactions to the polarizations of $B \to \phi K^*$*, Phys. Rev. **D71** (2005) 115004, arXiv:hep-ph/0504145.

[226] C.-S. Huang, P. Ko, X.-H. Wu, and Y.-D. Yang, *MSSM anatomy of the polarization puzzle in $B \to \phi K^*$ decays*, Phys. Rev. **D73** (2006) 034026, arXiv:hep-ph/0511129.

[227] A. Ali *et al.*, *Charmless non-leptonic B_s decays to PP, PV and VV final states in the pQCD approach*, Phys. Rev. **D76** (2007) 074018, arXiv:hep-ph/0703162.

[228] CDF Collaboration, D. Acosta *et al.*, *First evidence for $B_s^0 \to \phi\phi$ decay and measurements of branching ratio and A_{CP} for $B^+ \to \phi K^+$*, Phys. Rev. Lett. **95** (2005) 031801, arXiv:hep-ex/0502044.

[229] CDF Collaboration, T. Aaltonen *et al.*, *Measurement of polarization and search for CP-violation in $B_s^0 \to \phi\phi$ decays*, Phys. Rev. Lett. **107** (2011) 261802, arXiv:1107.4999.

[230] SLD Collaboration, K. Abe *et al.*, *Search for charmless hadronic decays of B mesons with the SLD detector*, Phys. Rev. **D62** (2000) 071101, arXiv:hep-ex/9910050.

[231] LHCb collaboration, R. Aaij *et al.*, *Measurement of b hadron production fractions in 7 TeV pp collisions*, Phys. Rev. **D85** (2012) 032008, arXiv:1111.2357.

[232] LHCb collaboration, R. Aaij *et al.*, *Measurement of the fragmentation fraction ratio f_s/f_d and its dependence on B meson kinematics*, JHEP **04** (2013) 001, arXiv:1301.5286.

[233] DM2 collaboration, D. Bisello *et al.*, *Study of the η_c decays*, Nucl. Phys. **B350** (1991) 1.

[234] BES Collaboration, M. Ablikim *et al.*, *Experimental study of η_c decays into vector-vector final states*, Phys. Rev. **D72** (2005) 072005, arXiv:hep-ex/0507100.

[235] C. Zemach, *Three pion decays of unstable particles*, Phys. Rev. **133** (1964) B1201.